INTEGRATION OF BIOMECHANICAL MODELS INTO IMAGE REGISTRATION IN THE PRESENCE OF LARGE DEFORMATIONS

BJOERN EIBEN

A dissertation submitted in partial fulfilment
of the requirements for the degree of
Doctor of Philosophy
of
UCL

Centre for Medical Image Computing
University College London
March 2016

DECLARATION

I, Bjoern Eiben, confirm that the work presented in this thesis is my own. Where information has been derived from other sources, I confirm that this has been indicated in the thesis.

London, March 2016

Bjoern Eiben

ABSTRACT

Prone-to-supine breast image registration has potential application in the fields of surgical and radiotherapy planning, and image guided interventions. However, breast image registration of three-dimensional images acquired in different patient positions is a challenging problem, due to large deformations induced to the soft breast tissue caused by the change in gravity loading. Biomechanical modelling is a promising tool to predict gravity induced deformations, however such simulations alone are unlikely to produce good alignment due to inter-patient variability and image acquisition related influences on the breast shape.

This thesis presents a symmetric, biomechanical simulation based registration framework which aligns images in a central, stress-free configuration. Soft tissue is modelled as a neo-Hookean material and external forces are considered as the main source of deformation in the original images. The framework successively applies image derived forces directly into the unloading simulation in place of a subsequent image registration step. This results in a biomechanically constrained deformation. Using a finite difference scheme enables simulations to be performed directly in the image space. Motion constrained boundary conditions have been incorporated which can capture tangential motion of membranes and fasciae. The accuracy of the approach is assessed by measuring the target registration error (TRE) using nine prone MRI and supine CT image pairs, one prone-supine CT image pair, and four prone-supine MRI image pairs. The registration reduced the combined mean TRE for all clinical data sets from initially 69.7 mm to 5.6 mm.

Prone-supine image pairs might not always be available in the clinical breast cancer workflow, especially prior to surgery. Hence an alternative surface driven registration methodology was also developed that incorporates biomechanical simulations, material parameter optimisation, and constrained surface matching. For three prone MR images and corresponding supine CT-derived surfaces a final mean TRE of 10.0 mm was measured.

> *How wonderful it is*
> *that nobody need wait a single moment*
> *before starting to improve the world.*
>
> — Anne Frank

ACKNOWLEDGMENTS

I feel very lucky and privileged to have had the opportunity to share the journey towards my PhD with a fantastic group of people and I would like to thank all of them for their guidance, friendship, and continuing support.

At CMIC I especially would like to thank Dave Hawkes, my primary supervisor. Dave always provided guidance by reminding me of the bigger picture and asking the right questions. His insatiable curiosity is a great motivation for me. Further I would like to thank John Hipwell, my co-supervisor, for always having an open door – and more importantly an open ear – for my concerns and needs. His friendly support, always with a hint of humour, made it a pleasure working with him. Vasilis Vavourakis taught me a great deal about biomechanical modelling, for which I would like to thank him. His dedication to research is infectious.

My supervisors at Philips Research in Hamburg, Sven Kabus, Thomas Bülow, and Cristian Lorenz, also provided amazing guidance and hospitality. We had very fruitful, productive discussions and a lot of experiments originated from our meetings. I could make great use of their combined expertise in mathematics and physics, and would like to thank them for the fantastic experiences we had together. The financial support from Philips Research, who completely funded my PhD, is highly appreciated.

Furthermore it was – and still is – a pleasure working together with everyone in the Breast Cancer Imaging Group, Thomy, Sara, Colleen, Peter and Rene, and everyone else at CMIC.

I highly value the truly multi-disciplinary experiences that I have made in the Picture project. It provided great insight into the clinical reality of breast cancer.

Thank you Mo Keshtgar and Norman Williams for helping me to get all approvals required for accessing and processing the MRI-CT data pairs. Furthermore, I would like to thank everyone else involved in the project but especially Jörg Sabczynski, Dominik Kutra, Hans Barschdorf, Kirsten Meetz, and Stewart Young from Philips Research.

I would also like to express thanks to the supervisors of my previous studies back in Germany, who inspired and encouraged me to start a PhD in the first place. These are in particular Marc Hensel, Christoph Palm, and Dietmar Kunz.

My whole family showed tremendous support during all those years of studies. I especially would like to thank my mum and my brother for always being there for me. Together with the whole rest of my family they provided me with a feeling of security and belonging – regardless of the distance.

Finally, I want to thank Meike, who always reminded me of the importance to enjoy what I am doing, even during difficult times.

Thank you all!

CONTENTS

List of Figures 12

List of Tables 24

List of Symbols 27

1 INTRODUCTION 35
- 1.1 Clinical Motivation . . . 36
- 1.2 Contribution . . . 38
- 1.3 Thesis Outline . . . 39

2 BACKGROUND AND STATE OF THE ART 41
- 2.1 Concepts in Continuum Mechanics . . . 41
  - 2.1.1 Displacement, Deformation, Strain . . . 42
  - 2.1.2 Hyperelastic Materials . . . 45
  - 2.1.3 Conservation Laws . . . 48
- 2.2 Breast Anatomy . . . 49
- 2.3 Biomechanical Modelling of Breast Tissue Deformations . . . 49
  - 2.3.1 Tissue Classes and Elasticities . . . 50
  - 2.3.2 Boundary Conditions and Loading . . . 54
- 2.4 Image Registration and Biomechanics . . . 57
- 2.5 Chapter Conclusion . . . 60

3 BIOMECHANICAL MODELS AND SIMULATIONS 61
- 3.1 PICTURE: Project Objectives . . . 63
- 3.2 FE-Model Generation . . . 65
  - 3.2.1 Image Segmentation . . . 65
  - 3.2.2 Mesh Generation . . . 66
  - 3.2.3 Model Assembly . . . 69
- 3.3 Obtaining the Unloaded Configuration . . . 70
  - 3.3.1 Image Data, Shape Phantom and Biomechnical Model Generation . . . 73
  - 3.3.2 Unloading Strategies . . . 74

3.3.3 Evaluation 77
3.3.4 Results 82
3.3.5 Discussion 86
3.4 Chapter Conclusion 87
4 BIOMECHANICAL REGISTRATION: INTENSITY DRIVEN 89
4.1 Sequential Registration Approach 93
4.1.1 Image Data 94
4.1.2 Biomechanical Model Construction 95
4.1.3 Zero Gravity State Estimation 96
4.1.4 Image Registration 96
4.1.5 Results 97
4.1.6 Discussion 100
4.2 Integrative Registration Approach 100
4.2.1 Comparison: Registration and Simulation 101
4.2.2 Overview of the Image Alignment Approach 105
4.2.3 3D Finite Difference Simulation 107
4.2.4 Material Optimisation 118
4.2.5 Integration of Image Derived Forces 119
4.2.6 Numerical Phantom Datasets 121
4.2.7 Prone-Supine Registration Results of Numerical Phantom Data 122
4.2.8 Clinical Datasets 124
4.2.9 Prone-Supine Registration Results of Clinical Data 127
4.2.10 Discussion 137
4.3 Potential Clinical Applications 167
4.4 Chapter Conclusion 171
5 BIOMECHANICAL REGISTRATION: SURFACE DRIVEN 175
5.1 Surface Alignment Approach 177
5.1.1 Material Parameter Optimisation and Global Alignment . . . 177
5.1.2 Surface Warping 181
5.1.3 Volume Mesh Warping 185
5.2 Clinical Image and Surface Data 186
5.3 Surface Registration Results 186

5.4 Clinical Applications 191
5.4.1 Surgical Planning and Image Guided Surgery 193
5.4.2 Aesthetic Outcome Prediction of Breast Conserving Surgery . 194
5.5 Chapter Conclusions 197
6 CONCLUSION 201
6.1 Limitations 204
6.2 Future Work 206
6.2.1 Exploring Modelling of Tissue Loss 207
6.2.2 Exploring Translation to Clinical Practice 208
A LIST OF PUBLICATIONS 211
B APPENDIX 215
B.1 Rotation and Small Strain Tensor 215
B.2 Truncation error and the finite difference method 216
BIBLIOGRAPHY 217

LIST OF FIGURES

Figure 2.1 Patient specific biomechanical model generated from segmented MR image. (a) The different tissue classes are adipose (brown), fibroglandular tissue (orange), pectoral muscle (light blue) and chest (dark blue) and are used to define appropriate material properties to the biomechanical model (b). 50

Figure 3.1 Prone post-surgical CT (a-c) and pre-surgical MR (e-g) image of the same patient with corresponding post-surgical (d) and pre-surgical (h) photographs respectively. The segmentation of the breast tissue in the CT image is contoured by a red outline. In the MR image a clear medial contact between the breast and coil can be observed medially resulting in significant deformation. Not all deformation can be attributed to the MR acquisition position since surgery took place between the MRI and CT acquisition, however pre-(h) and post-surgical (d) photographs indicate only minor influence on the shape due to surgery. 63

Figure 3.2 Overview of the mesh generation steps involved. The procedure begins with the segmented binary-mask image of a patient-specific breast; then a high-density surface mesh is generated, which is subsequently processed (i.e. clipped, coarsened and labelled) in order to finally construct the volume FE grid. 65

Figure 3.3 (a) Orthogonal views of the binary mask image resulting from image segmentation. (b) High-density surface mesh generated using the marching cubes algorithm and a windowed-sinc smoothing filter. (c) The rotation of the field of view against the physical coordinate system is taken into account in the clipping algorithm. Note the angle between the upper boundary of the breast mesh and the z-axis. (d) Coarsened FE mesh with properly labelled triangular face elements. Skin surface is shown in green, axial clipping plane in yellow and lateral clipping plane in blue. 67

Figure 3.4 Sample points $\mathbf{s}_1$ to $\mathbf{s}_5$ derived from the tetrahedral element to sample the internal tissue segmentation. 70

Figure 3.5 Unloaded (or gravity-free) configuration numerical prediction of a patient-specific breast geometry using an inverse analysis approach as described in Eiben et al. (2013, 2014). . 71

Figure 3.6 Workflow of the iterative zero-gravity state recovery procedure $M3$. The original model $\mathbf{z}_{\text{prone}}$ is to be recovered by a forward loading simulation. An initial guess of the zero gravity state $\mathbf{Z}_0$ is established by simulating gravity in the direction opposite to the original loading (1). Subsequently all stresses in the model are set to zero and gravity is reapplied in the original direction (2). This allows the error between the simulation and original model the to be measured (3). The update of the reference state (4) is derived from the difference $\mathbf{d}_i$ between the gravity loading simulation in the prone and the original prone model. 75

Figure 3.7 First three iterations of the iterative unloading scheme $M3$. The figures show the error vectors $\mathbf{d}_i$ in the prone loaded configuration that is measured between the original model $\mathbf{z}_{\text{prone}}$ and the prone forward simulation $\mathbf{z}_i$ (c.f. step (3) in figure 3.6). Before these error vectors are used to update the estimate of the unloaded configuration, the vectors are warped using the deformation gradient $\mathbf{F}$. The corresponding transformed vectors are shown in figure 3.8. 78
Figure 3.8 First three iterations of the iterative unloading scheme $M3$. The figures show the vectors $s\mathbf{D}_i$ which are used to update the zero gravity estimate (c.f. step (4) in figure 3.6). The update is derived from the error $\mathbf{d}_i$ in the loaded configuration as shown in figure 3.7 by applying the inverse deformation gradient $\mathbf{F}^{-1}$. 79
Figure 3.9 Mean and maximum of the error magnitude $\|\mathbf{d}_i\|$ during the iterations i for unloading procedure $M3$. Figure (a) visualises the convergence, when the residual error vectors are directly used to update the zero-gravity estimate as proposed by Carter et al. (2008). A faster convergence can be observed in figure (b), when the inverse deformation gradient is used to project the error vectors to the unloaded configuration before updating the nodal position of the zero-gravity estimate accordingly (Eiben et al., 2013, 2014). 80
Figure 3.10 Initial (red) and end result (grey) of unloading method $M3$. The initial estimate is also equivalent to the final result of method $M1$. 80
Figure 3.11 Comparison strategy for the different inverse approaches $M1$, $M2$ and $M3$ for biomechanical finite element models (B) built from segmented MR images (S) in terms of relative nodal distances $d_{1,2}$, $d_{1,3}$ and $d_{2,3}$. 81

Figure 3.12 A generic breast shape phantom (ph) represents the known unloaded configuration. In a forward simulation step the phantom geometry is loaded with gravity as a body force into the prone (P), supine (S), and upright (U) positions. From these loaded configurations the unloaded state ($g = 0$) is recovered using the three inversion methods M_1, M_2 and M_3 resulting in the node positions $\mathbf{Z}$ with the corresponding subscripts. The error of the recovery can be quantified directly by comparing the node positions with those of the original shape model. For the sensitivity experiments the material stiffness of the unloading step was modified to the one used for the loading simulations. 82

Figure 3.13 Simulation results of the sensitivity experiments using the breast shaped phantom. The horizontal axis for all graphs is material parameter μ (see equation (3.1)) associated with the shear stiffness of the model and is given in Pascal. . . . 85

Figure 4.1 Outline of the workflow used to align prone and supine image data using biomechanical unloading simulations and intensity based free form deformation registration. 93

Figure 4.2 One landmark followed through all different stages of the alignment process. (a) Prone, (b) prone zero-gravity state, (c) supine zero-gravity state registered to prone reference state, (d) supine zero-gravity state and (e) supine. 99

Figure 4.3 Orthogonal slices through a numerical breast phantom without (green) and with gravity applied (red). The corresponding binary images were used as reference and template images for the hyperelastic registration experiments. 103

Figure 4.4 Deformation vector fields from image registration (red-yellow arrows) and simulation (blue arrows) and quantitative difference in terms of angle and length. Significant differences in the angle of the displacement vectors can be observed at the sides of the phantom, where the gravity loading causes displacement vectors tangential to the object boundary, whereas the registration produces a contraction. . 104

Figure 4.5 Overview of the biomechanically constrained registration procedure. In a first step the effect of gravity is removed from the prone and supine breast image assuming generic material parameters. In a second step the material parameters are repeatedly updated until the image similarity no longer improves. The final step involves activation of image derived forces which aim to correct modelling inaccuracies and generate the final aligned images in the unloaded configuration. 106

Figure 4.6 Simulation results for loading a compressible medium with a homogeneous body force using the finite difference scheme with (a,c) and without clustering present (b,d). A central slice through the 3D cube geometry shows the final node positions (a,b). The consecutive application of the differentiation operator was used to produce figures (a) and (c) and resulted in clustering artefacts that are characterised by irregular node distances (see arrows in magnified view). For figures (b) and (d) repeated differentiation during the computations was avoided by reformulating the problem as described in the text. This resulted in regular node distances and resolved the clustering problem. The corresponding node displacements are shown in figures (c) and (d). These displacements are measured along the blue vertical line shown in (a) and (b), which corresponds to the horizontal axis of (c) and (d). 112

Figure 4.7 Displacement vector field and the relation between the initial loaded (solid white) and recovered unloaded (orange outline) configuration of a simple box unloading experiment. 113

Figure 4.8 Loading and unloading experiment. The left box depicts the original unloaded configuration with dimensions $15 \times 15 \times 15\,\mathrm{mm}^3$ which was exposed to gravity loading (central image). From this loaded configuration, the unloaded one was recovered, using the presented image based unloading mechanism. 115

Figure 4.9 Surface based motion constraint. A discretised approximation of the target surface, shown as gray shaded voxels, is generated from the chest-pectoral muscle interface based on the segmented image. From this segmentation a displacement vector field is pre-calculated which points to the target surface. This is used during the iterative solution process to displace nodes back to the target which due to the underlying material response might have moved out of this region. 116

Figure 4.10 Intensity inversion of the prone T2 weighted MR image (a) is used to generate an image (b) which appears similar to a CT image (c) in terms of tissue contrast such that a mono modal image similarity measure and corresponding image forces can be used. 120

Figure 4.11 A simplified geometric phantom was used to evaluate the performance of the presented algorithm. A cylinder represents the chest wall (black line in first row) and the skin is given by the function value of a two-dimensional Gaussian function (grey area over the cylinder section). A mesh of this geometry is generated and the biomechanical finite element model is built to simulate the effect of prone and supine gravity loading. The simulated prone and supine displacements are then used to transform the glandular structure of an MR image into the prone and supine position. 121

Figure 4.12 Registration results for the simulated prone and supine images. The first column (a,d,g) shows the state of the prone image during the course of the registration procedure, the second column (b,e,h) the corresponding states of the supine image and the third column (c,f,i) the difference images. The first row represents the warped images after the unloading procedure with generic material parameters. Obviously the material parameters were chosen to be too soft and thus were iteratively stiffened to obtain a better match in the unloaded configuration. The alignment was then improved by accumulating image forces leading to the results shown in the third row. The difference images 4.12c, 4.12f and 4.12i are scaled so that the intensity range is equal for all difference images. 125

Figure 4.13 The material optimisation process by iterative material softening steps n_{opt}. The optimisation steps for patient $P5$ in terms of SSD image similarity measure (a-f), as well as registration accuracy in terms of the TRE (g-l). The blue, green, and red curves in the TRE graphs represent the mean, maximum and minimum registration errors respectively. During the optimisation the image similarity measure $\mathcal{S}_{\text{SSD}}$ is observed and acts as a surrogate for the actual alignment quality in terms of the TRE. Note how the mean TRE and its surrogate $\mathcal{S}_{\text{SSD}}$ follow similar curves over the course of the simulations. 132

Figure 4.14 Orthogonal sections through the prone MRI and supine CT image of case P1 with corresponding landmarks selected by two observers. The first observer selected corresponding points in the prone and supine images (left and centre), whereas the control observer was asked to find the supine landmark when presented with the prone one (right). (a) shows an excellent agreement between the two observers (red and green crosses in the supine CT) resulting in a landmark distance of 1.1 mm. (b) is an example where both observers do not agree, identifying different structures with similar appearance resulting in a landmark distance of 15.2 mm. 133

Figure 4.15 Histogram of all inter-observer distances. 134

Figure 4.16 Anterior-posterior extent of the breast in the prone position (measured from the anterior surface of the pectoralis muscle to the nipple) plotted against the TRE. Cases P1 to P9 are marked as blue triangles, case P10* is marked with a blue square and cases M1 to M4 are marked as yellow circles. The linear regression for cases P1 to P10* is drawn as a blue line, and the regression line for all cases is drawn as a grey line. 136

Figure 4.17 Case P1: Intensity driven registration result images. 138
Figure 4.18 Case P1: Transformed landmark positions according to the intensity driven registration result. 139
Figure 4.19 Case P2: Intensity driven registration result images. 140
Figure 4.20 Case P2: Transformed landmark positions according to the intensity driven registration result. 141
Figure 4.21 Case P3: Intensity driven registration result images. 142
Figure 4.22 Case P3: Transformed landmark positions according to the intensity driven registration result. 143
Figure 4.23 Case P4: Intensity driven registration result images. 144
Figure 4.24 Case P4: Transformed landmark positions according to the intensity driven registration result. 145
Figure 4.25 Case P5: Intensity driven registration result images. 146
Figure 4.26 Case P5: Transformed landmark positions according to the intensity driven registration result. 147
Figure 4.27 Case P6: Intensity driven registration result images. 148
Figure 4.28 Case P6: Transformed landmark positions according to the intensity driven registration result. 149
Figure 4.29 Case P7: Intensity driven registration result images. 150
Figure 4.30 Case P7: Transformed landmark positions according to the intensity driven registration result. 151
Figure 4.31 Case P8: Intensity driven registration result images. 152
Figure 4.32 Case P8: Transformed landmark positions according to the intensity driven registration result. 153
Figure 4.33 Case P9: Intensity driven registration result images. 154
Figure 4.34 Case P9: Transformed landmark positions according to the intensity driven registration result. 155
Figure 4.35 Case P10*: Intensity driven registration result images. 156
Figure 4.36 Case P10*: Transformed landmark positions according to the intensity driven registration result. 157
Figure 4.37 Case M1: Intensity driven registration result images. 158

Figure 4.38 Case M1: Transformed landmark positions according to the intensity driven registration result. 159
Figure 4.39 Case M2: Intensity driven registration result images. 160
Figure 4.40 Case M2: Transformed landmark positions according to the intensity driven registration result. 161
Figure 4.41 Case M3: Intensity driven registration result images. 162
Figure 4.42 Case M3: Transformed landmark positions according to the intensity driven registration result. 163
Figure 4.43 Case M4: Intensity driven registration result images. 164
Figure 4.44 Case M4: Transformed landmark positions according to the intensity driven registration result. 165
Figure 5.1 Overview of the material parameter optimisation workflow that aligns the finite element biomechanical model with the upright or supine surface scan. The material parameters of the biomechanical model are optimised so that the rigid alignment of the surface scan and the simulated corresponding position show an improved match in terms of the similarity measure used. 178
Figure 5.2 MR image (a), biomechanical upright simulation (b) and scanned 3D surface (c) of the same patient. After the material parameter optimisation procedure the biomechanical model and the 3D target surface are reasonably well aligned. However, artefacts from the MR acquisition in the form of indentations into the simulated skin surface can clearly be observed (red arrows) when compared to the upright surface scan. 182
Figure 5.3 Calculation of the area constraint. 184

Figure 5.4 Surface warping example. (a) Shows the simulated upright surface after the material optimisation step (see section 5.1.1). The contact of the MRI breast coil propagates to the simulation result. To correct for this effect, a displacement vector field is calculated (b) as described in section 5.1.2. Application of the displacements to the simulated surface results in a corrected surface (c). 185

Figure 5.5 Results of the material parameter optimisation step for patients $P1$ to $P3$ over the iterations i. In the left column the Young's modulus of the adipose tissue, E_a, is shown in blue, and the one of figbroglandular tissue, E_f, is shown in green. The central column shows the skin parameter c_s and the right column the objective function m according to equation (5.4). 187

Figure 5.6 Pure surface driven registration result for all data sets. Breast conserving surgery was carried out on the left breast (right side on the image above) which causes morphological changes to the breast tissue between the MRI and the CT acquisition. 190

Figure 5.7 Result of the surface driven registration approach that aligns a prone MRI to an upright optical 3D surface scan of the same patient. A volume rendering of the transformed MR image and the target surface is shown in figures (a)-(d). Figure (e) shows the nipple location identified in the warped MRI as green spheres and those in the surface scan as crosshairs. 192

Figure 5.8 Frontal and oblique view of the textured surface mesh before (a) and after surgery (b). The breast model deformation is calculated by the biomechanical wound healing simulation (Vavourakis et al., 2016) and thereafter projected onto the transformed biomechanical model of the patient's chest in the upright position. The black wireframe shows the biomechanical model before application of the wound healing displacements (c.f. 5.4c). Where the mesh is in front of or lying on the textured surface it is visible, if behind it is invisible. 196
Figure 5.9 Steps of the scar visualisation procedure. A local coordinate system is used for each element of the reported incision poly-line (a) to apply local colour changes to the surface (b). The skin texture (c) then shows a scar visualisation, that could occur as a result to the incision (d). 197

LIST OF TABLES

Table 2.1 Material parameter intervals reported and used by different authors. E is Young's modulus and C_1 relates to the shear modulus via $C_1 = \mu/2$, c.f. equation (2.27). 51

Table 3.1 Evaluation using patient data: Mean $\bar{d}$, maximum $\max(d)$ and standard deviation $\mathrm{std}(d)$ of node distances in millimetres between the different methods (M_1, M_2, M_3), as well as the number of iterations required by M_3 in order to converge, n_{M3}. 83

Table 3.2 Evaluation using a breast shape phantom: Accuracy of the three unloading methodologies in terms of mean, maximum and standard deviation of nodal distance between the recovered stress-free state and the original unloaded configuration. All measurements are given in millimetres. 84

Table 4.1 Overview of modelling based prone-to-supine registration methods. For the final alignment, the transformation models are either Free Form Deformation (FFD) or fluid, where as the similarity metrics are either Normalised Cross Correlation (NCC) or Normalised Mutual Information (NMI). Lago et al. (2012) use prescribed surface displacements to align the biomechanical model with the supine image. Rajagopal et al. (2008a,b) and Babarenda Gamage et al. (2012) follow a "simulation only" approach without subsequent alignment. 92

Table 4.2 Mean landmark distance and standard deviation after initial rigid alignment of patient's rib cage, and after affine and non-linear registration in the zero-gravity state. To evaluate the landmark distance in the supine and prone configuration prone landmarks were furthermore propagated to the supine position and vice versa using the composed transformation according to (4.3) and (4.4) respectively. 98

Table 4.3 Target registration error of the alignment of the phantom dataset with known ground truth displacements. The results are based on 500 randomly positioned landmarks within the simulated breast region. 123

Table 4.4 Target registration error for clinical prone-supine MRI-CT datasets (P1-P9), CT-CT dataset (P10*), and MRI-MRI datasets (M1-M4). The upper part, "single observer", represents TRE measurements based on the manual selection of corresponding landmarks in the prone and supine image. The lower part, "two observers", considers only reliable landmarks, i.e. those where two observers for a given prone landmark agreed on a corresponding supine location no further than 10 mm apart. All values given in mm. 128

Table 4.5 Inter observer variability in the supine configuration before and after exclusion of unreliable landmarks. N_L is the total number of landmarks and N_O the number of landmarks which were above a threshold of 10 mm. Such landmarks were regarded as unreliable and excluded from the evaluation. 129

Table 5.1 Inter-observer landmark distance (IOD) in terms of landmark distances. All distance values are given in mm, the total number of landmarks are in given in the columns N. . 188

Table 5.2 Target registration error before and after surface warping for the evaluated cases in terms of mean, maximum and standard deviation of the TRE (results given in mm). The upper part of the table presents the results before and the lower one those after applying the surface warping. The first set of columns reports results for all landmarks from the first and the control observer, whereas the second and third set of columns evaluates only those which were not more than 15 mm or 10 mm apart respectively. 189

LIST OF SYMBOLS

$\mathrm{d}\mathbf{A}$	Infinitesimally area element	44
A_{0,D_m}	Surface area of a triangular element T_m at the beginning of the surface warping procedure	184
a	Accuracy threshold that has to be met by the iterative unloading method	75
α_l	Scaling parameter to balance the influence between linear elastic regularisation and image derived forces	101
α_p	Parameter used to define Ogden materials	48
α_s	Skin material parameter associated with the energy function proposed by Veronda and Westmann (1970)	179

$\mathbf{B}$	Left Cauchy-Green deformation tensor	43
β_s	Skin material parameter associated with the energy function proposed by Veronda and Westmann (1970)	179

$\mathbf{c}$	Right Cauchy-Green deformation tensor	116
$\mathbf{C}$	Right Cauchy-Green deformation tensor	43
$\hat{\mathbf{C}}$	Deviatoric right Cauchy-Green deformation tensor	45
c_s	Skin material parameter associated with the energy function proposed by Veronda and Westmann (1970)	179

$\mathcal{D}$	Functional used measure image similarity in image registration	57
D	Set of triangles connected to a single vertex point	184
$\mathbf{D}$	Diagonalised damping matrix	96

$\mathbf{D}$	Distance vector measured in the unloaded configuration	76
$\mathbf{d}$	Distance vector measured in the loaded configuration	75
d	Euclidean distances measured between two unloaded configurations	77
E	Young's modulus	179
$\mathbf{E}$	Green strain tensor	43
ε	Small strain tensor	43
$\mathbf{F}$	Deformation gradient	42
$\mathbf{f}_B$	External body force in the undeformed configuration	48
$\mathbf{f}_b$	External body force in the deformed configuration	74
$\mathbf{f}_{\mathrm{img}}$	Image derived body force	120
$\mathbf{f}_{\mathrm{inv}}$	Inverse deformation gradient	74
$\mathbf{G}$	Nodal connectivity matrix for a surface mesh	183
$\mathbf{g}$	External image forces used in (linear elastic) image registration	101
h	Discrete temporal (h_t) or spatial (h_x, h_y, h_z) step size	108
$\mathbf{I}$	3×3 identity tensor	42
$\tilde{I}_{\mathbf{C}}$	First principal invariant of the two-dimensional right Cauchy-Green deformation tensor	179
$I_{\mathbf{C}}$	First principal invariant of the right Cauchy-Green deformation tensor $\mathbf{C}$	44
$\tilde{II}_{\mathbf{C}}$	Second principal invariant of the two-dimensional right Cauchy-Green deformation tensor	179
$II_{\mathbf{C}}$	Second principal invariant of the right Cauchy-Green deformation tensor $\mathbf{C}$	44

$III_{\mathbf{C}}$	Third principal invariant of the right Cauchy-Green deformation tensor $\mathbf{C}$	44
$\hat{I}_{\hat{\mathbf{C}}}$	First principal invariant of the deviatoric right Cauchy-Green deformation tensor $\hat{\mathbf{C}}$	45
$\hat{II}_{\hat{\mathbf{C}}}$	Second principal invariant of the deviatoric right Cauchy-Green deformation tensor $\hat{\mathbf{C}}$	45
$\hat{III}_{\hat{\mathbf{C}}}$	Third principal invariant of the deviatoric right Cauchy-Green deformation tensor $\hat{\mathbf{C}}$	45

J	Volume change of an infinitesimally small volume element measured by the determinant of the deformation gradient $\mathbf{F}$	44

$\mathbf{K}$	Stiffness matrix	96
k_c	Circumferential stretching factor	95
K	Discretised version of $\mathbf{k}$	108
$\mathbf{k}$	Internal and external forces combined	108
κ	Bulk modulus	179

$\mathbf{L}$	Linear elastic operator	101
λ	Lamé's first parameter	46
λ_1	First principal stretch, i.e. first eigenvalue of stretch tensors $\mathbf{U}$ and $\mathbf{V}$	44
λ_2	Second principal stretch, i.e. second eigenvalue of stretch tensors $\mathbf{U}$ and $\mathbf{V}$	44
λ_3	Third principal stretch, i.e. third eigenvalue of stretch tensors $\mathbf{U}$ and $\mathbf{V}$	44

M	Material configuration that defines the explicit biomechanical simulation	113

m	Lumped mass matrix	180
M_1	Unloading strategy that simply reverses the direction of gravity as described in section 3.3.2.1	72
M_2	Unloading strategy that employs an inverse finite deformation approach as described in section 3.3.2.2	72
M_3	Unloading strategy that follows the fixed-point iterative scheme as described in section 3.3.2.3	72
$\mathbf{M}_\rho$	Lumped mass matrix	96
μ	Lamé's second parameter, or shear modulus	46
μ_p	Parameter used to define Ogden materials	48

N_{invert}	Number of iterations between material configuration (M) updates	114
n_{opt}	Material optimisation step	119
n_{M3}	Number of iterations required by the iterative unloading method $M3$ to converge to the specified accuracy a	83
$\mathbf{N}$	Nominal stress tensor	48
$\mathbf{n}$	Normal of an infinitesimally small area element $d\mathbf{A}$	44
ν	Poisson's ratio	179

Ω	Image domain	101

P	Prone image	119
$\mathbf{p}$	Vertex coordinate of a mesh element	70
ϕ	Angular component of a point θ specified in cylindrical coordinates	95
φ	Position of a matierlial point in the deformed configuration as a function of its original location $\mathbf{X}$ and time t	42
$\mathbf{P}$	First Piola-Kirchhoff stress tensor	74
Ψ	Strain energy density function	45

q	Relative area change of a triangle	184

R	Reference or fixed image	57
$\mathbf{R}$	3×3 rotation tensor	43
r	Speed proportional damping coefficient	102
$\mathbf{r}$	Set of displacement vectors pointing from vertices of a mesh to the closest point on an associated target surface	180
r_c	Radial component of a point θ specified in cylindrical coordinates	95
$\mathbf{R}_\mathrm{ext}$	External body forces	96
ρ_0	Mass density in the undeformed configuration	48

$\mathbf{S}$	Second Piola-Kirchhoff stress tensor	46
$\mathcal{S}$	Functional used for regularising deformation vector fields in image registration	47
S	Supine image	119
$\mathbf{s}$	Sample point within a tetrahedral element determined by the vertex coordinates $\mathbf{p}$	70
s	Scaling factor with $0 \leq s \leq 1$	75
s_D	Scaling coefficient to control the speed of a node towards the target surface	183
$\boldsymbol{\sigma}$	Cauchy stress tensor	74
s_L	Scaling coefficient to control the smoothness constraint during mesh alignment	183
s_m	Scaling function dependent on the speed v_s of a motion constrained node towards the target surface	117
s_p	Scaling function that adds incremental image forces smoothly during the course of the simulation	120
S_scan	Surface mesh used as a target in the surface driven registration approach	180

S'_{scan}	Rigidly transformed surface mesh S_{scan}	183
T	Template or moving image	57
Θ	Mapping from Cartesian coordinates to cylindrical coordinates	95
θ	Point in Cartesian coordinates	95
t	Time	42
$\mathbf{T}_{p_0 s_0}$	Transformation from the estimated gravity-free prone configuration (p_0) to the estimated gravity-free supine configuration (s_0)	97
$\mathbf{T}_{p p_0}$	Transformation from the loaded prone (p) to the estimated gravity free prone configuration (p_0)	96
$\mathbf{T}_{ps}$	Transformation from prone to supine	97
$\mathbf{T}_{ps}$	Transformation from supine to prone	97
$\mathbf{T}_{s s_0}$	Transformation from the loaded supine (s) to the estimated gravity free supine configuration (s_0)	96
$\mathbf{U}$	Stretch tensor obtained through factorisation of the deformation gradient $\mathbf{F}$ into rotation $\mathbf{R}$ and stretch $\mathbf{U}$	43
$\mathbf{u}$	Displacement vector field, measured relative to the undeformed position	42
U	Discretised version of the continuous, time dependent vector field $\mathbf{u}(\mathbf{X}, t)$	108
$\mathbf{U}_N$	Nodal displacement matrix	96
v_s	Speed of a node with imposed motion constraint towards the target surface	117
$\mathbf{V}$	Stretch tensor obtained through factorisation of the deformation gradient $\mathbf{F}$ into stretch $\mathbf{V}$ and rotation $\mathbf{R}$	43
$\mathbf{v}$	Vector defining the side of a triangle	184
$\mathbf{w}$	Vector defining the side of a triangle	184

w	Set of neighbours of a vertex point $\mathbf{p}$	183
$\mathbf{X}$	Point in the undeformed configuration	42
$\mathbf{x}$	Point in the deformed configuration	42
$\mathbf{Z}$	Node positions of a biomechanical model in the undeformed or unloaded configuration	75
$\mathbf{z}$	Node positions of a biomechanical model in the deformed or loaded configuration	75
z_c	Axial component of a point θ specified in cylindrical coordinates	95

1

INTRODUCTION

Breast cancer today is the most common type of cancer in western countries, including Europe, Australia, New Zealand and North America. According to Cancer Research UK (2012) in 2010 the lifetime risk for a women in the UK being diagnosed with an invasive breast carcinoma was one in eight. Since 2005 the overall incidence rate in the UK remained relatively stable after a constant increase since the 1970s. In 2012 this led to 52399 newly diagnosed breast cancer cases in the UK, where the total number of breast cancer related deaths for the same year was 11679 (European Cancer Observatory, 2012). For the whole of Europe Ferlay et al. (2013) report 464.000 new cases in 2012, leading to 131.000 breast cancer related deaths.

On the individual level the diagnosis breast cancer is for every patient a high psychological burden. Improved cancer management strategies that help making the clinical workflow smoother and potentially improve the clinical outcome are required, without introducing the risk of over-diagnosis.

Breast cancer does not describe one single homogeneous disease, but rather can be categorised according to aggressiveness (invasive versus in-situ), region of occurrence (lobular versus ductal), receptor and molecular status (Curtis et al., 2012). Appropriate patient specific therapy strategies have to be chosen accordingly. These include – but are not limited to – surgery, radiotherapy, hormone therapy, and chemotherapy. Often a combination of these therapy options is proposed by the clinical team in order to optimise the outcome.

Imaging of the breast is used to detect, diagnose, and stage breast cancer in order to inform selection of appropriate therapies. For improved guidances of interventions and surgery, however, accurate spatial correspondence between images – or between images and the surgical setting – has to be established. Since the breast undergoes large deformations between imaging positions and the surgical setting, this renders a very challenging registration task that standard image registration methods are unlikely to solve. As a result, biomechanical modelling of breast tissue becomes more and more important.

Biomechanical modelling of the breast and associated image registration techniques are a promising tool in order to improve several application scenarios of current breast cancer management. Possible application areas include

- surgical planning and image guided surgery,
- radiotherapy planning, and
- cosmetic outcome prediction of breast conserving surgery.

These are briefly outlined in the following and the link with biomechanical modelling is highlighted.

1.1 CLINICAL MOTIVATION

SURGICAL PLANNING AND IMAGE GUIDED SURGERY Pre-operative image acquisition of Dynamic Contrast Enhanced Magnetic Resonance Imaging (DCE-MRI) is usually performed in the prone position with the patient lying on her front, with the breast mostly freely pendant in a dedicated MR-transmitter coil. This ensures the best image quality as (i) motion artefacts due to breathing are minimised (ii) the receiving coil is close to the imaged tissue and (iii) the extended shape of the breast due to gravity improves spatial differentiability.

The imaging position is ideal for diagnostics and staging but unfortunately not very useful for the surgeon in the operating theatre, since surgery is performed in the supine position with the patient lying on her back. The very soft tissue of the breast deforms significantly due to the change in direction of gravity. Being able to transform the prone image data into the surgical position could provide the surgeon with important information about the extent and location of the lesion and thus could improve the achieved margins.

Improved diagnostics and screening programmes lead to an increase of small lesions being detected (Dua et al., 2011). If breast conserving surgery is part of the therapeutic plan, this leaves the surgical team with the challenge that the main mode of tumour localisation during surgery – which is palpation – is not available for small tumours with diameters below 15 mm. Furthermore, not all tumours are visible on inter-operative imaging techniques such as ultra sound (US). Wire-guided localisation is currently used in these cases where the centre of the lesion is marked with the barbed tip of a guide wire. This procedure imposes severe implications on the clinical logistics in terms of scheduling and coordination of radiologists and surgeons, since wire localisation has to be performed on the day of surgery. This effectively limits the number of cases that can be operated using this technique (Dua et al., 2011). Image guidance could help the surgeon in theatre to approach the lesion in an optimal fashion without the restrictions that are imposed by a wire.

RADIOTHERAPY PLANNING In the case where breast conserving surgery is accompanied with adjuvant radiotherapy in the treatment plan, prone and supine position again play a significant role as the radiation is commonly applied in the supine position. The dose delivery plan is established from a supine chest Computed Tomography (CT) planning scan which allows the position of the tumour bed to be localised as surgical clips which were put in place by the surgeon. A fully three-dimensional extent of the tumour bed thus is difficult to estimate in the post-surgical CT without the tumour location. Biomechanical modelling in this application could help to project the pre-surgical lesion extent onto the planning CT. It should be noted here, that this scenario is beyond mechanical simulations alone as a surgical intervention takes place between the DCE-MRI acquisition and the CT planning scan.

COSMETIC OUTCOME PREDICTION When tissues are removed from the intact breast during breast conserving therapy, this has an impact on the shape of the breast. The most obvious change is volume loss, but also healing processes and radiotherapy have an influence on the shape of the breast. Being able to handle different gravitational loadings appropriately is a first step towards modelling the whole procedure including not only the mechanical aspects but also the tissue remodelling based on mechano-biological processes.

1.2 CONTRIBUTION

The contributions presented in this thesis are:

- Biomechanical model generation based on prone MR images of the breast. Since the MR-based biomechanical model represents the breast in a gravity loaded configuration, different numerical unloading strategies to recover the zero-gravity state are compared and evaluated using phantom data and patient specific biomechanical models (Eiben et al., 2014).
  The biomechanical model generation process forms a minor contribution and is described in detail in section 3.2. It combines existing segmentation and meshing methodologies into a processing pipeline. The three unloading strategies investigated in chapter 3 are described and evaluated in sections 3.3.2 and 3.3.3 respectively. While all unloading methodologies were described previously in the literature, the iterative method (c.f. section 3.3.2.3) proposed by Carter et al. (2008) was extended by properly considering the difference between the loaded and the unloaded configuration to calculate the update of estimated gravity-free configuration. This leads to a faster convergence of the scheme.

- Development of a registration strategy to align volumetric breast images that were acquired in different patient positions, i.e. in the prone and supine configuration. This strategy integrates biomechanical simulations and image registration components into a single optimisation framework. Gravity and image derived forces are simultaneously integrated into a biomechanical simulation, which avoids the need of a subsequent, generic image registration step, hence the deformations are constrained by the biomechanical material model. Motion of the breast tissue along the chest is considered, as well as pre-stressing of the breast tissue due to gravity loading (Eiben et al. (2013) and (Eiben et al., 2016a)).
  The integrated biomechanical image registration methodology (section 4.2) forms a main contribution of this thesis and is a completely new development. However, it is informed by experiments described in section 4.1 which utilised

existing registration software and the iterative unloading methodology of section 3.3.2.3.

- Evaluation of the developed intensity based registration framework using a phantom breast geometry and clinical datasets comprising of MR-MR, MR-CT and CT-CT image data pairs (Eiben et al., 2016a).
  The evaluation of the integrated registration framework (sections 4.2.6 to 4.2.9) is closely related to the previous point and is a main contribution of this thesis.

- Development of a biomechancially guided registration methodology to align prone MR images with a target surface that represents the patient's skin outline in a different position, i.e. upright or supine. The methodology optimises the material parameters of the biomechanical model that is utilised to simulate the gross deformation from the prone to the target configuration. Residual misalignment is corrected by using a surface- and thereafter a volume-warping methodology (work accepted for oral presentation at SPIE Medical Imaging 2016 (Eiben et al., 2016b)).
  The major contribution of the surface driven registration as described in chapter 5 is the constrained, non-rigid surface alignment (section 5.1.2) as well as the combination of all components (i.e. material parameter optimisation, surface alignment and volume mesh warping) into a single alignment framework.

1.3 THESIS OUTLINE

The remainder of this thesis is structured as follows. In chapter 2 an overview of the current state of the art in biomechanical modelling is presented. This includes fundamental concepts in continuum mechanics, aspects more specifically related to breast deformation modelling and image registration techniques, which incorporate biomechanical concepts. Chapter 3 describes the biomechanical model generation in detail and evaluates different strategies that recover the unloaded configuration from a pre-stressed geometry. Such methods are required when patient position changes are simulated since the breast geometry is always imaged with gravity loading present. In chapter 4 it is shown that currently a tight integration between biomechanical simulations and intensity based image registration does not exist thus an integrated simulation based registration framework is developed and evaluated. Clinical applicability of a biomechanical registration could potentially be increased, if the image as target information is replaced with a surface, which is potentially more readily available. A corresponding methodology is developed in chapter 5. Chapter 6 concludes this thesis.

2

BACKGROUND AND STATE OF THE ART

CHAPTER OVERVIEW This chapter presents the theoretical background and reviews the relevant literature on topics that are covered in this thesis. First a brief introduction to continuum solid mechanics is presented. Then biomechanical modelling and related techniques which are concerned with breast deformation simulations are reviewed. This includes reviewing existing numerical solution techniques as well as experimental work on breast tissue biomechanical constitutive modelling. One major application for breast deformation simulations is the fusion of information from different imaging modalities. Image alignment is a prerequisite for this task. Since image alignment is exactly the task of image registration, relevant literature in this field will be reviewed thereafter. Image registration techniques which utilise biomechanical concepts are summarised and eventually the focus is put onto techniques with applications in breast image registration.

2.1 CONCEPTS IN CONTINUUM MECHANICS

Continuum mechanics aims to describe the motion of materials. The fundamental assumption is that matter is continuously distributed in space. Hence, relevant quantities such as mass density, external body forces, stresses and strains can be described as continuous functions of space. This gives rise to the development of field theories, where physical terms and processes are described by means of spatial fields (Haupt, 2002). This section can only provide a brief overview and the interested reader is referred to the extensive literature that is available on that topic (e.g. the textbooks by Bonet and Wood (2008), Ibrahimbegovic (2009), Haupt (2002), etc.). All biomechanical simulations of breast tissue deformation described in this thesis are based on the concepts presented below. Moreover, understanding the underlying principles is essential to develop the intensity driven, biomechanically constrained image registration method presented in chapter 4.

2.1.1 *Displacement, Deformation, Strain*

A deformable body can be described in two main substantially different configurations: The undeformed and the deformed configuration. In continuum mechanics these configurations must clearly be differentiated. Although the undeformed configuration is not inherently equivalent to the reference configuration – as the reference configuration is the configuration to which the stresses and strains are being measured and in general can be chosen arbitrarily – in the course of this work, the reference configuration will always be the undeformed configuration. In continuum mechanic terms the "total Lagrangian perspective" is adopted. (All definitions in this section are summarised from the works presented by Bonet and Wood (2008) and Kaye et al. (2009).)

Let a point in the undeformed configuration be denoted by $\mathbf{X} = (X_1, X_2, X_3)^{\mathrm{T}}$ and in the deformed configuration $\mathbf{x} = (x_1, x_2, x_3)^{\mathrm{T}}$, then the function $\mathbf{u}(\mathbf{X}, t) = (u_1, u_2, u_3)^{\mathrm{T}}$ describes the relative displacement

$$\mathbf{u}(\mathbf{X}, t) = \mathbf{x}(t) - \mathbf{X} = \varphi(\mathbf{X}, t) - \mathbf{X}. \tag{2.1}$$

The displacement is a function of time t and alternatively the position of a material point originally at $\mathbf{X}$ can also be described with $\varphi(\mathbf{X}, t)$. Moving on from a single material point to a continuous material, the neighbourhood of a point has to be described, too, which leads to the deformation gradient $\mathbf{F}$, defined as

$$\mathbf{F} = \frac{\partial \mathbf{x}}{\partial \mathbf{X}} = \mathbf{I} + \frac{\partial \mathbf{u}}{\partial \mathbf{X}}, \tag{2.2}$$

where $\mathbf{I}$ is the identity matrix. The deformation gradient is a two-point tensor as it relates infinitesimal displacements or line elements in the undeformed configuration with corresponding displacements in the deformed configuration. It captures local elongations as well as rotations. Using a polar decomposition of the deformation gradient $\mathbf{F}$, the overall deformation can be decomposed into the stretch tensors $\mathbf{U}$ and $\mathbf{V}$ and a rotation tensor $\mathbf{R}$.

$$\begin{aligned} \mathbf{F} &= \mathbf{RU} \\ &= \mathbf{VR} \end{aligned} \tag{2.3}$$

From the deformation gradient the left and right Cauchy-Green deformation tensors can be derived

$$\mathbf{B} = \mathbf{F}\mathbf{F}^{\mathrm{T}} \tag{2.4}$$

$$\mathbf{C} = \mathbf{F}^{\mathrm{T}}\mathbf{F} \tag{2.5}$$

where $\mathbf{B}$ is the left and $\mathbf{C}$ is the right Cauchy-Green deformation tensor. Both tensors are independent of the rotation and only measure local stretches as can be easily shown by using the polar decomposition (2.3). Any deformation which deposits energy in a material is independent of any rotation $\mathbf{R}$. Thus the eigenvalues of $\mathbf{U}$ and $\mathbf{V}$ are called the principal stretches $\lambda_i > 0$, $i = 1, 2, 3$ and the eigenvalues of $\mathbf{B}$ and $\mathbf{C}$ are λ_i^2.

From the deformation gradient the Green Strain tensor can be defined as

$$\begin{aligned} \mathbf{E} &= \frac{1}{2}\left(\mathbf{F}^{\mathrm{T}}\mathbf{F} - \mathbf{I}\right) \\ &= \frac{1}{2}\left(\mathbf{U}^2 - \mathbf{I}\right) \end{aligned} \tag{2.6}$$

with $\mathbf{I}$ being the identity tensor. When no deformation is present, then the deformation gradient $\mathbf{F} = \mathbf{I}$ whereas the strain becomes $\mathbf{E} = \mathbf{0}$. This deformation measure is a key quantity in the total Lagrangian formulation which relates all quantities to the undeformed configuration.

Using (2.2) to substitute the deformation gradient with the gradient of the displacement field $\mathbf{F} = \mathbf{I} + \nabla\mathbf{u}$ the Green Strain Tensor can be rewritten as

$$\begin{aligned} \mathbf{E} &= \frac{1}{2}\left((\mathbf{I} + \nabla\mathbf{u})^{\mathrm{T}}(\mathbf{I} + \nabla\mathbf{u}) - \mathbf{I}\right) \\ &= \frac{1}{2}\left(\nabla\mathbf{u} + (\nabla\mathbf{u})^{\mathrm{T}} + (\nabla\mathbf{u})^{\mathrm{T}}\nabla\mathbf{u}\right) \\ &\approx \frac{1}{2}\left(\nabla\mathbf{u} + (\nabla\mathbf{u})^{\mathrm{T}}\right) := \boldsymbol{\varepsilon} \end{aligned} \tag{2.7}$$

For small deformations the approximate equality of the last equation holds, which defines the small strain tensor $\boldsymbol{\varepsilon}$. However, care has to be taken when this approximation is used, since even rigid body rotations result in a non-zero response of this strain measure. A corresponding example is presented in the appendix B.1.

The scalar valued principal invariants (i.e. no dependence changeHA8.1on rotations of the coordinate system) of the right Cauchy-Green deformation tensor $\mathbf{C}$ can be chosen as follows:

$$I_{\mathbf{C}} = \mathrm{tr}\left(\mathbf{C}\right) \tag{2.8}$$

$$II_{\mathbf{C}} = \frac{1}{2}\left(\mathrm{tr}^2(\mathbf{C}) - \mathrm{tr}\left(\mathbf{C}^2\right)\right) \tag{2.9}$$

$$III_{\mathbf{C}} = \det \mathbf{C} \tag{2.10}$$

For the description of an isotropic homogeneous incompressible material the definition of $I_{\mathbf{C}}$ and $II_{\mathbf{C}}$ are sufficient. For compressible materials $III_{\mathbf{C}}$ also has to be taken into consideration. In some cases it is convenient to express the invariants in terms of the principal stretches λ_i as

$$I_{\mathbf{C}} = {\lambda_1}^2 + {\lambda_2}^2 + {\lambda_3}^2 \tag{2.11}$$

$$II_{\mathbf{C}} = (\lambda_1\lambda_2)^2 + (\lambda_2\lambda_3)^2 + (\lambda_1\lambda_3)^2 \tag{2.12}$$

$$III_{\mathbf{C}} = (\lambda_1\lambda_2\lambda_3)^2 \tag{2.13}$$

The deformation of different element types from the undeformed to the deformed configuration is given as follows:

- Line element:

$$\mathrm{d}\mathbf{x} = \mathbf{F}\mathrm{d}\mathbf{X} \tag{2.14}$$

- Area element (Nanson's formula):

$$\mathbf{n}\mathrm{d}\mathbf{A} = J\mathbf{F}^{-\mathrm{T}}\mathrm{d}\mathbf{A} \tag{2.15}$$

- Volume element:

$$\mathrm{d}\mathbf{v} = J\mathrm{d}\mathbf{V} \tag{2.16}$$

As can be seen from equation (2.16), the volume change of a volume element is completely defined by the scalar factor J which is nothing else than the determinant of the deformation gradient $\mathbf{F}$

$$J = \det(\mathbf{F}) > 0. \tag{2.17}$$

The deformation gradient $\mathbf{F}$ captures the whole deformation of a material and does not allow a direct differentiation between a distortional – also called isochoric – and a volumetric component. This differentiation however is necessary when incompressible or nearly incompressible materials are considered. Following the argumentation of Bonet and Wood (2008) the volumetric change captured by the deformation gradient can be achieved by multiplying $\mathbf{F}$ with a suitable factor

$$\hat{\mathbf{F}} = J^{-1/3}\mathbf{F} \tag{2.18}$$

so that $\det(\hat{\mathbf{F}}) = 1$ is guaranteed. This allows definition of the distortional – or deviatoric – right Cauchy-Green deformation tensor $\hat{\mathbf{C}}$ as

$$\hat{\mathbf{C}} = \hat{\mathbf{F}}^{\mathrm{T}}\hat{\mathbf{F}} \tag{2.19}$$

with the invariants $\hat{I}_{\hat{\mathbf{C}}}$, $\hat{II}_{\hat{\mathbf{C}}}$, and $\hat{III}_{\hat{\mathbf{C}}}$ corresponding to the definitions given in equations (2.8) to (2.10).

2.1.2 *Hyperelastic Materials*

Breast tissue is often modelled as a hyperelastic material. Moreover, some image registration methods regularise the deformation based on the relations introduced here, which motivates a closer review of this topic in this section.

Deformation of an object in general requires energy. The strain measures introduced in the previous section allow description of the deformation of an object, but do not contain information about how much energy is required to achieve any degree of deformation. To facilitate this description this section introduces the strain energy density function – or stored energy potential – Ψ. If furthermore the stored internal energy of a deformed object is path independent, the material is said to be hyperelastic (Bonet and Wood, 2008). Thus in turn it is sufficient to describe a hyperelastic material by its strain energy function.

2.1.2.1 *Hyperelasticity and Invariants*

For isotropic materials the strain energy density Ψ only depends on the first three invariants of the right Cauchy-Green deformation tensor (Bonet and Wood, 2008).

For transversely isotropic and anisotropic materials, further invariants with respect to one or more predominant directions need to be defined. Anisotropy however is not considered here.

$$\Psi(\mathbf{C}(\mathbf{X}), \mathbf{X}) = \Psi(I_{\mathbf{C}}, I\!I_{\mathbf{C}}, I\!I\!I_{\mathbf{C}}, \mathbf{X}) \tag{2.20}$$

The second Piola-Kirchhoff stress can be calculated from

$$\mathbf{S} = 2\frac{\partial \Psi}{\partial \mathbf{C}} = \frac{\partial \Psi}{\partial \mathbf{E}} \tag{2.21}$$

In the cases covered by (2.20), **S** can be calculated using the chain rule.

$$\mathbf{S} = 2\left(\frac{\partial \Psi}{\partial I_{\mathbf{C}}}\frac{\partial I_{\mathbf{C}}}{\partial \mathbf{C}} + \frac{\partial \Psi}{\partial I\!I_{\mathbf{C}}}\frac{\partial I\!I_{\mathbf{C}}}{\partial \mathbf{C}} + \frac{\partial \Psi}{\partial I\!I\!I_{\mathbf{C}}}\frac{\partial I\!I\!I_{\mathbf{C}}}{\partial \mathbf{C}}\right) \tag{2.22}$$

The derivatives of the invariants with respect to **C** can be precalculated and are e.g. given as (Ibrahimbegovic, 2009)

$$\frac{\partial I_{\mathbf{C}}}{\partial \mathbf{C}} = \mathbf{I} \qquad \frac{\partial I\!I_{\mathbf{C}}}{\partial \mathbf{C}} = \operatorname{tr}(\mathbf{C})\mathbf{I} - \mathbf{C} \qquad \frac{\partial I\!I\!I_{\mathbf{C}}}{\partial \mathbf{C}} = J^2\mathbf{C}^{-1}. \tag{2.23}$$

Note that there are several definitions of principal invariants possible and used in the literature which requires the corresponding derivatives to be revised accordingly. With the invariants introduced above (c.f. equations (2.8), (2.9), and (2.10)) (2.22) refurnishes to

$$\mathbf{S} = 2\left(\frac{\partial \Psi}{\partial I_{\mathbf{C}}}\mathbf{I} + \frac{\partial \Psi}{\partial I\!I_{\mathbf{C}}}\left(\operatorname{tr}(\mathbf{C})\mathbf{I} - \mathbf{C}\right) + J^2\frac{\partial \Psi}{\partial I\!I\!I_{\mathbf{C}}}\mathbf{C}^{-1}\right). \tag{2.24}$$

This form allows the second Piola-Kirchhoff strain to be determined if the strain energy density function is defined in terms of right Cauchy-Green strain invariants. Equivalent expressions exist for cases when the principal stretches are used to define the strain energy density Ψ. The following sections introduce a few material constitutive relations that are linked to regularisation terms used in image registration.

2.1.2.2 *Saint Venant-Kirchhoff Materials*

The Saint Venant-Kirchhoff material represents the simplest hyperelastic material for which the strain energy density function in terms of the Green Strain tensor (2.6) is given as

$$\Psi(\mathbf{E}) = \frac{\lambda}{2}\left(\operatorname{tr}(\mathbf{E})\right)^2 + \mu \operatorname{tr}(\mathbf{E}^2) \tag{2.25}$$

Conveniently the second Piola-Kirchhoff stress $\mathbf{S}$ can be computed as

$$\mathbf{S} = \lambda \operatorname{tr}(\mathbf{E})\mathbf{I} + 2\mu\mathbf{E} \tag{2.26}$$

using the relation (2.21).

While this material can handle large displacements due to the use of the finite strain measure, it should only be used in a small strain regime since it does not handle volume changes correctly. The interested reader is referred to the example given by Hjelmstad (2004) (c.f. pages 147f.). This material model is the straight forward extension of the linear elastic material laws with rotational invariant strain measures (Belytschko et al., 2000).

The Saint Venant-Kirchhoff model was used as a regulariser for non-linear image registration by Yanovsky et al. (2008) and is called a quadratic regulariser $\mathcal{S}^{\text{quad}}$ by Burger et al. (2013) who also illustrate the relation to linear elastic regularisation by substituting the Green Strain Tensor $\mathbf{E}$ with the small strain tensor ε (c.f. equation (2.7)).

2.1.2.3 *Compressible Neo-Hookean Materials*

In contrast to the Saint Venant-Kirchhoff material, the neo-Hookean material is defined in terms of the first and third invariant of the right Cauchy-Green deformation tensor and is thus better equipped to also deal with large strains.

$$\Psi = \frac{\mu}{2}(I_{\mathbf{C}} - 3) - \mu \ln J + \frac{\lambda}{2}(\ln J)^2 \tag{2.27}$$

with $J^2 = I\!I\!I_{\mathbf{C}}$ and the material coefficients μ and λ. Note that several equivalent formulations of this material law exist, especially in terms of the deviatoric part of the Cauchy-Green deformation tensor.

The corresponding second Piola-Kirchhoff Stress tensor can be derived from (2.24) and is given by

$$\mathbf{S} = \mu(\mathbf{I} - \mathbf{C}^{-1}) + \lambda \ln(J)\,\mathbf{C}^{-1}. \tag{2.28}$$

2.1.2.4 *Ogden Materials*

The Ogden constitutive law (Ogden, 1972) defines the strain energy density in terms of the principal stretches λ_i which are given by the eigenvalues of the stretch tensor $\mathbf{U}$ or $\mathbf{V}$ of equation (2.3):

$$\Psi(\lambda_1, \lambda_2, \lambda_3) = \sum_{p=1}^{N} \frac{\mu_p}{\alpha_p} \left({\lambda_1}^{\alpha_p} + {\lambda_2}^{\alpha_p} + {\lambda_3}^{\alpha_p} - 3 \right) \tag{2.29}$$

For incompressible materials the relation $\det(\mathbf{F}) = 1$ is used which relates to the principal stretches as $\lambda_1 \lambda_2 \lambda_3 = 1$. For this (2.29) can be reformulated as

$$\Psi(\lambda_1, \lambda_2, \lambda_3) = \sum_{p=1}^{N} \frac{\mu_p}{\alpha_p} \left({\lambda_1}^{\alpha_p} + {\lambda_2}^{\alpha_p} + \frac{1}{(\lambda_1 \lambda_2)^{\alpha_p}} - 3 \right) \tag{2.30}$$

2.1.3 *Conservation Laws*

Conservation laws are fundamental to describing the behaviour of physical systems. Here the presentation of Belytschko et al. (2000) is summarised who elaborate on (i) conservation of mass, (ii) conservation of linear momentum, (iii) conservation of angular momentum, and (iv) conservation of energy. Of special interest is the conservation of linear momentum, which in the total Lagrangian framework reads

$$\nabla_0 \cdot \mathbf{N} + \rho_0 \mathbf{f}_B = \partial_{tt} \mathbf{u}. \tag{2.31}$$

Here $\mathbf{N}$ is the nominal stress, ρ_0 is the mass density in the unloaded configuration, $\mathbf{f}_B$ is a force acting on the body, and $\mathbf{u}$ is the displacement vector. In essence this equation is the continuum version of Newton's second law of motion, which relates forces acting on a body to a corresponding acceleration. In chapter 4 this conservation law will be used as a basis to develop a biomechanically constrained registration method. The so called strong form above can be used directly by employing a finite difference discretisation. For the solution with a finite element method however, this conservation law needs to be transformed into a variational, or weak formulation. The interested reader is referred to the extensive literature on finite element methods by Belytschko et al. (2000), Zienkiewicz et al. (2013), or Bathe (2006) for example.

2.2 BREAST ANATOMY

Kopans (2007) describes the breast anatomy from the imaging perspective as a modified skin gland. The bulk of breast tissue in the adult female is usually located anterior on the upper torso between the second and the seventh rib, laterally it can extend up to the mid-axillary line and medially to the sternum. The breast lies on chest wall, mainly the pectoralis major muscle.

A ductal system of 20 or more major lactiferous ducts, or lobes, exit the breast through the skin at the nipple. These hollow, tree-like structures branch into finer ducts until the actual milk producing glands, the lobules, are reached. Lobules are arranged in clusters and are surrounded by specialised connective tissue, which in turn is embedded in the stromal connective tissue that can be found throughout the breast.

Breast tissue develops surrounded by subcutaneous fat between a deep and a superficial fascia which are sometimes more or less distinct. The deep layer of the fascia, the retromammary fascia delineates the breast tissue posteriorly and lies on the pectoralis fascia. Hence some mobility is possible between the pectoralis muscle and the breast tissue. Additional retromammary fat is also common anterior to the fascia.

The ductal system is interspersed with adipose tissue and supported by fibrous tissue. Kopans (2007) highlights the large variability of the interlacing support network with varying thickness and distinctiveness in the form of planar sheets, which are known as Cooper's ligaments. These ligaments extend to the skin as retinacula cutis and, due to the limited support posteriorly, the skin acts as the primary support of the breast.

2.3 BIOMECHANICAL MODELLING OF BREAST TISSUE DEFORMATIONS

Deformation simulations of breast tissue use different numerical solution approaches to predict the underlying physical behaviour of this organ. These include mass-spring methods employed for instance by Roose et al. (2005) and Patete et al. (2013), mass tensor methods employed by Roose et al. (2006) and the

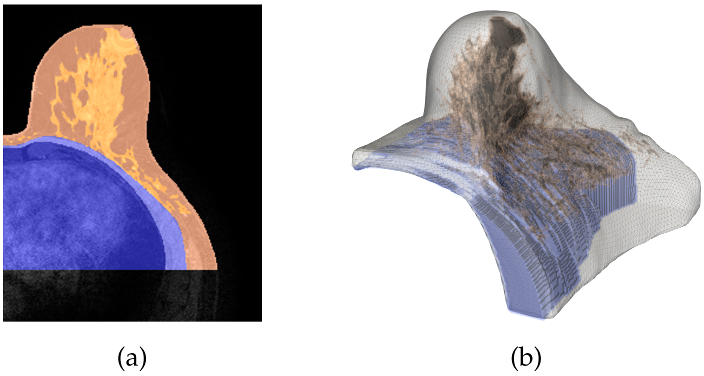
(a) (b)

Figure 2.1: *Patient specific biomechanical model generated from segmented MR image. (a) The different tissue classes are adipose (brown), fibroglandular tissue (orange), pectoral muscle (light blue) and chest (dark blue) and are used to define appropriate material properties to the biomechanical model (b).*

widely popular finite element methods (FEM) for which the review article by Babarenda Gamage et al. (2012) provides an in depth overview. In order to simulate the deformation of a very soft organ such as the breast, a three-dimensional patient-specific model is required. This is necessary because breast shape, size, and internal structure varies significantly over the population. Thus a patient-specific biomechanical model should represent the overall breast shape of a patient as accurately as possible.

Besides the patient-specific geometry, more detailed mechanical breast models also consider the internal tissue heterogeneity. Fat, glandular and fibrous tissue as well as skin are the most commonly considered components of such models; some include adjacent tissues such as the pectoral muscle. For this reason, three-dimensional images, which enable these tissue classes to be differentiated are therefore well suited to the purpose of building biomechanical models.

2.3.1 *Tissue Classes and Elasticities*

Early work by Samani et al. (2001) identified adipose and fibroglandular tissue as well as skin as the main components contributing to heterogeneous mechanical properties of the breast and at the same time being distinguishable in MR

Author	Application	Constitutive Law	Elasticity Parameters [kPa]	
			fat	fibroglandular
Rajagopal et al. (2008a)	gravity loading	neo-Hookean	$C_1 = [0.08, 0.13]$	$C_1 = [0.08, 0.13]$
Carter et al. (2009)	gravity loading	neo-Hookean	$C_1 = [0.3, 0.8]$	$C_1 = [0.3, 0.4]$
del Palomar et al. (2008)	gravity loading	neo-Hookean	$C_1 = 3$	$C_1 = 12$
Krouskop et al. (1998)[1]	ex-vivo indentation	linear elastic	$E = 18 \pm 7$	$E = 28 \pm 14$
Wellman et al. (1999)[2]	ex-vivo indentation	various strain levels	$E = 6.6 \pm 7$	$E = 33 \pm 12$
Samani and Plewes (2007)	ex-vivo indentation	indentation tests	$E = 1.9 \pm 2.5$	$E = 1.9 \pm 8.6$

Table 2.1: *Material parameter intervals reported and used by different authors. E is Young's modulus and C_1 relates to the shear modulus via $C_1 = \mu/2$, c.f. equation (2.27).*

images (see Fig. 2.1). They pioneered building patient-specific meshes from three-dimensional breast MR image data. Krouskop et al. (1998) and Pathmanathan et al. (2008) made the observation that, in general, fibrous and glandular tissue must be separated anatomically to be correctly modelled. However this is not generally possible using clinical MRI, CT or any other available three-dimensional imaging modality. Consequently, to date, all studies that incorporate heterogeneous material characteristics, group these tissue classes together into a single "fibroglandular" class.

Table 2.1 extends the overview of material parameters provided by Rajagopal et al. (2008a). Clearly there is no general agreement on the elastic moduli of fat or glandular tissues, even when small strain assumptions are used. For small strains, a differentiation between tissue classes in healthy subjects is disputed by Samani et al. (2007). Such results are in agreement with in vivo Magentic Resonance Elastography (MRE) measurements published by Sinkus et al. (2005). For larger strains however, the non-linear material characteristics of these tissue types become dominant and separate treatments of adipose and fibroglandular tissue must be considered.

Regarding suitable hyper-elastic constitutive laws, O'Hagan and Samani (2009) compared the ability of a variety of strain energy function classes to represent stress-strain measurements from real ex vivo tissue samples using iterative fitting techniques. The functions tested were polynomial, Yeoh, Arruda-Boyce, Ogden, and Veronda-Westmann models. Most accurate results could be achieved with the Yeoh, polynomial and Ogden models. Unfortunately performance of the simple and thus widely used neo-Hookean constitutive model was not part of their investigations (see e.g. Rajagopal et al. (2008a,b); Carter et al. (2008); del Palomar et al. (2008); Lee et al. (2010); Han et al. (2011); Lapuebla-Ferri et al. (2011)). The huge popularity of the neo-Hookean material model for biomechanical simulations probably reflects a reasonable compromise between the low number of parameters required and at the same time describing fully non-linear elastic behaviour.

Due to the lack of routinely performed in-vivo measurements, such as MRE, optimisation schemes have been proposed for different applications. Plate compression experiments performed on subjects in an MR scanner were reported by Tanner et al. (2006). The volunteer was asked to lie in the prone position and the breast was compressed up to a for the volunteer acceptable amount using a custom made MR-compatible device. In the same experimental setting Tanner et al. (2011) observe anisotropic tissue behaviour with less extension of the breast in the anterior-posterior direction. Carter et al. (2009) used the deformation vector field from non-linear, intensity based B-spline image registration as a ground truth, and optimised the material parameters of the neo-Hookean constitutive relation to simulate the deformation from prone loading to a neutral buoyancy condition using finite element techniques. Han et al. (2010) on the other hand incorporated a material parameter optimisation into a registration algorithm and optimised the image similarity between a real compressed MR image and the corresponding simulated compression. In subsequent work Han et al. (2011, 2014) applied the material parameter optimisation to the prone-to-supine image registration problem. The main contribution here was the integration of the material parameter optimisation into a sequential simulation-registration framework which uses a patient-specific biomechanical model that allows the breast and pectoral muscle to slide on the chest wall. However, the prone configuration of the breast was regarded as stress free and the final free-form deformation step from the registration does not guarantee a physically plausible deformation.

Rajagopal et al. (2008a) considered the gravitational loading of the breast in the MR scanner. The authors optimised patient-specific material parameters by minimising the surface distance between a neutral buoyancy configuration, which was acquired in the MR scanner, and an inverted gravity loading simulation of the prone configuration.

In a study by Unnikrishnan et al. (2012) the elastic properties of breast tissue were regarded in a multi-scale fashion. At the microscopic level the load bearing component is primarily collagen which constitutes the extra cellular matrix. The mechanical properties of the breast tissue are thus directly related to factors like orientation and volume fraction of collagen fibres. For deformation modelling of the whole breast however it is not feasible to consider the distribution of collagen fibres directly. At the macroscopic level constitutive relations are required which describe the material as a continuum. For this reason Unnikrishnan et al. (2012) approach this problem by mathematical homogenisation, where the heterogeneous material is represented by an equivalent continuum. They consider the collagen volume fraction and fibre orientation distribution to determine the elastic modulus of the hyperelastic neo-Hookean constitutive relation. Although their work is mainly motivated by describing the stiffness changes in cancerous tissue, the main assumptions hold for the entire breast.

Moreover, Samani et al. (2007) and O'Hagan and Samani (2009) report, amongst others, significantly stiffer material properties for cancerous tissues when compared to healthy tissues. A correlation between stiffness and tumour grade, or invasiveness, was also reported. In biomechanical simulations of mammographic tissue compression Wessel et al. (2012) investigated the effect of shape and stiffness of the tumour on the local stress distribution. Such an approach is a step towards considering the complex tumour environment more precisely. A large body of work was published with respect to modelling tumours and their complex physical, chemical and biological interactions within their micro-environment. This field of research is beyond the scope of this thesis, but the interested reader is referred to the review articles by Edelman et al. (2010), Deisboeck et al. (2011) and Masoudi-Nejad et al. (2015).

2.3.2 *Boundary Conditions and Loading*

The boundary and loading conditions in biomechanical simulations aim to describe the influence on the breast of image modality specific settings such as plate compression during X-ray mammographic image acquisition or gravitational loading during MR acquisition. Furthermore they need to approximate the interaction with the adjacent anatomy.

2.3.2.1 *Anatomy Related*

Numerical procedures, such as finite element methods, necessitate discretisation of the region of interest to solve the underlying partial differential equations and calculate the resultant displacements within this region. This in turn requires that the transitions to neighbouring anatomical structures be defined as boundary conditions of the discretised breast domain.

Posteriorly the breast is delimited by the retromammary fascia which separates the pectoral muscle from the breast tissue (Gefen and Dilmoney, 2007). This allows some sliding motion between these two entities. The amount of sliding, however, depends on the individual, the allowed motion, pose change or outer forces, and constraints and is therefore difficult to quantify.

In general three different boundary conditions have been used to model the interaction between the chest wall and breast tissue. These are

- prescribed zero-displacements, i.e. fixed (see e.g. Samani et al. (2001), Williams et al. (2003), Zyganitidis et al. (2007), Whiteley et al. (2007) and Rajagopal et al. (2008a)),
- prescribed non-zero displacements (see e.g. Carter et al. (2008)), and
- traction free sliding motion (see e.g. Han et al. (2011, 2014)).

Tanner et al. (2006) explored the influences of several aspects of biomechanical simulations including the boundary conditions. They concluded that inaccurate boundary conditions have a major impact on simulation accuracy. They derived accurate displacement boundary conditions from non-linear image registration to establish a point-to-point correspondence where this condition is to be enforced. Roose et al.

(2008) explored alternative strategies to incorporate more flexible boundary conditions. This overcomes the need for a-priori known point-to-point correspondences. In a temporal intra-patient registration task they allowed for sliding motion between the target and moving skin surface.

Details of the boundary conditions at the medial, lateral, superior and inferior model boundaries are often not described in detail. Tanner et al. (2006) provide the most comprehensive evaluation of the boundary conditions in these areas.

2.3.2.2 *Imaging Modality Related*

Mammographic imaging imposes large but highly constrained deformations on the breast. During this routinely performed procedure the breast is placed between two compression plates one of which is lowered to compress the breast to about 50% of its original thickness. This stabilises the breast and improves the visibility of internal structures by increasing the cross-sectional area of the breast exposed to the incident X-ray beam. The resulting images are two-dimensional X-ray attenuated projections of the compressed breast. One application of major interest is image registration between X-ray mammograms and breast MR images.

To link the 2D X-ray projection image to a 3D MR image, a non-trivial image registration task has to be solved. The major difficulties are

- the dimensionality change from 2D to 3D,
- the large scale deformation between the freely pendulous breast under gravity loading in the MR scanner and the breast being compressed during mammography, and
- the differing image contrasts between X-ray and MRI associated with the disparate physical interactions involved in the imaging process.

Ruiter et al. (2006) use a biomechanical model and finite element techniques to simulate the deformation between the uncompressed model, based on the MR image data, and the compressed state during mammographic image acquisition. The compression step is simulated by adding two compression plates to the simulation scenario and moving them together during the course of the simulation. From this deformation an X-ray mammogram is simulated. Remaining differences between the real X-ray mammogram and the simulated image are compensated by post-simulation steps. Mertzanidou et al. (2014) integrate the simulation of the deformation into a single optimisation procedure with seven degrees of freedom. These are two rigid in-plane translations, two rotations of the compression plates – about the anterior-posterior axis and about the superior-inferior axis – the amount of compression, the Poisson ratio and the ratio of tissue enhancement coefficient. The compression plates implement a frictionless contact model.

Gravitational effects are usually ignored when mammographic compressions are simulated as the relatively small body force has only minor influence compared to the forces originating from the compression plates. Applications which solely involve changes in direction of gravity however, present a different type of problem. A conventional breast MR scan is taken with the patient lying in the scanner on her front (prone position) with her breasts mainly freely pendulous in a dedicated breast MR coil. Clearly, gravity acts on the breast and extends the breast in the (vertical) anterior direction. When the position of the patient is changed, so does the direction of gravity and the configuration of the breast. This renders the task of presenting prone diagnostic information, from prone Dynamic Contrast Enhanced-MRI (DCE-MRI), to a surgeon for pre-operative planning or image guided surgery in the supine position, particularly challenging (Carter et al., 2005, see e.g.).

Simulations of gravity inversion are performed using two different approaches. Rajagopal et al. (2007) as well as Pathmanathan et al. (2008) recover the unloaded configuration from a loaded one by regarding the unloaded configuration as the unknown of the solution process. This requires reformulation of the solution procedure and potentially limits its applicability to non-commercial solvers which can be modified accordingly. Carter et al. (2009) suggest a fixed point iteration scheme to solve the backward problem by iteratively calculating the forward solution. This approach is very flexible and allows usage of any solver available. Han et al. (2011, 2014) regard the prone breast configuration as being stress free and simply apply gravity in the superior direction. Although this is physically not correct, results suggest that the error can be compensated by a sophisticated hybrid simulation and registration approach.

2.4 IMAGE REGISTRATION AND BIOMECHANICS

Image registration is the task to find corresponding points in two (or more) images. In the field of breast image registration usually images of the same patient but either from different imaging modalities, or different time points are aligned. This is referred to as multi-modal intra-patient image registration. Here the focus will be on the prone-supine image registration task.

In order to define a registration algorithm, four main components have to be in place, namely

- an image similarity measure to quantify the similarity between the images,
- a regularisation to constrain the registration to plausible deformations,
- a transformation model which is capable of describing the expected deformation between the images and
- an optimisation technique to find the best transformation for the given regularisation and image similarity measure.

Usually the first two items are combined together into the objective function which drives the optimisation procedure. Image registration can be classified into parametric and non-parametric registration approaches. Parametric image registration uses a transformation model, that can be described by a number of parameters. To this class of algorithms belong rigid and affine, but also the widely popular non-linear B-spline registration that was originally proposed by Rueckert et al. (1998).

Non-parametric registration on the other hand uses a variational approach to formulate a minimisation problem where a dense deformation vector field is directly optimised (see e.g. Modersitzki (2004)).

$$\mathcal{D}_{R,T}[\mathbf{u}] + \alpha\mathcal{S}[\mathbf{u}] \underset{\mathbf{u}}{\rightarrow} \min \tag{2.32}$$

Here $\mathcal{D}$ describes the image similarity between the images R and T as a function of the displacement vector field u and $\mathcal{S}$ the regularisation. The regularisation becomes necessary as image registration is in general an ill-posed problem and thus solutions to the minimisation problem are required to be sufficiently smooth. To achieve this, different regularisers were proposed that in some cases borrow heavily from the physics of fluid or solid mechanics. These regularisers resemble diffusive (c.f. Modersitzki (2004)), linear elastic (c.f. Broit (1981), Bajcsy and Kovačič (1989), Miller et al. (1993)) or fluid-like (c.f. Christensen et al. (1996), Bro-Nielsen and Gramkow (1996), Crum et al. (2005)) material behaviour. Another regularisation that is designed to handle large deformations is the "Large Deformation Diffeomorphic Metric Mapping" (LDDMM) method (c.f. Dupuis et al. (1998), Trouve (1998), Beg et al. (2005)). Here the velocity of the deformation vector field is constrained to change smoothly over time.

Hyperelastic regularisation was proposed e.g. by Burger et al. (2013) in order to achieve large and at the same time smooth deformations. They borrow the underlying concept from continuum mechanics and especially highlight the necessity to move from small strain measures – which are used in linear elastic registration algorithms – to finite deformation strain measures. Using the notation introduced in (2.7) the linear elastic regularisation term can be written as

$$\mathcal{S}_{\text{lin.elast.}} = \int \xi (\text{tr}\,(\varepsilon))^2 + \mu \; \text{tr}\,(\varepsilon^2) \mathrm{d}x. \tag{2.33}$$

Simple substitution of the small strain tensor ε with the finite deformation Green-Strain tensor $\mathbf{E}$ yields what Burger et al. (2013) name quadratic regularisation:

$$\mathcal{S}_{\text{quad}} = \int \xi (\text{tr}\,(\mathbf{E}))^2 + \mu \; \text{tr}\,(\mathbf{E}^2) \mathrm{d}x. \tag{2.34}$$

By choosing $\xi = {}^{\lambda}/_{2}$, it can be clearly seen that the Saint Venant Kirchhoff strain energy density function is used for regularisation (c.f. (2.25)). Strictly speaking this material constitutive relation already describes a hyperelastic material and thus the name quadratic regularisation is misleading from the mechanical perspective. To proceed to hyperelastic regularisation they employ a length, a surface and a volume term, ϕ_L, ϕ_S and ϕ_V respectively, which – when viewed in combination with the arguments – find a loose correspondence in the first three invariants of the right Cauchy-Green deformation tensor.

$$\mathcal{S}_{\text{hyp.elast.}} = \int \alpha_1 \phi_L(\mathbf{F}) + \alpha_2 \phi_S(\text{cof}\,(\mathbf{F})) + \alpha_3 \phi_V(\det \mathbf{F}) \mathrm{d}x \tag{2.35}$$

Here, cof denotes the cofactor (as defined in (Burger et al., 2013)) and the functions ϕ_L, ϕ_S and ϕ_V are chosen to be convex for optimisation reasons but from a mechanical standpoint can be regarded as an Ogden material.

The work by Burger et al. (2013) clearly originates from an image registration background. Veress et al. (2005) on the other hand approach the registration problem with a clear modelling focus and name their approach hyperelastic warping. As the name suggests, they use hyperelastic constitutive laws in combination with a finite element discretisation to regularise their elastic registration. Their energy functional which they aim to minimise is given by

$$\mathcal{E}(\mathbf{u},\mathbf{X}) = \int_{\Omega_0} \Psi(\mathbf{X},\mathbf{u})\,\mathrm{d}V - \int_{\Omega_0} U(R(\mathbf{X},\mathbf{u}),T(\mathbf{X},\mathbf{u}))\,\mathrm{d}V \tag{2.36}$$

where the strain energy density function is given by Ψ and the image similarity measure between the images R and T is given by U. They show a high flexibility in terms of material laws. In their applications they use neo-Hookean as well as transversely isotropic constitutive laws, whereas the only image similarity used is limited to the mono modal sum of squared differences. Previous to this work Rabbitt et al. (1995), Bowden et al. (1998), Weiss et al. (1998) and Veress et al. (2002) used the same formulation with only slight modifications.

Regularisation in image registration aims to constrain the deformation to a physically realistic transformation. Within an organ, physically realistic deformations are usually related to smooth variations in the displacement vector field (DVF). However, between organs, where sliding motion might occur, the smoothness assumption is violated. For the application of breast image registration, sliding motion can occur at the interface between retromammary fascia and pectoralis muscle. However, a larger body of work that introduces sliding motion into image registration focusses on the lung and liver. If an accurate segmentation of the organ of interest exists, the registration could be limited to the organ itself, ignoring deformations outside the mask (Kabus et al., 2009; McClelland et al., 2011). Alternatively, the mask could be utilised to locally inform and adapt the regularisation (Schmidt-Richberg et al., 2009). Other approaches automatically generate a segmentation mask (e.g. Vandemeulebroucke et al. (2012)) or avoid an explicit generation of such a mask altogether by allowing discontinuities in the DVF through the use of edge-preserving, bilateral filtering of the DVF (Papież et al., 2014).

2.5 CHAPTER CONCLUSION

Continuum mechanics forms the basis for large deformation simulations of the breast. Patient specific biomechanical models were proposed in the literature to account for the large variability of breast shape between individual women. Beyond the shape, a large range of stiffness values was reported, too. Since patient-specific measurements of the breast stiffness are usually not performed, in some registration algorithms corresponding optimisation procedures were proposed. The simulated deformation furthermore depends on the assumed loading and boundary conditions that are applied to the model, and need to be selected in correspondence with the application for instance mammographic compression or gravity loading.

Prone MR images are most commonly used as a basis to define the geometry of the breast. One main limitation of this procedure is that the prone MR image shows the breast in a gravity loaded configuration. This body force extends the tissue significantly towards anterior. Despite this some authors do not consider the initial loading (Han et al., 2011, 2014; Lago et al., 2012). However, recovering the unloaded shape from a pre-stressed geometry is technically feasible and will be further explored in chapter 3.

Prone-to-supine image alignment is presented in the literature usually as a sequential two-step approach comprising of a simulation and a registration component. The combined simulation and registration are disjunct procedures with no (Lee et al., 2010) or very limited interaction or feedback (Han et al., 2011, 2014). Furthermore physically plausible deformations might no longer be guaranteed, if the deformation model of the final registration step is not sufficiently constrained.

From the image registration perspective very Burger et al. (2013) introduced hyperelastic regularisation in order to account for large deformations. Intensity based registration procedures are however completely image driven and thus do not allow to incorporate physical loadings such as gravity. An integrated alignment approach which combines biomechanical simulation and registration into a common framework is currently missing from the literature. This will be developed in chapter 4.

3

BIOMECHANICAL MODELS AND SIMULATIONS

CHAPTER OVERVIEW In this chapter, the foundations of continuum mechanics, breast anatomy, and published work on breast biomechanical modelling as described in chapter 2 are put together into a biomechanical model generation workflow. This workflow is based on prone MR images that show the breast in a pre-stressed, gravity loaded state. In order to simulate the breast shape under different loading conditions from such a pre-stressed configuration, it is essential to consider and remove the effects of gravity. Hence, numerical unloading strategies are investigated. One of these strategies, the iterative unloading methodology by Carter et al. (2008), is improved – forming a minor contribution of this thesis – to converge faster towards a solution.

Three-dimensional MR images represent a convenient basis to build biomechanical models of the breast. MR images are acquired relatively early during the clinical workflow and could thus be used for tasks further downstream such as surgical planning and guidance. Prone DCE-MRI images are part of the standard clinical procedure for patients (i) where the extent of an invasive cancer shows an ambiguity between clinical and imaging assessment, (ii) where mammograms of highly dense breasts do not allow accurate diagnosis, or (iii) where the lesion extent of lobular invasive cancer needs to be assessed prior to breast conserving surgery (NICE, National Institute For Health and Care Excellence, 2009). Further clinical indications for MR imaging, however, may exist on an individual basis.

MR images allow differentiation of the relevant anatomical structures such as adipose and fibroglandular tissue as well as the location of the chest wall and the pectoral muscle. Another advantage is that MR images are acquired without the use of ionising radiation. However, when biomechanical models are derived from MR images, some problems arise that need to be considered.

- The breast is shown in the gravity loaded prone position only,

- the material parameters and constitutive relation of in vivo breast tissue is generally unknown, and
- often a considerable deformation of the breast is introduced due to contact with the MR coil.

This chapter is a precursor to the developments in chapters 4 and 5 and describes the biomechanical model generation process in detail, that was developed in the context of the PICTURE project[1] (Sabczynski et al., 2014). Thereafter, an unloading strategy is developed and compared against other methods used in the literature alongside a sensitivity analysis with respect to the material parameters in the widely used neo-Hookean constitutive relation – and hence touches on the second point of the list above. In chapters 4 and 5 strategies will be explored, which combine biomechanical models with intensity and surface target information in registration methods that – among others objectives – aim to overcome deformations such as those mentioned above.

Regarding the last point of the list above, figure 3.1 visualises the effect that contact of the breast with the MR scanner can have on the breast shape. The upper row shows a prone CT image and the row below an MR image of the same patient. Both volumetric images were manually aligned using features on the chest. The CT image can be regarded as freely pendulous, since the patient support was visible in the image and no contact could be identified in the proximity of the breast. In the MRI patient position configuration, on the other hand, a medial contact pushes the breast in the lateral direction. Furthermore the superior and inferior extent appears to be confined by the scanner. While the relative deformation between the images is apparent in the figure, the usefulness of this case for a quantitative evaluation is limited since surgery took place between both acquisitions – i.e. MRI before and CT after surgery. However, the effect of surgery on the overall breast shape appears to be small, which can be observed in corresponding baseline and follow-up photographs of that patient that are also shown alongside the CT and the MR image.

---

[1] `www.vph-picture.eu` accessed September 2015.

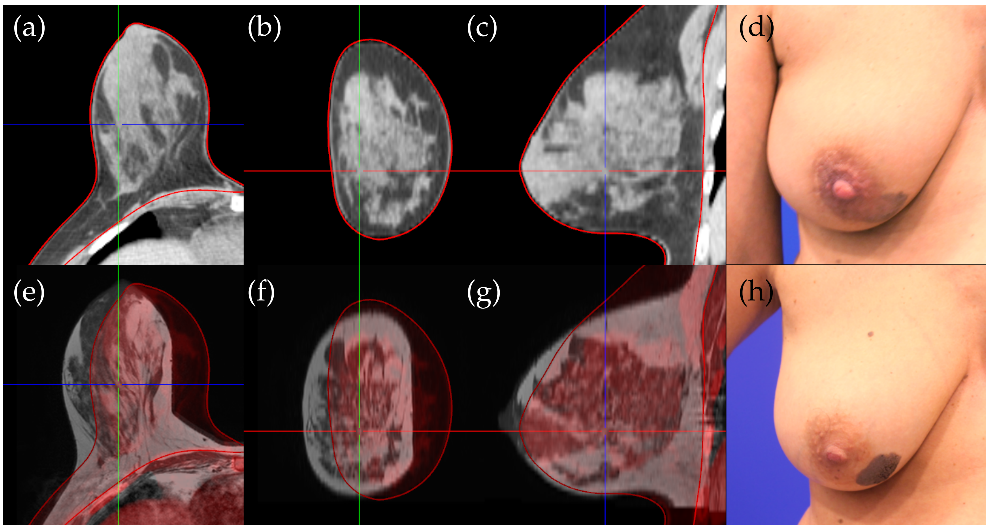

Figure 3.1: *Prone post-surgical CT (a-c) and pre-surgical MR (e-g) image of the same patient with corresponding post-surgical (d) and pre-surgical (h) photographs respectively. The segmentation of the breast tissue in the CT image is contoured by a red outline. In the MR image a clear medial contact between the breast and coil can be observed medially resulting in significant deformation. Not all deformation can be attributed to the MR acquisition position since surgery took place between the MRI and CT acquisition, however pre-(h) and post-surgical (d) photographs indicate only minor influence on the shape due to surgery.*

3.1 PICTURE: PROJECT OBJECTIVES

An overview of the project *Patient Information Combined for the Assessment of Specific Surgical Outcomes in Breast Cancer*, or Picture for short, was presented by Sabczynski et al. (2014). Since Picture is an international multi-disciplinary EU-funded project with a three year duration, only a brief overview is presented in this section.

Triggered by the increased life expectancy after breast conserving treatment, the scope of breast cancer care extends into areas beyond primary cancer care. One aspect that might be overlooked at first is the psychological burden on the patient as a result of having cancer and living with the consequences of treatment. Aesthetically negative outcomes of treatment can have a direct impact on the patients' well-being and self-esteem with a related effect on psychological recovery.

It was reported by Hill-Kayser et al. (2012) that up to 30% of breast conserving treatments result in suboptimal aesthetic appearance.

Picture has the aim of developing a breast surgery demonstrator, that combines patient and population data into a *Digital Breast Surgery Patient*. This virtual representation of the real patient can then be utilised to plan surgery and to simulate the predicted outcome of a selected procedure. The resulting surgical simulation can in turn be utilised in a shared decision making process that involves the surgeon, the clinical multi-disciplinary team, and the patient. Quantitative evaluation of the aesthetic outcome prediction will also be made available and might inform the decision about different surgical approaches.

The data that are collected in the project include standard clinical images, such as prone DCE-MRI and X-Ray mammography. In order to also present any predicted surgical outcomes in a visually comprehensive way, surface data are acquired which capture the shape and texture of the torso with the patient standing upright using 3D optical imaging technologies. Magnetic Resonance Elastography (MRE) will be acquired on a population level, i.e. only for a limited number of volunteer patients. These data will be made available for cases where MRE was not acquired through the development of a generic breast model from which the missing information can be derived.

When the data are prepared for surgical planning the biomechanical simulations come to play an important role. In order to capture a surgical procedure on a patient-specific level, surgeons prefer to interact with the digital breast surgery patient in the supine position which resembles the surgical setting. However, no patient representation, derived from routine clinical imaging, currently captures this configuration. To generate a patient-specific supine position, biomechanical models are utilised. The pure biomechanical simulations will be used to integrate information between different loading configurations and are based on the prone MR image data. Beyond the biomechanical simulations, a core aspect of the technical developments in Picture is the mechano-biological simulation of the outcome of breast conserving treatment that is based on the individual surgical plan.

In order to facilitate the biomechanical simulations, corresponding finite element models are required. The generation process is described in the following section.

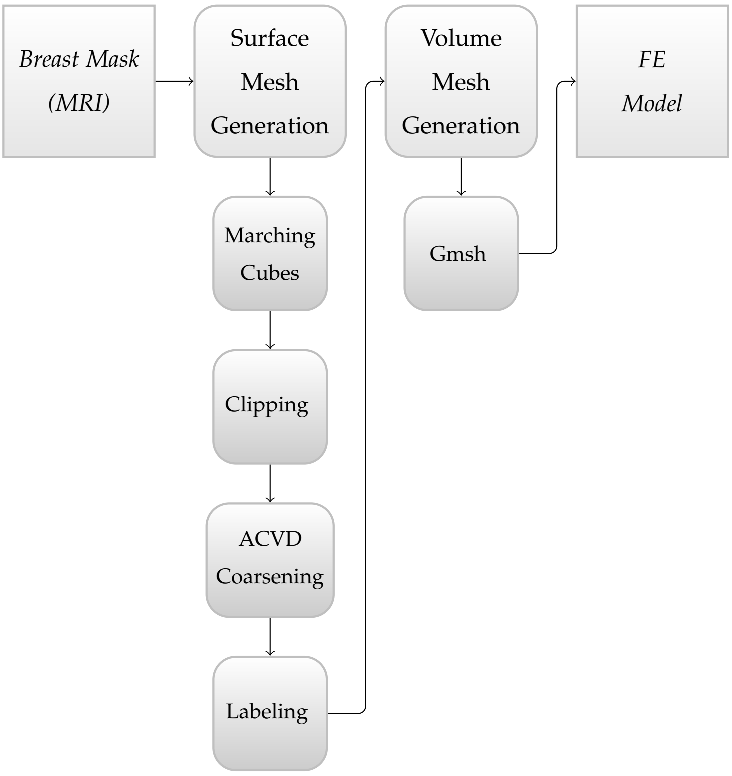

Figure 3.2: *Overview of the mesh generation steps involved. The procedure begins with the segmented binary-mask image of a patient-specific breast; then a high-density surface mesh is generated, which is subsequently processed (i.e. clipped, coarsened and labelled) in order to finally construct the volume FE grid.*

3.2 FE-MODEL GENERATION

The process of generating patient-specific biomechanical models from three-dimensional clinical MR image data consists of three distinct sequential steps: image segmentation, mesh generation, and model assembly. These steps are elaborated separately in this section, while an illustration of the separate steps is provided in figure 3.2 .

3.2.1 *Image Segmentation*

Image segmentation delineates the structure of interest from an image – in this case the breast is segmented from the MR image. When the organ itself is identified, internal structures can be further differentiated into adipose and fibroglandular structures. The methodology used is briefly outlined below.

The main processing steps in this image segmentation task are:

- Perform an initial bias-field correction to remove unwanted image inhomogeneities (Tustison et al., 2010);
- segment the patient foreground from the background (via grey-scale "closing" and automated thresholding);
- identify relevant landmarks (e.g. the mamillae and the mid-sternum);
- eliminate the arms by properly cropping the image;
- segment the pectoral muscle surface using an automated image classification technique, and
- assign a probability model of voxels inside the breast (belonging to the adipose or fibroglandular tissue-classes) (Van Leemput et al., 1999).

The segmented breast image defines the volume of the biomechanical model (see figure 3.3a). For prone-to-supine simulations the breast tissue is expected to be displaced in the lateral and posterior direction. Since boundary conditions need to be assigned to the boundaries of the simulated domain and might limit the magnitude of the resulting displacements, care was taken to extend the segmentation as far posterior as possible. The challenge here is that posterior image areas suffer a loss of signal-to-noise ratio, due to the increased distance of the tissue to the MR receiver coil. This makes the segmentation in this area potentially less accurate. As a result of the lateral and posterior extension of the segmentation region, the breast biomechanical model covers a larger volume than is anatomically defined as breast tissue.

3.2.2 *Mesh Generation*

In the mesh generation step, the MR reconstructed breast geometry is discretised using finite elements. Figure 3.2 illustrates the developed sequential procedure to generate a high-quality tetrahedral mesh for a patient-specific FE model.

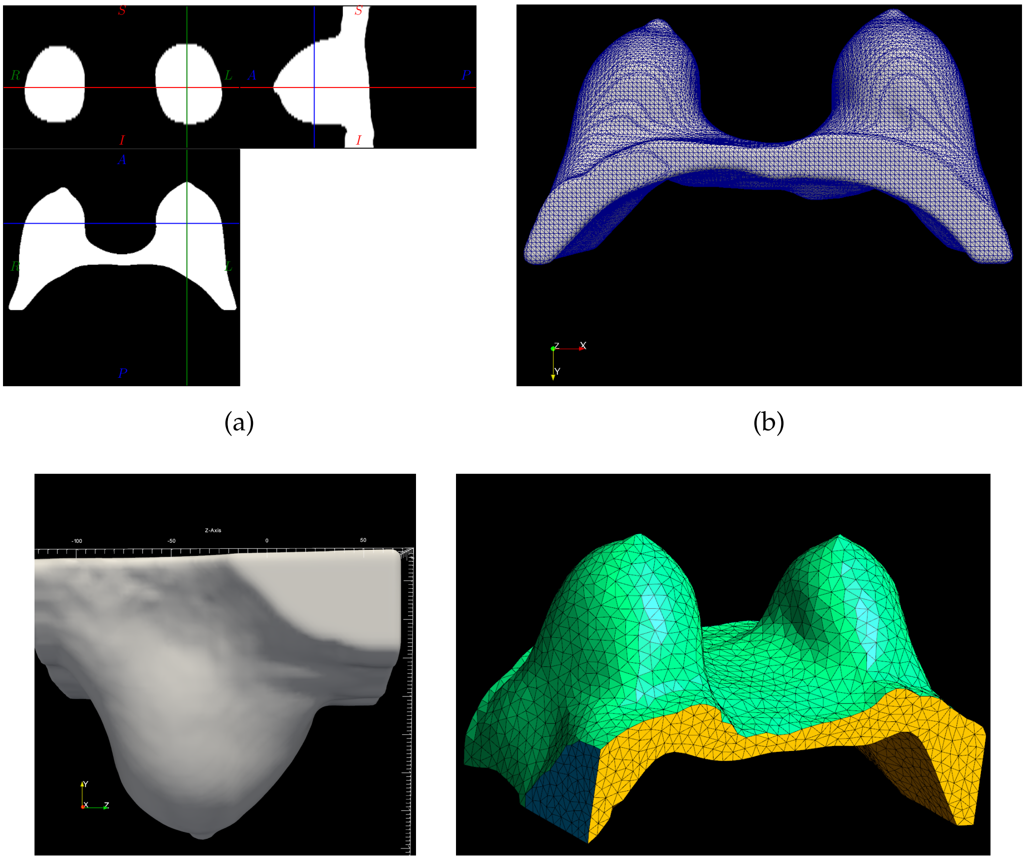

(a) (b)

(c) (d)

Figure 3.3: *(a) Orthogonal views of the binary mask image resulting from image segmentation. (b) High-density surface mesh generated using the marching cubes algorithm and a windowed-sinc smoothing filter. (c) The rotation of the field of view against the physical coordinate system is taken into account in the clipping algorithm. Note the angle between the upper boundary of the breast mesh and the z-axis. (d) Coarsened FE mesh with properly labelled triangular face elements. Skin surface is shown in green, axial clipping plane in yellow and lateral clipping plane in blue.*

Starting from the segmented MR image, the transition from the voxel based image domain to a node-element based representation of the analysed breast geometry domain needs to be made. To accomplish this, surface mesh generation from a Cartesian (voxel based) grid can be achieved by utilising the well established marching cubes algorithm (Lorensen and Cline, 1987). The implementation of the Visualisation Tool Kit (VTK)[2] (Schroeder et al., 2006) is employed with a subsequent application of a windowed-sinc smoothing filter (Taubin et al., 1996). This combination of algorithms is observed to effectively reduce step-like artefacts that arise from the marching cubes algorithm and as a result triangular surface meshes of very good quality can be produced.

However, as shown in figure 3.3b, the surface mesh at this stage usually shows smooth boundaries at the transition from the anatomical skin and pectoralis muscle surface to the transverse, coronal, and sagittal boundaries defined by the image's field of view (FoV) or the clipping introduced in the segmentation. To address this, the triangulated surface mesh is clipped on the superior, inferior, posterior and lateral face of the image in order to obtain a crisp transition between the surfaces (see figure 3.3d). Clipping of the surface mesh shown in figure 3.3b is achieved by applying a VTK closed-surface clipping filter.

Since the boundaries of the MR image define the lateral, superior and inferior extent in the first place, the additional clipping planes are aligned with the FoV of the image[3] rather than with the physical coordinate axes. Even so, careful consideration is required when applying the clipping planes filter, especially when the FoV of the MR scanner is not aligned with the real-world (or physical) coordinate system. Incorrect filter application could result in important image information loss. Figure 3.3c demonstrates an example of a small rotation between the reconstructed breast geometry (no clipping filter applied) and the physical coordinate system. Larger rotations between the image axes and the physical coordinate system were observed.

---

[2] `www.vtk.org` accessed 4.5.2015.

[3] The extent and orientation of the FoV, which is covered by a medical image, can be selected by the operator to best suit the breast shape and patient position. This has no effect on the quality of the scan, however smaller FOVs generally reduce the acquisition time.

After the triangulated surface mesh is clipped, the approximated centroid Voronoi diagram (ACVD) coarsening algorithm (Valette and Chassery, 2004) is utilised in order to correct and control the surface mesh discretisation level. Then, the face elements of the newly created mesh are labelled accordingly to distinguish the boundary conditions in the FE model, as shown in figure 3.3d. Labels are assigned for skin and pectoralis boundaries, as well as for the clipping planes, i.e. lateral, superior, inferior, and posterior. The labelled triangular surface grid of the breast boundary is denoted Γ_B. Finally, the analysed patient-specific breast geometry is discretised using three-dimensional volume elements using the open-source meshing platform *Gmsh* (Geuzaine and Remacle, 2009). In this thesis volume meshes of linear tetrahedral elements are constructed using an Advancing Front algorithm (Schöberl, 1997), which also incorporates *Netgen*[4] mesh optimization routines.

3.2.3 *Model Assembly*

In this step, the input for the FE solver is produced. Given the volume mesh generated in the previous section, it is necessary to assign biomechanical properties to each element of the discretised domain into the model. Hence, all tetrahedral elements need to be assigned with a label associated to a tissue-class, i.e. assign adipose, fibroglandular or skin tissue properties. This is accomplished by incorporating the image segmentation results of the medical images.

A tetrahedral element, as shown in figure 3.4, has the vertices: $\mathbf{p}_1$, $\mathbf{p}_2$, $\mathbf{p}_3$ and $\mathbf{p}_4$. The tissue-class of the element is sampled from the label image at five positions $\mathbf{s}_1$ to $\mathbf{s}_5$, which are calculated using a linear combination of the original tetrahedral vertex points, as

$$\begin{aligned}
&\mathbf{s}_1 = {}^1\!/_8\,(5\mathbf{p}_1 + \mathbf{p}_2 + \mathbf{p}_3 + \mathbf{p}_4)\ , \quad \mathbf{s}_2 = {}^1\!/_8\,(\mathbf{p}_1 + 5\mathbf{p}_2 + \mathbf{p}_3 + \mathbf{p}_4)\ , \\
&\mathbf{s}_3 = {}^1\!/_8\,(\mathbf{p}_1 + \mathbf{p}_2 + 5\mathbf{p}_3 + \mathbf{p}_4)\ , \quad \mathbf{s}_4 = {}^1\!/_8\,(\mathbf{p}_1 + \mathbf{p}_2 + \mathbf{p}_3 + 5\mathbf{p}_4)\ , \\
&\mathbf{s}_5 = {}^1\!/_4\,(\mathbf{p}_1 + \mathbf{p}_2 + \mathbf{p}_3 + \mathbf{p}_4)\ .
\end{aligned}$$

---

[4] `www.hpfem.jku.at/netgen` accessed 5.1.2015.

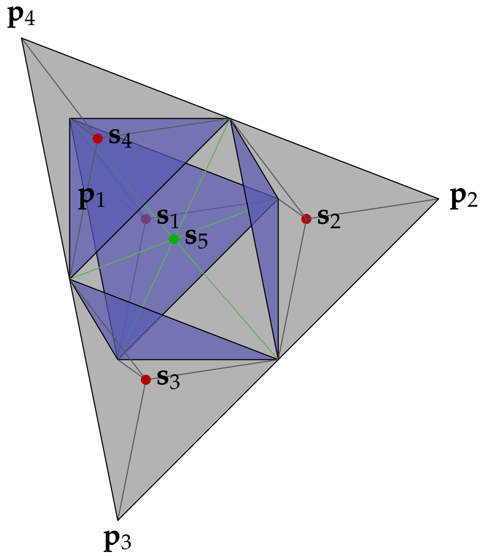

Figure 3.4: *Sample points* $\mathbf{s}_1$ *to* $\mathbf{s}_5$ *derived from the tetrahedral element to sample the internal tissue segmentation.*

The tissue-class of the element is then determined by the median value of the samples. Denser sampling might give more accurate estimate of the corresponding tissue-class for the tetrahedral element than using only the geometric centre $\mathbf{s}_5$ as a sample point.

Finally, the FE model is properly informed, where all tetrahedral elements in the grid are labelled as adipose or fibroglandular tissue. Moreover, the surface triangular elements are also labelled according to their surface properties, as skin, pectoralis fascia or clipping plane.

To finalise the model description, boundary conditions are selected for each labelled surface. The skin and lateral clipping planes are modelled as being traction free whereas the retromammary region and the posterior clipped plane are assigned with a prescribed zero-displacement condition. Nodes in the superior and inferior clipping planes are allowed to move within this plane.

3.3 OBTAINING THE UNLOADED CONFIGURATION

Typically, breast MRI acquisitions take place with the patient prone, in which the breasts are mostly freely pendulous being pulled in the anterior direction due to

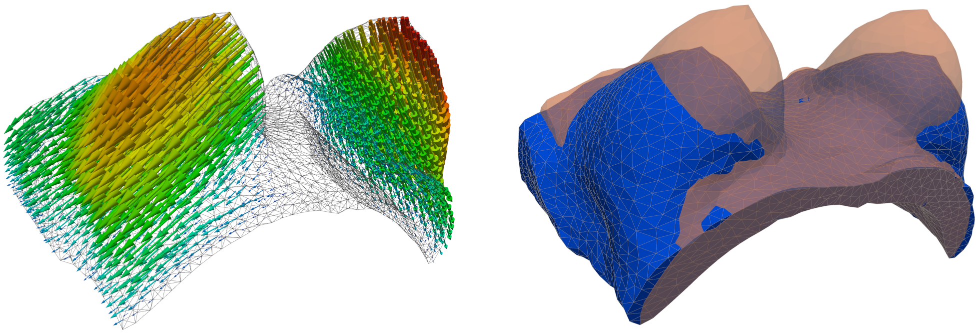

(a) *Displacement vectors illustrating the result of the inverse – or unloading – analysis*

(b) *Overlay of the prone (transparent orange) and the predicted unloaded breast geometry (blue surface)*

Figure 3.5: *Unloaded (or gravity-free) configuration numerical prediction of a patient-specific breast geometry using an inverse analysis approach as described in Eiben et al. (2013, 2014).*

gravity. As a result, the image derived patient-specific breast geometry, and hence the state of the biomechanical model, is initially situated in a loaded condition under mechanical stress. This requires the evaluation of the unloaded – or gravity-free – configuration of the breast geometry. Figure 3.5 shows an example of a recovered unloaded configuration from a prone loaded one using the numerical scheme described below in section 3.3.2.3.

Several approaches to recover the stress-free – or undeformed configuration – of an elastic body have been proposed in the literature. In the context of the inverse finite deformation approach, the initial stress-free (or unloaded) configuration of an elastic body is determined from a given deformed state and thus, the stress state within its current (or loaded) configuration is evaluated. Govindjee and Mihalic (1996) proposed a numerical approach that solves the inverse motion i.e. the deformation that maps the current configuration to the reference (or unloaded) configuration directly from the boundary-value equilibrium problem. They developed a finite element methodology that involves modifications to standard forward analysis platforms. The formulation proposed is based on a re-parameterisation of the equilibrium equations and it has a direct physical connection to the problem at hand, eliminating boundary condition difficulties. This numerical formulation was later extended to isotropic near-incompressible materials (Govindjee and Mihalic,

1998) as well as anisotropic hyperelastic solids (Lu et al., 2007). On the other hand, Carter et al. (2008) proposed a fixed point type iterative scheme, later extended by myself in (Eiben et al., 2013), which allows the recovery of the unloaded configuration by using only forward simulations and thus is able to work with any finite deformation simulation software.

The contents of this section was presented at *SPIE Medical Imaging 2014* (Eiben et al., 2014) and compares three different numerical approaches to obtain an unloaded configuration of biological tissues from the loaded geometry and highlights the pros and cons of each method. The methods being compared are: *(i)* the crude approximation where the initial loading of the imaging position is not considered and only the direction of gravity is inverted, M_1, *(ii)* the inverse finite deformation approach which requires the parametrisation of the governing equations, M_2, and *(iii)* the iterative fixed point type approach, where only forward simulations are utilised to optimise the node position in the unloaded configuration, M_3. Since I extended the latter approach and compared these three methods, the description of this methodology is given in detail in section 3.3.2.3.

As the prone and supine MR images show the breasts in a gravity loaded configuration, the true unloaded state remains unknown. Several groups approximated the unloaded state by creating a neutral buoyancy condition (Rajagopal et al., 2008b; Carter et al., 2009) by immersing the subject's breasts into water while they were placed in the prone configuration. In these cases the simulation accuracy can be evaluated by either the use of fiducial markers or image derived correspondences. Due to the lack of such images and to avoid any inaccuracies inherent to these procedures, here a purely simulation based approach is followed in order to quantify the accuracy of the recovery of the unloaded configuration. A quantitative comparison of the unloading methodologies of patient-specific models is first presented. Thereafter a numerical breast shaped phantom is used to investigate the sensitivity of all methods to the chosen material parameters. The sensitivity analysis is performed with respect to the shear modulus of the hyperelastic material model.

3.3.1 *Image Data, Shape Phantom and Biomechnical Model Generation*

The basis for the patient-specific models used in this study are prone and supine MR image pairs of three patients and of a volunteer which were acquired with a Philips Intera 1.5T. For the prone acquisitions a dedicated breast coil was used, whereas for the supine images the Q-body coil of the scanner was used to avoid any external force on the breast surface. These images were then segmented into adipose and fibroglandular tissue and the retromammary boundary was identified. From the label images biomechanical models were generated as described in sections 3.2.2 and 3.2.3, however, breast models were separately generated for the left and right breast respectively. The simulations in this section utilised a compressible hyperelastic neo-Hookean constitutive material model (Holzapfel, 2000), with the strain energy-density function

$$\Psi = \frac{\mu}{2}\left(I_{\mathbf{C}} - \ln \mathit{III}_{\mathbf{C}} - 3\right) + \frac{\lambda}{8}\ln^2 \mathit{III}_{\mathbf{C}}. \tag{3.1}$$

Here μ and λ are material parameters and were selected to be in the range defined by previous research (del Palomar et al., 2008; Han et al., 2012; Eiben et al., 2013) as $\mu_{\text{adipose}} = 300\,\text{Pa}$, $\mu_{\text{fibroglandular}} = 450\,\text{Pa}$ and $\lambda_{\text{adipose}} = \lambda_{\text{fibroglandular}} = 5 \cdot 10^4\,\text{Pa}$ for adipose and fibroglandular tissues, respectively. $I_{\mathbf{C}}$ and $\mathit{III}_{\mathbf{C}}$ are the first and third invariants of the right Green-Cauchy deformation tensor. The breast was assumed to be fixed to the pectoral muscle and the corresponding nodes were assigned with a zero-displacement boundary condition. Images and corresponding models were denoted $S1$ to $S4$, the patient position is given as P or S for prone and supine respectively and the left or right breast is indicated with L or R.

For the phantom experiments a numerical breast-shaped phantom was generated using a two-dimensional Gaussian distribution supported by a cylinder representing the pectoral muscle surface (see figure 4.11 on page 121 and section 4.2.6 for further details about the phantom geometry). A homogeneous hyperelastic neo-Hookean material distribution was assumed and three loaded configurations were simulated by applying gravitational body forces in the directions corresponding to the prone, supine and upright subject positions.

3.3.2 *Unloading Strategies*

The three numerical unloading strategies that are compared in this sections are described below.

3.3.2.1 *Inversion of Gravity*

The first approach, M_1, uses a conventional forward simulation and approximates the unloaded configuration by simple inversion of the direction of gravity. It does not consider the gravitational loading and resulting initial stresses of the breast in the imaging position. Hence, the biomechanical model that is built from the prone or supine MRI is regarded as stress-free and loaded with the gravitational body force $\mathbf{f}_B$ in the posterior and anterior direction respectively. For this standard forward problem, solution of the equilibrium equation

$$\nabla_0 \cdot \mathbf{P} + \mathbf{f}_B = \mathbf{0} \tag{3.2}$$

is accomplished via the finite element method (FEM). $\nabla_0 \cdot \mathbf{P}$ is the divergence of the first Piola-Kirchhoff stress tensor $\mathbf{P} = {}^{\partial\Psi}/_{\partial\mathbf{F}}$ which relates the strain energy density function Ψ and the deformation gradient $\mathbf{F}$.

3.3.2.2 *Inverse Finite Deformation Approach*

For the inverse finite deformation approach, M_2, the method of Govindjee and Mihalic (1996) is implemented into our in-house C++ code. Re-parametrisation of the equilibrium equation (3.2) presented by the authors results in

$$\nabla \cdot \boldsymbol{\sigma} + \mathbf{f}_b = \mathbf{0}. \tag{3.3}$$

Since the deformed configuration is known and the undeformed (or reference) configuration is the primary unknown, an Eulerian framework is advantageous here and that's why the strain measure used is the Cauchy stress $\boldsymbol{\sigma}$ and the body force in the deformed configuration is given by $\mathbf{f}_b$. The inverse deformation gradient $\mathbf{f}_{\text{inv}}$ and the deformation gradient $\mathbf{F}$ relate via the push forward operation $\mathbf{F} = (\mathbf{f}_{\text{inv}})^{-1} \circ \varphi$, where φ maps the undeformed to the deformed configuration.

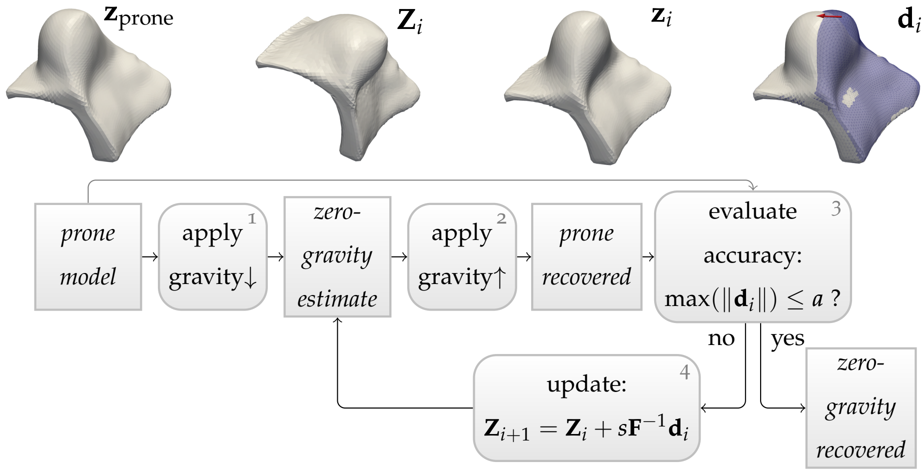

Figure 3.6: *Workflow of the iterative zero-gravity state recovery procedure* M_3*. The original model* $\mathbf{z}_{prone}$ *is to be recovered by a forward loading simulation. An initial guess of the zero gravity state* $\mathbf{Z}_0$ *is established by simulating gravity in the direction opposite to the original loading (1). Subsequently all stresses in the model are set to zero and gravity is reapplied in the original direction (2). This allows the error between the simulation and original model the to be measured (3). The update of the reference state (4) is derived from the difference* $\mathbf{d}_i$ *between the gravity loading simulation in the prone and the original prone model.*

Then the Cauchy stress can be calculated as $\boldsymbol{\sigma} = \det(\mathbf{f}_{\text{inv}})\mathbf{P}(\mathbf{f}_{\text{inv}})^{-1}(\mathbf{f}_{\text{inv}})^{-\text{T}}$. For more details of the mathematical and numerical aspects of this approach the reader is referred to the original work by Govindjee and Mihalic (1996).

3.3.2.3 *Fixed-Point Iterative Scheme*

The third method, M_3, used to estimate the unloaded configuration, is the approach originally presented by Carter et al. (2008) and extended by myself (Eiben et al., 2013) by implementing an improved method to calculate the iterative update. Figure 3.6 shows an overview of this iterative unloading approach. In principle, this method can be used with any open-source or commercial FEM package. Here however, the fixed point iterative scheme utilises an updated Lagrangian FE formulation, where only forward simulations are required. Figure 3.6 shows the prediction-correction workflow of this approach and the separate steps are numbered accordingly from (1) to (4).

The term "fixed point iteration" is known from numerical analysis where the problem $f(x) = x$ is solved by the iterative scheme $x_{n+1} = f(x_n)$, and x called a fixed point of f if the scheme converges. The unknown unloaded configurations takes the role of x and the iterative scheme is defined as follows.

The method is initialised with simple gravity inversion (1), as performed in method M_1, producing displaced node positions $\mathbf{Z}_0$ and offers the first prediction of the unloaded configuration. In order to correct the error when the gravity loading in the MRI configuration is not considered, all stresses in the current reference state prediction are set to zero and gravity is reapplied in the opposite direction (2). This results in the simulated prone loading with the corresponding node positions $\mathbf{z}_0$ and reveals the difference $\mathbf{d}_0$ in node positions between the originally loaded configuration as represented by the MRI $\mathbf{z}_{\text{prone}}$ and that from the simulation $\mathbf{z}_0$ (3).

$$\mathbf{d}_i = \mathbf{z}_{\text{prone}} - \mathbf{z}_i \tag{3.4}$$

If the maximum magnitude of the error vectors is below a predefined accuracy a, then the scheme converged and the unloaded configuration is recovered. Otherwise the difference vectors are used to update the current reference state prediction in a corresponding correction step. Using the deformation gradient, the update for the unloaded configuration (4) can be calculated by

$$\mathbf{D}_i = \mathbf{F}^{-1}\mathbf{d}_i. \tag{3.5}$$

Note that lower case and capital symbols for the error $\mathbf{d}$, $\mathbf{D}$ and the node position $\mathbf{z}$, $\mathbf{Z}$ indicate the loaded and unloaded configurations respectively. For each node, $\mathbf{F}$ is calculated using a vector median as proposed by Astola et al. (1990). The zero-gravity estimate is then updated with $\mathbf{Z}_{i+1} = \mathbf{Z}_i + s\,\mathbf{D}$, where s is a scaling factor which reduces the magnitude of the update in such cases when the new reference state estimate causes subsequent loading simulations to diverge.

The extension to the method originally proposed by Carter et al. (2008) refines the way how the reference state estimation is updated. While in the original work the measured error between the forward simulation and the loaded configuration was directly applied to update the reference state estimate, here the deformation gradient is used to transform the error form the loaded back to the unloaded configuration to obtain the update (see equation (3.5)). Figure 3.7 shows the errors

$\mathbf{d}_i$ measured in the loaded configuration for the first three unloading iterations $i = \{0, 1, 2\}$ of an example case taken from the PICTURE project. The corresponding derived nodal updates $s\mathbf{D}_i$ are shown in figure 3.8. Note how the application of the inverse deformation gradient $\mathbf{F}^{-1}$ transforms the errors $\mathbf{d}_i$ to the unloaded configuration. Hence the update follows the breast deformation and eventually leads to a faster convergence of the numerical method. This is illustrated in figure 3.9, where the mean and maximum magnitudes of the residual nodal errors $\|\mathbf{d}_i\|$ for the same case are plotted over the iterations i. In the first case (figure 3.9a) the errors were directly applied to update the zero-gravity estimate, whereas in the second case (figure 3.9b) the deformation gradient was used as proposed above. The latter method reduces the number of iterations required to reach the convergence criterion of $\max(\|\mathbf{d}_i\|) \leq a$ with $a = 0.5\,\mathrm{mm}$ from twelve to seven iterations.

Moreover, figure 3.10 visualises the initial estimate of the gravity free configuration of method M_3 shown as a red wireframe overlayed with the final result shown in grey. Since the initial estimate of M_3 also coincides with the final result of M_1, a visual comparison of the expected error when the latter method is employed can be made.

The forward simulations of methods M_1 and M_3 were carried out with the open source software FEBio.[5]

3.3.3 *Evaluation*

PATIENT SPECIFIC MODEL UNLOADING Figure 3.11 shows an overview of the strategy followed for the patient-specific unloading evaluation. The zero-gravity state estimates, in terms of nodal distance between each method combination, are compared. For this let the final unloaded node positions recovered with the methods M_1, M_2 and M_3 be $\mathbf{Z}_{M_1}$, $\mathbf{Z}_{M_2}$ and $\mathbf{Z}_{M_3}$ respectively, then the distances between the nodes is given as the Euclidean distances $d_{i,j} = \|\mathbf{Z}_{M_i} - \mathbf{Z}_{M_j}\|_2$. The node distances then can be evaluated by calculating the mean ($\bar{d}_{i,j}$), maximum ($\max\left(d_{i,j}\right)$), and standard deviation ($\mathrm{std}\left(d_{i,j}\right)$).

---

[5] `www.febio.org` accessed 15.11.2012

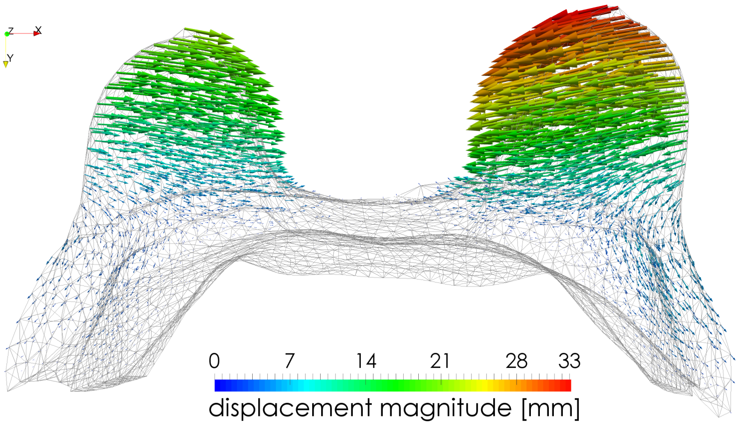

(a) $\mathbf{d}_0$

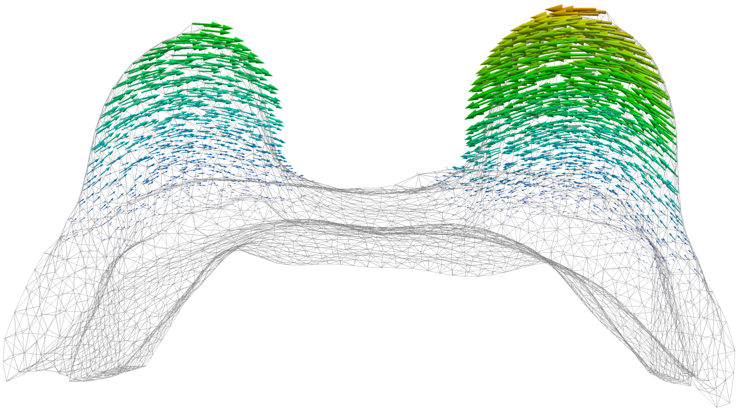

(b) $\mathbf{d}_1$

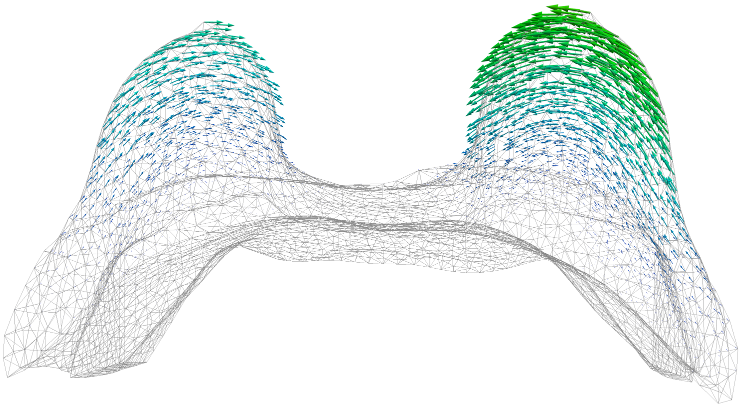

(c) $\mathbf{d}_2$

Figure 3.7: *First three iterations of the iterative unloading scheme* M_3*. The figures show the error vectors* $\mathbf{d}_i$ *in the prone loaded configuration that is measured between the original model* $\mathbf{z}_{prone}$ *and the prone forward simulation* $\mathbf{z}_i$ *(c.f. step (3) in figure 3.6). Before these error vectors are used to update the estimate of the unloaded configuration, the vectors are warped using the deformation gradient* $\mathbf{F}$*. The corresponding transformed vectors are shown in figure 3.8.*

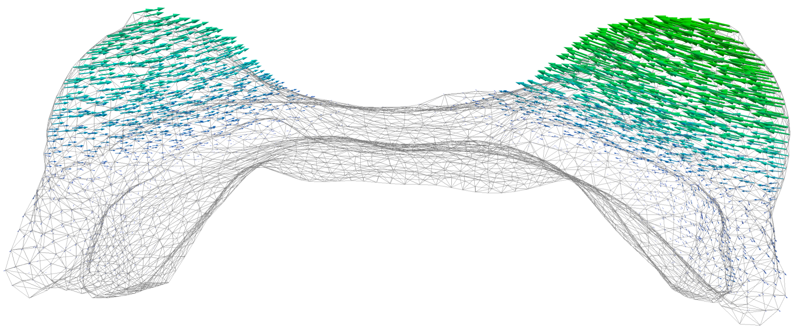

(a) $s\mathbf{D}_0$

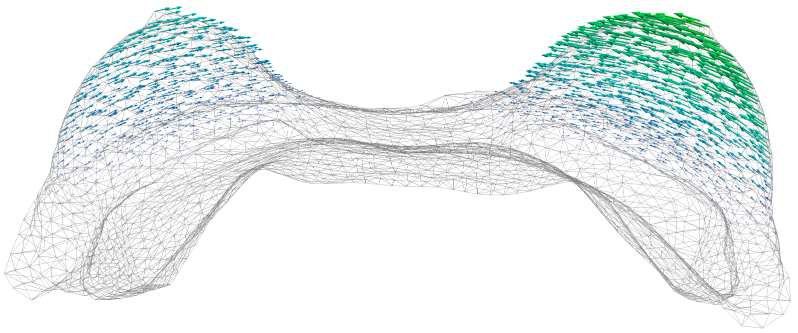

(b) $s\mathbf{D}_1$

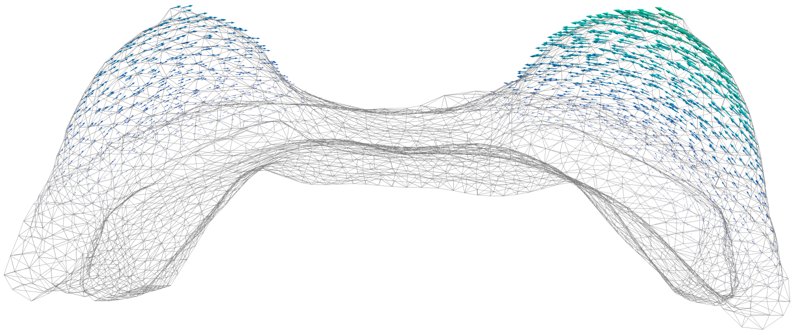

(c) $s\mathbf{D}_2$

Figure 3.8: *First three iterations of the iterative unloading scheme M_3. The figures show the vectors $s\mathbf{D}_i$ which are used to update the zero gravity estimate (c.f. step (4) in figure 3.6). The update is derived from the error $\mathbf{d}_i$ in the loaded configuration as shown in figure 3.7 by applying the inverse deformation gradient $\mathbf{F}^{-1}$.*

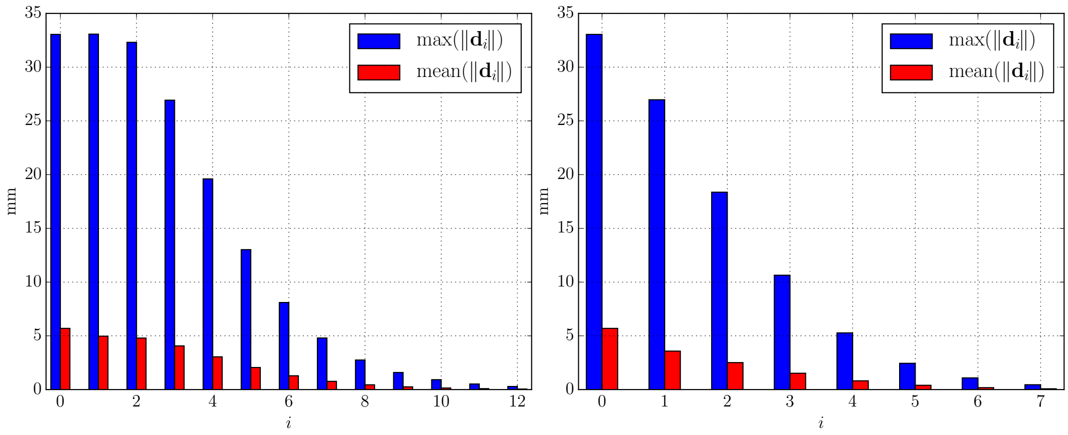

(a)

(b)

Figure 3.9: *Mean and maximum of the error magnitude* $\|\mathbf{d}_i\|$ *during the iterations i for unloading procedure* M_3*. Figure (a) visualises the convergence, when the residual error vectors are directly used to update the zero-gravity estimate as proposed by Carter et al. (2008). A faster convergence can be observed in figure (b), when the inverse deformation gradient is used to project the error vectors to the unloaded configuration before updating the nodal position of the zero-gravity estimate accordingly (Eiben et al., 2013, 2014).*

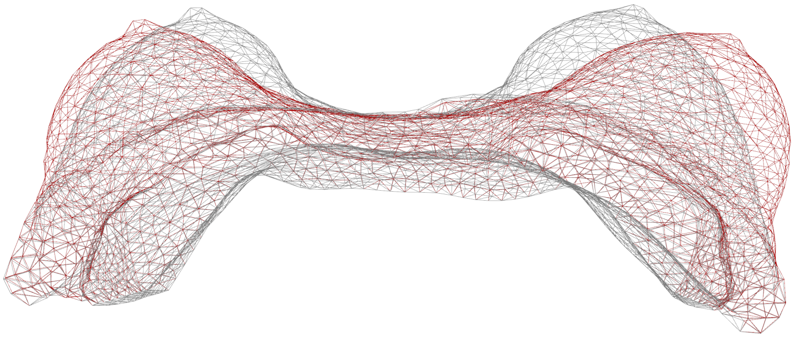

Figure 3.10: *Initial (red) and end result (grey) of unloading method* M_3*. The initial estimate is also equivalent to the final result of method* M_1*.*

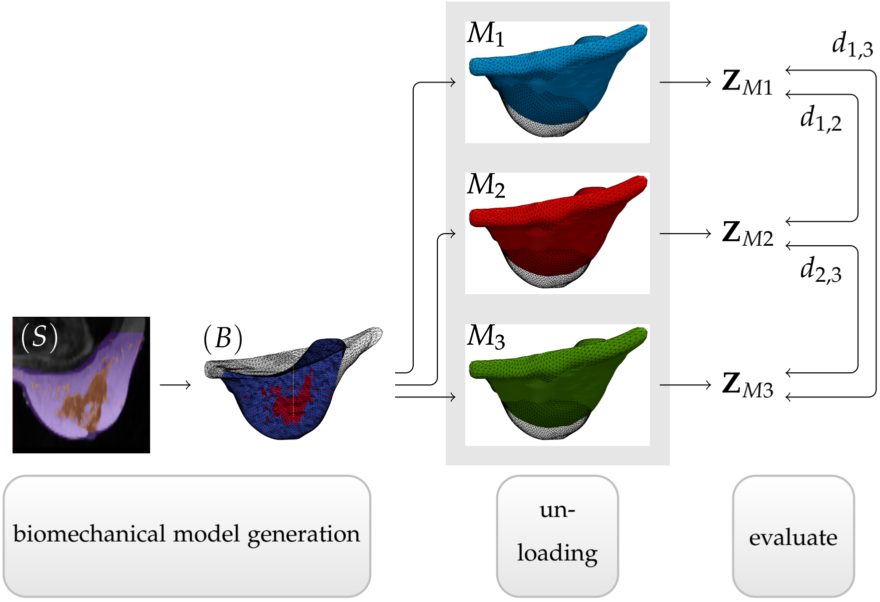

Figure 3.11: *Comparison strategy for the different inverse approaches* M_1, M_2 *and* M_3 *for biomechanical finite element models (B) built from segmented MR images (S) in terms of relative nodal distances* $d_{1,2}$, $d_{1,3}$ *and* $d_{2,3}$.

SHAPE PHANTOM UNLOADING AND MATERIAL PARAMETER SENSITIVITY

In order to overcome the challenges associated with an unknown unloaded configuration in the case of the patient-specific models, a phantom geometry was used to which known body force loadings were applied. The unloaded configurations were then recovered from the loaded states using the three methods described above. A quantification of the recovery error is possible by comparing the recovered node positions with those of the original shape phantom (see figure 3.12).

When the loading and unloading steps are performed with the same constitutive relation and the same associated parameters, a high accuracy for the recovery of the unloaded configuration is expected, provided the underlying assumptions about initial stresses are correct, i.e. in the cases of M_2 and M_3. However, in real case scenarios the true material parameters are often not known a priori. Thus, this experiment was extended to quantify the sensitivity of the unloading methods with respect to the model stiffness. For the forward simulations a shear modulus of $\mu = 300\,\mathrm{Pa}$ was used (which is in the range used by previous researchers for

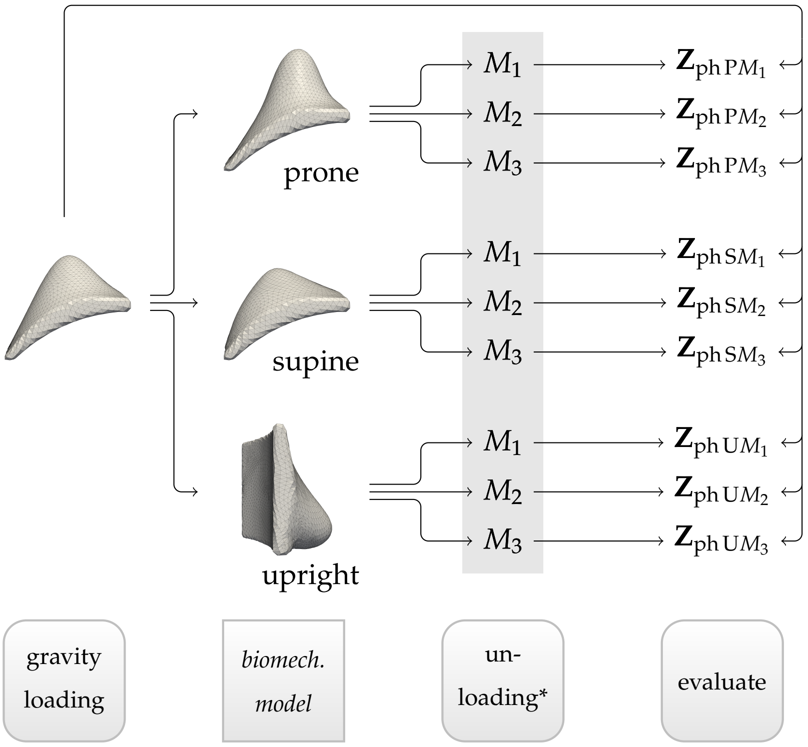

Figure 3.12: *A generic breast shape phantom (ph) represents the known unloaded configuration. In a forward simulation step the phantom geometry is loaded with gravity as a body force into the prone (P), supine (S), and upright (U) positions. From these loaded configurations the unloaded state ($g = 0$) is recovered using the three inversion methods M_1, M_2 and M_3 resulting in the node positions $\mathbf{Z}$ with the corresponding subscripts. The error of the recovery can be quantified directly by comparing the node positions with those of the original shape model. For the sensitivity experiments the material stiffness of the unloading step was modified to the one used for the loading simulations.*

this application such as Carter et al. (2009)), and the recovery was performed in the range of $\mu = [250, 260, \dots, 350]$ Pa (see asterisk in figure 3.12).

3.3.4 *Results*

In this study, ten MRI reconstructed breast geometries from four individuals in the prone and supine position were used. The mean, maximum and standard deviation of the relative distances between the node positions of the estimated unloaded configurations using methods M_1, M_2 and M_3 are given in Table 3.1. The last

	M_1 vs. M_2			M_1 vs. M_3			M_2 vs. M_3			M_3
Subject	$\bar{d}_{1,2}$	$\max(d_{1,2})$	$\mathrm{std}(d_{1,2})$	$\bar{d}_{1,3}$	$\max(d_{1,3})$	$\mathrm{std}(d_{1,3})$	$\bar{d}_{2,3}$	$\max(d_{2,3})$	$\mathrm{std}(d_{2,3})$	n_{M3}
S1 PL	0.92	3.10	0.87	0.89	2.89	0.83	0.05	0.24	0.06	5
S1 SL	0.73	2.32	0.66	0.60	2.12	0.59	0.19	0.87	0.20	3
S2 PR	14.25	54.34	16.52	14.32	54.72	16.64	0.13	0.66	0.13	[2,4,5]
S2 SR	0.89	3.38	0.90	0.86	3.05	0.84	0.10	0.60	0.14	6
S3 PL	0.45	1.85	0.48	0.42	1.62	0.42	0.05	0.28	0.06	4
S3 PR	0.48	1.91	0.52	0.44	1.67	0.46	0.06	0.28	0.07	4
S3 SL	0.16	0.70	0.17	0.08	0.39	0.09	0.09	0.31	0.09	2
S3 SR	0.20	0.88	0.22	0.10	0.49	0.12	0.10	0.40	0.11	2
S4 PR	1.09	4.28	1.26	1.03	3.98	1.18	0.08	0.32	0.09	5
S4 SR	0.33	1.34	0.36	0.26	1.13	0.28	0.09	0.45	0.11	3

Table 3.1: *Evaluation using patient data: Mean* $\bar{d}$*, maximum* $\max(d)$ *and standard deviation* $\mathrm{std}(d)$ *of node distances in millimetres between the different methods (*M_1*,* M_2*,* M_3*), as well as the number of iterations required by* M_3 *in order to converge,* n_{M3}*.*

column of this table provides the number of iterations required by M_3 to converge to the required error tolerance which was set for all experiments to 0.5 mm.

It can be observed that the inverse approach (M_2) and the iterative approach (M_3) produce comparable results, as the maximum node distance is below the voxel size of these clinical breast MR images. Thus, for image guidance applications, for example, both approaches can be regarded as producing equivalent results. For case *S2 PR* the initial guess for M_3 produced with the simple gravity inversion was, presumably due to the volume of the breast, so far off the zero-gravity state that it did not produce meaningful results. To circumvent this problem, the reference state was evaluated for increasing gravitational loadings i.e. $\{\mathbf{f}_B/4;\ \mathbf{f}_B/2;\ \mathbf{f}_B\}$. The results of each load then initialised the next step.

The disagreement of the simple inversion of gravity, M_1 and the other two methods is always bigger for the prone configurations than for the supine ones. This suggests that the accuracy achieved with M_1 depends largely on the geometry of the problem at hand, i.e. in the supine position the breast is compressed against the chest wall and thus experiences support on the whole retromammary surface, whereas in the prone case the breast is pulled away from chest wall without any

	M_1			M_2			M_3		
	$\bar{d}_{1,R}$	$\max(d_{1,R})$	$\text{std}(d_{1,R})$	$\bar{d}_{2,R}$	$\max(d_{2,R})$	$\text{std}(d_{2,R})$	$\bar{d}_{3,R}$	$\max(d_{3,R})$	$\text{std}(d_{3,R})$
prone	1.93	11.91	2.68	0.018	0.048	0.015	0.062	0.386	0.078
supine	1.01	3.90	0.95	0.027	0.075	0.023	0.088	0.504	0.100
upright	4.28	17.89	4.83	0.013	0.053	0.013	0.088	0.963	0.084

Table 3.2: *Evaluation using a breast shape phantom: Accuracy of the three unloading methodologies in terms of mean, maximum and standard deviation of nodal distance between the recovered stress-free state and the original unloaded configuration. All measurements are given in millimetres.*

support underneath. For the fixed point iterative type method, M_3, this results in more iterations to achieve the specified accuracy in the unloading of the prone cases.

The results for the phantom experiments are given in Table 3.2. The unloading error of the simple inversion method M_1 is about an order of magnitude larger than that of the more sophisticated approaches, M_2 and M_3. The accuracy of M_2 outperforms that of M_3 but as the recovery accuracy was set to 0.5 mm this is not surprising. If an application had a smaller tolerance regarding accuracy, this could be achieved with M_3 via more iterations.

The similarity between the inversion methods M_2 and M_3 is also reflected by the results of the sensitivity experiments which are shown in figure 3.13. The box-plots show the deviation of the recovered node positions from the known unloaded configuration in terms of the median, maximum, minimum, as well as lower and upper quartiles. As can be expected, the recovery accuracy deteriorates the further the material stiffness varies from the true value (in this case $\mu = 300\,\text{Pa}$). The error introduced by the deviation of the material stiffness from the true value by only 10 Pa already introduces errors significantly larger than the accuracy gain of method M_2 over M_3.

As noted earlier, the accuracy of the simple inversion of gravity, M_1, also depends on the loading geometry, i.e. unloading from the prone, supine or upright position. For accuracy requirements of around 5 mm the unloading with M_1 appears to be a viable option to unload the supine position only (see figure 3.13d), whereas it is

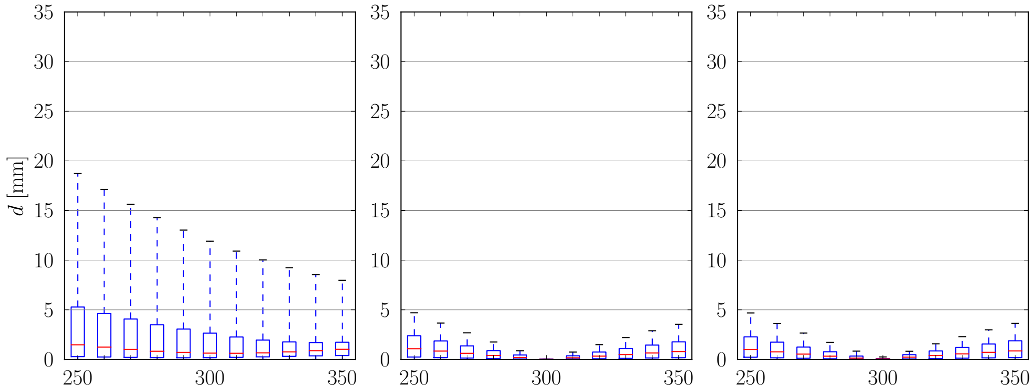

(a) *prone*, M_1 (b) *prone*, M_2 (c) *prone*, M_3

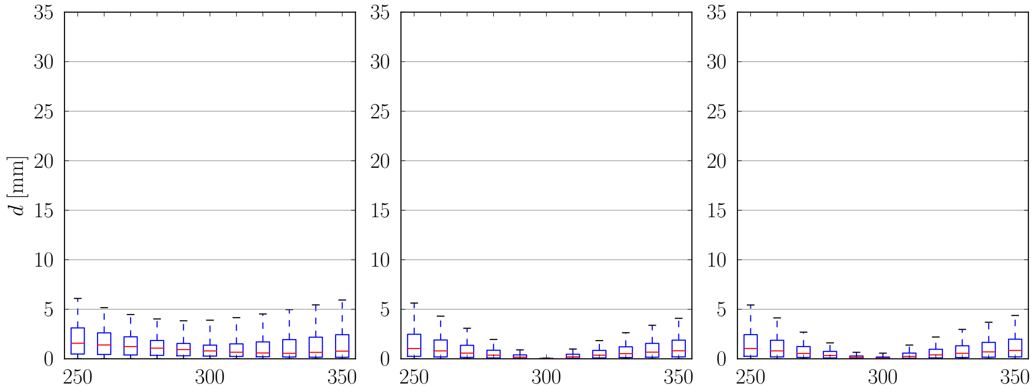

(d) *supine*, M_1 (e) *supine*, M_2 (f) *supine*, M_3

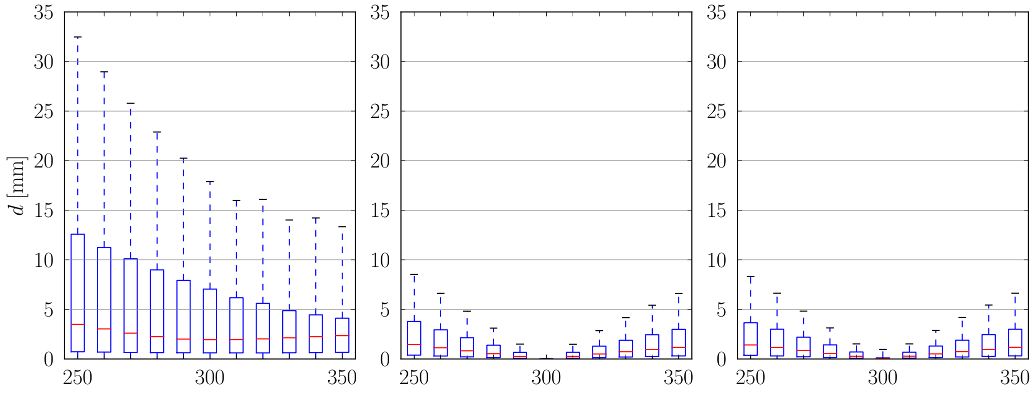

(g) *upright*, M_1 (h) *upright*, M_2 (i) *upright*, M_3

Figure 3.13: *Simulation results of the sensitivity experiments using the breast shaped phantom. The horizontal axis for all graphs is material parameter* μ *(see equation* (3.1)*) associated with the shear stiffness of the model and is given in Pascal.*

unlikely to produce accurate results for prone or upright loadings. Moreover, it is important to note the variability of the results of M_1 when patient-specific models are being recovered due to varying breast volumes.

A trend that can be observed for cases where gravity is removed from the prone configuration can also be seen in figure 3.10. The simple inversion of the direction of gravity results in an estimate of the unloaded configuration, whose position is too far lateral (red wireframe) when compared to the result of the iterative unloading M_3 (grey wireframe).

3.3.5 *Discussion*

In the context of finite deformation biomechanics of the breast, three different approaches estimating the unloaded configuration of patient-specific breast geometries were compared. These methods were the simple inversion of gravity, without considering pre-stresses in the imaging configuration, M_1, the inverse finite deformation approach M_2, and the iterative fixed-point – or prediction-correction – algorithm M_3.

The simple inversion of gravity can be a good estimate for reasonably small breasts, especially when the model is built from the supine position. However, this is difficult in the current clinical context, as the standard imaging position for MR images is the prone one. Furthermore it was observed that M_1 could yield completely different results from more sophisticated inversion techniques, i.e. M_2 and M_3, when biomechanical models of larger breasts are considered. Also the sensitivity to the choice of material stiffness parameters for method M_1 is substantially higher.

The second approach based on the inverse design, which is founded on a reparametrisation of the equilibrium equations for hyperelastic solids, M_2, exhibits excellent numerical results for various breast geometries. It could also be further extended to account for near-incompressible and anisotropic materials. However, as was shown in the sensitivity analysis, the high accuracy should be seen in the context of the accuracy of the material parameters. If the material parameters are not accurately known, then the error associated with the sensitivity to the material stiffness becomes significantly larger than the numerical accuracy gain of M_2 over M_3. In such a case there is little difference between M_2 and M_3.

The iterative fixed-point methodology, M_3 is highly flexible, as it can be used with any conventional FEM solver. This allows utilisation of all advantages of the selected solver such as element types, boundary conditions, material models as well as numerical optimisations. An integration into existing modelling frameworks can therefore be easily achieved. Only forward prediction and correction simulations are performed. Also, the required accuracy of the node position in the loaded configuration can be specified and adapted according to the application. A drawback, however, is the number of forward simulations required, which leads to longer execution times especially when several incremental gravitational loads are necessary for the method to converge.

Summarising the above, the results of the iterative M_2 and the inverse M_3 approaches are sufficiently close that, for the application of prone-supine breast deformation estimation, no significant numerical differences can be observed and the decision for or against one method can be solely made on the advantages and disadvantages outlined above.

3.4 CHAPTER CONCLUSION

Biomechanical models of the breast play a central role in the PICTURE project, which is concerned with predicting and quantifying the cosmetic outcome of breast conserving cancer treatment. Generating such models from segmented MR images is an involved process and was described in detail in this chapter. Since every imaging modality captures the breast under gravity loading, every derived model will represent a pre-stressed breast geometry – the loading conditions however may change significantly between modalities, in particular in terms of direction of gravity relative to the patient coordinate system.

Recovering the unloaded – or gravity free – configuration from a pre-stressed geometry is an important task in biomechanical modelling of the breast, since it allows simulation of every other loading condition such as those experienced by the patient in the supine or upright positions. Although the change of the direction of gravity is expected to produce the largest changes on the breast shape it is nonetheless important to note that MR images do not necessarily represent the breast geometry under gravity loading only. Contact of the breast with the scanner can distort its shape. This topic will be subject to further investigations in chapter 5.

Three different numerical strategies that aim to recover the unloaded configuration were compared. Reversing the direction of gravity and ignoring any pre-stresses, M_1 (c.f. section 3.3.2.1), was found to produce zero-gravity predictions with insufficient and widely varying accuracy. Since the physical conditions of the biomechanical system are ignored by this approach, this is not surprising. The inverse finite deformation approach by Govindjee and Mihalic (1996), M_2 (c.f. section 3.3.2.2), on the other hand produced excellent numerical results that were validated in phantom experiments with known ground truth deformations. The availability of this numerical approach cannot be guaranteed for every solver and might require custom implementation. On the other hand, the iterative fixed-point prediction-correction method, M_3 (c.f. section 3.3.2.3), required several iterations to converge to the predefined accuracy, however, it has the flexibility to be used with every solver that allows regular forward simulations. Thus it can be incorporated easily into an existing simulation workflow.

The iterative unloading was used by Morin et al. (2015) to simulate supine ultrasound images on the basis of prone MR images in a project unrelated to PICTURE . To accomplish this the MR images were first transformed into the corresponding gravity-free configuration and thereafter into the supine position using the methodology described in this chapter. Based on the transformed MR images the ultrasound signal could be simulated.

The prediction of an unloaded configuration requires knowledge of the material behaviour, in terms of the constitutive stress-strain relation and associated parameters. It was shown that variations in the material stiffness have a direct impact on the zero-gravity estimate. As a result, from the experiments described here, the registration methods developed in the following chapters should consider pre-stresses in a physically correct way and provide strategies to handle potentially unknown material parameters.

4

BIOMECHANICAL REGISTRATION: INTENSITY DRIVEN

CHAPTER OVERVIEW The evaluation of the unloading strategies in chapter 3 showed that it is essential to properly consider pre-stresses in the breast in order to simulate large, gravity induced deformations. This chapter extends the biomechanical simulation of chapter 3 with image registration components. This leads to a registration methodology that simultaneously

(i) considers pre-stresses in the initial patient position,

(ii) allows constrained motion of the breast tissue along the chest wall,

(iii) uses a biomechanically constrained deformation model throughout,

(iv) optimises the material parameters, and

(v) incorporates image information to correct residual misalignment,

does not currently exist.

In the first part of this chapter a sequential registration scheme is investigated which was presented at the *International Symposium for Biomedical Imaging (ISBI 2013)* (Eiben et al., 2013). It was used as a tool to establish the registration workflow. The main contribution of this work is that the large deformation between prone and supine patient positioning is approached in an approximately symmetric way. The biomechanical simulation is symmetric in the sense that it estimates an unloaded configuration of the prone and supine MR image respectively, whereas the subsequent image registration step is non-symmetric. Hence the large deformation from prone to supine is split between two separate unloading simulations. The gravity free configurations are estimated by using the iterative unloading procedure (section 3.3.2.3) and the final intensity based alignment follows a free form registration paradigm. While this initial symmetric sequential approach addresses the pre-stresses in the original imaging position (i) and corrects residual misalignment by using a free form deformation registration (v), the motion of the breast relative to the chest wall (ii) is still insufficiently addressed by using prescribed displacements. Furthermore, only one set of material parameters was used and thus the optimisation aspect (iv) was not covered. Lastly, by using an FFD registration the final transformation is not biomechanically constrained (iii).

In the second part of this chapter the sequential approach is developed into an integrated simulation based registration scheme which is fully symmetric (see section 4.2). The proposed method addresses all of the above issues (i) to (v) by integrating image registration components, i.e. image derived forces, directly into patient-specific biomechanical simulations. The symmetric, biomechanical image registration aligns the images in a central, virtually unloaded configuration and considers gravity as the main cause of pre-stresses in the breast as represented in the images. Hence the first step includes an unloading simulation, which only considers gravity as a body force. Subsequently the alignment is improved by first updating the global material parameters, and second by adding local image derived forces to the system. These account for the residual misalignment and in turn update the unloaded configuration. This results in a biomechanically constrained deformation. The breast tissue can move along the chest wall by using a tangential motion constraint in the retromammary area. Moreover, a finite difference numerical solution scheme (FDM) permits calculations to be carried out directly on the image grid. The implemented method is used to align prone-supine MR image pairs and prone MRI with supine CT breast images.

Routine, diagnostic, pre-surgical, Dynamic Contrast Enhanced (DCE) MR images contain valuable information about the extent and location of cancer in the pendulous, prone orientated breast. The prone positioning of the patient in the MR scanner is advantageous because it allows good image quality to be achieved due to the proximity of the transceiver coil to the breast tissue and the reduction of motion artefacts due to breathing motion. However, surgery and radiotherapy are performed with the patient in the supine position. In this chapter methodologies are developed and evaluated for prone-supine image-to-image registration.

A prone-supine image pair is an essential requirement for an intensity based registration method to work. Such an image pair could be generated, for instance, through acquisition of an additional supine MR image, onto which the high quality prone MR image information could then be mapped. No contrast enhancement would be required in the supine configuration, which would be unacceptable from the clinical perspective due to scanner time and potential complications associated with the administration of the contrast agent. Hence a number of potential applications for a prone-supine image registration method can be identified:

- *surgical planning:* assuming an additional structural MR image has been acquired representing the approximate position of the patient in the operating room (OR),
- *initial pre-incision surgical guidance:* assuming the same supine MR image as above has been acquired and a methodology to transform the supine image into the physical coordinate system of the OR is also available (alignment with the OR coordinate system and consideration of surgical incision and cutting of tissues beyond the scope of this thesis), and
- *radiotherapy planning:* by relating the pre-operative MR image to a post-operative planning CT scan. The multi-modal aspect of this registration problem is covered here, however, modelling of the tumour excision will also be required and is beyond the scope of this work.

A more detailed discussion with respect to the clinical applications is provided at the end of this chapter (c.f. section 4.3).

Prone-to-supine image registration is to date an active topic of research. An overview is presented in table 4.1. Rajagopal et al. (2008b) and Babarenda Gamage et al. (2012) approached this registration task with a pure biomechanical simulation. Their method used a patient-specific model, derived from prone MR images, to first remove the effects of gravity (Rajagopal et al., 2007) and subsequently reapply gravity loading into the supine direction. However – as will be discussed in more depth in chapter 5 – the assumption that only the direction of gravity changes from the prone imaging position to the supine surgical pose is an oversimplification. For instance, contact of the breast with the coil during the MR acquisition can introduce significant deformations which cannot be easily corrected using this method.

Table 4.1: *Overview of modelling based prone-to-supine registration methods. For the final alignment, the transformation models are either Free Form Deformation (FFD) or fluid, where as the similarity metrics are either Normalised Cross Correlation (NCC) or Normalised Mutual Information (NMI). Lago et al. (2012) use prescribed surface displacements to align the biomechanical model with the supine image. Rajagopal et al. (2008a,b) and Babarenda Gamage et al. (2012) follow a "simulation only" approach without subsequent alignment.*

	Simulation				Registration	
Author	Material Type	Unloading	Element Type	Chest Motion	Deformation	Similarity
Rajagopal et al. (2008a,b)	neo-Hookean	inv. finite deform. Rajagopal et al. (2007)	Cubic Hermetian	Fixed	FEM	(sim. only)
Carter et al. (2008)	neo-Hookean	Iterative	Hexahedra	Prescirbed	FEM+Fluid	NCC
Lee et al. (2010)	neo-Hookean	not specified	Cubic Hermetian	Fixed	FEM+ FFD	NMI
Babarenda Gamage et al. (2012)	neo-Hookean	inv. finite deform. Rajagopal et al. (2007)	Cubic Hermetian	fixed	FEM	(sim. only)
Lago et al. (2012)	Mooney-Rivlin	simple inversion	not specified	Fixed	FEM	(surf. disp.)
Eiben et al. (2013)	neo-Hookean	iterative	Tetrahedra	Prescribed	FEM + FFD	NMI
Han et al. (2014)	neo-Hookean	simple inversion	Tetrahedra	Sliding	FEM + FFD	NMI

In contrast Carter et al. (2006a), Lee et al. (2010) and Han et al. (2014) also used a biomechanical finite element model to estimate the gravity induced deformation, but corrected for the residual misalignment using a subsequent intensity based image registration step. This sequential approach clearly separates the biomechanical simulation from the intensity based registration step. The key idea in all approaches is that the gross deformation can be roughly modelled by a biomechanical simulation, whereas residual deformations need to be taken into account by a final intensity based registration step. In the published literature about sequential registration only Carter et al. (2006b) and Lee et al. (2010) considered the pre-stresses of the prone position due to gravity loading in a physically correct manner. Other approaches regarded the model derived from the clinical image as stress free (Han et al., 2014).

Motion of the breast tissue relative to the chest wall is also considered differently. While some models do not allow motion along the chest wall (Lee et al., 2010; Lago et al., 2012), others use prescribed displacements (Carter et al., 2008) or fric-

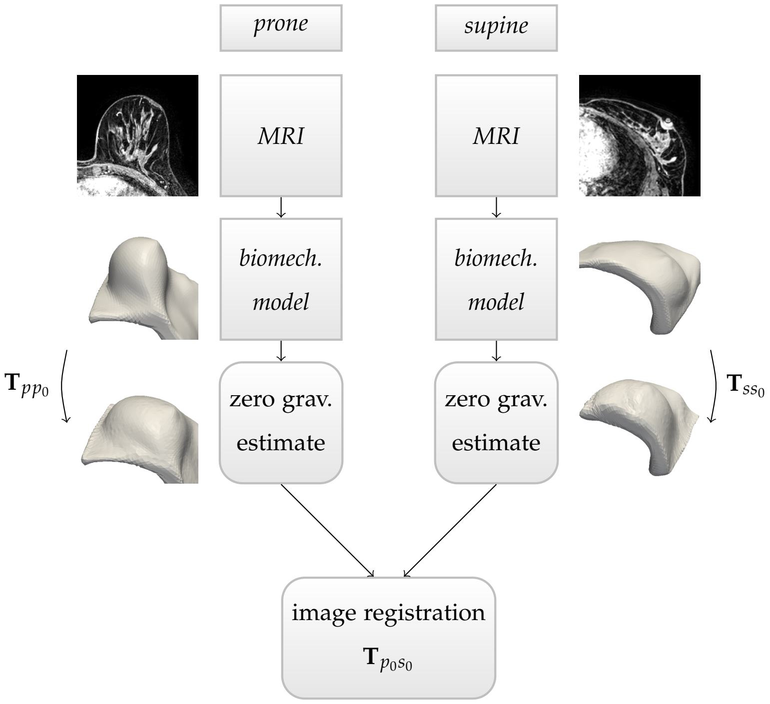

Figure 4.1: *Outline of the workflow used to align prone and supine image data using biomechanical unloading simulations and intensity based free form deformation registration.*

tionless sliding (Han et al., 2014). Defining appropriate prescribed displacements usually requires manual pre-processing which is undesirable in a clinical context. Lastly, a large variation in soft tissue elasticities might require an optimisation of the corresponding material parameters (Han et al., 2010, 2014). In the following, first a sequential and thereafter a fully symmetric, integrated registration methodology is presented.

4.1 SEQUENTIAL REGISTRATION APPROACH

In this section the zero-gravity state recovery scheme presented in section 3.3.2.3 and intensity based image registration are combined into a nearly symmetric alignment workflow, where image registration links the two unloaded reference states. This approach produces clinically useful alignment accuracies with a target registration error of 5.6 mm in the unloaded configuration. This error is comparable to published work and the inter-observer landmark selection variability. In addition this method considers the loading conditions in a physically correct manner.

Figure 4.1 shows the overall alignment strategy as was presented at the *International Symposium for Biomedical Imaging (ISBI 2013)* (Eiben et al., 2013). This section (4.1) describes the work in detail. Note, since the biomechanical model generation procedure was significantly improved since publication of this work, for completeness the procedure that was used to generate the results is included here.

4.1.1 *Image Data*

The prone-supine MR image data pair contains T1-weighted fat-suppressed and T2-weighted structural images with a resolution of $0.75 \times 0.75 \times 1$ mm for the prone and $0.96 \times 0.96 \times 1$ mm for the supine images. MR images were acquired at the University of Chicago Hospital using a Philips Achieva 1.5 T scanner. A gradient echo (GR) sequence with a flip angle of 12°, an echo time of 2.7 ms (2.4 ms) and a repetition time of 5.5 ms (4.4 ms) was used to acquire the T1-weighted images (MR imaging parameters for the supine acquisition are given in brackets if different from the prone acquisition parameters). The prone T1-weighted image was the pre-contrast image of a dynamic contrast enhanced sequence whereas the supine image was acquired for the purpose of this study. The structural T2-weighted images were acquired using a spin echo sequence with an echo time of 327 ms (218 ms) a repetition time of 2000 ms and a flip angle of 90°. Consent of the 57 year old patient was obtained to acquire the additional supine scans and to further process the data for scientific purposes. For the supine imaging a cardiac surface coil was carefully placed on the chest of the patient to minimise deformation of the breast while providing good image quality.

For validation of the developed image registration technique, 14 corresponding landmarks – including the nipple position and visually distinct glandular structures – were chosen by three medical image processing experts. The mean inter-observer error was calculated as 5.7 mm with a standard deviation of 6.3 mm in the supine image.

4.1.2 *Biomechanical Model Construction*

In order to build patient-specific biomechanical breast models, in a first step the prone and supine images were segmented into fat, fibro-glandular tissue and muscle. The T2-weighted and T1-weighted fat-suppressed images were then combined to obtain a closed skin surface. After noise reduction with a bilateral filter (Tomasi and Manduchi, 1998) a level-set evolution segmented the background from the body. Automatic segmentation of the internal body structures is difficult to achieve as algorithms might be designed for the prone image position only (i.e. not supine) or are not publicly available. Thus the chest wall and the pectoral muscle were segmented manually from the image. The remaining tissue was further segmented into adipose and fibroglandular tissue using an expectation maximisation algorithm with a Markov Random Field regularisation and a bias field correction (Van Leemput et al., 1999; Cardoso et al., 2011)[1].

From the label image a surface mesh was created using a marching cubes algorithm. The mesh quality was improved with *Meshlab's*[2] Laplacian smoothing and iso-parametrisation resampling. The tetrahedral mesh was then built using *Tetgen*[3] and material parameters were assigned using the label image from the segmentation step.

The boundary conditions are selected such that nodes on the inferior and superior boundary of the model could move in the axial plane. Nodes on the chest wall are displaced to approximate relative movement of the breast tissue on the pectoral muscle. Let $\theta = \Theta(\mathbf{x})$ be the mapping of Cartesian coordinates $\mathbf{x} = (x, y, z)$ into cylindrical coordinates $\theta = (r_c, z_c, \phi)$ and the angle ϕ be defined such that the superior-inferior body axis is aligned with the cylinder axis. The anterior direction is assigned with the angle zero. Displacing the nodes on the chest wall from $\mathbf{x}$ to $\mathbf{x}_r$ according to

$$\mathbf{x}_r = \Theta^{-1}(r_c, z_c, k_c\phi) \tag{4.1}$$

---

[1] `http://sourceforge.net/projects/niftyseg` accessed October 2012.

[2] `http://meshlab.sourceforge.net` accessed 3.12.2013.

[3] `http://tetgen.org` accessed 16.07.2012.

results in circumferentially stretched facets. Here k_c is the stretching factor which is chosen by comparison of the lateral boundary of the breast in the prone and the supine configuration. A stretching factor of $k_{cp} = 5/4$ for the prone and $k_{cs} = 4/5$ for the supine configuration is selected, so that application of the circumferential stretching – in the form of a displacement boundary condition – during the unloading simulation aligns the lateral breast boundaries.

4.1.3 *Zero Gravity State Estimation*

Simulations were performed using the open-source package *Nifty Sim*[4], a Total Lagrangian Explicit Dynamic Solver (TLED) which utilises the Graphics Processing Unit Taylor et al. (2008); Johnsen et al. (2014). This algorithm solves the basic equation of motion

$$\mathbf{M}_\rho \, \partial_{tt} \mathbf{U}_N + \mathbf{D} \, \partial_t \mathbf{U}_N + \mathbf{K} \left(\mathbf{U}_N \right) \mathbf{U}_N = \mathbf{R}_{\text{ext}}, \tag{4.2}$$

where $\mathbf{U}_N$ is the nodal displacement, $\mathbf{M}_\rho$ is the diagonalised lumped mass matrix, $\mathbf{D}$ is the diagonalised damping matrix, $\mathbf{K}$ is the stiffness matrix and $\mathbf{R}_{\text{ext}}$ are the external forces acting on the body. One major advantage of the TLED algorithm is that the nodal reaction forces are calculated per element. Thus assembly of the stiffness matrix is not necessary which allows efficient parallelisation.

Using the procedure outlined in section 3.3.2.3 the transformations $\mathbf{T}_{pp_0}$ and $\mathbf{T}_{ss_0}$ for the prone and the supine model which describe the deformation from the loaded configuration to the corresponding zero-gravity estimates are calculated.

4.1.4 *Image Registration*

To measure the initial landmark distance, prone and supine images are rigidly aligned. The transformation is calculated using an orthogonal Procrustes method from corresponding points on the costal cartilage and anterior rib cage (see e.g. Hill et al. (2001) and references therein). This rigid structure adjacent to the breast tissue allows alignment of the patient's body between the two positions.

---

[4] `http://sourceforge.net/projects/niftysim` accessed 4.10.2012.

In the estimated zero-gravity state *Nifty Reg*[5] is used for affine and non-linear registration. Nifty Reg is a fast implementation of the free form deformation algorithm (Rueckert et al., 1999; Modat et al., 2010) that uses cubic B-splines as a transformation model. The objective function is composed of the normalised mutual information (NMI) and a regularisation term which penalises high bending and thus unrealistically large deformations.

This intensity based image registration is used to establish point-wise correspondence in the zero-gravity state, $\mathbf{T}_{p_0s_0}$. Thus it is possible to obtain the complete transformation from prone to supine and vice versa as a composition of the appropriate transformations (see figure 4.1). The transformation $\mathbf{T}_{ps}$ from prone to supine is given by

$$\mathbf{T}_{ps} = (\mathbf{T}_{ss_0})^{-1} \circ \mathbf{T}_{p_0s_0} \circ \mathbf{T}_{pp_0} \tag{4.3}$$

and that from supine to prone is given by

$$\mathbf{T}_{ps} = (\mathbf{T}_{pp_0})^{-1} \circ (\mathbf{T}_{p_0s_0})^{-1} \circ \mathbf{T}_{ss_0}, \tag{4.4}$$

where $\circ$ denotes the composition of the transformations.

4.1.5 *Results*

The results are given in terms of the distances between corresponding, manually selected landmarks (see section 4.1.1) in the prone and the supine images before and after registration. The mean Euclidean distance $\overline{d}$ between corresponding landmarks and their standard deviation $\mathrm{std}(d)$ were measured. The numerical results are summarised in table 4.2.

An initial landmark distance of 103.6 mm was calculated (see section 4.1.4), which is nearly five times as large as the largest nipple displacement in numerical prone-to-supine simulations carried out by Pathmanathan et al. (2008) and highlights the scale of the deformation which is to be recovered. However, one has to acknowledge that the magnitude of breast deformations largely depend on the size and volume of the simulated organ.

---

[5] `http://sourceforge.net/projects/niftyreg` accessed 12.6.2013.

Table 4.2: *Mean landmark distance and standard deviation after initial rigid alignment of patient's rib cage, and after affine and non-linear registration in the zero-gravity state. To evaluate the landmark distance in the supine and prone configuration prone landmarks were furthermore propagated to the supine position and vice versa using the composed transformation according to* (4.3) *and* (4.4) *respectively.*

Configuration	registration type	$\bar{d}$ [mm]	std(d) [mm]
Initial	rigid	103.6	4.3
Zero-gravity	simulation & affine	10.7	6.3
	simulation & nonlinear	5.6	4.8
Supine	simulation & nonlinear	5.3	4.6
Prone	simulation & nonlinear	6.8	6.9

The zero-gravity state estimations were used to transform the original MRI data and these transformed volumes were then registered affinely and subsequently non-linearly. The affine registration resulted in a mean landmark distance in the gravity-free configuration of 10.7 mm with a standard deviation of 6.3 mm.

The non-linear registration was performed on the transformed fat-suppressed MR images. This resulted in a mean landmark distance of 5.6 mm in the zero-gravity configuration. Although it was possible to generate slightly better numerical values than those reported in table 4.2 by decreasing the regularisation of the intensity based B-Spline image registration, the images showed signs of under-constrained deformation and thus these results were discarded.

To evaluate the complete transformation from prone to supine, the prone landmarks were propagated to the supine configuration using the composed transformation (4.3) and then compared with the selected supine landmarks. This resulted in a mean landmark distance of 5.3 mm in the supine configuration. In the opposite direction, the supine landmarks were propagated to the prone position and then compared with the originally selected landmarks in this configuration. This resulted in a mean landmark distance of 6.8 mm in the prone configuration.

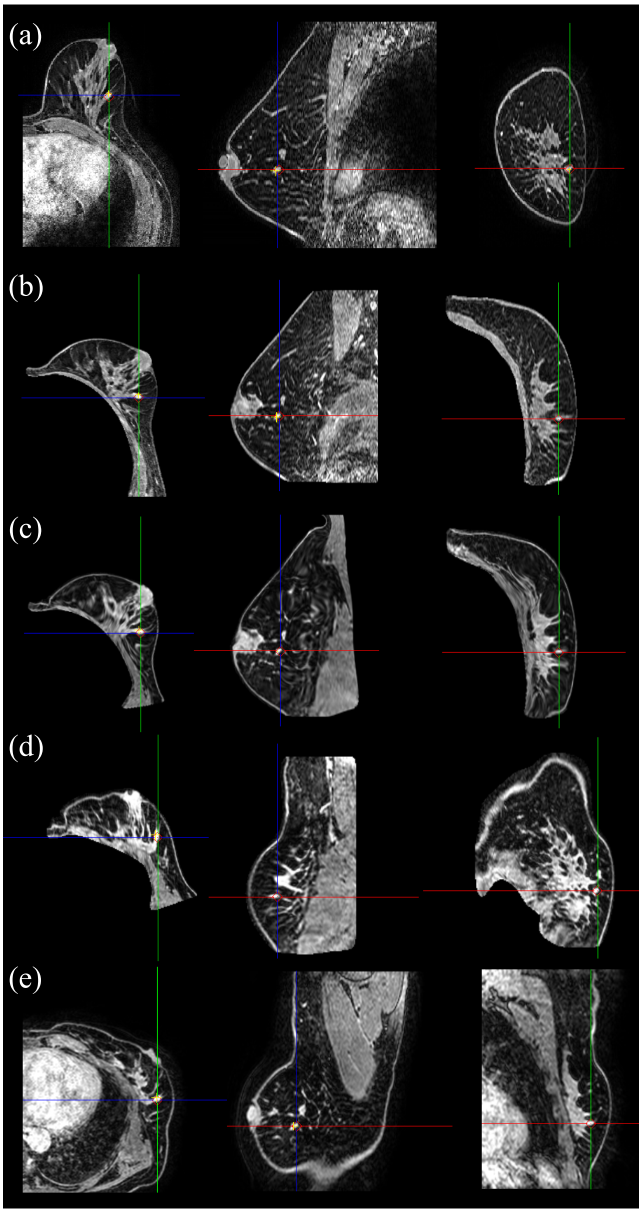

Figure 4.2: *One landmark followed through all different stages of the alignment process. (a) Prone, (b) prone zero-gravity state, (c) supine zero-gravity state registered to prone reference state, (d) supine zero-gravity state and (e) supine.*

The inter-observer variability was evaluated between three independent users who picked landmarks in the supine image given those in the prone (see section 4.1.1). This resulted in a mean landmark distance of 5.7 mm and is about the same magnitude as the evaluated registration error.

Figure 4.2 illustrates the position of one single landmark followed through all different deformation stages of the alignment process.

4.1.6 *Discussion*

In this section the feasibility of a symmetric workflow for prone-to-supine image alignment was presented which achieves, for a single patient, an accuracy of 5.3 mm in the supine configuration. This is close to the landmark inter-observer variability of 5.7 mm. Thus it is possible to align images of soft tissues which undergo large deformations with clinically useful accuracy. Exploiting the zero-gravity state makes the simulations physically more realistic compared to approaches which consider loaded configurations as being stress free.

The method described so far in this section presents a stepping stone for the subsequent development where the major shortcomings of the method were addressed. These shortcomings are – according to the numbering of the list provided on page 89 – (ii) the prescribed circumferential stretching of the retromammary elements is not flexible and does not necessarily describe anatomically plausible motion in this region (iv) the material parameters vary significantly across different patients and are not known a priori but were set here to fixed values taken from the literature, and (iii) by design the subsequent free form image registration step is not biomechanically constrained and thus could produce physically non-plausible deformations.

4.2 INTEGRATIVE REGISTRATION APPROACH

The nearly symmetric registration algorithm presented in the previous section performs a simulation and an intensity based registration step sequentially. It forms the basis for a major contribution of this thesis, which is the tight integration of image registration and biomechanical simulations into a common framework. To this end it is advantageous to investigate the differences and commonalities between elastic registration and biomechanical simulation. This is pursued in section 4.2.1, before the actual integration is presented in sections 4.2.2 to 4.2.9.

4.2.1 *Comparison: Registration and Simulation*

Elastic and hyperelastic regularisation has been proposed for image registration algorithms. As was elaborated in section 2.4, these registration methodologies use image derived forces to deform a moving image to match a target image. For large deformation problems, as they occur in prone-to-supine registration, image derived forces alone might not be sufficient as a driving force, due to the limited overlap of corresponding image structures.

As was suggested in the literature and the previous section, the key to a successful alignment in the presence of large deformations is to incorporate prior knowledge about the cause of the deformation, namely the change of direction of gravity. Since both, registration and simulation, use iterative procedures in order to deform objects on the basis of similar mathematical formulations, it should be possible to merge both into a common framework.

Elastic registration algorithms use the linear elastic potential for regularisation.[6]

$$\mathcal{S}_{\text{lin.elast.}}(\mu,\lambda)[\mathbf{u}] = \int_\Omega \frac{\mu}{4}\sum_{i,j=1}^{3}\left(\partial_{x_j}u_i(\mathbf{x}) + \partial_{x_i}u_j(\mathbf{x})\right)^2 + \frac{\lambda}{2}\left(\nabla\cdot\mathbf{u}(\mathbf{x})\right)^2 \mathrm{d}\mathbf{x} \qquad (4.5)$$

The corresponding Euler-Lagrange equation for this functional is according to Kabus and Lorenz (2010) given by

$$\begin{aligned} -\mu\Delta\mathbf{u}(\mathbf{x}) - (\lambda+\mu)\nabla\cdot\nabla\mathbf{u}(\mathbf{x}) &= 0 \\ \mathbf{L}\mathbf{u}(\mathbf{x}) &= 0 \end{aligned} \qquad (4.6)$$

and can be interpreted as the internal force of the continuous elastic material with the Lamé parameters μ and λ which is deformed by the deformation u. From this a minimisation problem can be formulated (2.32) as a linear system of equations which equalises the internal with external forces $\mathbf{g}(R,T,\mathbf{u}(\mathbf{x}))$ which are derived from a similarity measure calculated between the images R and T.

$$\alpha_1\mathbf{L}\mathbf{u}(\mathbf{x}) = \mathbf{g}(R,T,\mathbf{u}(\mathbf{x})) \qquad (4.7)$$

---

[6] For an in depth introduction see for example Modersitzki (2004, 2009), c.f. section 2.4.

The linear operator $\mathbf{L}$ is applied to $\mathbf{u}$ and calculates the internal forces according to equation 4.6. This force equilibrium can also be interpreted as the static solution to the well known Navier equation with some velocity dependent damping:

$$\rho_0 \frac{\partial^2 \mathbf{u}}{\partial t^2} = (\lambda + \mu) \nabla (\nabla \cdot \mathbf{u}) + \mu \nabla^2 \mathbf{u} + \rho_0 \mathbf{f}_B - r \frac{\partial \mathbf{u}}{\partial t} \tag{4.8}$$

Through comparison of (4.8) with (4.7) it can be seen, that the image forces of the registration fulfil the same role as the body forces in the Navier equation. The scaling α_1 accounts for the fact, that the image forces cannot be directly related to physical forces. The regularisation above only represents linear elastic materials. To move on to non-linear hyperelastic materials, the internal stress evaluation needs to be changed accordingly, arriving at the non-linear equilibrium equation of motion

$$\rho_0 \frac{\partial^2 \mathbf{u}}{\partial t^2} = \nabla_0 \cdot \mathbf{N} + \rho_0 \mathbf{f}_B - r \frac{\partial \mathbf{u}}{\partial t}. \tag{4.9}$$

Here $\mathbf{u}$ is the displacement vector, ρ_0 the mass density in the undeformed configuration, t the time, $\mathbf{N}$ the nominal stress second order tensor (or the transpose of the first Piola-Kirchhoff stress tensor), $\mathbf{f}_B$ the body force and r the speed-proportional damping coefficient. Note that the inner product $\nabla_0 \cdot \mathbf{N}$ reduces the order of tensor $\mathbf{N}$ by one (c.f. equation (4.16)). Furthermore, the subscript 0 of ∇_0 indicates that the Lagrangian frame of reference is used.

Due to the strong connection between between the basic equations of elastic registration and non-linear simulation, the differential form of the equilibrium equation (4.9) will be utilised in the following sections as a basis to develop a biomechanically constrained registration method. To achieve this, image derived forces will be combined with external body forces such as gravity; both forces then act on the body which is considered as a continuous material. Furthermore, in order to consider the gravitational forces in the prone-to-supine breast registration task in a physically correct way, the unloading also needs to be addressed.

NUMERICAL EXPERIMENT In order to estimate the difference between an existing hyperelastic image registration method (Modersitzki, 2009) and a mechanical simulation in terms of the resulting deformations, a finite element model of a numerical phantom was built. A homogeneous hyperelastic neo-Hookean material was assumed and gravity was applied in the anterior (upwards) direction (see

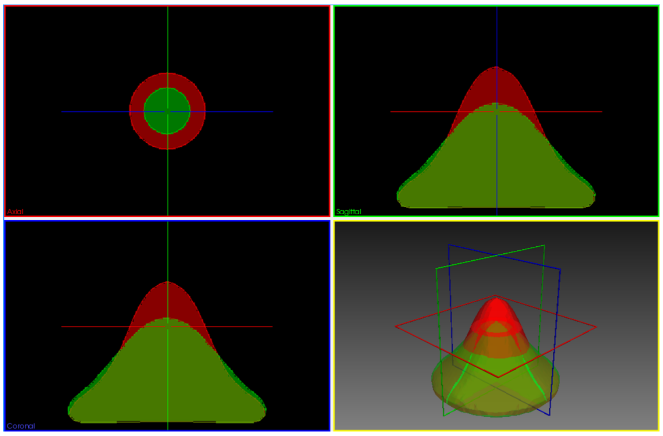

Figure 4.3: *Orthogonal slices through a numerical breast phantom without (green) and with gravity applied (red). The corresponding binary images were used as reference and template images for the hyperelastic registration experiments.*

figure 4.3). The geometry of the deformed and undeformed phantom was used to generate binary input images for the registration algorithm. The working hypothesis is, that a clear difference between the registration and the simulation should become apparent due to the different load types: The simulation considers a homogeneous loading of the body with gravity, whereas the image derived forces only act on the boundary of the object.

To allow a direct comparison between the simulation and the registration deformation vector fields, the reference image for the registration was the image generated from the unloaded phantom and the moving image was the one generated from the gravity loaded configuration. Figure 4.4 shows a visualisation of the results in terms of displacement vectors as well as the quantitative angular and magnitude difference.

It can be observed that at the tip of phantom the displacement vectors are aligned well. However, a key difference between the deformation vector fields appears at the sides of the phantom. The simulation produces a deformation vector field close to tangential to the model boundary in this area, whereas the registration contracts the object in this area. Note the corresponding differences in the angle and magnitude. Increasing the weight of the volume preserving term in (2.35) can improve this behaviour slightly but the key difference is not eliminated. As hypothesised, in the registration scheme the image similarity acts as a driving force

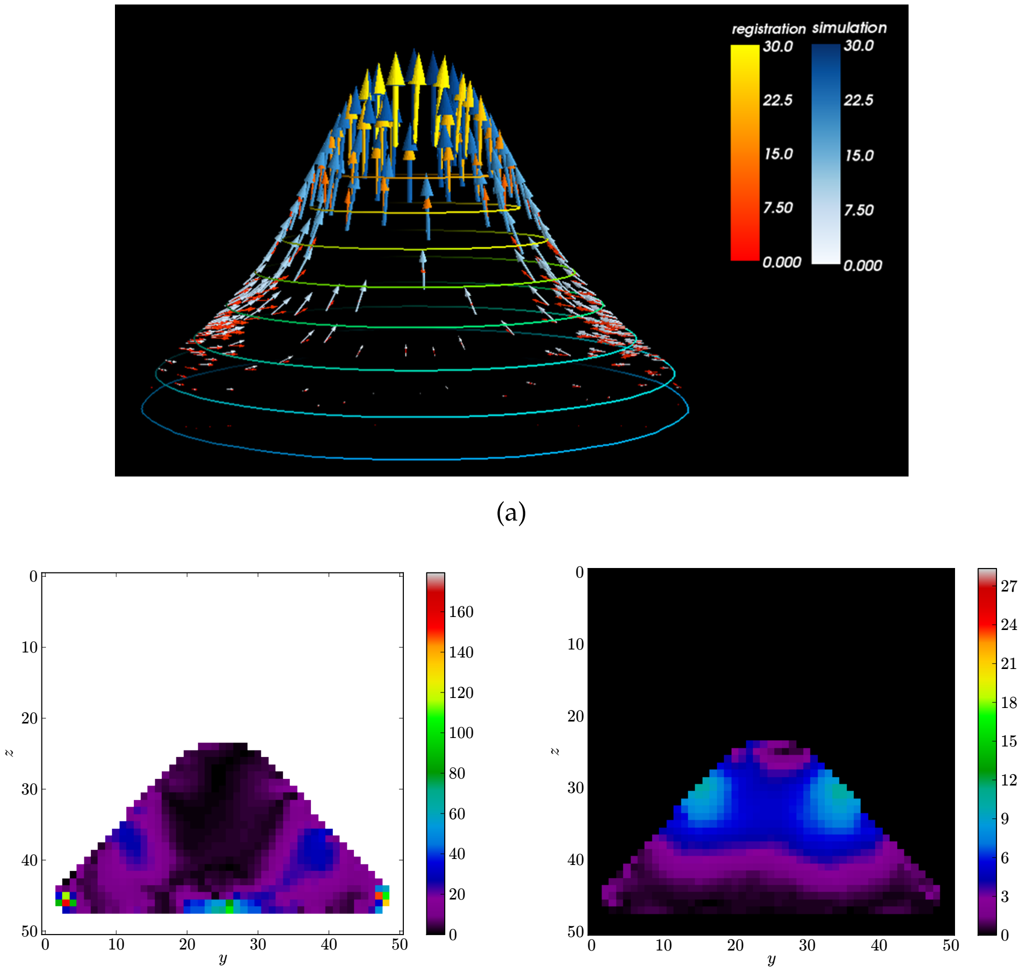

(a)

(b) *Angular difference between displacment vectors.*

(c) *Length difference between displacement vectors.*

Figure 4.4: *Deformation vector fields from image registration (red-yellow arrows) and simulation (blue arrows) and quantitative difference in terms of angle and length. Significant differences in the angle of the displacement vectors can be observed at the sides of the phantom, where the gravity loading causes displacement vectors tangential to the object boundary, whereas the registration produces a contraction.*

only on the object boundaries, whereas the gravitation acts as a body force on the whole body. This is reflected by the deformation vector fields.

Summarising the findings of this experiment, the integration of a hyperelastic regularisation into an image registration scheme alone does not guarantee the resulting deformation vector field to be similar to the one generated from a biomechanical gravity loading simulation – the acting forces are substantially different. Hence the appropriate consideration of external loading, i.e. gravity, is required. Thus in the following a biomechanical simulation based on finite differences is presented which then is extended to incorporate additional image derived forces.

4.2.2 *Overview of the Image Alignment Approach*

The computational framework developed here is a symmetric, intensity based, biomechanically driven image registration method to align prone and supine breast images. It is a significant extension to the approach presented in the previous section 4.1 and follows the idea that the main source of geometric deformation of the breast between the prone and the supine image arises from the relative difference in gravity loading. Thus when the effect of gravity is removed from the loaded breast configurations, the images being transformed accordingly, the registration task becomes less challenging. The remaining dissimilarities arise primarily from modelling inaccuracies such as unknown material parameters, missing knowledge about the exact patient-specific constitutive relation of in-vivo breast tissue and insufficient definition of boundary conditions due to contact with imaging equipment or undefined motion of the breast and muscle tissue on the chest wall.

Figure 4.5 shows an overview of the complete algorithm. The main building blocks are:

- A biomechanical deformation model (section 4.2.3),
- the calculation of the patient-specific unloaded configuration (section 4.2.3.1),
- a tangential motion constraint to enforce the motion of the pectoral muscle along the chest surface (section 4.2.3.2),

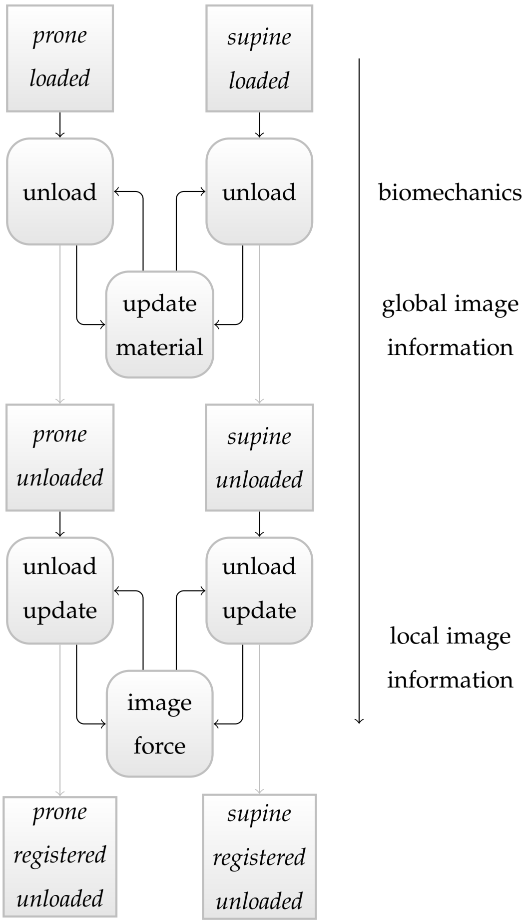

Figure 4.5: *Overview of the biomechanically constrained registration procedure. In a first step the effect of gravity is removed from the prone and supine breast image assuming generic material parameters. In a second step the material parameters are repeatedly updated until the image similarity no longer improves. The final step involves activation of image derived forces which aim to correct modelling inaccuracies and generate the final aligned images in the unloaded configuration.*

- a material update scheme (section 4.2.4), and
- image derived forces (section 4.2.5).

The algorithm is designed to start with a pure biomechanical simulation but in the course of the alignment image information is incorporated progressively, directly into the unloading simulation: first on a global and then on a local scale.

4.2.3 *3D Finite Difference Simulation*

Constitutive relations and corresponding material parameters of breast tissues are open research topics. Samani et al. (2001) and Samani and Plewes (2007) carried out mechanical tests on ex-vivo breast tissue samples. The mechanical properties of tissues however change significantly after removal from the in-vivo environment. Eder et al. (2014) used a biomechanical finite element simulation based on prone MR images to simulate the breast shape in the upright standing position of a patient. The simulation was evaluated against surface scans of the same patients in the same position. They report that the material relations proposed by Tanner et al. (2006) and Rajagopal et al. (2008a) produced the most accurate simulations. Interestingly both cited approaches use a simple neo-Hookean material constitutive relation. Hence the proposed image registration framework adopts this biomechanical description of breast tissue, which requires only two material coefficients (Lame parameters: λ and μ) (Bonet and Wood, 2008). This is an advantage if the knowledge about the exact material properties is limited either due to the lack of in-vivo measurements or incoherent literature values. Furthermore, in a clinical application scenario in-vivo measurements are usually not available.

The basis for the non-linear biomechanical deformation model is given by the principle of conservation of linear momentum as described in section 2.1.3 and also shown in equation (4.9). To calculate the material response with respect to deformation, the nominal stress tensor $\mathbf{N} = \mathbf{S}\mathbf{F}^{\mathrm{T}}$ is required which, for the neo-Hookean model according to (2.28), is given by

$$\mathbf{N}_{\mathrm{NH}} = \left(\mu\left(\mathbf{I} - \mathbf{C}^{-1}\right) + \lambda \ln(J)\mathbf{C}^{-1}\right)\mathbf{F}^{\mathrm{T}}. \tag{4.10}$$

Explicit time integration of equation (4.9) is obtained via a discrete central difference with respect to time which can be solved directly for the displacement at the next time step. The first and second time derivatives of the displacement vector field $\mathbf{u}$ can be approximated by the following forward, ∂_t^+, and central, $\partial_{tt}^\pm$, difference operators

$$\partial_t \mathbf{u} \approx \partial_t^+ U_{i,j,k}^n = \frac{1}{h_t}\left(U_{i,j,k}^{n+1} - U_{i,j,k}^n\right) \tag{4.11}$$

$$\partial_{tt} \mathbf{u} \approx \partial_{tt}^\pm U_{i,j,k}^n = \frac{1}{h_t^2}\left(U_{i,j,k}^{n+1} - 2U_{i,j,k}^n + U_{i,j,k}^{n-1}\right) \tag{4.12}$$

where $U_{i,j,k}^n$ is the discrete version of the continuous and time dependent deformation vector field $\mathbf{u}(\mathbf{X}, t)$ with spatial indices i, j, k corresponding to the position $\mathbf{X}$ and temporal index n corresponding to a point in time t.

Substituting the internal and external forces of (4.9) by $\mathbf{k}$ this equation can be rewritten:

$$\partial_{tt}\mathbf{u} = \mathbf{k} - \frac{r}{\rho_0}\partial_t \mathbf{u} \tag{4.13}$$

Using the discrete time derivatives (4.11) and (4.12) and the appropriate discrete version of $\mathbf{k}$ denoted by $K_{i,j,k}^n$, an explicit time integration scheme is formulated by solving for $U_{i,j,k}^{n+1}$:

$$U_{i,j,k}^{n+1} = \frac{(2\rho_0 + h_t r)\, U_{i,j,k}^n - \rho_0 U_{i,j,k}^{n-1} + h_t^2 \rho_0 K_{i,j,k}^n}{\rho_0 + h_t r} \tag{4.14}$$

As this scheme is only conditionally stable, the Courant-Friedrichs-Lewy (CFL) condition (Courant et al., 1928) has to be obeyed and the time increment has to be smaller than the critical time step.

Similar to the discrete differential operators (4.11) and (4.12) which are defined with respect to time, discrete spatial derivatives can be formulated by substituting the time step h_t with a spatial step h_x, h_y, h_z. The mixed spatial derivatives are required to solve (4.9) and can be approximated by the following differential operator:

$$\begin{aligned}\partial_{xy}\mathbf{u} \approx \partial_{xy}^\pm U_{i,j,k}^t = \frac{1}{4h_x h_y}\Big(&U_{j+1,k+1,l}^n + U_{j-1,k-1,l}^n \\ &-U_{j-1,k+1,l}^n - U_{j+1,k-1,l}^n\Big)\end{aligned} \tag{4.15}$$

The spatial derivatives $\partial_{yy}\mathbf{u}$, $\partial_{zz}\mathbf{u}$, $\partial_{yz}\mathbf{u}$ and $\partial_{xz}\mathbf{u}$ follow by appropriate permutation of the discrete indices i, j, k in the equations above. Note that the central difference scheme used here offers second order accuracy with respect to the truncation error but can be extended to higher orders if required (Fornberg, 1988). A derivation of the one-dimensional finite difference quotient from the Taylor series with the corresponding truncation errors is given in appendix B.2.

To complete the initial boundary value problem, an initial displacement of $\mathbf{u}_{t=0} = \mathbf{0}$ and a homogeneous Dirichlet boundary condition on the boundary of the image domain Ω as $\mathbf{u}(\partial\Omega) = \mathbf{0}$ is defined.

Revising the quantities required to solve the equilibrium equation (4.9) with an explicit time integration scheme reveals that the internal forces are derived from the divergence of the nominal stress $\mathbf{N}$, which depends on the deformation gradient $\mathbf{F}$. For both calculations – divergence of the stress and the deformation gradient – differential operators are required. Thus a straight forward implementation could first apply a discrete difference operator on the deformation vector field to obtain $\mathbf{F}$. From $\mathbf{F}$ the nominal stress can be calculated and second apply the discrete difference operator once again on the stress field to obtain the divergence. In some of our numerical experiments this approach has been observed to lead to instabilities which result in nodes clustering together.

To verify that the consecutive application of the discrete differentiation operators is the source of the clustering effects, first a two-dimensional version of the iterative solution was implemented and then the equilibrium equations were expanded such that the scheme emerging from (4.9) could be written completely in terms of the deformation gradient and its first derivatives.

The divergence of the nominal stress $\nabla_0 \cdot \mathbf{N}$ is the key quantity that has to be calculated to obtain the material response to a given deformation. Using the relation of the nominal stress and the second Piola-Kirchhoff Stress $\mathbf{N} = \mathbf{S}\mathbf{F}^{\mathrm{T}}$, the divergence of the nominal stress in two dimensions is given by

$$\begin{aligned} \nabla_0 \cdot \mathbf{N} &= \begin{pmatrix} \partial_x N_{11} + \partial_y N_{21} \\ \partial_x N_{12} + \partial_y N_{22} \end{pmatrix} \\ &= \begin{pmatrix} \partial_x \left(S_{11}F_{11} + S_{12}F_{12}\right) + \partial_y \left(S_{12}F_{11} + S_{22}F_{12}\right) \\ \partial_x \left(S_{11}F_{21} + S_{12}F_{22}\right) + \partial_y \left(S_{12}F_{21} + S_{22}F_{22}\right) \end{pmatrix} . \end{aligned} \tag{4.16}$$

In the last equality, the product rule has to be applied appropriately. Hence the deformation gradient $\mathbf{F}$ and the second Piola-Kirchhoff stress $\mathbf{S}$, as well as their spatial derivatives $\partial_x\mathbf{F}$, $\partial_y\mathbf{F}$, $\partial_x\mathbf{S}$, $\partial_y\mathbf{S}$ are required.

Let $\mathbf{u} = (u, v)^{\mathrm{T}}$ be the deformation at a given position, then the two-dimensional deformation gradient and its spatial derivatives are given by

$$\mathbf{F} = \mathbf{I} + \begin{pmatrix} \partial_x u & \partial_y u \\ \partial_x v & \partial_y v \end{pmatrix} \quad \partial_x\mathbf{F} = \begin{pmatrix} \partial_{xx} u & \partial_{xy} u \\ \partial_{xx} v & \partial_{xy} v \end{pmatrix} \quad \partial_y\mathbf{F} = \begin{pmatrix} \partial_{xy} u & \partial_{yy} u \\ \partial_{xy} v & \partial_{yy} v \end{pmatrix}. \tag{4.17}$$

Note that the components of the mixed derivatives appear in $\partial_x\mathbf{F}$ and $\partial_y\mathbf{F}$ which can be exploited when it comes to the implementation.

However, if a straight forward expansion of the second Piola-Kirchhoff stress is used, it will only be computable with an acceptable execution time for two-dimensions. Using a neo-Hookean material, $\mathbf{S}$ is given by (2.28) and the spatial derivative in the x-direction follows:

$$\begin{aligned}
\partial_x\mathbf{S} &= \partial_x\left(\mu\left(\mathbf{I} - \mathbf{C}^{-1}\right) + \lambda\ln(J)\mathbf{C}^{-1}\right) \\
&= \partial_x(\mu)\,\mathbf{I} - \partial_x(\mu)\,\mathbf{C}^{-1} - \mu\,\partial_x\mathbf{C}^{-1} \\
&\quad + \partial_x(\lambda)\ln(J)\,\mathbf{C}^{-1} + \lambda\frac{\partial_x J}{J}\,\mathbf{C}^{-1} + \lambda\ln(J)\,\partial_x\mathbf{C}^{-1} \\
&= \partial_x(\mu)\,\mathbf{I} + \left(-\partial_x(\mu) + \partial_x(\lambda)\ln(J) + \lambda\frac{\partial_x J}{J}\right)\mathbf{C}^{-1} + (-\mu + \lambda\ln(J))\,\partial_x\mathbf{C}^{-1}
\end{aligned} \tag{4.18}$$

Note that the material parameters are also a function of space. The derivative of $\mathbf{C}^{-1}$ however becomes a complex expression when explicitly written in terms of the deformation gradient. At this stage it becomes essential to find a simpler expression for $\partial_x\mathbf{C}^{-1}$, otherwise the usefulness of (4.18) is questionable for three dimensions. Therefore let $\mathbf{A}$ be a non-singular matrix and the entries are functions of the variable x. Then the derivative of the inverse matrix is given by

$$\partial_x\mathbf{A}^{-1} = -\mathbf{A}^{-1}\cdot\frac{\partial\mathbf{A}}{\partial x}\cdot\mathbf{A}^{-1}. \tag{4.19}$$

Using (4.19) to evaluate the spatial derivatives of the inverse right Cauchy Green deformation tensor, e.g. $\partial_x\mathbf{C}^{-1}$, allows straight forward implementation of (4.18) in three dimensions. For this the following equations are used which are all based directly on the deformation gradient, hence the consecutive use of the discrete differentiation operator can be avoided.

$$\partial_x J = \partial_x(\det(\mathbf{F})) \tag{4.20}$$

$$\partial_x \mathbf{C} = \partial_x(\mathbf{F}^{\mathrm{T}}\mathbf{F}) = \partial_x(\mathbf{F}^{\mathrm{T}})\mathbf{F} + \mathbf{F}^{\mathrm{T}}\partial_x(\mathbf{F}) \tag{4.21}$$

$$\partial_x \mathbf{C}^{-1} = -\mathbf{C}^{-1}\partial_x(\mathbf{C})\mathbf{C}^{-1} \tag{4.22}$$

NUMERICAL EXPERIMENT The following experimental setup was used to illustrate the clustering effect as well as the proposed solution. A rectangular domain of size $x_1 - x_0 = y_1 - y_0 = z_1 - z_0 = 1\,\mathrm{m}$ and $M_x, M_y, M_z = 17$ nodes with a homogeneous compressible neo-Hookean material was used. A body force of $f_x = 10\,\mathrm{N/kg}$ was applied. The damping coefficient was set to $r = 10^4\,\mathrm{kg/m^3/s}$. Figure 4.6 shows the node positions at the end of the simulation (figures 4.6a and 4.6b) as well as the corresponding displacements (figures 4.6c and 4.6d). The result shown in 4.6a was obtained by two consecutive applications of the discrete differentiation operator, whereas 4.6b shows the result obtained with the solution outlined above. r

The clustering effect is not immediately apparent when observing the nodal position alone, but looking at the displacement in the x-direction along a central vertical line reveals the numerical failure of this scheme (see figure 4.6c).

4.2.3.1 *Unloading of Gravity*

One of the major assumptions made up to this point is that the geometry in the unloaded (or stress-free) state is known. Of course the equation of motion still holds true for pre-stressed objects as long as pre-stressing is considered in subsequent analysis. However, measuring tissue pre-stressing in the context of in vivo breast imaging is currently not feasible. Thus the stress-free breast geometry is unknown. However, the concept of the unloaded configuration permits reduction of the scale of the deformation problem at hand.

The method presented here translates the iterative prediction-correction scheme (Carter et al., 2006a; Eiben et al., 2013, 2014) into the FDM framework. It uses the explicit time integration to recover the unloaded configuration in only one forward simulation by correcting the prediction during the course of the simulation – as

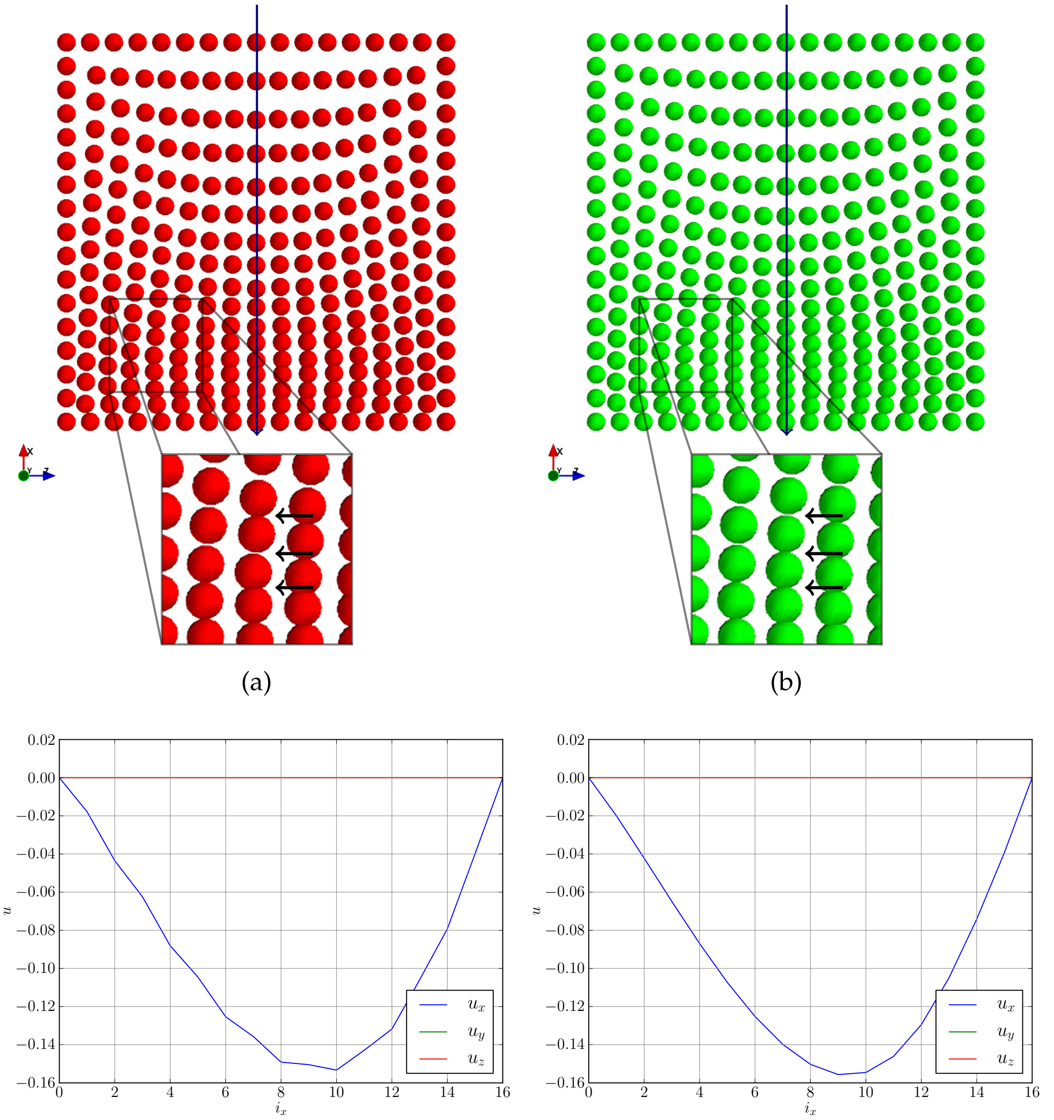

(a) (b)

(c) (d)

Figure 4.6: *Simulation results for loading a compressible medium with a homogeneous body force using the finite difference scheme with (a,c) and without clustering present (b,d). A central slice through the 3D cube geometry shows the final node positions (a,b). The consecutive application of the differentiation operator was used to produce figures (a) and (c) and resulted in clustering artefacts that are characterised by irregular node distances (see arrows in magnified view). For figures (b) and (d) repeated differentiation during the computations was avoided by reformulating the problem as described in the text. This resulted in regular node distances and resolved the clustering problem. The corresponding node displacements are shown in figures (c) and (d). These displacements are measured along the blue vertical line shown in (a) and (b), which corresponds to the horizontal axis of (c) and (d).*

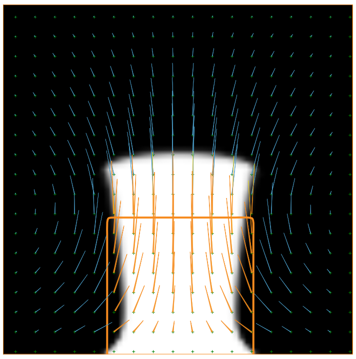

Figure 4.7: *Displacement vector field and the relation between the initial loaded (solid white) and recovered unloaded (orange outline) configuration of a simple box unloading experiment.*

compared to application of a correction step to the predicted stress-free state after each loading simulation (c.f. 3.3.2.3). In the FDM framework the spatial material distribution of the involved compartments in the loaded configuration, namely chest, fat, gland, and background are directly related to the segmentation of the clinical MR or CT images. The unloading aims to find the displacement vector field (DVF) which points from the unknown unloaded to the known loaded configuration as represented in the clinical images. Hence the DVF is determined by the biomechanical simulation and is unique for a given hyperelastic material configuration.

An overview of the developed unloading procedure using the example of the prone breast is given in the following paragraphs. Figure 4.7 shows a loaded and recovered unloaded box geometry to visualise the final DVF: starting with the geometry segmented from the prone loaded MR image, the biomechanical model is built and the forward loading simulation is initiated by applying gravity in the anterior direction. This means, that the material parameters $\mu_m(\mathbf{X})$ and $\lambda_m(\mathbf{X})$, the mass density $\rho_{0,m}(\mathbf{X})$ and body force $\mathbf{f}_{B,m}(\mathbf{X})$ define the simulation at unloading step m and are initially for $m = 0$ identical to the configuration shown in the clinical image

$$M_m(\mathbf{X}) := \{\lambda_m(\mathbf{X}), \mu_m(\mathbf{X}), \rho_{0,m}(\mathbf{X}), \mathbf{f}_{B,m}(\mathbf{X})\}. \tag{4.23}$$

The simulation itself describes the forward mapping $\varphi(\mathbf{X}, n, M_m) = \mathbf{x}$ of a material point $\mathbf{X}$. As a consequence of the application of gravity, the breast extends further anteriorly. Hence a correction of the basis of the biomechanical model – the interim unloaded configuration $M_m(\mathbf{X})$ – is required: the loaded spatial material configuration as represented in the clinical images is pulled back – or warped – from the tip to the start of the vectors of the DVF, which means, that the breast virtually contracts in the posterior direction, moving closer towards the estimated unloaded configuration.

$$M_{m+1}(\mathbf{X}) = M_0(\boldsymbol{\varphi}(\mathbf{X}, n, M_m)) = M_0(\mathbf{x}) \tag{4.24}$$

In the field of image processing this step is known as resampling and is equivalent to the inverse mapping $\boldsymbol{\varphi}^{-1} : \mathbf{x} \mapsto \mathbf{X}$. With the updated unloaded configuration, the loading simulation is continued with repeated resampling steps at given time points. If the update of the material configuration becomes small such that $M_{m+1} \approx M_m$, the unloaded configuration has been recovered. This is the case when the dynamic biomechanical simulation reaches a quasi-static state.

Inverting a deformation vector field to pull-back M_0 into the current estimate of the unloaded configuration is a costly and usually iterative procedure (Crum et al., 2007). However the backward Lagrangian perspective utilised in image transformation can be applied and inherently yields the inverse deformation. Thus the update procedure with the inverse displacement vector field simplifies to an image transformation or warping task known from image processing and efficient implementations can be adopted.

Updating the material configuration M is not required at each temporal simulation step n, since deformation increments are sufficiently small. The number of iterations between material configuration updates is N_{invert}. An evaluation of the unloading scheme is provided in the following numerical experiment.

NUMERICAL EXPERIMENT To test the newly developed unloading mechanism, a simple mechanical loading-unloading experiment was conducted. A box geometry of size $15 \times 15 \times 15\,\text{mm}^3$, with a Young's modulus of $500\,\text{Pa}$ and a Poisson's ratio of $\nu = 0.45$ was applied with a body force and the material map resampled according to the forward simulation. Then, using the same material parameters and the warped geometry, the unloaded geometry was recovered using our proposed method. The results are shown in figure 4.8, where volume renderings of the material maps are presented. The left box depicts the original unloaded configuration,

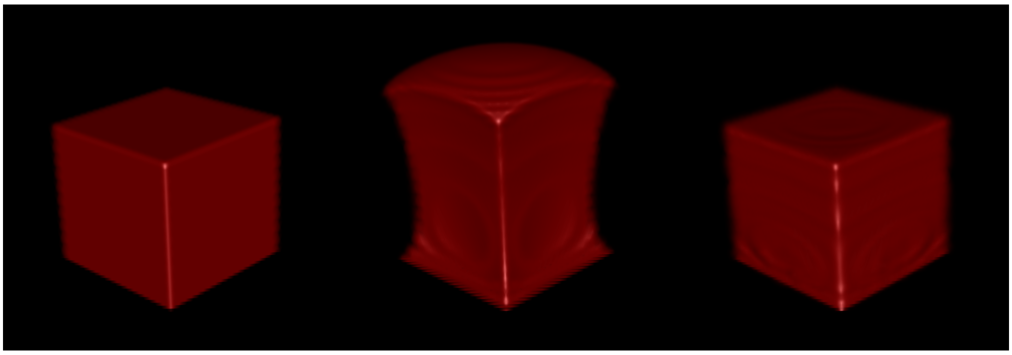

Figure 4.8: *Loading and unloading experiment. The left box depicts the original unloaded configuration with dimensions* $15 \times 15 \times 15\,\mathrm{mm}^3$ *which was exposed to gravity loading (central image). From this loaded configuration, the unloaded one was recovered, using the presented image based unloading mechanism.*

the central box the geometry after application of gravity, and the right box depicts the recovered unloaded configuration based on the central one. One can observe that the overall geometry was recovered well. Minor resampling artefacts can be observed. Since the unloading includes image processing steps, these artefacts can be attributed to the subsequent forward and backward resampling. Such artefacts however are not likely to be observable in the registration scheme, since repeated resampling is avoided in the symmetric design of the algorithm. Since the unloading is computed using a forward simulation only, the results can be compared directly. With a maximum displacement error of $0.6\,\mathrm{mm}$ and a 95-th percentile displacement error of $0.1\,\mathrm{mm}$, the error is as expected of the order of the size of the image grid spacing, i.e. $0.5\,\mathrm{mm}$.

4.2.3.2 *Surface-Based Motion Constraint*

The explicit time integration scheme allows direct imposition of motion constraints or displacement updates on selected (slave) nodes. The technique described below is used here to constrain nodes on the chest wall to only move tangentially along the chest surface.

One alternative to constrain the chest nodes to lie on the chest boundary could be to use a prescribed displacement constraint on these nodes directly. This however is difficult and possibly error prone as a point-to-point correspondence on the chest between the prone or supine loaded configuration and the corresponding unloaded

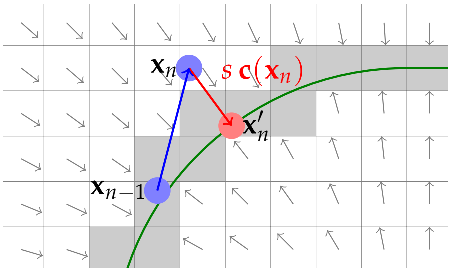

Figure 4.9: *Surface based motion constraint. A discretised approximation of the target surface, shown as gray shaded voxels, is generated from the chest-pectoral muscle interface based on the segmented image. From this segmentation a displacement vector field is pre-calculated which points to the target surface. This is used during the iterative solution process to displace nodes back to the target which due to the underlying material response might have moved out of this region.*

one is generally unknown. Furthermore due to a limited number of features on the retromammary region this patient-specific correspondence cannot be established easily a-priori.

In section 4.1 circumferential stretching was employed when simulating the unloaded configuration from the prone and circumferential compression when simulating the unloaded configuration from the supine image to approximate the natural motion of breast tissue between the prone and supine position. However, this approximation is an oversimplification of the underlying anatomy and the prescribed displacements can compromise the alignment accuracy in this area directly. Thus a more flexible approach is followed here, where internal forces of the biomechanical simulation act as a regulariser for displacements parallel to the surface whereas normal to the surface, small correction displacements are applied. Figure 4.9 shows the general principle of the approach by depicting the course of a slave node during the simulation.

From the segmented prone MR and supine CT image, the target surface position of the chest is established and a corresponding Euclidean distance transformation is calculated. The gradient of the distance transform results in a correction vector field $\mathbf{c}(\mathbf{X})$. This then directs chest nodes, which during the course of the simulation move outside the target surface region, back towards the closest point on the surface. The chest-muscle boundary is extracted from the segmentation of the original prone and supine image and the corresponding nodes are labelled as chest or "slave nodes". During the course of the registration the position of these nodes is updated via

$$\mathbf{x}'_n = \mathbf{x}_n + s_m(v_s)\mathbf{c}(\mathbf{x}_n), \tag{4.25}$$

if a node does not lie on the target surface. The scaling function $s_m(v_s)$ controls the speed of the imposed surface alignment. This function has been chosen such that the explicit time integration converges. The scaling was made dependent on the speed of a node towards the target surface v_s. When a slave node moves above a certain speed limit in the correction direction, the amount of the correction is decreased using a logistic function. This function was chosen due to its smooth sigmoidal shape and adapted, so that it decreases above a specified value. However it is expected that other functions with similar characteristics work equally well. The speed limit improves the stability of the dynamic system since repeated correction displacements accelerate the slave nodes which eventually might cause the system to diverge. The logistic function takes the form

$$s_m(v_s) = p\left(1 + \mathrm{e}^{l(v_s - v_{\max})}\right)^{-1} \tag{4.26}$$

with $l = {}^{10\ln(9)}/_{v_{\max}}$ and the constant correction parameter p. We observed that through the introduction of the speed dependent correction, the system became largely insensitive to the choice of p. We set $p = 0.005$ and $v_{\max} = 0.05\,\mathrm{m/s}$ for all experiments.

Additional flexibility regarding the motion constraint can be achieved by varying the design of the correction vector field $\mathbf{c}(\mathbf{X})$. As specified in (4.25), either a tied surface boundary condition or a one sided sliding condition can be imposed.

Summarising the computations up to this point, algorithm 4.1 shows an overview of the approach as is described in detail in this and the previous section. It allows the calculation of the unloaded configuration while considering a surface based motion constraint using the finite difference computational method. This methodology is used for each unloading step shown in the overview figure 4.5.

```
function INVERSE FDM-HE($\mathbf{u}_0$, $\mu_0$, $\lambda_0$, $\mathbf{f}_0$)
    $U^{n+1}_{i,j,k}, U^{n}_{i,j,k}, U^{n-1}_{i,j,k} \leftarrow \mathbf{u}_0$    ▷ initialise deformation vector fields
    $M_m(\mathbf{X}) \leftarrow M_0(\mathbf{X}) \leftarrow \{\lambda_0(\mathbf{X}), \mu_0(\mathbf{X}), \ldots, \rho_0(\mathbf{X}), \mathbf{f}_0(\mathbf{X})\}$    ▷ initialise material configuration
    while $n \leq N_{\max}$ do
        $U^{n+1}_{i,j,k} \leftarrow \frac{(2\rho_0 + h_t r) U^{n}_{i,j,k} - \rho_0 U^{n-1}_{i,j,k} + h_t^2 \rho_0 K^{n}_{i,j,k}}{\rho_0 + h_t r}$    ▷ explicit time stepping (4.14) dependent on $M_m$
        if $\mathrm{mod}(n, N_{\mathrm{invert}}) == 0$ then    ▷ every $N_{\mathrm{invert}}$ iterations...
            $M_m(\mathbf{X}) \leftarrow M_0(\varphi_i(\mathbf{X}))$    ▷ ... transform material configuration
        end if
        $U^{n+1}_{i,j,k}(X_{\mathrm{chest}}) \leftarrow U^{n+1}_{i,j,k}(X_{\mathrm{chest}}) + s_m\,\mathbf{c}(x_{n,\mathrm{chest}})$    ▷ apply motion constraint
        $U^{n+1}_{i,j,k}(X_{\mathrm{boundary}}) \leftarrow 0$    ▷ apply boundary condition
        $n \leftarrow n + 1$    ▷ increment time step
    end while
end function
```

Algorithm 4.1: *The base algorithm to calculate the unloaded configuration using a hyperelastic material, and the motion constraint for nodes on the chest wall.*

4.2.4 *Material Optimisation*

Significantly different breast tissue stiffness values have been reported in the literature. As a result, strategies to optimise the material parameters of a selected model have been investigated previously (Han et al., 2010, 2014; Eder et al., 2014).

The main objective of the material optimisation is an improved alignment of the prone and supine image before the image forces are accumulated (see section 4.2.5). Alignment quality ideally is measured in terms of the target registration error. However, measurement of this quantity in a clinical application is not directly possible, or very difficult to measure. Hence, the image similarity measure $\mathcal{S}_{\mathrm{SSD}}$ (4.27) is used as a surrogate measure. To achieve improved alignment, a one-dimensional line-search is performed. Here the stiffness of the biomechanical system is changed iteratively, until no further improvement in the image similarity measure is observed. The generic unloading simulation is initialised with an extreme material property – either very soft in the case of the numerical phantom experiments or very stiff for the clinical cases (during the development of the algorithm we tried both, stiffening and softening directions, and found no difference in the final alignment quality with respect to the direction from which the optimum was approached). At each material update step, n_{opt}, a constant factor is multiplied to the material parameters μ and λ. Then the unloaded state is simulatedand the image similarity is measured. The process is repeated until the minimum value for $\mathcal{S}_{\mathrm{SSD}}$ is evaluated. This approach does not find the best possible parameters – due to the fixed step size and the stiffening and softening of the system as a whole – but results in a better starting position for the intensity based alignment. Also see figure 4.13 on page 132 for an example of the course of the TRE and its surrogate image similarity measure $\mathcal{S}_{\mathrm{SSD}}$ over the material update steps n_{opt} for a clinical prone-supine image pair.

4.2.5 *Integration of Image Derived Forces*

In image registration an essential building block is a similarity or distance metric. But where in standard image registration only image forces act to align objects – usually counter balanced by a regularisation to obtain a smooth deformation vector field – here the physical forces such as gravity, as well as image forces, are considered simultaneously. The underlying hyper-elastic material law acts as a regulariser. Image forces lack physical meaning, but they are essential to drive the model in the direction required to align the images and thus help overcome modelling inaccuracies that were described earlier.

For a mono-modal alignment task, the simplest and most widely used distance metric is the sum-of-squared-differences (SSD) which is defined as

$$\mathcal{S}_{\mathrm{SSD}} := \frac{1}{2} \int_{\Omega} \left(P(\mathbf{X}) - S(\mathbf{X}) \right)^2 \mathrm{d}\mathbf{X}. \tag{4.27}$$

Here P and S denote the prone and supine image, warped into the unloaded configuration $\mathbf{X}$. Since we are interested in aligning the prone to the supine unloaded image and vice versa symmetrically, the forces need to be evaluated separately for prone and supine by establishing the Euler-Lagrange equation of (4.27), which gives (Modersitzki, 2004):

$$\mathbf{f}_P^{\mathrm{SSD}}(\mathbf{X}) = -\left(P(\mathbf{X}) - S(\mathbf{X}) \right) \nabla P(\mathbf{X}) \tag{4.28}$$

$$\mathbf{f}_S^{\mathrm{SSD}}(\mathbf{X}) = -\left(S(\mathbf{X}) - P(\mathbf{X}) \right) \nabla S(\mathbf{X}) \tag{4.29}$$

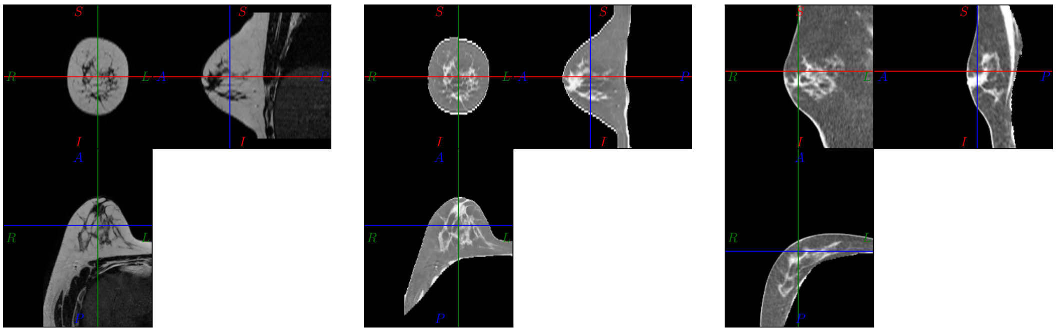

(a) (b) (c)

Figure 4.10: *Intensity inversion of the prone T2 weighted MR image (a) is used to generate an image (b) which appears similar to a CT image (c) in terms of tissue contrast such that a mono modal image similarity measure and corresponding image forces can be used.*

To incorporate the image forces into the simulation, these are accumulated incrementally, i.e.

$$\mathbf{f}_{\text{img}} = s_p(t)\mathbf{F}_N\mathbf{f}_N^{\text{SSD}} + \sum_{j=1}^{N-1} \mathbf{F}_j\mathbf{f}_j^{\text{SSD}}. \tag{4.30}$$

Note, since the image is resampled from the gravity loaded prone and supine configuration, the image forces are transformed with the deformation gradient **F** computed from the corresponding prone and supine unloading simulations. Furthermore the last evaluated image force is added using a polygonal loading function $s_p(t)$ where $s_p(0) = 0$ and $s_p(T) = 1$. In order to keep a consistent track of the accumulated image forces, these are recorded in the loaded configuration, from which every quantity is subsequently resampled (see section 4.2.3.1). The image forces are added as an additional force to the equation of motion (4.9) which then becomes

$$\rho_0 \frac{\partial^2 \mathbf{u}}{\partial t^2} = \nabla_0 \cdot \mathbf{N} + \rho_0 \mathbf{f}_B + \mathbf{f}_{\text{img}} - r\frac{\partial \mathbf{u}}{\partial t}. \tag{4.31}$$

The prone MRI to supine CT image registration task is obviously not of mono-modal nature (c.f. discussion in section 4.2.10). In this respect two different strategies could be followed. Either a multi-modal image similarity measure and corresponding image forces could be used or one of the images is adapted so that the tissues appear with the same intensity as in the other modality. Here the latter approach was chosen since only two tissue classes are present in the region of

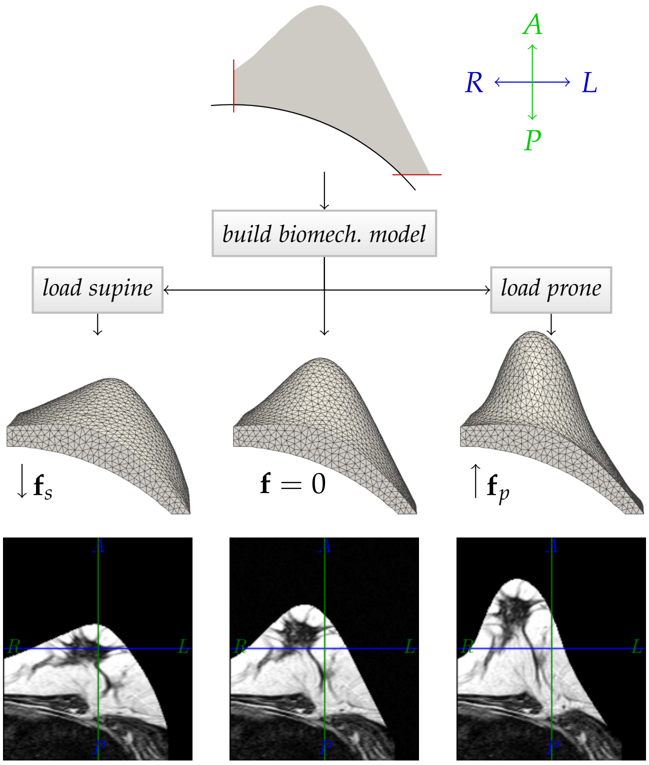

Figure 4.11: *A simplified geometric phantom was used to evaluate the performance of the presented algorithm. A cylinder represents the chest wall (black line in first row) and the skin is given by the function value of a two-dimensional Gaussian function (grey area over the cylinder section). A mesh of this geometry is generated and the biomechanical finite element model is built to simulate the effect of prone and supine gravity loading. The simulated prone and supine displacements are then used to transform the glandular structure of an MR image into the prone and supine position.*

interest and thus a simple intensity inversion in this region with a linear scaling is sufficient, outside the segmented breast region the intensity for air was applied. Namely the MR images are converted into pseudo CT intensities. An example for this intensity modification is shown in figure 4.10.

4.2.6 *Numerical Phantom Datasets*

To evaluate the performance of the developed algorithm, different types of images were used. In order to assess the accuracy and the performance of the developed algorithm in a controlled environment, a numerical phantom dataset was generated.

It allows the use of known ground-truth deformations which were generated using the finite element method. However, the simulated deformations are an idealisation of the deformations expected for the clinical cases.

To approximate the geometry of the breast in the unloaded configuration, the surfaces of the chest wall and the skin were approximated by simple geometric forms. The chest wall was defined by a cylinder with its axis resembling the cranio-caudal patient axis. To define the skin surface, the height of a two-dimensional Gaussian function was added to the anterior elevation of the cylinder as shown in the first row of Fig. 4.11. The boundaries were defined as axial coronal and sagittal planes and in the simplest experiments set to fixed boundary condition for the FE simulations. This geometry was meshed and a biomechanical model with homogeneous neo-Hookean material properties was generated. Gravity was added as a body force acting on the unloaded configuration in the anterior and posterior directions to simulate the prone and supine gravity loaded configurations using *Nifty Sim* (Johnsen et al., 2014). The parameters of the geometry were chosen such that the numerical phantom geometry was comparable to a medium sized breast in terms of volume, extent and chest diameter. The left-right, anterior-posterior and superior-inferior extent of the numerical phantom were 160.4 mm, 137.8 mm, and 159.5 mm respectively and the enclosed volume was 1.14 litres.

From the unloaded and simulated geometries corresponding images were generated by assigning the image texture of an MRI breast dataset to the unloaded geometry and warping it according to the simulated displacements.

4.2.7 *Prone-Supine Registration Results of Numerical Phantom Data*

In order to quantify the performance of the registration algorithm in a controlled setting with known ground-truth, the simulated prone and supine phantom images were registered using the proposed algorithm. The chest wall was assigned with a prescribed zero-displacement condition as the motion constraint used in the registration was not available in the finite element simulations. The registration was performed with an isotropic simulation grid spacing of $\Delta x_{\mathrm{sim}} = \Delta y_{\mathrm{sim}} = \Delta z_{\mathrm{sim}} =$ 9.07 mm and an image similarity or force resolution of $\Delta x_{\mathrm{img}} = \Delta y_{\mathrm{img}} = \Delta z_{\mathrm{img}} =$

Table 4.3: *Target registration error of the alignment of the phantom dataset with known ground truth displacements. The results are based on 500 randomly positioned landmarks within the simulated breast region.*

	TRE [mm]		
Registration step	mean	std	max
No registration	19.3	16.2	58.7
Unloading, generic material	11.6	5.5	26.6
Material updated	5.4	2.9	20.1
Image forces	0.9	0.8	6.1

2.27 mm. The critical time step of the explicit time integration scheme depends on the grid spacing and thus a relatively coarse grid was chosen for the purpose of acceptable computational times. The image forces were calculated two levels finer than the simulation itself and transferred to the coarser resolution level to update the simulated unloaded configuration. The material update performed three stiffening steps with a factor of 1.2 for the parameters μ and λ (see equation (4.10)), and is terminated when a decrease in the similarity was detected, while the final unsuccessful update is discarded.

Figure 4.12 shows the intermediate and final results of the numerical phantom registration experiment. One can observe, that the initial material parameter estimates were indeed incorrect as the prone and supine images deform beyond the unloaded state (compare figs. 4.12a, 4.12b and 4.12c with 4.11). After the material update step the alignment was significantly improved, but not ideal. This can be attributed to the coarse material optimisation steps as well as to the coarse simulation resolution. This step provides a better starting point to achieve the final alignment however. To this end image forces were accumulated to update the unloaded configurations accordingly. The final alignment is visually excellent as can be seen in the difference image 4.12i. Furthermore the recovered unloaded configuration coincides with the initial one.

The target registration error (TRE) was evaluated for 500 pseudo-landmarks randomly distributed across the initial numerical phantom domain. The term pseudo-landmarks was selected in this context, since the points for the numerical phantom evaluation were not selected according to image features but randomly distributed across the region of interest. The quantitative results are given in table 4.3. The mean TRE was reduced from 19.3 ± 16.2 mm to 0.9 ± 0.8 mm. Note that the relatively large maximum error of 6.1 mm after registration occurred at the border of the model, where the boundary conditions of the finite element simulation and the finite difference framework were not equivalent. In order to allow more deformation at the image borders, in the registration framework we apply padding around the image before registration. This differs from the ground-truth deformation and the absence of image information in this region explains this behaviour. However, the initial maximum TRE was reduced by an order of magnitude.

4.2.8 *Clinical Datasets*

The set of clinical image data consisted of nine prone MR and supine CT image pairs (P1-P9) which were acquired as part of the standard care for these breast cancer patients. The MR images were captured pre-operatively for diagnostic purposes and the CT images were post-operative planning CT scans acquired just before radiotherapy. To avoid differences in the images caused by surgical tissue removal, the registration and corresponding evaluation is carried out only on the healthy, contra-lateral breast. Note, that the estimated time between the MRI and the CT acquisition is usually about six weeks.

A prone-supine CT image data pair from a tenth patient (P10*) was also added to the clinical data set. Since both images were acquired post surgery, seven marker clips were present and well visible in both images. These clips are utilised to locate the tumour bed for radiotherapy in the clinical workflow. In the context of this study these clips could be used to generate a ground-truth deformation between the two loading positions. To this end the seven markers were identified manually and warped according to the deformation vector field produced by the registration

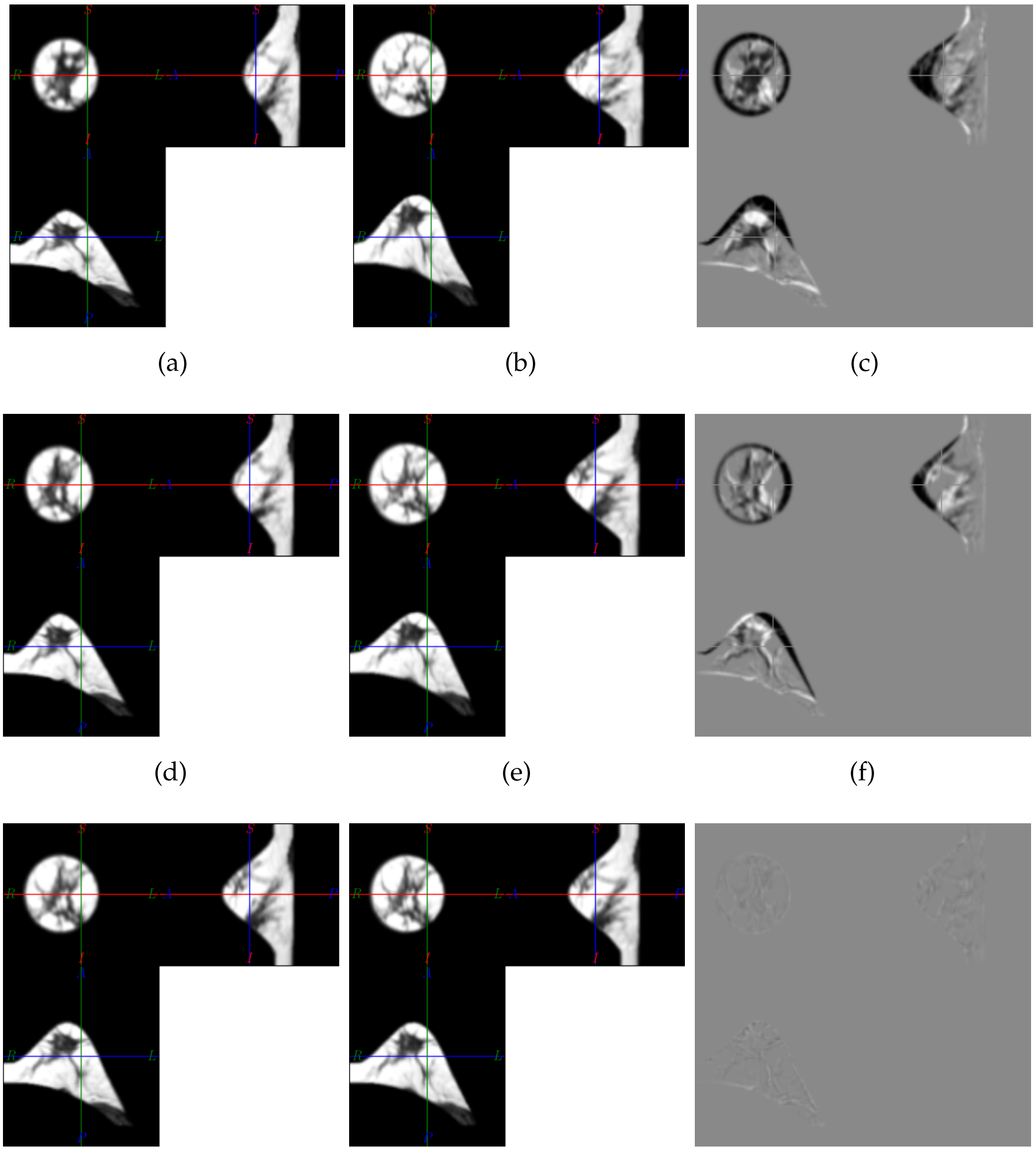

(a) (b) (c)

(d) (e) (f)

(g) (h) (i)

Figure 4.12: *Registration results for the simulated prone and supine images. The first column (a,d,g) shows the state of the prone image during the course of the registration procedure, the second column (b,e,h) the corresponding states of the supine image and the third column (c,f,i) the difference images. The first row represents the warped images after the unloading procedure with generic material parameters. Obviously the material parameters were chosen to be too soft and thus were iteratively stiffened to obtain a better match in the unloaded configuration. The alignment was then improved by accumulating image forces leading to the results shown in the third row. The difference images 4.12c, 4.12f and 4.12i are scaled so that the intensity range is equal for all difference images.*

algorithm. The region of and around the markers was assigned with a registration mask so that no image forces were calculated here. Hence a bias in the registration result is avoided. Note however, that the clips are located only in the region of the original tumour location and thus cannot represent the registration accuracy for the entire breast. On the other hand, it is precisely this region in and around the tumour which would be of most interest in clinical practice.

Furthermore, four prone-supine MR image pairs were added to the clinical data set to allow a comparison of the registration performance between MRI-CT and MRI-MRI registration (M1-M4).

To access and process the data, approval of the local ethics committee was obtained and the study was approved by the research and development unit of the clinical site. The MR images for cases P1-P9 were acquired with a Philips Achieva 1.5 T scanner and have a native resolution of $0.63 \times 0.63 \times 3\,\text{mm}^3$. A turbo spin echo (TSE) sequence was used with a flip angle of 90°, an echo time of 120 ms, and a repetition time between 4084 ms and 6806 ms. The CT images of cases P1-P10* have a resolution of $1.1 \times 1.1 \times 3\,\text{mm}^3$. The prone MR images of the MRI image pairs M1-M4 have a native resolution of $0.7 \times 2.2 \times 0.7\,\text{mm}^3$ and the corresponding supine images one of $0.7 \times 0.7 \times 2.5\,\text{mm}^3$. The MR image pairs M1-M4 were acquired with a Philips Gyroscan Intera 1.5 T scanner using a T1 weighted gradient echo sequence with a flip angle of 25°, an echo time between 4.1 ms and 4.3 ms, and a repetition time between 4.1 ms and 4.5 ms. The patient age was available only for the the MRI-CT cases (P1-P9). For these cases the average age was 47 years ranging between 29 and 60 years.

Processing of the images involved resampling to an isotropic resolution of $1 \times 1 \times 1\,\text{mm}^3$, bias-field correction of the MR images and segmentation of both modalities into background, chest, fibro-glandular and adipose tissue, which first determines the patient outline and then the pectoralis-breast boundary. This area is further segmented with an expectation maximisation algorithm into fat and fibroglandular tissue. As a last step the chest wall of the supine image was manually, rigidly aligned to the chest of the prone image.

4.2.9 *Prone-Supine Registration Results of Clinical Data*

In order to align prone MR images to the corresponding supine CT images (P1-P9), the intensities of the MR images were modified such that the grey values of fat and glandular tissue appeared similar in both images. To achieve this the intensity inversion within the breast segmentation mask was applied as described in section 4.2.5. Furthermore a region of interest which contained the breast that was not operated was selected to avoid effects of tissue removal between the images. The supine CT image was then manually rigidly aligned on the chest wall and sternum using the costal cartilage and adjacent rigid structures visible in both modalities. The prone-supine CT image pair (P10*) and the four MR image pairs (M1-M4) were processed in the same way, except for the modification of the image intensities.

The image registration was performed with three progressively finer image resolution levels with $\Delta x_{\text{img}} = \Delta y_{\text{img}} = \Delta z_{\text{img}} = \{4, 2, 1\}$mm following the well established methodology of multi-scale registration (Modersitzki, 2004). The simulation level was kept at a constant isotropic resolution of $\Delta x_{\text{sim}} = \Delta y_{\text{sim}} = \Delta z_{\text{sim}} = 8\,\text{mm}$. Initial sensitivity experiments with twice the resolution of the simulation grid resulted in near identical registration results with differences at the scale of the voxel resolution. The difference in displacement measured $2.2\,\text{mm}(\pm 0.8\,\text{mm})$. For computational efficiency therefore we decided not to choose a finer grid for the registrations. Furthermore, no correlation between registration error and breast size could be identified.

Measurement of the registration accuracy in the presence of large-deformations is non-trivial. However, several methods could be considered: (i) overlap measures such as the Dice coefficient (Dice, 1945), (ii) surrogate measures such as image similarity measures, (iii) surface distance measures, or (iv) distance measurements between manually selected correspondences which are in this thesis referred to as “landmarks”.

(i) Overlap measures, such as the dice coefficient, require an accurate segmentation of the internal breast structures and indicate the resulting overlap with a value between zero and one. The value might be difficult to interpret, but more importantly, is dependent on the shape of the segmented structures. If for instance

Table 4.4: *Target registration error for clinical prone-supine MRI-CT datasets (P1-P9), CT-CT dataset (P10*), and MRI-MRI datasets (M1-M4). The upper part, "single observer", represents TRE measurements based on the manual selection of corresponding landmarks in the prone and supine image. The lower part, "two observers", considers only reliable landmarks, i.e. those where two observers for a given prone landmark agreed on a corresponding supine location no further than* 10 mm *apart. All values given in* mm.

	single observer								
	rigid			unloading			image forces		
	mean	max.	std.	mean	max.	std.	mean	max.	std.
P1	63.7	83.3	20.9	15.4	30.7	5.8	6.2	10.8	2.8
P2	58.7	88.5	17.1	16.1	24.4	7.1	8.0	12.8	3.4
P3	90.2	109.3	12.6	13.4	18.3	3.2	4.5	11.5	3.4
P4	93.9	131.3	20.2	19.9	33.9	7.1	9.6	28.6	7.2
P5	38.8	56.4	11.9	12.2	20.5	4.5	7.2	11.5	3.5
P6	50.6	58.4	7.7	6.5	11.9	3.3	4.8	10.5	2.6
P7	54.3	76.8	16.2	12.3	31.2	8.6	8.7	18.2	5.5
P8	91.8	125.7	25.8	24.3	34.4	5.8	5.6	13.9	3.7
P9	62.1	87.6	22.2	16.5	29.4	7.4	7.7	15.0	3.9
P10*	133.1	154.2	18.9	14.6	27.8	8.5	5.4	22.1	5.4
M1	54.7	67.7	7.2	10.3	22.0	5.2	3.1	6.9	1.9
M2	48.2	70.4	11.7	9.5	24.0	5.1	3.8	13.1	2.9
M3	51.8	61.1	6.9	11.9	19.7	4.4	4.5	6.7	1.2
M4	70.6	80.3	7.0	12.6	17.1	3.2	2.9	5.3	1.6
P1-P10*	73.7			15.1			6.8		
M1-M4	56.3			11.1			3.6		
P1-M4	68.7			14.0			5.9		

	two observers, combined								
	rigid			unloading			image forces		
	mean	max.	std.	mean	max.	std.	mean	max.	std.
P1	62.4	80.6	20.5	15.0	30.7	5.6	6.5	12.8	3.1
P2	61.5	88.5	17.9	14.3	24.1	6.6	7.0	12.8	3.3
P3	95.8	110.7	8.6	14.7	22.9	3.1	5.0	16.6	4.2
P4	98.4	134.9	22.7	22.5	35.3	7.1	9.1	20.2	5.3
P5	35.7	51.2	11.6	11.1	20.5	4.6	6.1	13.2	3.4
P6	49.1	58.6	9.9	7.5	12.4	3.0	4.2	9.1	2.0
P7	55.0	76.9	14.7	12.7	31.2	9.9	8.5	18.6	6.6
P8	101.2	125.7	18.2	25.4	35.0	5.9	5.4	12.3	2.9
P9	54.7	87.6	25.0	18.9	30.3	7.4	8.3	15.6	4.3
P10*	134.0	151.3	17.5	13.3	27.1	7.9	4.0	8.2	2.3
M1	59.4	67.7	4.5	9.2	16.7	4.2	3.0	4.3	1.1
M2	47.7	70.4	12.4	9.6	24.0	5.2	4.1	13.1	3.0
M3	49.9	64.4	7.4	11.3	16.6	4.1	4.6	8.5	1.8
M4	70.6	80.3	6.8	12.5	17.3	3.3	2.9	6.0	1.6
P1-P10*	74.8			15.5			6.4		
M1-M4	56.8			10.6			3.7		
P1-M4	69.7			14.1			5.6		

Table 4.5: *Inter observer variability in the supine configuration before and after exclusion of unreliable landmarks.* N_L *is the total number of landmarks and* N_O *the number of landmarks which were above a threshold of* 10 mm. *Such landmarks were regarded as unreliable and excluded from the evaluation.*

	inter observer distance			distance after exclusion				
	mean	max.	std.	mean	max.	std.	N_L	N_O
P1	5.1	15.2	3.9	4.2	10.0	2.5	12	1
P2	5.7	15.1	4.8	3.1	7.3	1.9	8	2
P3	7.3	24.6	8.2	3.0	9.2	2.3	13	3
P4	9.6	29.9	9.2	4.7	7.2	1.6	11	3
P5	6.7	21.6	6.2	3.9	8.5	2.4	9	2
P6	8.3	18.3	4.8	5.4	8.9	2.3	9	3
P7	7.6	15.2	4.7	5.5	9.6	3.5	8	2
P8	7.0	21.7	5.9	4.5	9.7	2.7	10	2
P9	7.6	16.5	6.0	2.8	4.8	1.3	10	4
P10*	8.5	29.8	9.5	3.6	9.2	2.4	13	3
M1	10.9	22.1	7.1	4.0	6.0	1.4	11	6
M2	5.7	28.6	7.0	3.3	8.9	2.1	14	2
M3	7.2	16.4	5.1	3.6	4.7	0.8	11	4
M4	1.8	2.9	0.8	1.8	2.9	0.8	10	0
P1-P10*	7.3			4.1				24.3%
M1-M4	6.4			3.2				26.3%
P1-M4	7.1			3.8				24.8%

the overlap of the fibroglandular tissue was used for evaluation, the same residual misalignment could result in different dice coefficients. Dense breasts with compact regions of fibroglandular tissue could potentially give better dice scores than breasts with finely structured fibroglandular tissue.

(ii) Image similarity measures are not suitable to measure misalignment of image registration methods, since these are optimised by the algorithm directly. Furthermore similarity values alone do not allow intuitive estimation of the alignment error.

(iii) In contrast to the previous two measures, surface distances can be easier interpreted in a clinical context. However, it is not possible to measure in-plane misalignment, which inherently results in an underestimation of the registration error. Furthermore, since the developed algorithm is driven by image forces, it is expected that especially the skin surface, an area of high image contrast, is aligned well. This further adds to the effect of error underestimation.

(iv) Manually identified landmarks in prone and supine images can measure the target registration error directly, given that correspondences can be sufficiently well identified. Due to the large deformation between the patient configurations, this process is cumbersome and observer-dependent. Observer dependence however might be reduced by introducing more observers. While this evaluation method still has disadvantages, it does not inherently underestimate the error and the results are easier to interpret. Hence landmarks were used to measure the TRE – first with a single observer and later on with an additional control observer.

The term "landmarks" usually refers to anatomically characteristic points that can be identified across subjects (West et al., 1997). However, points that can be identified in the breast across subjects are very sparse. Hence the term landmark is used in this thesis as an anatomical feature (pair) that was visually identified by an observer.

First, landmarks manually identified by one observer were used for the evaluation of the alignment quality in the central configuration. For each case eight to fourteen landmarks were selected. The landmarks were transformed from the prone and from the supine configuration according to the transformation types used, i.e. rigid chest alignment, unloading simulation after material optimisation and final alignment using image forces. The distances between corresponding landmarks were measured for each case and the mean, maximumg and standarad deviation was computed per patient, resulting in the TRE measurements presented as follows. The upper part of table 4.4 labelled with "single observer" shows the corresponding target registration errors for all evaluated cases. Since the images were aligned rigidly, the landmark distance before the registration allows measurement of the scale of the tissue motion between prone and supine positions to be made. The mean landmark distance between the unregistered prone and supine positions, for all cases, ranges between 38.8 mm and 133.1 mm and the maximum landmark distance between 56.4 mm and 154.2 mm.

A significant reduction in the TRE can be observed by performing the unloading simulation and material optimisation. An example of the image similarity measure as well as the mean, maximum and minimum TRE over the course of the optimisation process is shown in figure 4.13. From one iteration to the next the material stiffness was decreased by 10%. As the minimum of the objective function is approached, the absolute change of the SSD similarity decreases, indicating a flat optimum (figures 4.13a to 4.13f). The same can be observed for the change in the evaluated TRE quantities, which also change less as the minimum similarity is approached (figures 4.13g to 4.13l). Hence a more accurate global optimisation with smaller material updates might not be required. The similar results for SSD and TRE – the latter not being available for unseen patients – indicate that the material optimisation can be performed based on the surrogate SSD measurements.

The unloading procedure results in an overall mean TRE of 14.0 mm varying between 6.5 mm and 24.3 mm and a maximum TRE between 11.9 mm and 34.4 mm. Subsequently the final alignment was calculated by refining the unloaded configuration by adding image forces to the system. This resulted in a final overall mean TRE of 5.9 mm varying between 2.9 mm and 9.6 mm and maximum TREs between 5.3 mm and 28.6 mm. The final mean TRE for the MRI cases (M1-M4) is with 3.6 mm smaller than the 6.8 mm achieved for the cases P1-P10*.

For a clinically applicable registration quality, a registration error below 10.0 mm is desirable. This figure was obtained following discussions with clinicians. The mean TRE evaluated on landmarks selected by a single observer fulfils this criterion,

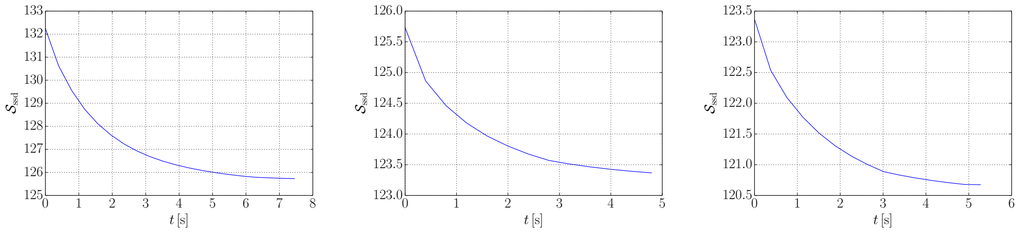

(a) $\mathcal{S}_{\mathrm{SSD}}(n_{\mathrm{opt}} = 1)$ (b) $\mathcal{S}_{\mathrm{SSD}}(n_{\mathrm{opt}} = 2)$ (c) $\mathcal{S}_{\mathrm{SSD}}(n_{\mathrm{opt}} = 3)$

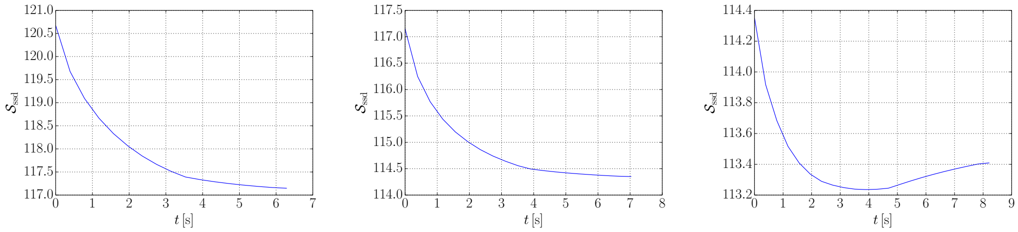

(d) $\mathcal{S}_{\mathrm{SSD}}(n_{\mathrm{opt}} = 4)$ (e) $\mathcal{S}_{\mathrm{SSD}}(n_{\mathrm{opt}} = 5)$ (f) $\mathcal{S}_{\mathrm{SSD}}(n_{\mathrm{opt}} = 6)$

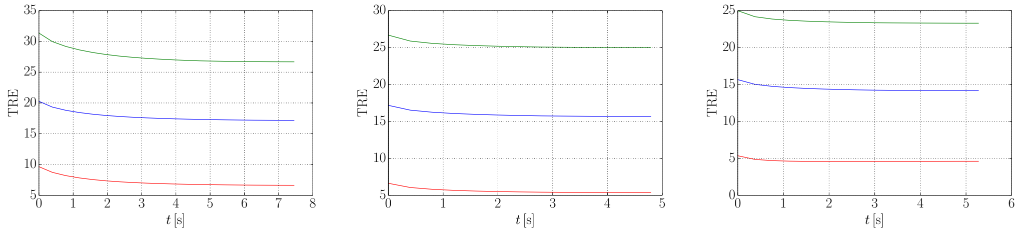

(g) $\mathrm{TRE}(n_{\mathrm{opt}} = 1)$ (h) $\mathrm{TRE}(n_{\mathrm{opt}} = 2)$ (i) $\mathrm{TRE}(n_{\mathrm{opt}} = 3)$

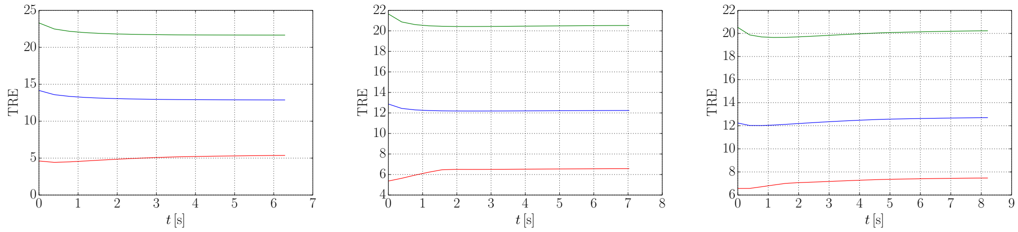

(j) $\mathrm{TRE}(n_{\mathrm{opt}} = 4)$ (k) $\mathrm{TRE}(n_{\mathrm{opt}} = 5)$ (l) $\mathrm{TRE}(n_{\mathrm{opt}} = 6)$

Figure 4.13: *The material optimisation process by iterative material softening steps* n_{opt}. *The optimisation steps for patient P5 in terms of SSD image similarity measure (a-f), as well as registration accuracy in terms of the TRE (g-l). The blue, green, and red curves in the TRE graphs represent the mean, maximum and minimum registration errors respectively. During the optimisation the image similarity measure* $\mathcal{S}_{\mathrm{SSD}}$ *is observed and acts as a surrogate for the actual alignment quality in terms of the TRE. Note how the mean TRE and its surrogate* $\mathcal{S}_{\mathrm{SSD}}$ *follow similar curves over the course of the simulations.*

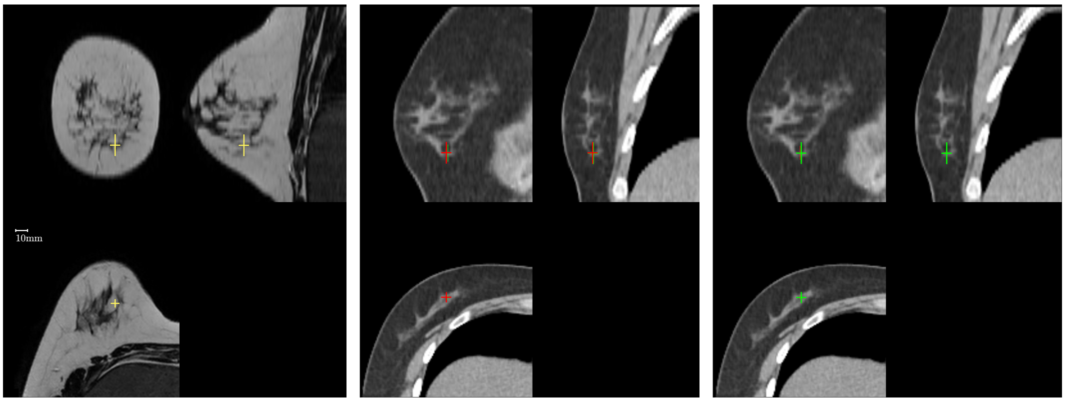

(a)

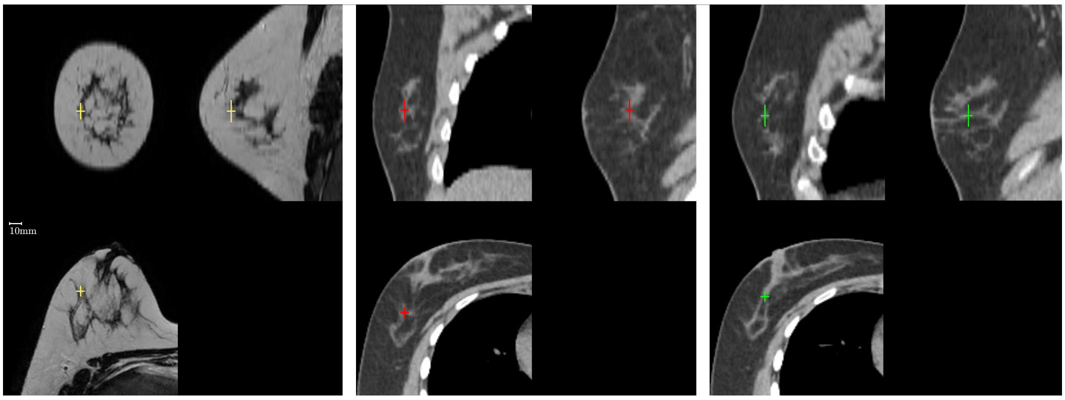

(b)

Figure 4.14: *Orthogonal sections through the prone MRI and supine CT image of case P1 with corresponding landmarks selected by two observers. The first observer selected corresponding points in the prone and supine images (left and centre), whereas the control observer was asked to find the supine landmark when presented with the prone one (right). (a) shows an excellent agreement between the two observers (red and green crosses in the supine CT) resulting in a landmark distance of* 1.1 mm. *(b) is an example where both observers do not agree, identifying different structures with similar appearance resulting in a landmark distance of* 15.2 mm.

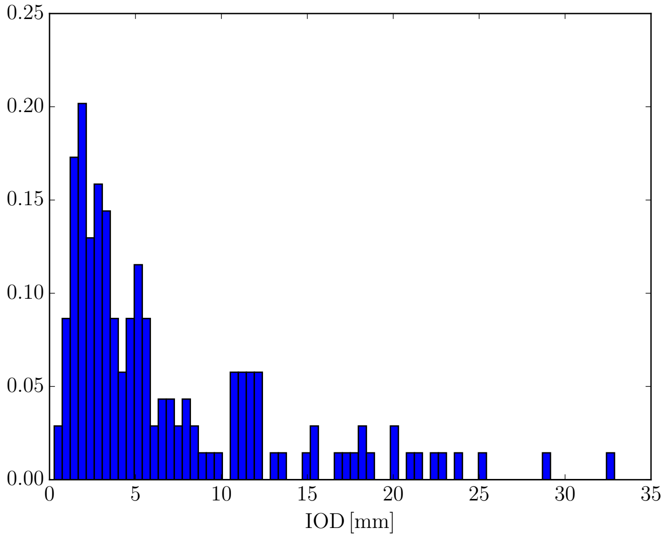

Figure 4.15: *Histogram of all inter-observer distances.*

but the maximum TRE of 28.6 mm does not. However, the landmark selection process is inherently observer dependent and potentially error prone and the high maximum value might originate from an erroneously identified correspondence. Hence, in a second step the quality of the landmarks was assessed by a second control observer with the aim to eliminate unreliable landmarks. A control observer was presented with the prone landmarks selected by the first observer and then given the task of identifying the corresponding locations in the supine image. This means that for each prone landmark two corresponding supine landmarks exist, one from each observer. The distance measured between corresponding supine landmarks defines the inter-observer distance, which is the basis to quantify the inter-observer variability. The results of this inter-observer variability experiment are given in table 4.5. Furthermore, two examples of the 149 landmarks are shown in figure 4.14. The first example (fig. 4.14a) shows a very good agreement between the observers, which is reflected by a landmark distance of 1.1 mm. Figure 4.14b on the other hand shows poor agreement between the observers, apparently due to the presence of visually similar but different structures. The landmark distance for this case is 15.2 mm. Eliminating such landmarks increases the confidence in the remaining landmarks to better reflect the correct TRE.

Landmarks for which the distance between the first and the control observer were larger than 10 mm were eliminated from the evaluation therefore. Visual inspection of the statistical distribution of all inter-observer distances, as shown in figure 4.15, suggests a mixed distribution, with a cluster of values centred around 3.5 mm and a distinct drop at 10 mm. Furthermore, with increasing inter-observer distance, the chance increases that different structures within the breast were identified. For this reason 10 mm was taken to be a plausible threshold distance, above which two landmarks can be considered placed on different features (see also 10mm mark in figure 4.14).

The overall mean inter-observer distance was 7.1 mm before and 3.8 mm after the exclusion of the unreliable landmarks. The inter observer distance for cases P1-P10* is 7.3 mm and only slightly higher than the distance measured for cases M1-M4, which is 6.4 mm. For both groups, P1-P10* and M1-M4, about a quarter of the landmarks were excluded. This suggests, that there is a negligible difference in the accuracy of the landmark selection between MRI-MRI and MRI-CT cases. Accordingly, the bottom part of table 4.4 labelled as "two observers, combined" shows the TRE evaluation using the trusted landmarks only, which was computed as follows. Since for each prone landmark two supine landmarks exist – each transformed either rigidly, or according to the unloading simulation or accorging to the simulation with added image forces – two distances are measured per landmark triplet, i.e. 1) (transformed) prone to (transformed) supine landmark identified by the first observer and 2) (transformed) prone to (transformed) supine landmark identified by the control observer. Both distances equally contribute to the computation of the mean, maximum and standard deviation of the TRE for each case. It should be noted that the distance measurements are, due to the nature of the described landmark selection process, not completely independent.

The maximum TRE alignment error of 28.6 mm previously observed for P4 by using only a single observer was reduced to 20.2 mm by adding the control observer and the 10 mm exclusion criterion to the evaluation procedure. The overall mean registration error reduced slightly from 5.9 mm to 5.6 mm.

To investigate a potential correlation of the achieved TRE with respect to breast size, for each patient the anterior-posterior (AP) extent from pectoralis surface to

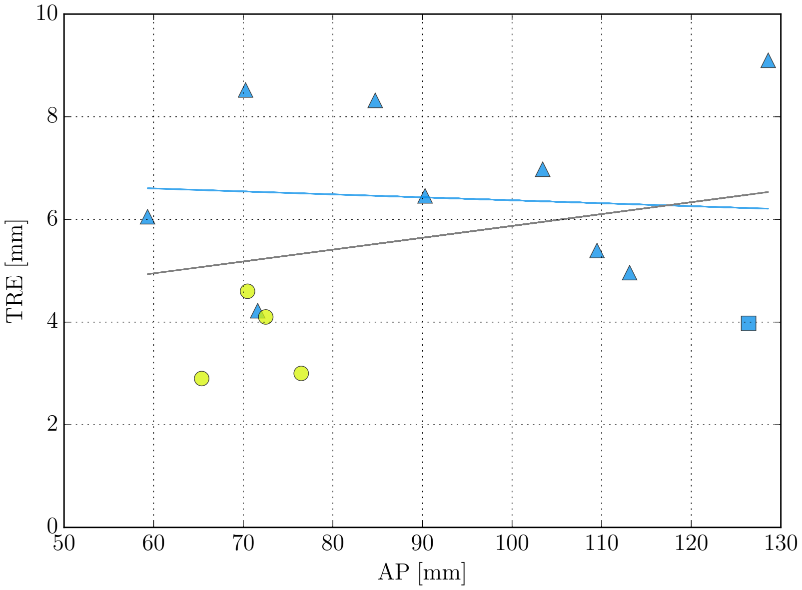

Figure 4.16: *Anterior-posterior extent of the breast in the prone position (measured from the anterior surface of the pectoralis muscle to the nipple) plotted against the TRE. Cases P1 to P9 are marked as blue triangles, case P10* is marked with a blue square and cases M1 to M4 are marked as yellow circles. The linear regression for cases P1 to P10* is drawn as a blue line, and the regression line for all cases is drawn as a grey line.*

nipple was measured in the prone configuration and plotted against the achieved registration error (TRE measures were taken from the two-observer experiment). The result is shown in figure 4.16. The AP-extent varies between 59 mm and 128 mm. Two linear regression lines are also plotted: the blue one shows the trend for cases P1 to P10*, whereas the grey one shows the trend for all cases, P1 to M4. Adding the MRI-MRI cases changes the slope of the trend-line from near horizontal (blue line) to a slight upward trend (grey line). This effect however should be considered with care, due to the narrow AP and TRE range of the MRI-MRI cases. For the evaluated cases it appears, that the registration performance does not strongly depend on the breast size. Furthermore, a slightly better performance can be observed for the single modality cases M1 to M4 and P10* when compared to the multi-modal cases P1 to P9. This could potentially be attributed to the approach how multi-modal cases are prepared for the SSD force evaluation (see section 4.2.5.)

In addition to the manually selected landmarks as presented in table 4.4, implanted fiducial markers could be used to evaluate the registration accuracy for the CT-CT case P10*, without inter-observer variability but only for a small region of the breast. In the prone configuration the axis aligned bounding box enclosing the seven landmarks measured $11.0 \times 16.6 \times 10.1\,\mathrm{mm}^3$. The rigid alignment of the images on the chest resulted in a mean (maximum) fiducial registration error (FRE) of 136.9 mm (139.6 mm). After the unloading and material optimisation the mean (maximum) FRE was reduced to 18.7 mm (22.4 mm). The final mean (maximum) FRE with accumulated image forces measured 3.61 mm (5.13 mm).

The initial images, the registered images, and the landmarks for all fourteen clinical cases are shown in figures 4.17–4.44 (pages 138–165). Figures on even pages show the prone, supine, and difference images at the beginning and at the end of the registration procedure. Figures on odd pages show the landmark distance in the central configuration as projections into the coronal, sagittal and axial planes for all evaluated clinical cases. The landmarks transformed from the prone position are depicted as circles whereas those transformed from the supine position are shown as small squares. Landmarks from the first observer are coloured blue and those from the control observer are coloured green. The correspondence is visualised as connecting lines, and the colour indicates the total Euclidean landmark distance. This allows a visual assessment of the distribution of the selected landmarks and of the registration accuracy throughout the breast.

By comparing the original prone and supine images (a) and (c) in figures on right hand pages starting from figure 4.17–4.43, breast tissue motion along the chest wall appears to be present in all cases to varying degrees. Case P10* (c.f. figure 4.35 on page 156) for example shows a very large displacement, whereas for case P1 this displacement does not seem to be as pronounced (c.f. figure 4.17 on page 138)

4.2.10 *Discussion*

The proposed algorithm is the first symmetric integrated simulation based registration approach which accounts for large deformations present in prone-MRI-to-supine-CT breast image alignment. The algorithm takes into account pre-loading of the breast geometry with gravity and calculates a virtually unloaded configuration. After an optimisation of soft tissues material parameters, the unloaded configuration is updated by accumulating image derived forces directly into the unloading

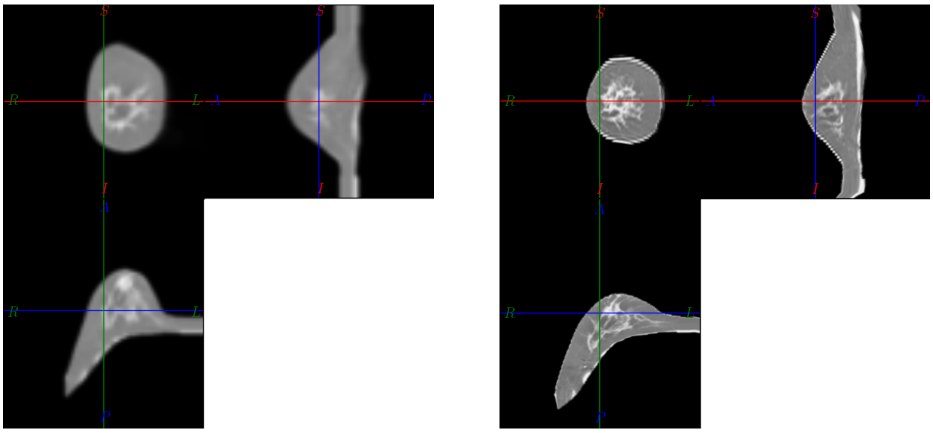

(a) *Prone image before registration* (b) *Prone image after registration*

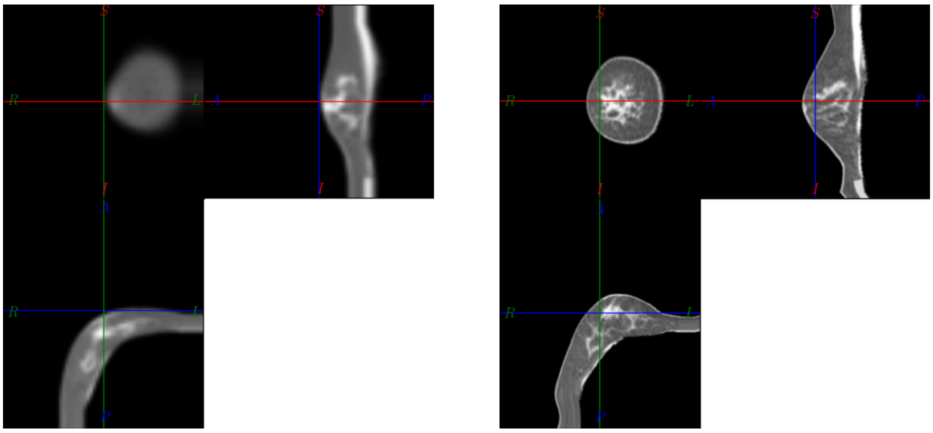

(c) *Supine image before registration* (d) *Supine image after registration*

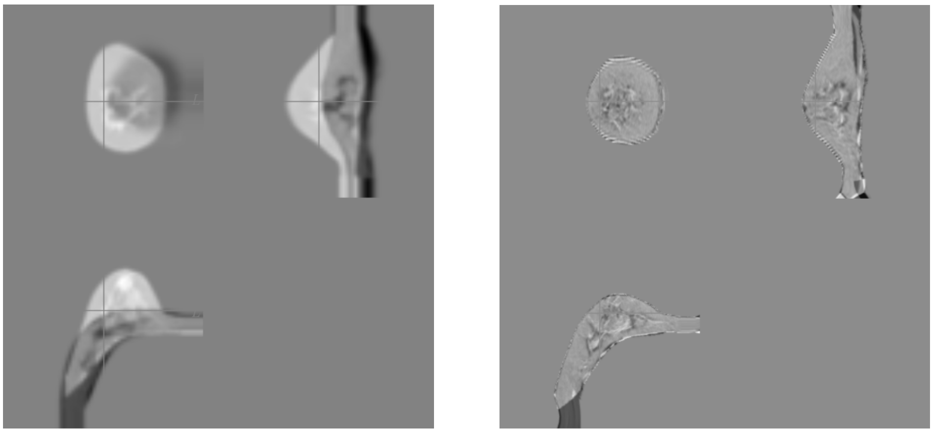

(e) *Difference before registration: (a)-(c)* (f) *Difference after registration: (b)-(d)*

Figure 4.17: *Result of the intensity driven registration approach for case P1. The images before registration, (a) and (c), show the original prone and supine configuration at the coarsest resolution level with the corresponding difference image (e). Figures (b) and (d) show the final registration result as the warped prone (b) and supine image (d) at the finest resolution level with the corresponding difference image (f).*

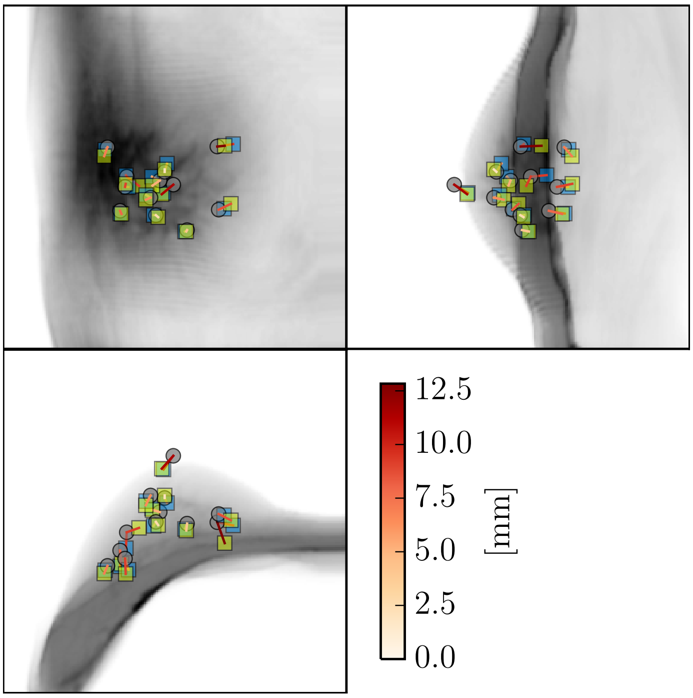

(a) *All landmarks of the first and the control observer.*

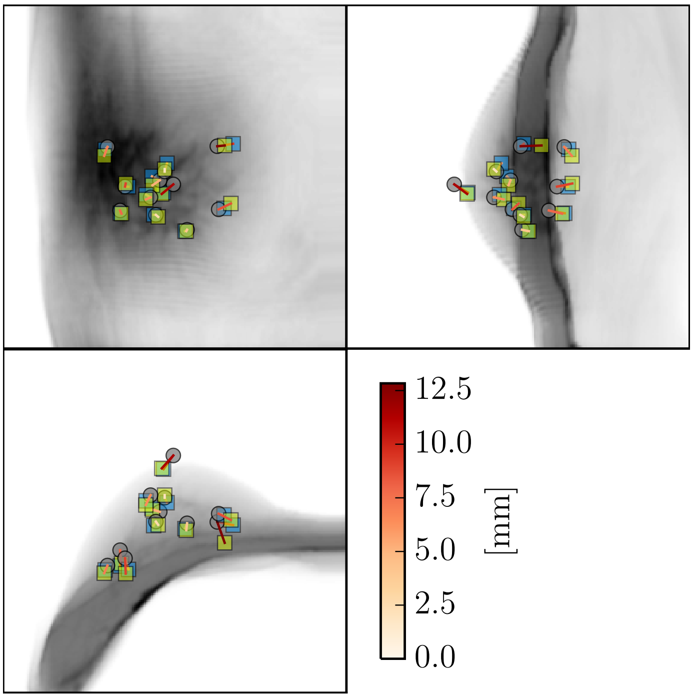

(b) *Reliable landmarks with an inter-observer distance below* 10 mm.

Figure 4.18: *Intensity based registration result for case P1 in terms of transformed landmark positions. The circles represent the landmarks that were transformed from the prone position. The blue and the green squares mark the positions of the first and the control observer respectively after transformation transformation from the supine position.*

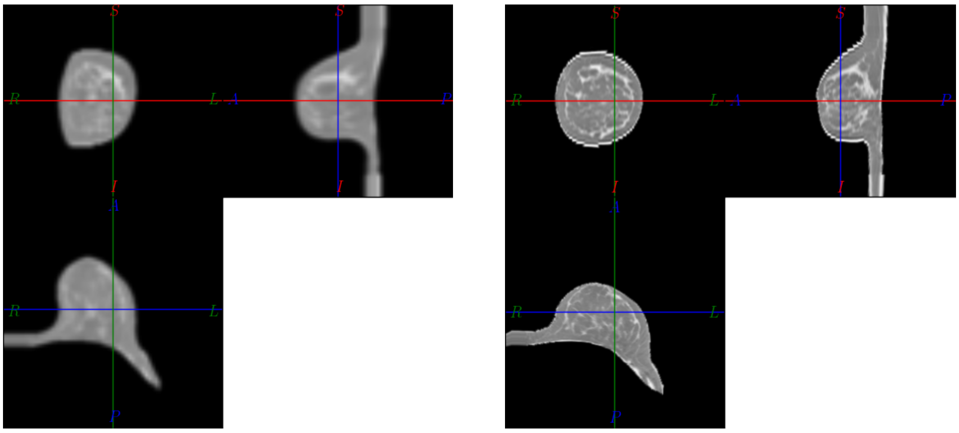

(a) *Prone image before registration* (b) *Prone image after registration*

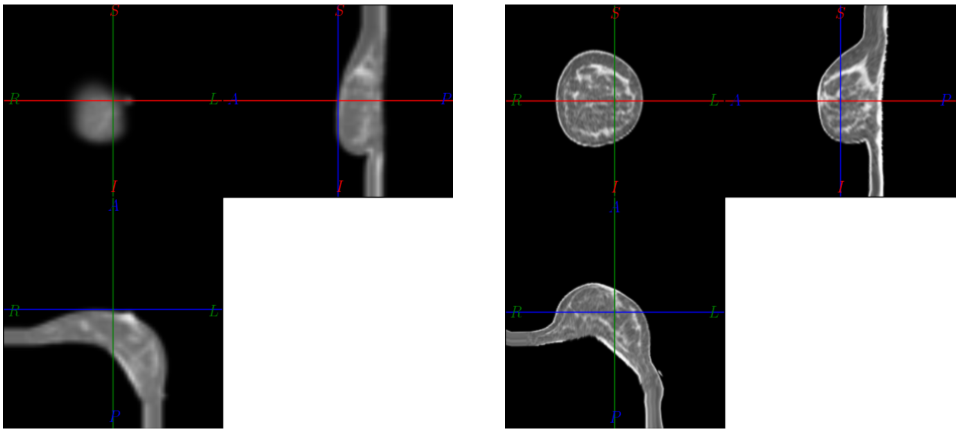

(c) *Supine image before registration* (d) *Supine image after registration*

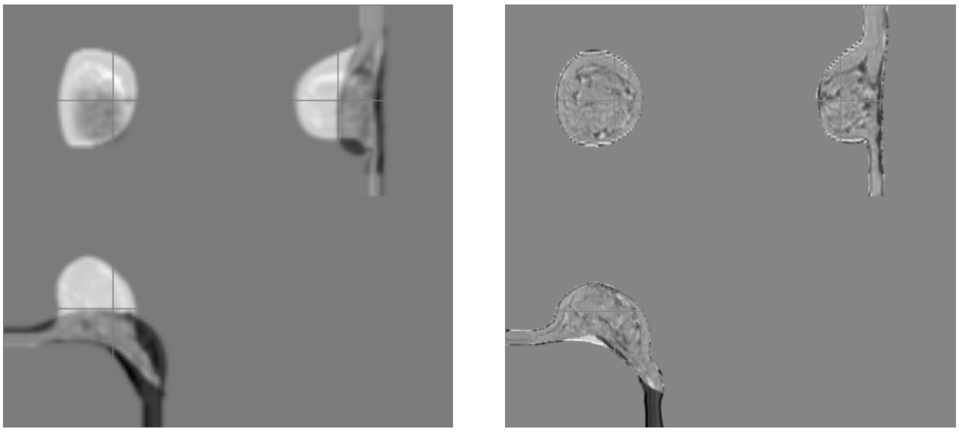

(e) *Difference before registration: (a)-(c)* (f) *Difference after registration: (b)-(d)*

Figure 4.19: *Result of the intensity driven registration approach for case P2. The images before registration, (a) and (c), show the original prone and supine configuration at the coarsest resolution level with the corresponding difference image (e). Figures (b) and (d) show the final registration result as the warped prone (b) and supine image (d) at the finest resolution level with the corresponding difference image (f).*

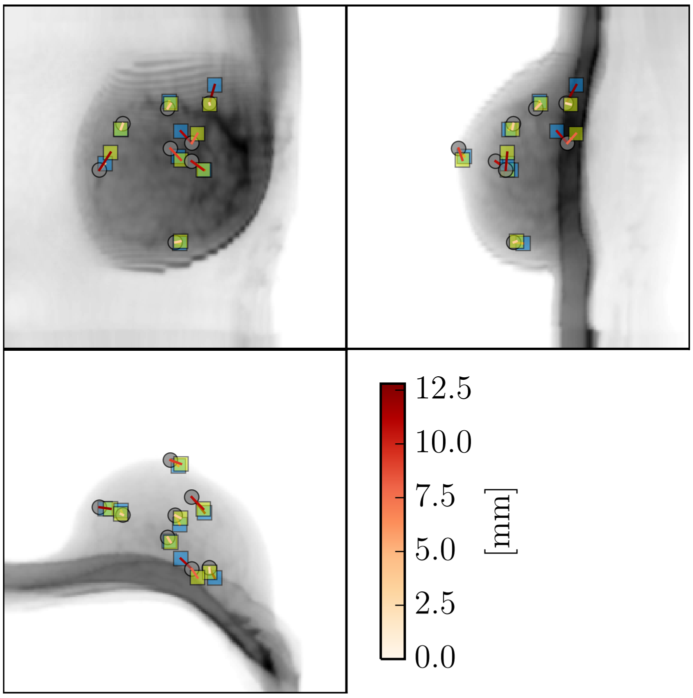

(a) *All landmarks of the first and the control observer.*

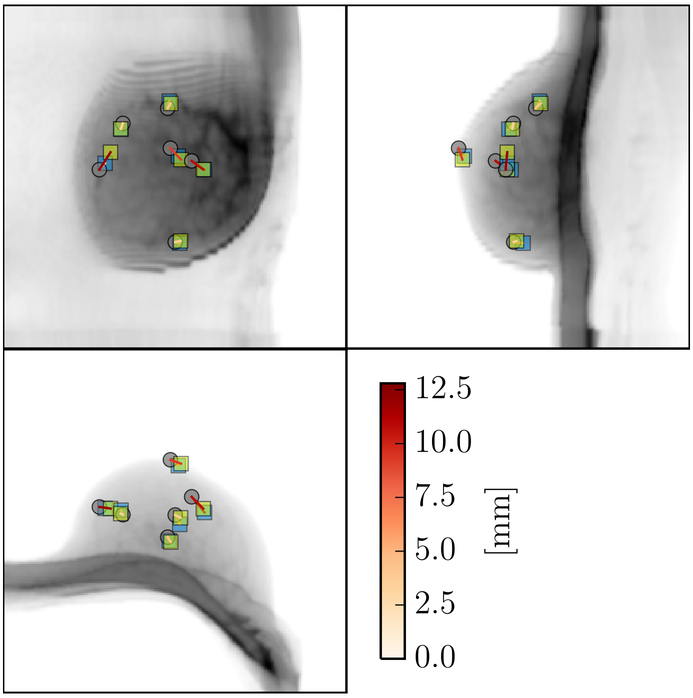

(b) *Reliable landmarks with an inter-observer distance below* 10 mm.

Figure 4.20: *Intensity based registration result for case P2 in terms of transformed landmark positions. The circles represent the landmarks that were transformed from the prone position. The blue and the green squares mark the positions of the first and the control observer respectively after transformation transformation from the supine position.*

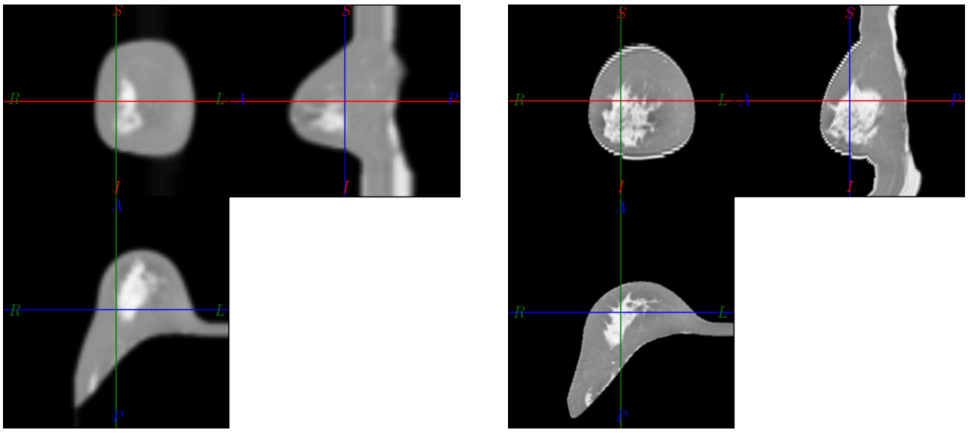

(a) *Prone image before registration* (b) *Prone image after registration*

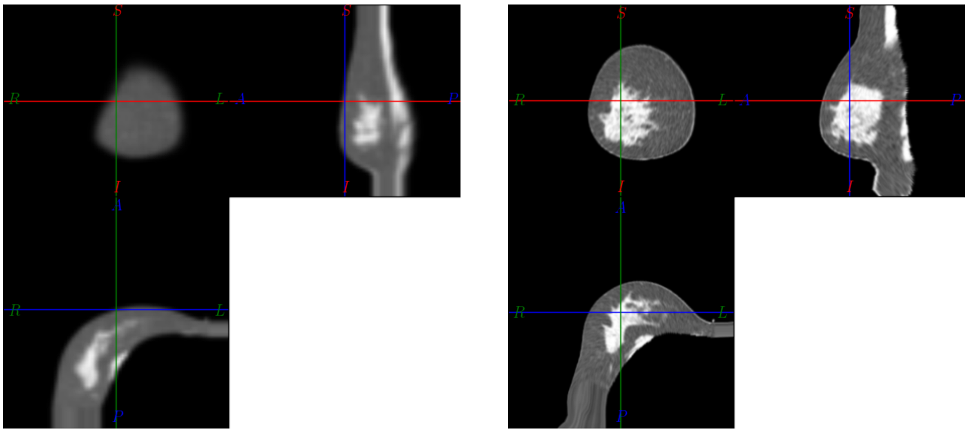

(c) *Supine image before registration* (d) *Supine image after registration*

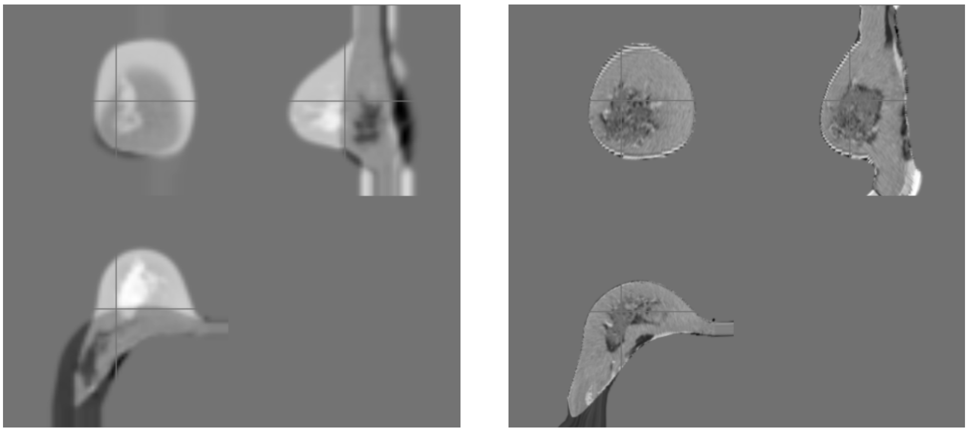

(e) *Difference before registration: (a)-(c)* (f) *Difference after registration: (b)-(d)*

Figure 4.21: *Result of the intensity driven registration approach for case P3. The images before registration, (a) and (c), show the original prone and supine configuration at the coarsest resolution level with the corresponding difference image (e). Figures (b) and (d) show the final registration result as the warped prone (b) and supine image (d) at the finest resolution level with the corresponding difference image (f).*

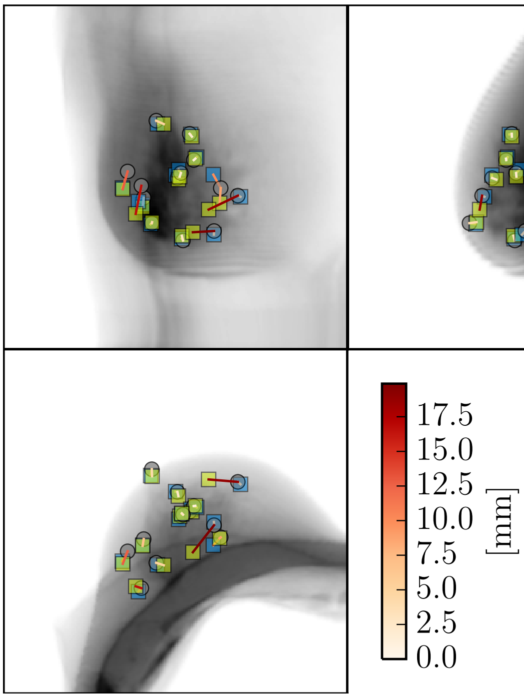

(a) *All landmarks of the first and the control observer.*

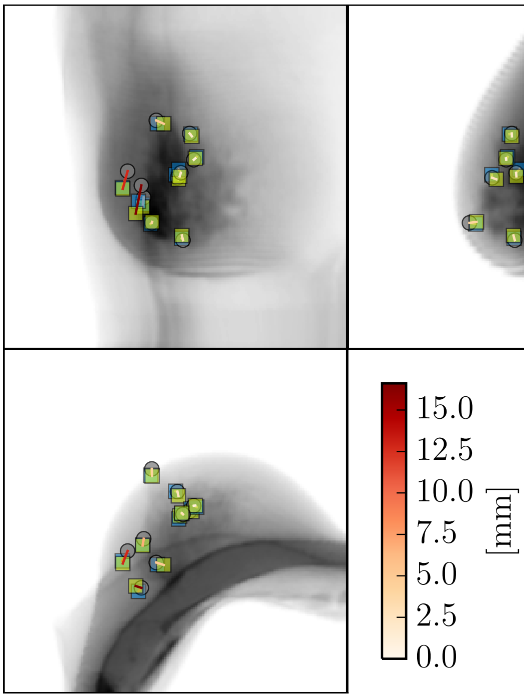

(b) *Reliable landmarks with an inter-observer distance below* 10 mm.

Figure 4.22: *Intensity based registration result for case P3 in terms of transformed landmark positions. The circles represent the landmarks that were transformed from the prone position. The blue and the green squares mark the positions of the first and the control observer respectively after transformation transformation from the supine position.*

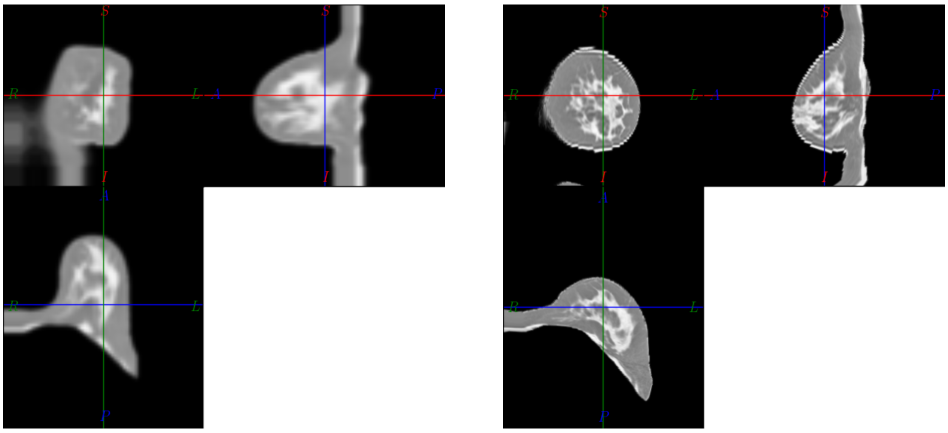

(a) *Prone image before registration* (b) *Prone image after registration*

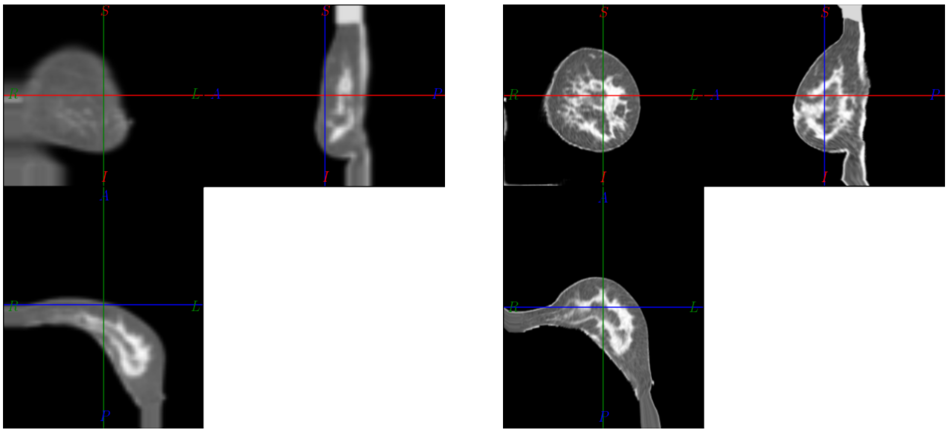

(c) *Supine image before registration* (d) *Supine image after registration*

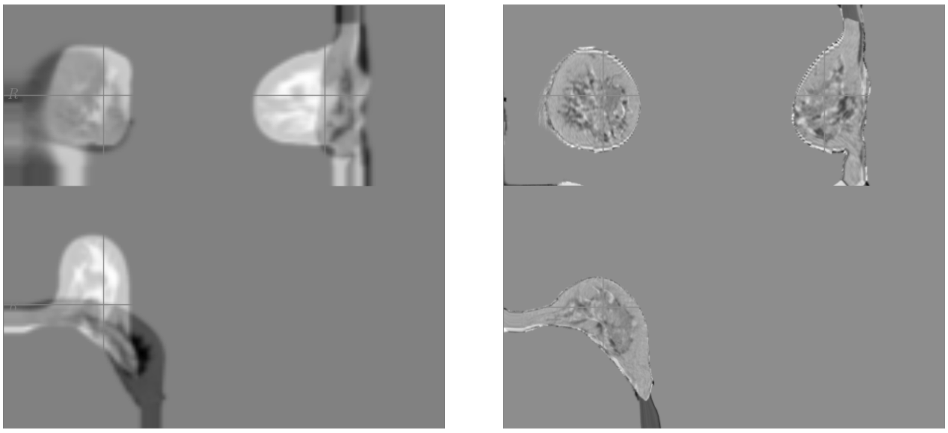

(e) *Difference before registration: (a)-(c)* (f) *Difference after registration: (b)-(d)*

Figure 4.23: *Result of the intensity driven registration approach for case P4. The images before registration, (a) and (c), show the original prone and supine configuration at the coarsest resolution level with the corresponding difference image (e). Figures (b) and (d) show the final registration result as the warped prone (b) and supine image (d) at the finest resolution level with the corresponding difference image (f).*

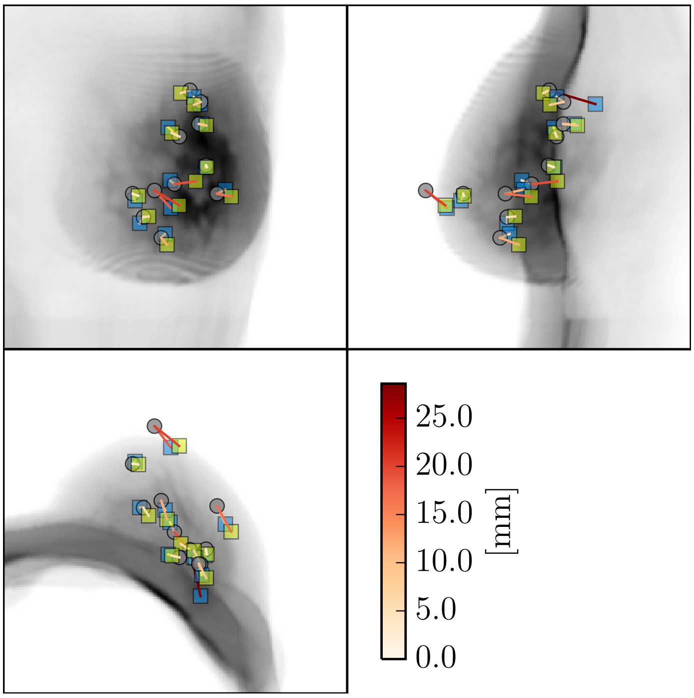

(a) *All landmarks of the first and the control observer.*

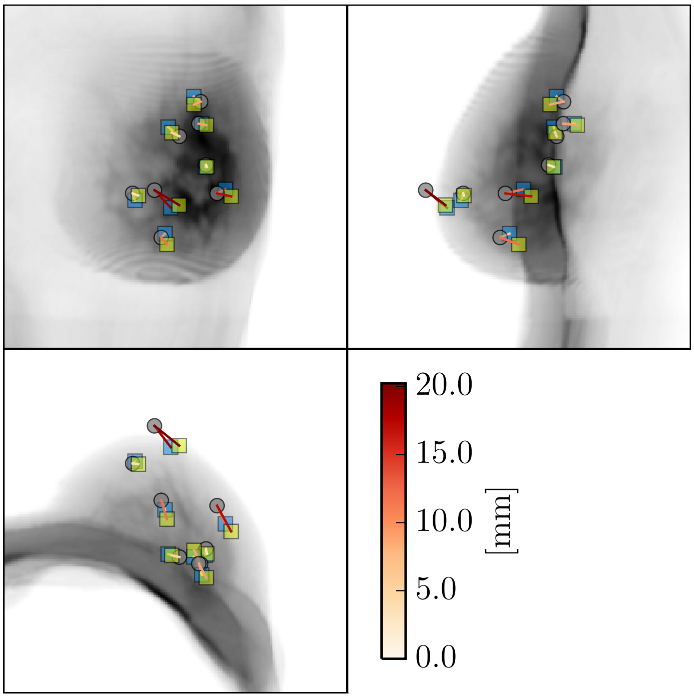

(b) *Reliable landmarks with an inter-observer distance below* 10 mm.

Figure 4.24: *Intensity based registration result for case P4 in terms of transformed landmark positions. The circles represent the landmarks that were transformed from the prone position. The blue and the green squares mark the positions of the first and the control observer respectively after transformation transformation from the supine position.*

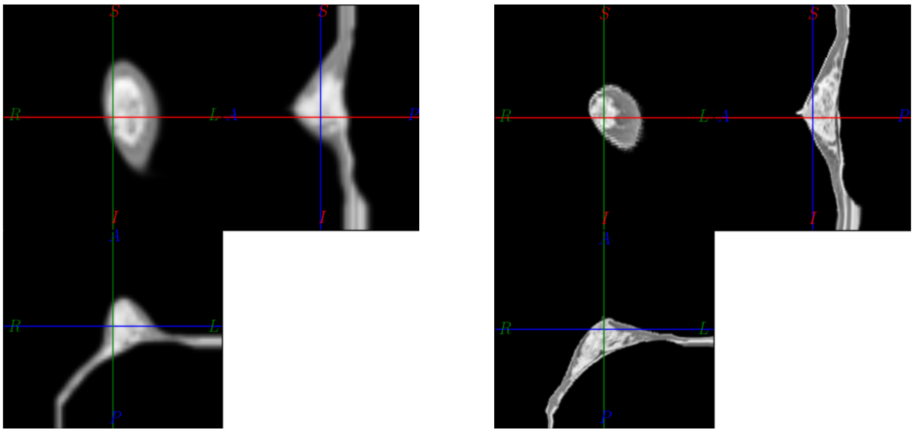

(a) *Prone image before registration* (b) *Prone image after registration*

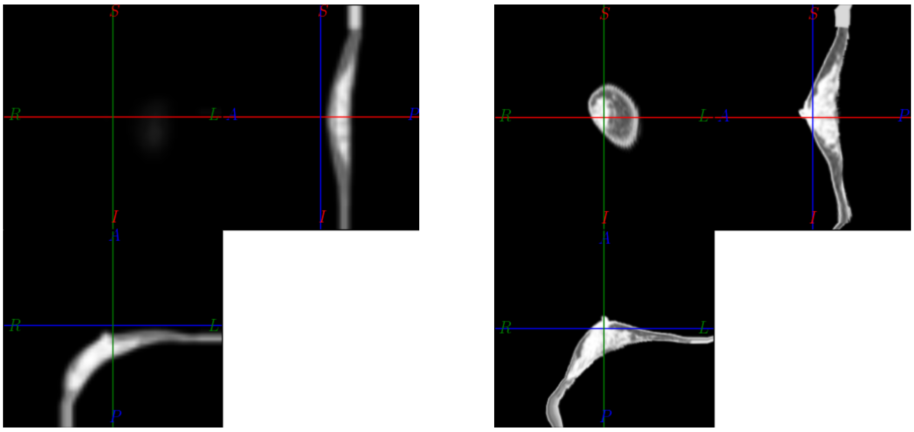

(c) *Supine image before registration* (d) *Supine image after registration*

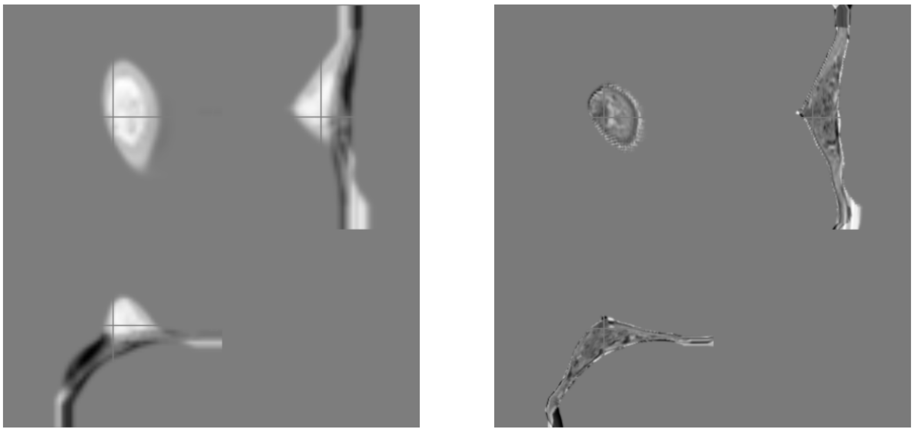

(e) *Difference before registration: (a)-(c)* (f) *Difference after registration: (b)-(d)*

Figure 4.25: *Result of the intensity driven registration approach for case P5. The images before registration, (a) and (c), show the original prone and supine configuration at the coarsest resolution level with the corresponding difference image (e). Figures (b) and (d) show the final registration result as the warped prone (b) and supine image (d) at the finest resolution level with the corresponding difference image (f).*

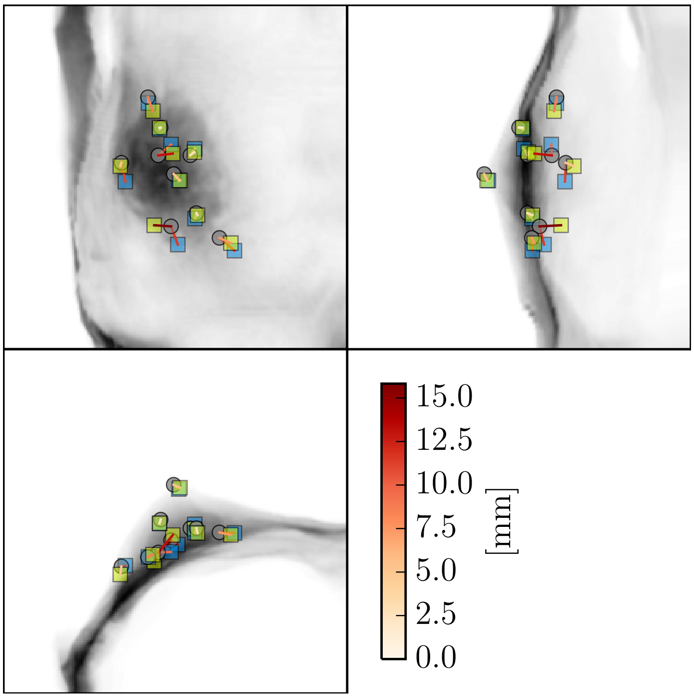

(a) *All landmarks of the first and the control observer.*

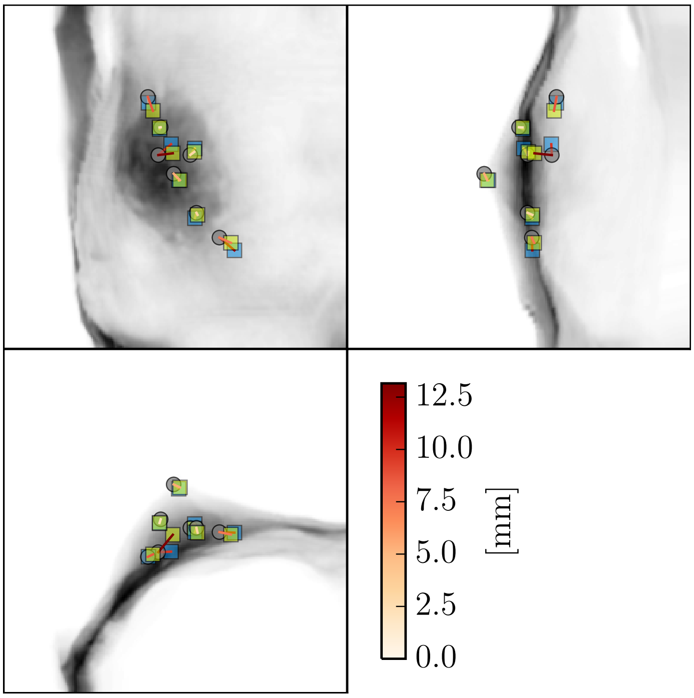

(b) *Reliable landmarks with an inter-observer distance below* 10 mm.

Figure 4.26: *Intensity based registration result for case P5 in terms of transformed landmark positions. The circles represent the landmarks that were transformed from the prone position. The blue and the green squares mark the positions of the first and the control observer respectively after transformation transformation from the supine position.*

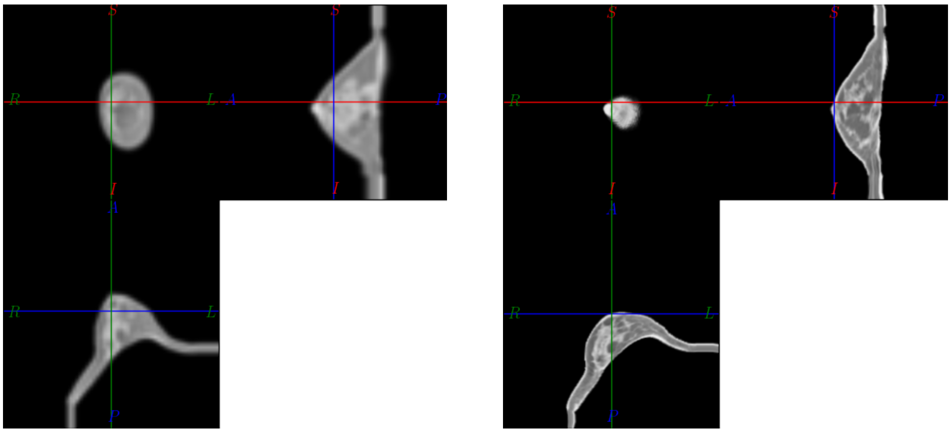

(a) *Prone image before registration* (b) *Prone image after registration*

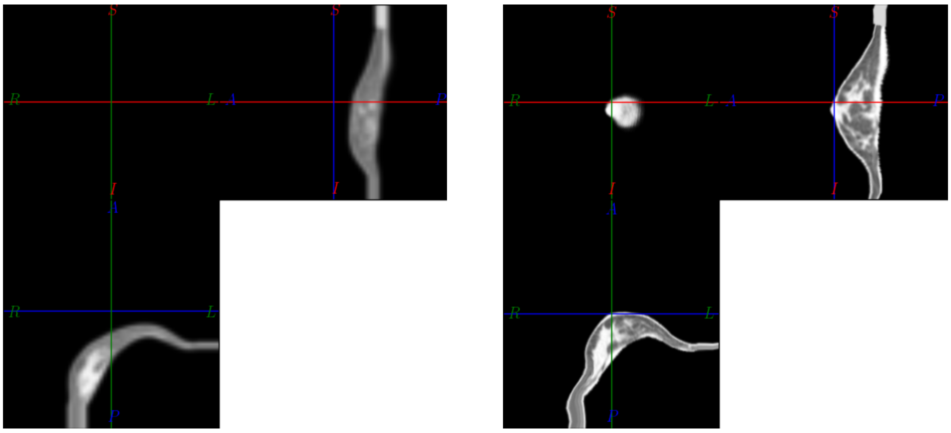

(c) *Supine image before registration* (d) *Supine image after registration*

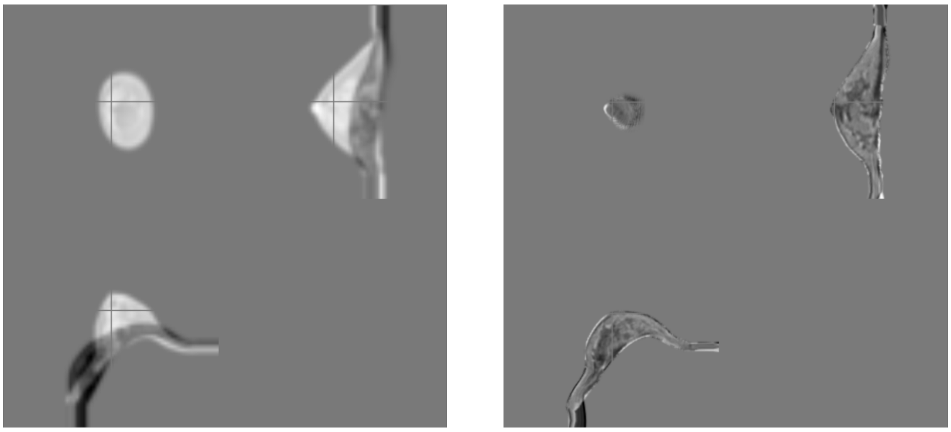

(e) *Difference before registration: (a)-(c)* (f) *Difference after registration: (b)-(d)*

Figure 4.27: *Result of the intensity driven registration approach for case P6. The images before registration, (a) and (c), show the original prone and supine configuration at the coarsest resolution level with the corresponding difference image (e). Figures (b) and (d) show the final registration result as the warped prone (b) and supine image (d) at the finest resolution level with the corresponding difference image (f).*

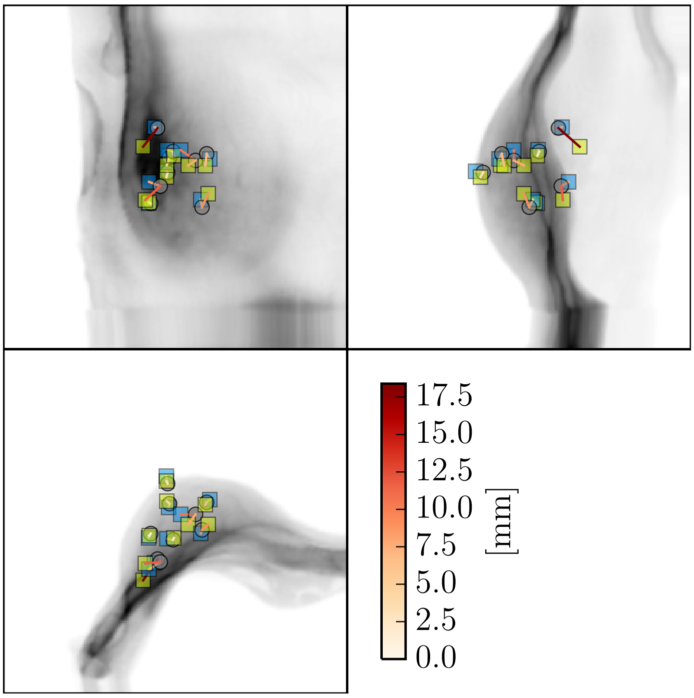

(a) *All landmarks of the first and the control observer.*

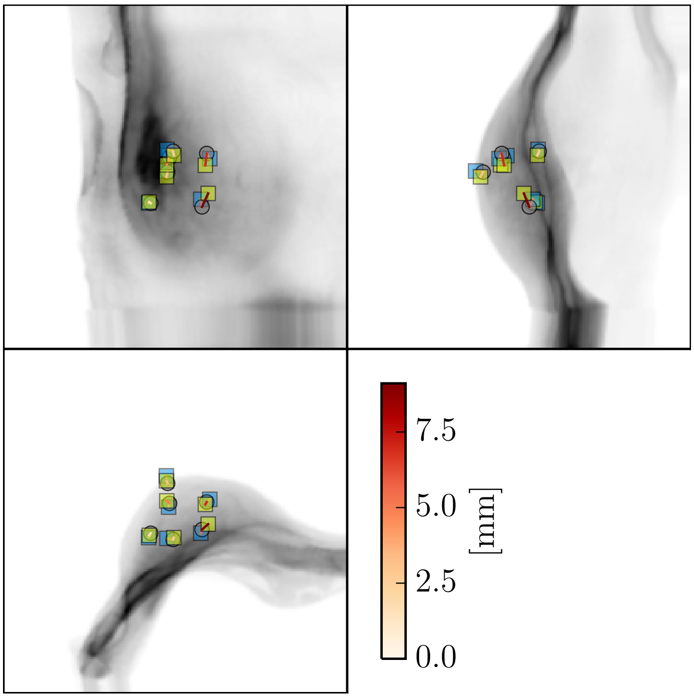

(b) *Reliable landmarks with an inter-observer distance below* 10 mm.

Figure 4.28: *Intensity based registration result for case P6 in terms of transformed landmark positions. The circles represent the landmarks that were transformed from the prone position. The blue and the green squares mark the positions of the first and the control observer respectively after transformation transformation from the supine position.*

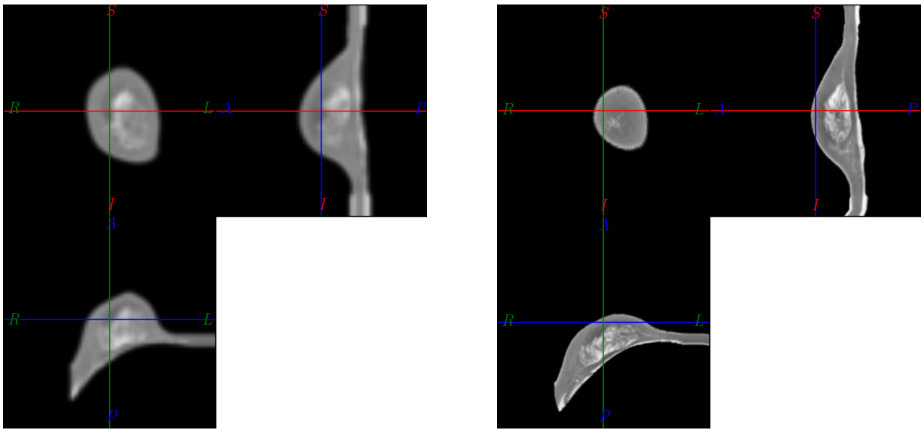

(a) *Prone image before registration* (b) *Prone image after registration*

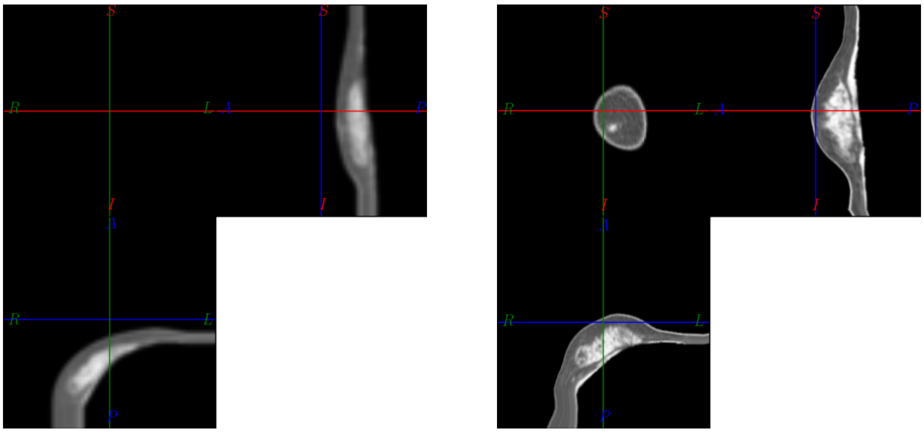

(c) *Supine image before registration* (d) *Supine image after registration*

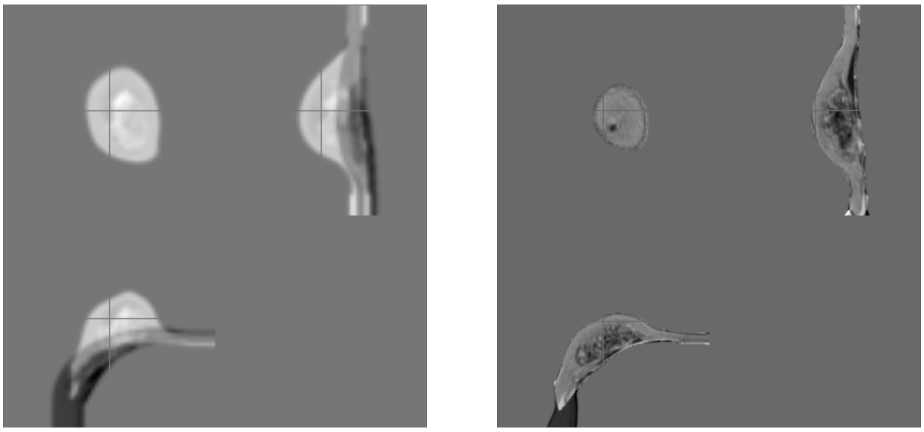

(e) *Difference before registration: (a)-(c)* (f) *Difference after registration: (b)-(d)*

Figure 4.29: *Result of the intensity driven registration approach for case P7. The images before registration, (a) and (c), show the original prone and supine configuration at the coarsest resolution level with the corresponding difference image (e). Figures (b) and (d) show the final registration result as the warped prone (b) and supine image (d) at the finest resolution level with the corresponding difference image (f).*

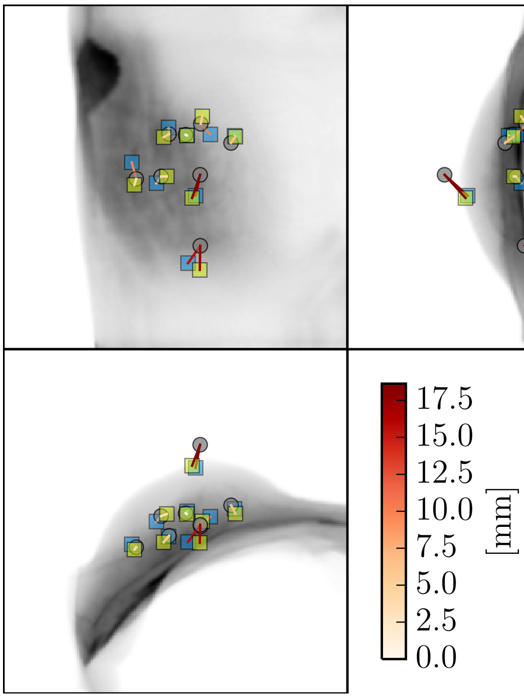

(a) *All landmarks of the first and the control observer.*

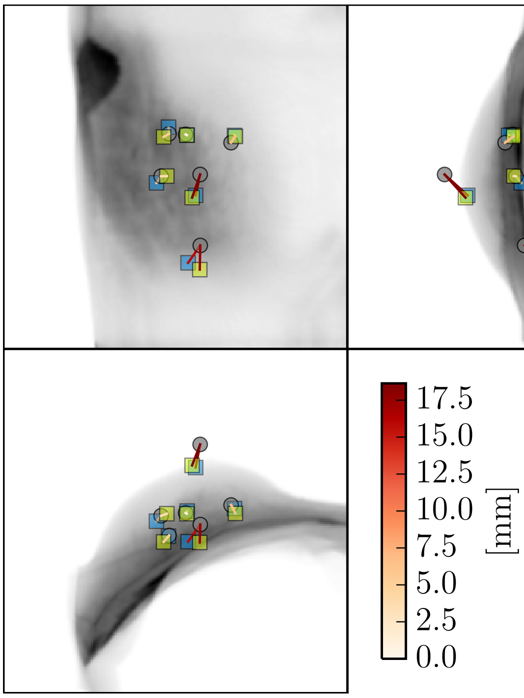

(b) *Reliable landmarks with an inter-observer distance below* 10 mm.

Figure 4.30: *Intensity based registration result for case P7 in terms of transformed landmark positions. The circles represent the landmarks that were transformed from the prone position. The blue and the green squares mark the positions of the first and the control observer respectively after transformation transformation from the supine position.*

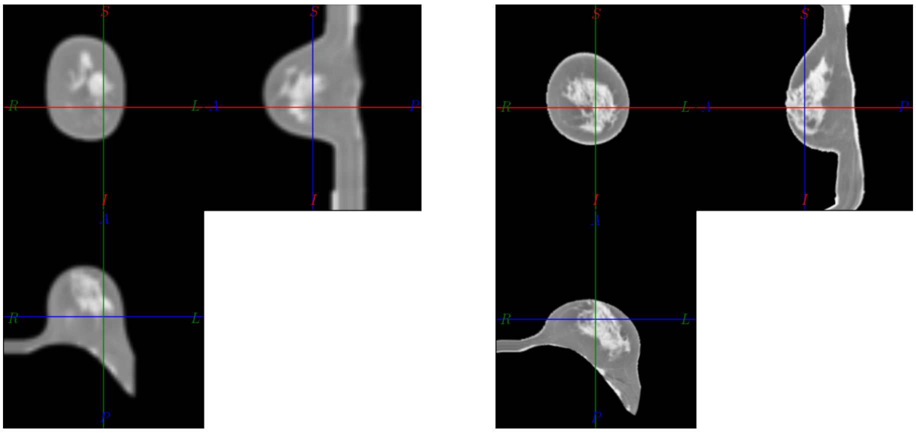

(a) *Prone image before registration* (b) *Prone image after registration*

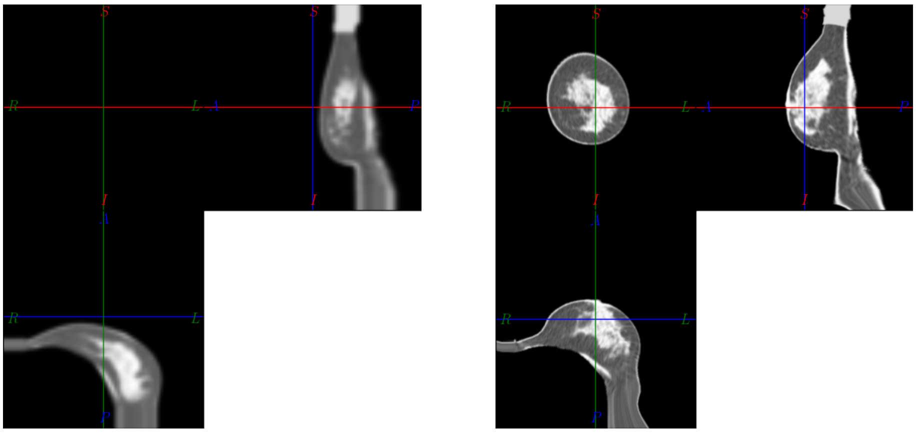

(c) *Supine image before registration* (d) *Supine image after registration*

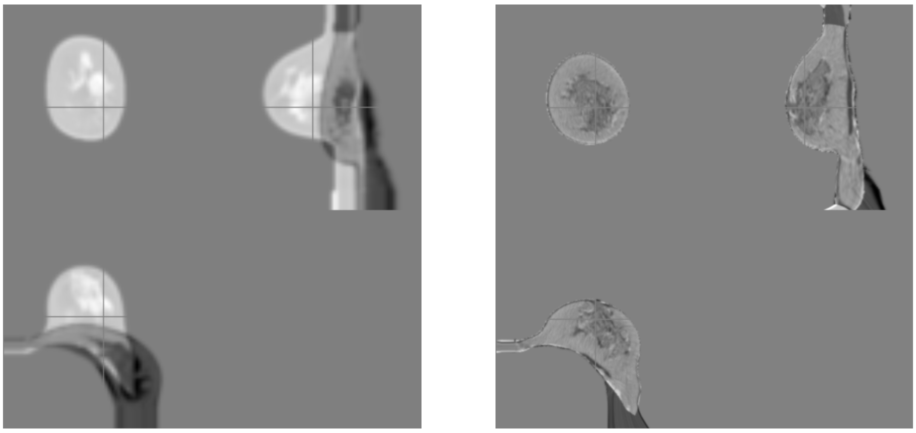

(e) *Difference before registration: (a)-(c)* (f) *Difference after registration: (b)-(d)*

Figure 4.31: *Result of the intensity driven registration approach for case P8. The images before registration, (a) and (c), show the original prone and supine configuration at the coarsest resolution level with the corresponding difference image (e). Figures (b) and (d) show the final registration result as the warped prone (b) and supine image (d) at the finest resolution level with the corresponding difference image (f).*

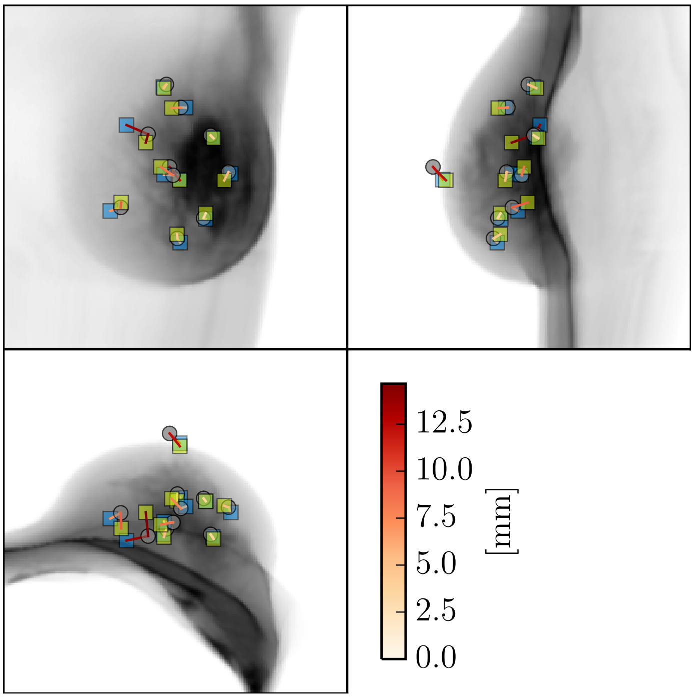

(a) *All landmarks of the first and the control observer.*

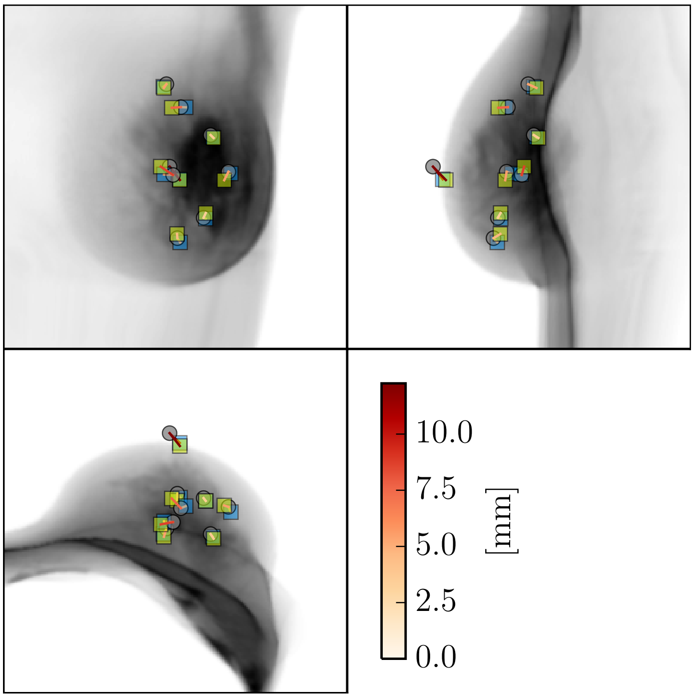

(b) *Reliable landmarks with an inter-observer distance below* 10 mm.

Figure 4.32: *Intensity based registration result for case P8 in terms of transformed landmark positions. The circles represent the landmarks that were transformed from the prone position. The blue and the green squares mark the positions of the first and the control observer respectively after transformation transformation from the supine position.*

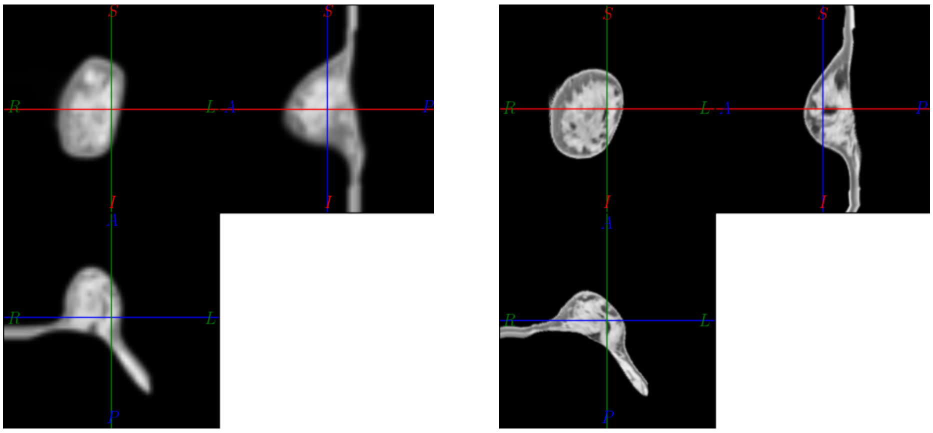

(a) *Prone image before registration* (b) *Prone image after registration*

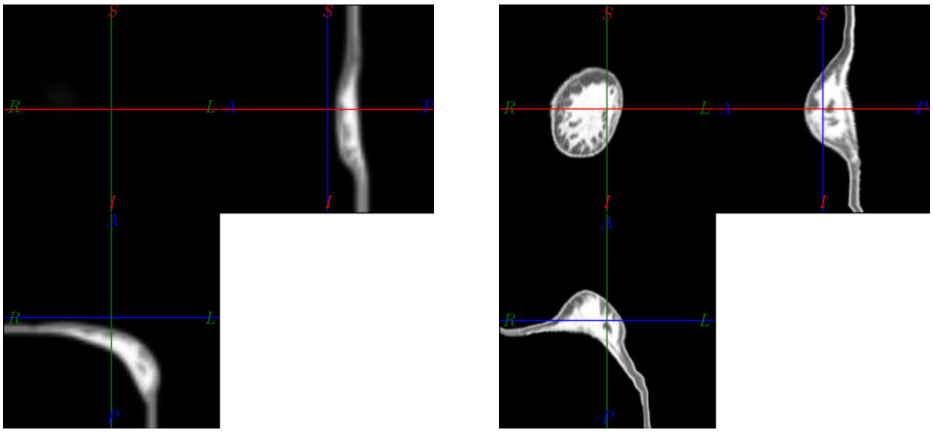

(c) *Supine image before registration* (d) *Supine image after registration*

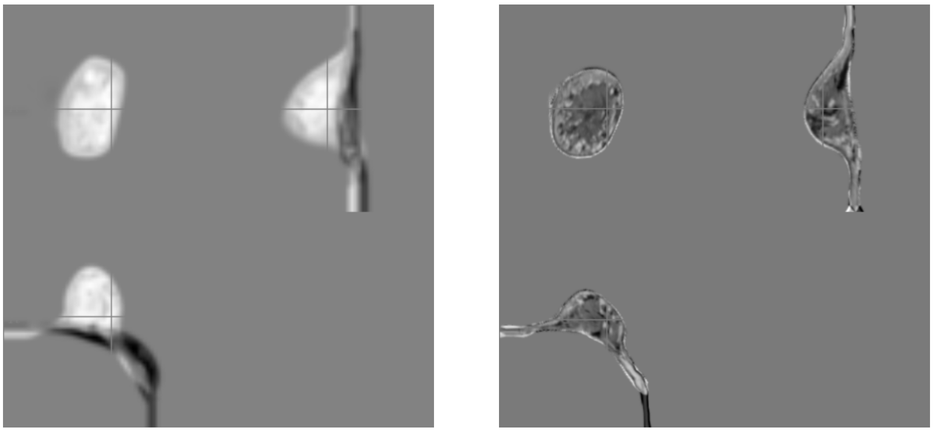

(e) *Difference before registration: (a)-(c)* (f) *Difference after registration: (b)-(d)*

Figure 4.33: *Result of the intensity driven registration approach for case P9. The images before registration, (a) and (c), show the original prone and supine configuration at the coarsest resolution level with the corresponding difference image (e). Figures (b) and (d) show the final registration result as the warped prone (b) and supine image (d) at the finest resolution level with the corresponding difference image (f).*

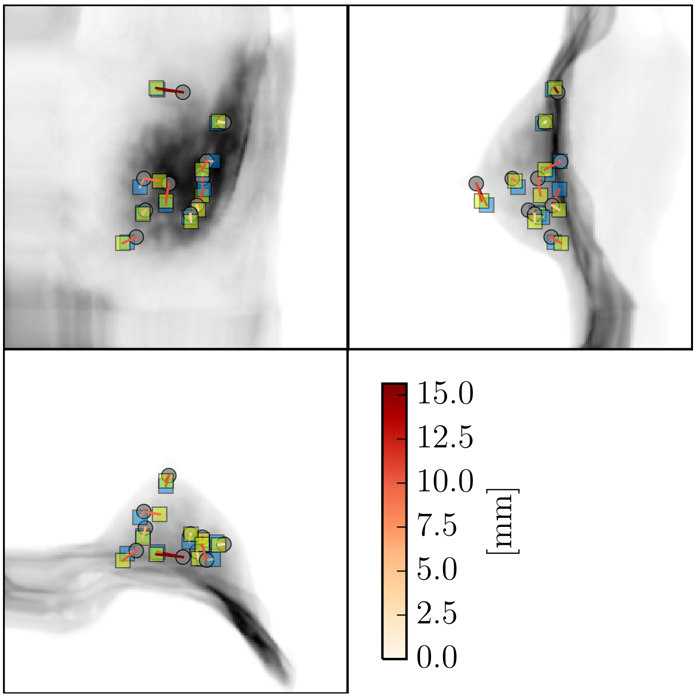

(a) *All landmarks of the first and the control observer.*

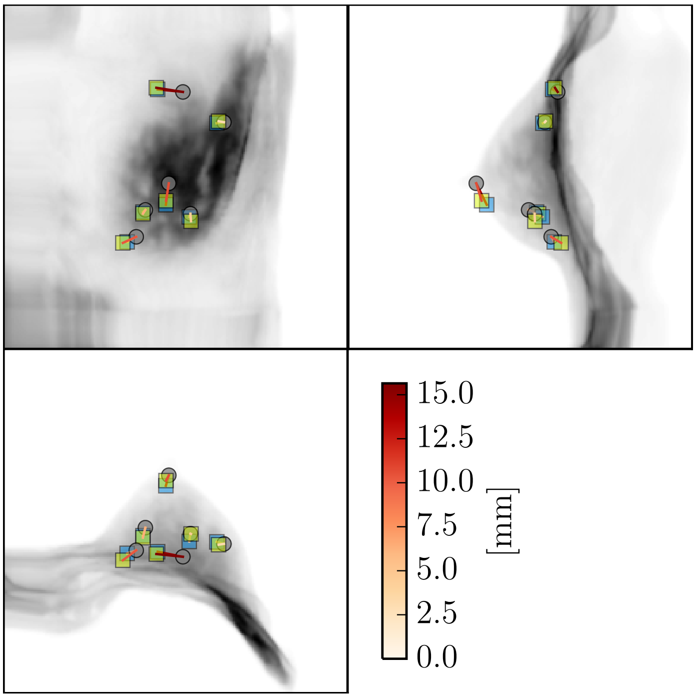

(b) *Reliable landmarks with an inter-observer distance below* 10 mm.

Figure 4.34: *Intensity based registration result for case P9 in terms of transformed landmark positions. The circles represent the landmarks that were transformed from the prone position. The blue and the green squares mark the positions of the first and the control observer respectively after transformation transformation from the supine position.*

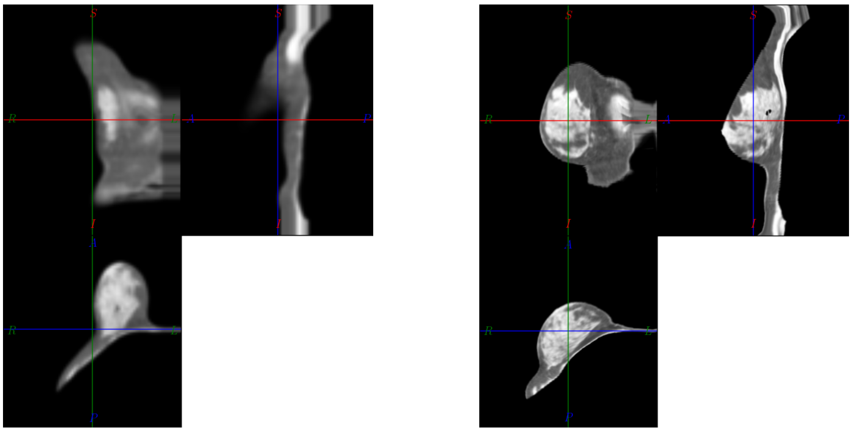

(a) *Prone image before registration*

(b) *Prone image after registration*

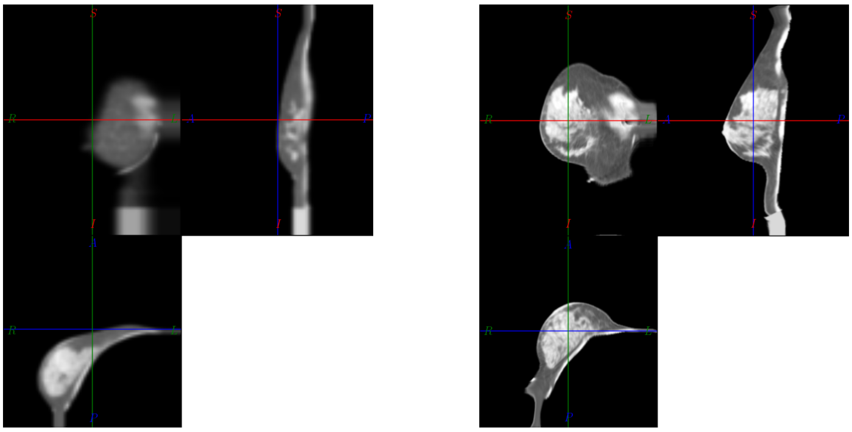

(c) *Supine image before registration*

(d) *Supine image after registration*

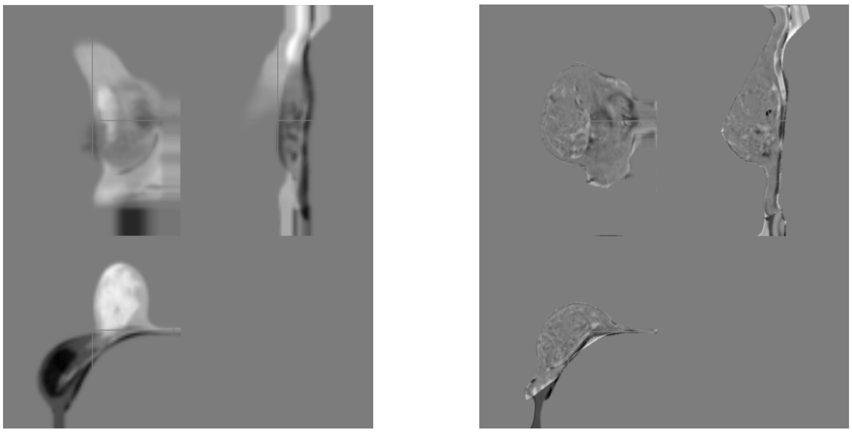

(e) *Difference before registration: (a)-(c)*

(f) *Difference after registration: (b)-(d)*

Figure 4.35: *Result of the intensity driven registration approach for case P10*. The images before registration, (a) and (c), show the original prone and supine configuration at the coarsest resolution level with the corresponding difference image (e). Figures (b) and (d) show the final registration result as the warped prone (b) and supine image (d) at the finest resolution level with the corresponding difference image (f).*

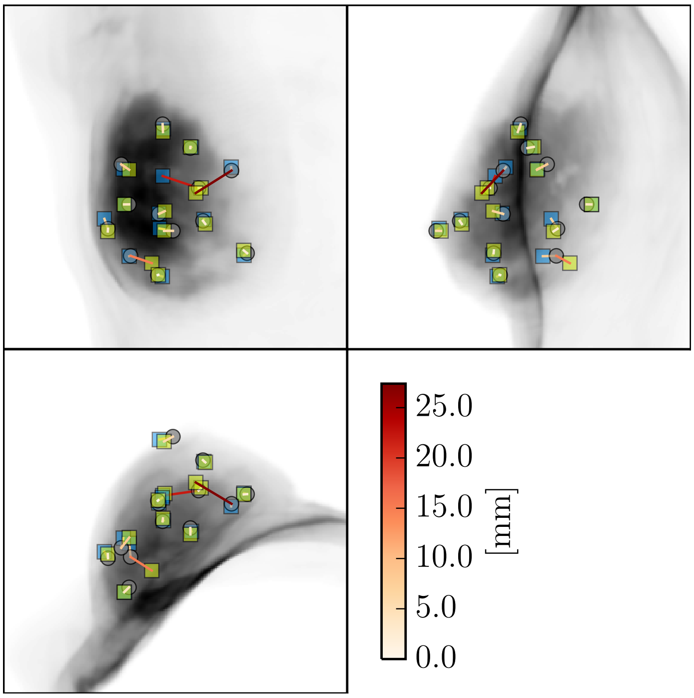

(a) *All landmarks of the first and the control observer.*

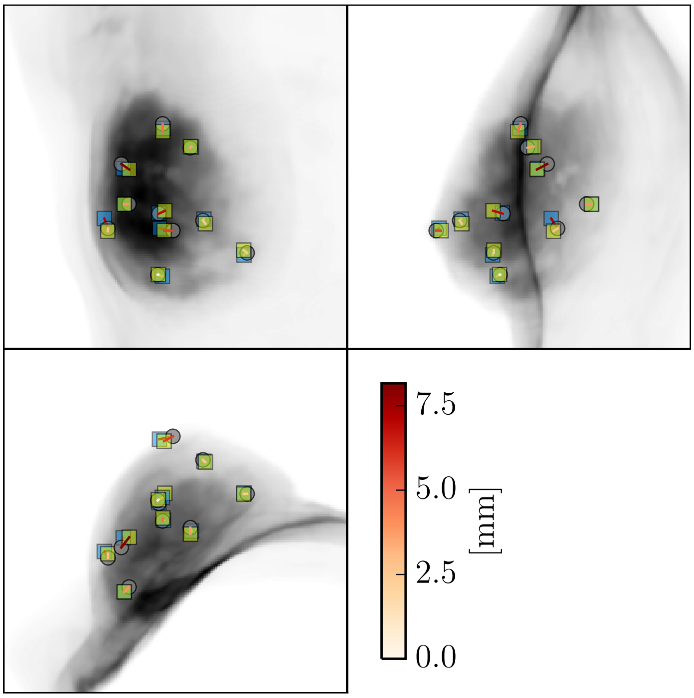

(b) *Reliable landmarks with an inter-observer distance below* 10 mm.

Figure 4.36: *Intensity based registration result for case P10* in terms of transformed landmark positions. The circles represent the landmarks that were transformed from the prone position. The blue and the green squares mark the positions of the first and the control observer respectively after transformation transformation from the supine position.*

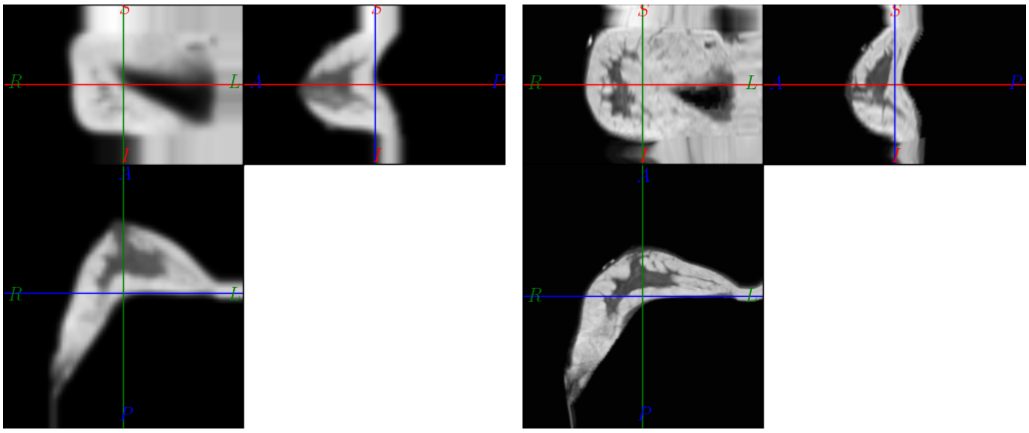

(a) *Prone image before registration*

(b) *Prone image after registration*

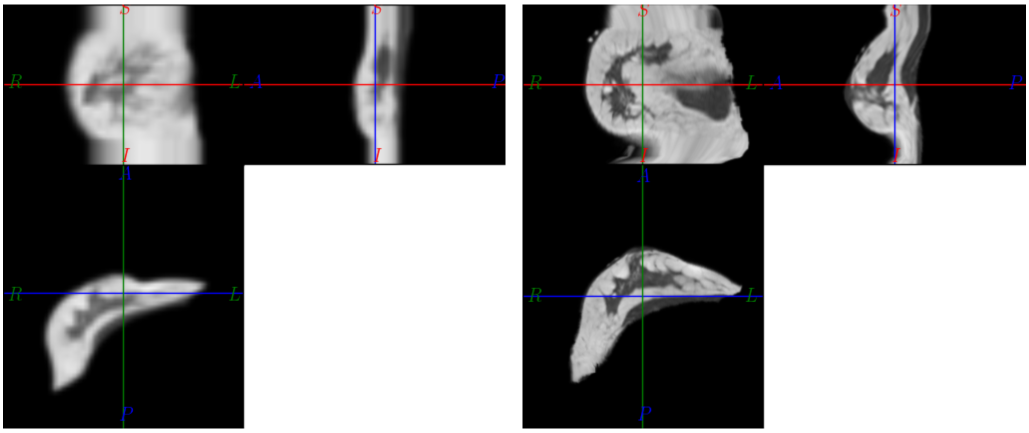

(c) *Supine image before registration*

(d) *Supine image after registration*

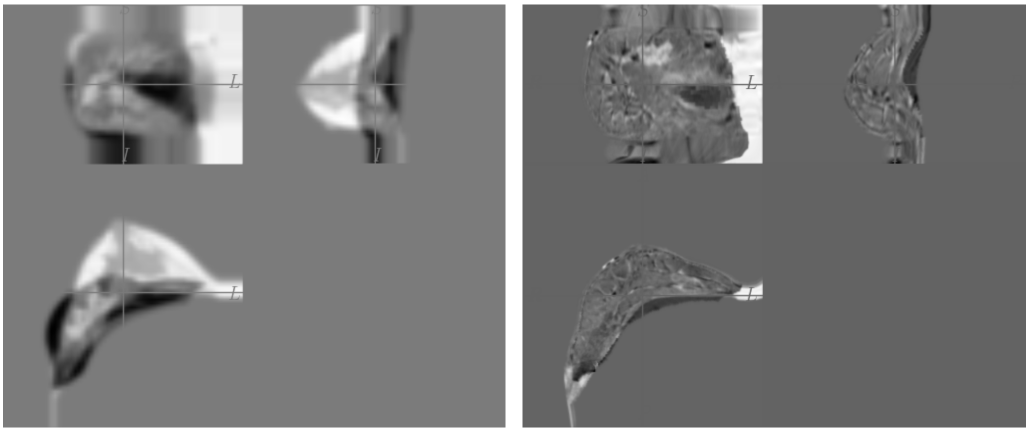

(e) *Difference before registration: (a)-(c)*

(f) *Difference after registration: (b)-(d)*

Figure 4.37: *Result of the intensity driven registration approach for case M1. The images before registration, (a) and (c), show the original prone and supine configuration at the coarsest resolution level with the corresponding difference image (e). Figures (b) and (d) show the final registration result as the warped prone (b) and supine image (d) at the finest resolution level with the corresponding difference image (f).*

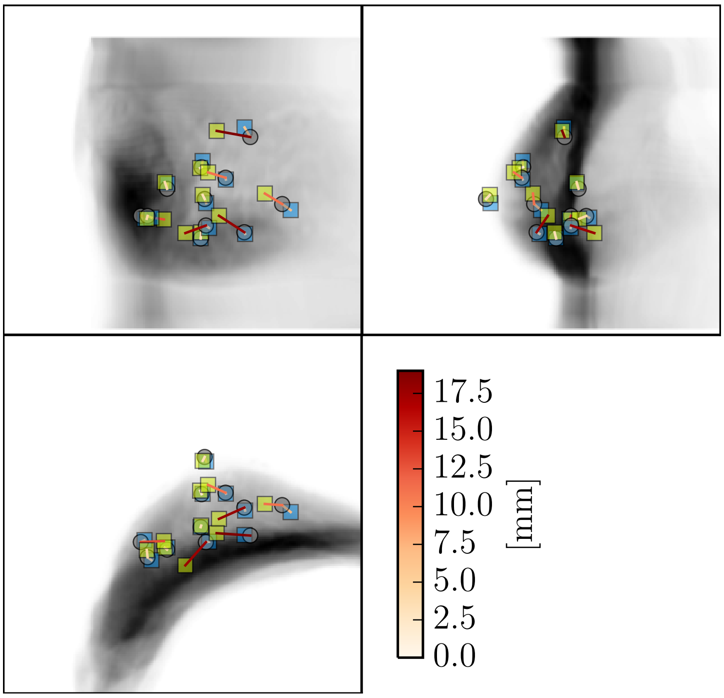

(a) *All landmarks of the first and the control observer.*

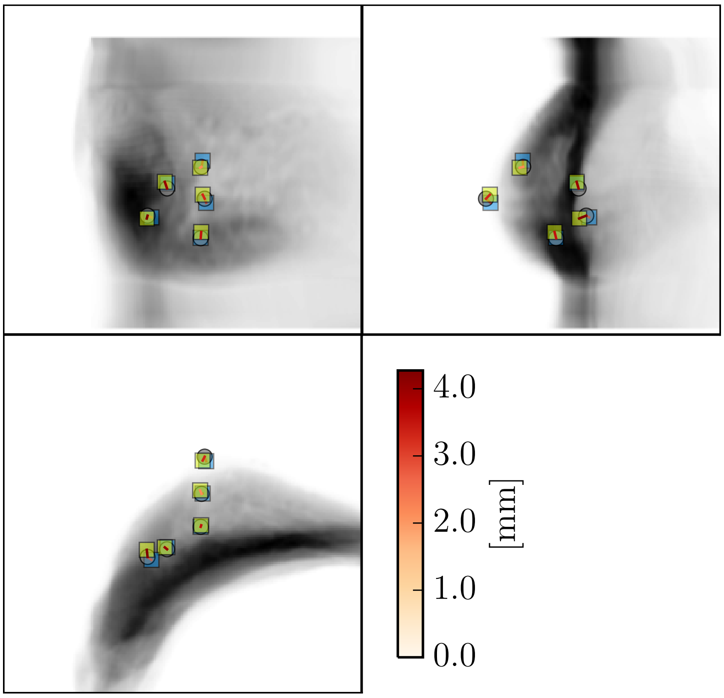

(b) *Reliable landmarks with an inter-observer distance below* 10 mm.

Figure 4.38: *Intensity based registration result for case M1 in terms of transformed landmark positions. The circles represent the landmarks that were transformed from the prone position. The blue and the green squares mark the positions of the first and the control observer respectively after transformation transformation from the supine position.*

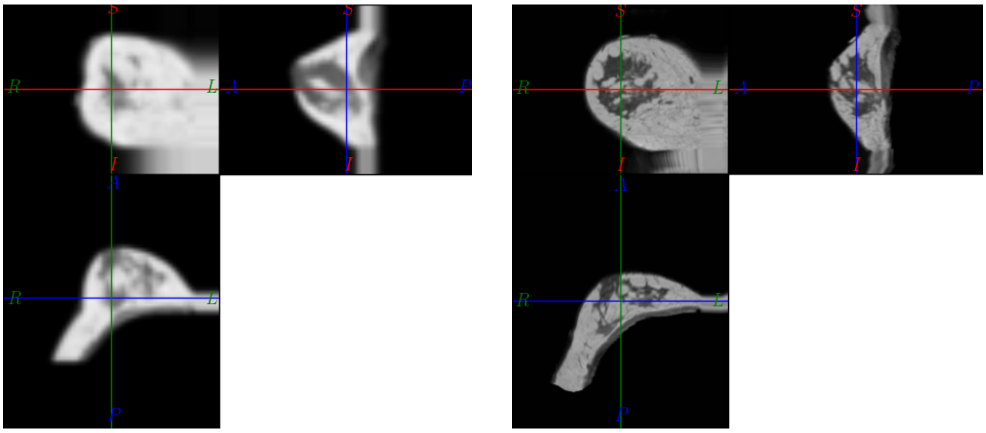

(a) *Prone image before registration*   (b) *Prone image after registration*

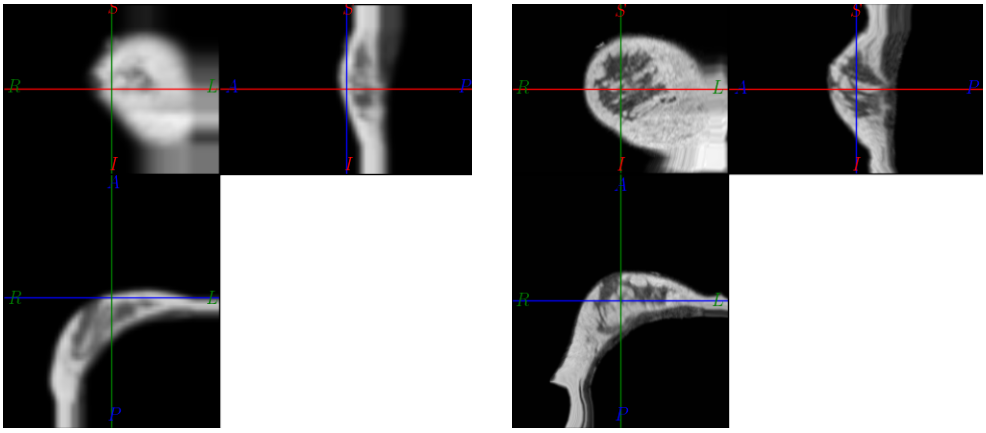

(c) *Supine image before registration*   (d) *Supine image after registration*

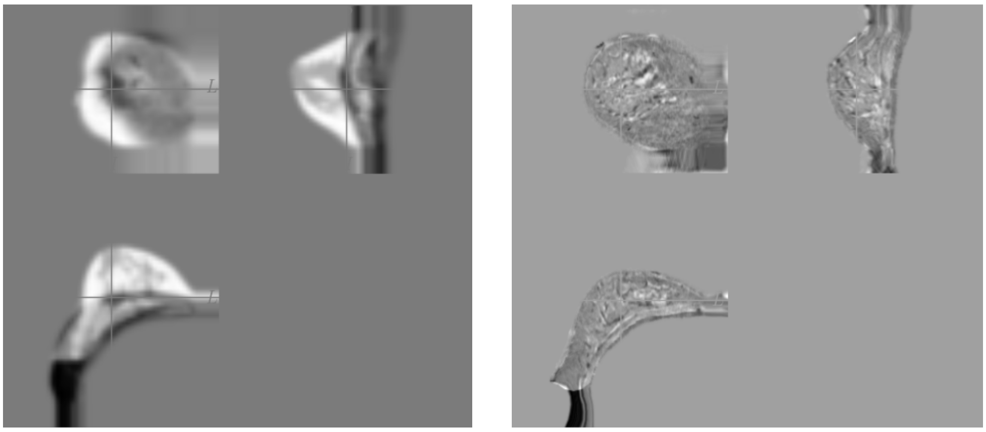

(e) *Difference before registration: (a)-(c)*   (f) *Difference after registration: (b)-(d)*

Figure 4.39: *Result of the intensity driven registration approach for case M2. The images before registration, (a) and (c), show the original prone and supine configuration at the coarsest resolution level with the corresponding difference image (e). Figures (b) and (d) show the final registration result as the warped prone (b) and supine image (d) at the finest resolution level with the corresponding difference image (f).*

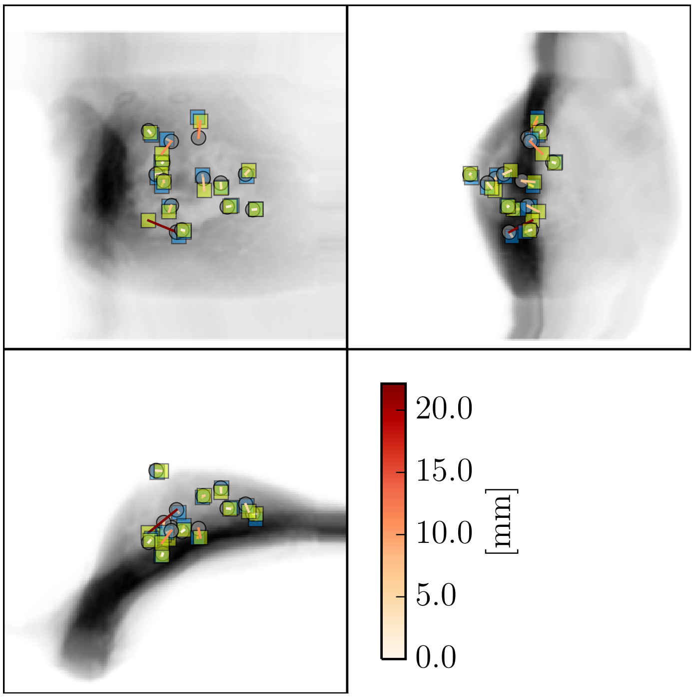

(a) *All landmarks of the first and the control observer.*

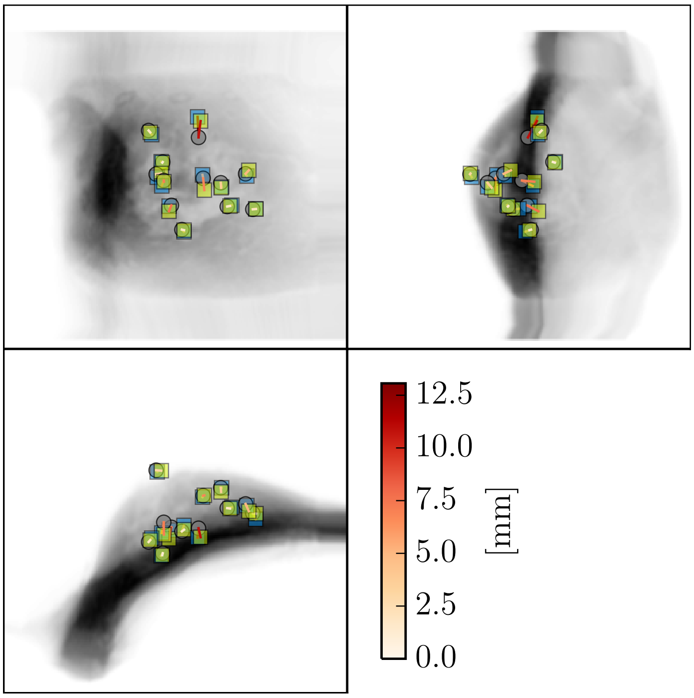

(b) *Reliable landmarks with an inter-observer distance below* 10 mm.

Figure 4.40: *Intensity based registration result for case M2 in terms of transformed landmark positions. The circles represent the landmarks that were transformed from the prone position. The blue and the green squares mark the positions of the first and the control observer respectively after transformation transformation from the supine position.*

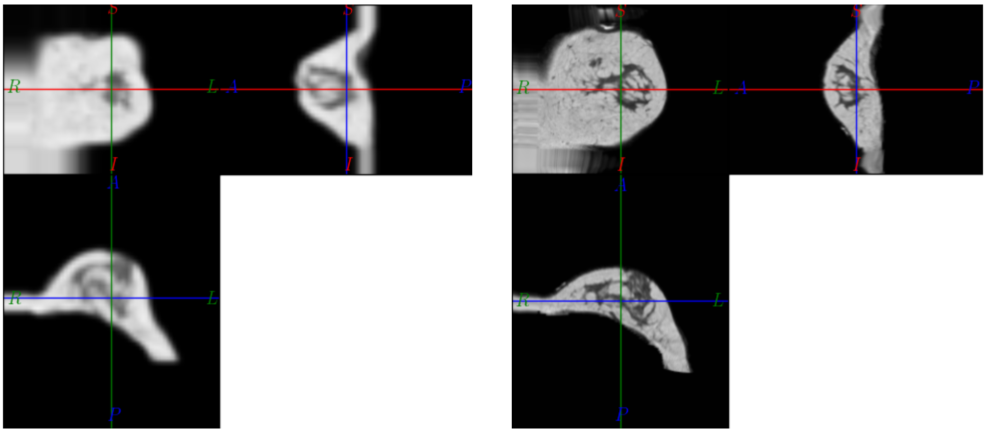

(a) *Prone image before registration* (b) *Prone image after registration*

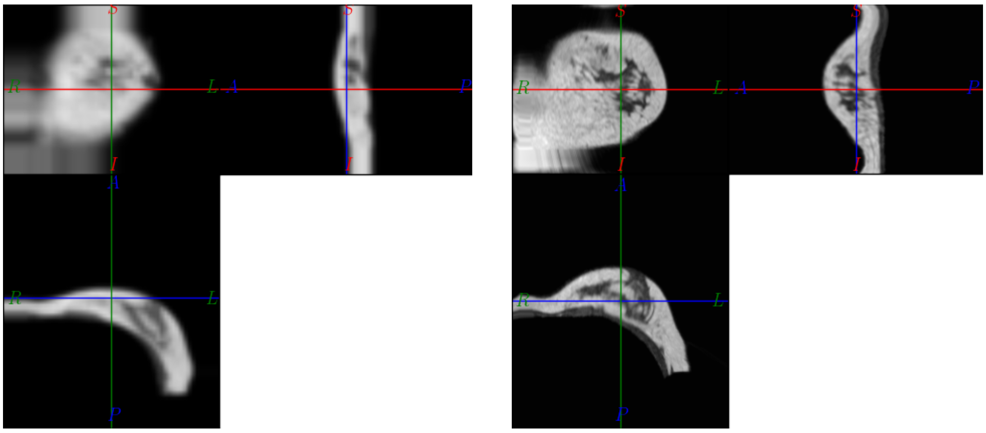

(c) *Supine image before registration* (d) *Supine image after registration*

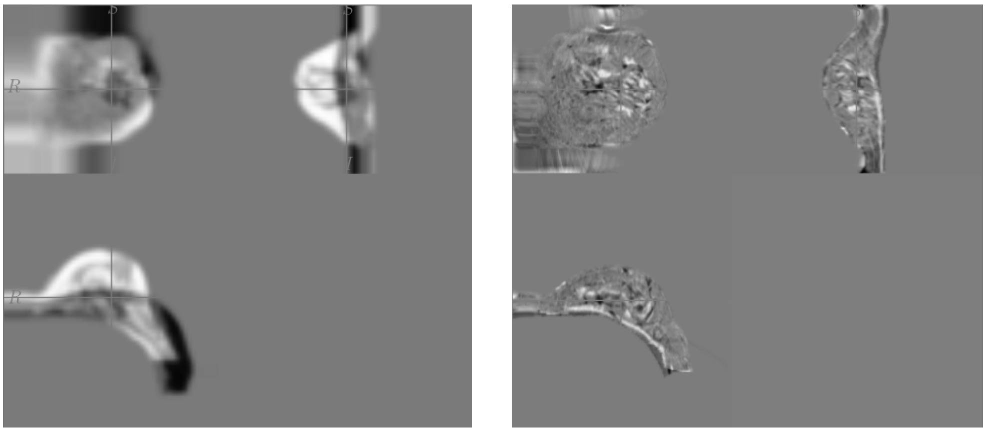

(e) *Difference before registration: (a)-(c)* (f) *Difference after registration: (b)-(d)*

Figure 4.41: *Result of the intensity driven registration approach for case M3. The images before registration, (a) and (c), show the original prone and supine configuration at the coarsest resolution level with the corresponding difference image (e). Figures (b) and (d) show the final registration result as the warped prone (b) and supine image (d) at the finest resolution level with the corresponding difference image (f).*

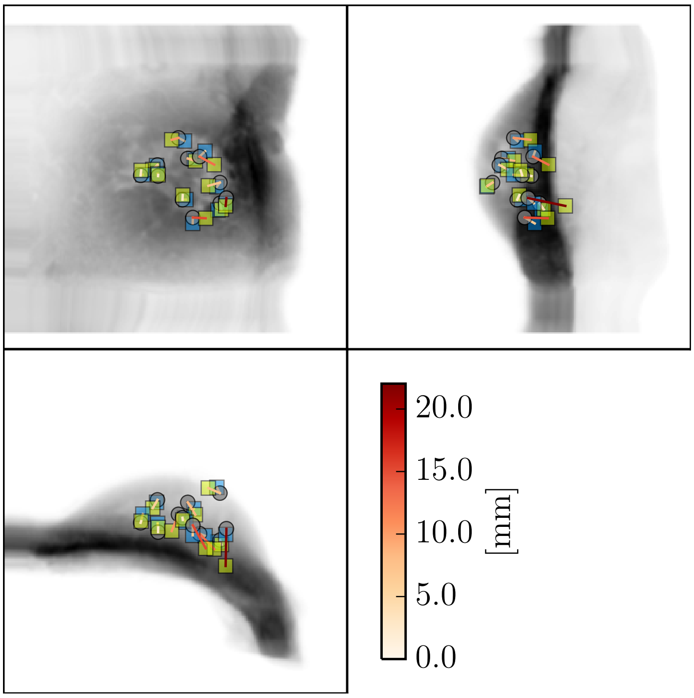

(a) *All landmarks of the first and the control observer.*

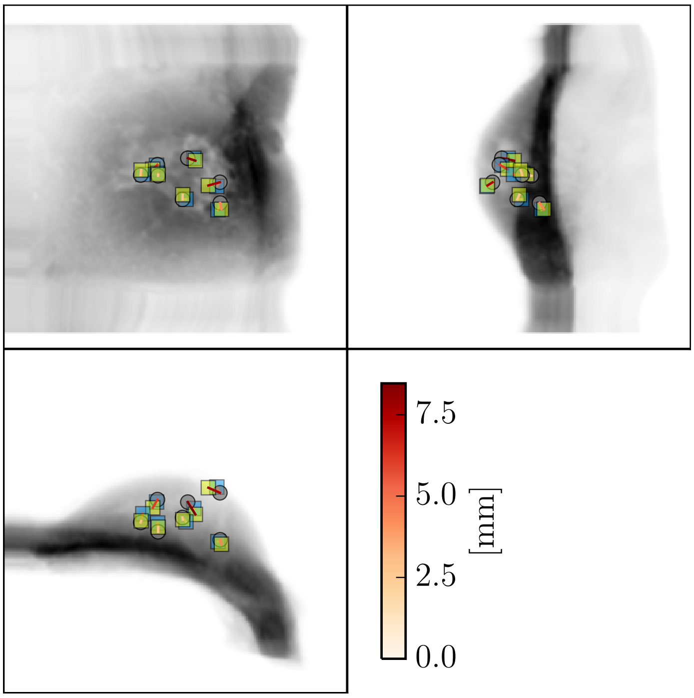

(b) *Reliable landmarks with an inter-observer distance below* 10 mm.

Figure 4.42: *Intensity based registration result for case M3 in terms of transformed landmark positions. The circles represent the landmarks that were transformed from the prone position. The blue and the green squares mark the positions of the first and the control observer respectively after transformation transformation from the supine position.*

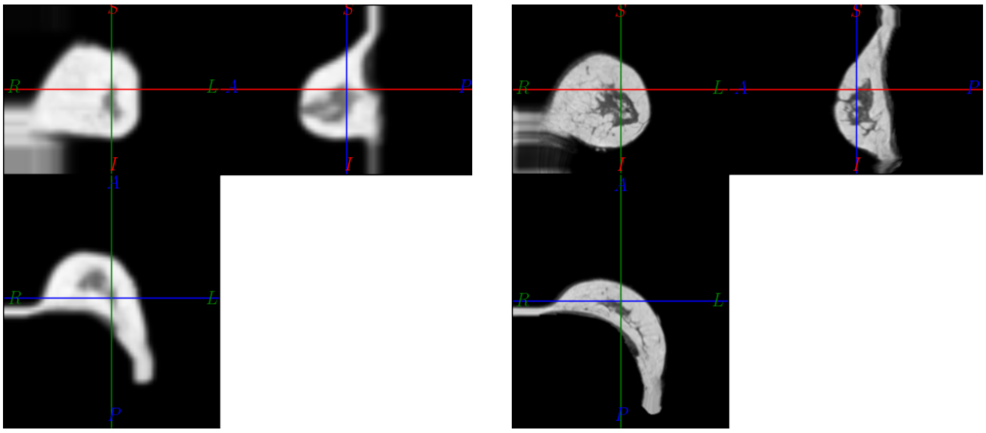

(a) *Prone image before registration* (b) *Prone image after registration*

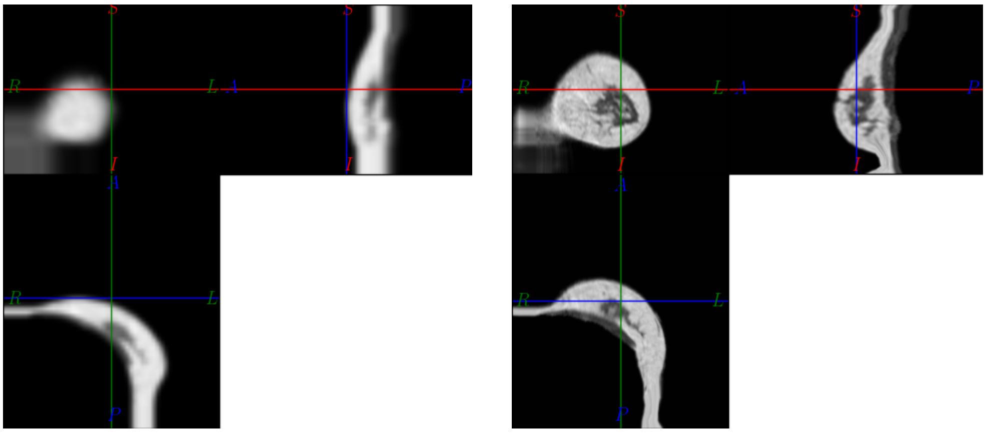

(c) *Supine image before registration* (d) *Supine image after registration*

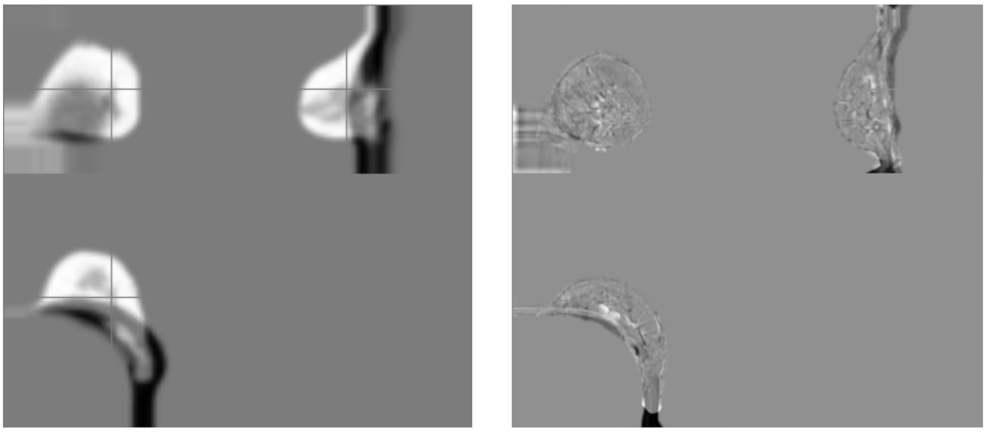

(e) *Difference before registration: (a)-(c)* (f) *Difference after registration: (b)-(d)*

Figure 4.43: *Result of the intensity driven registration approach for case M4. The images before registration, (a) and (c), show the original prone and supine configuration at the coarsest resolution level with the corresponding difference image (e). Figures (b) and (d) show the final registration result as the warped prone (b) and supine image (d) at the finest resolution level with the corresponding difference image (f).*

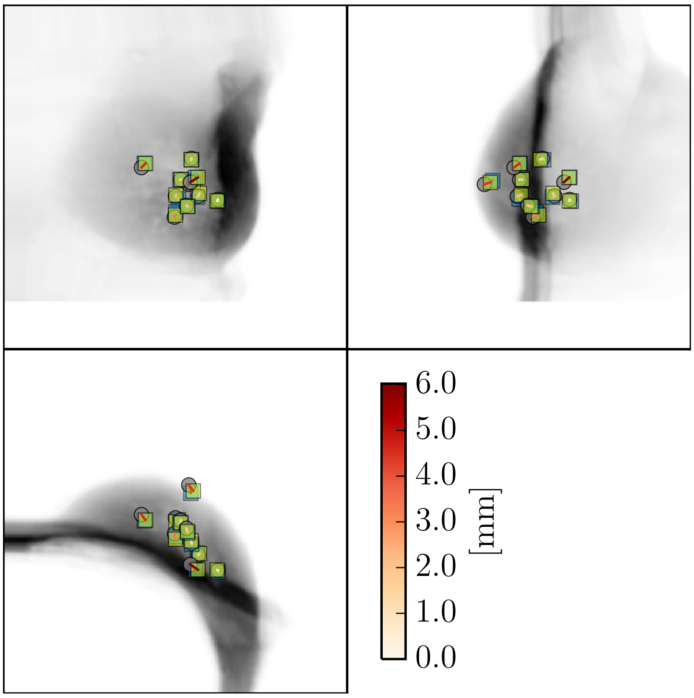

(a) *All landmarks of the first and the control observer.*

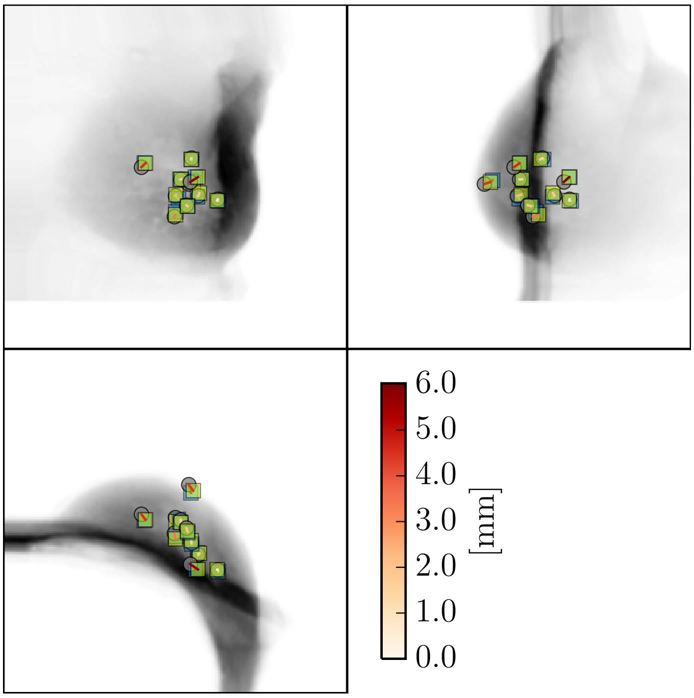

(b) *Reliable landmarks with an inter-observer distance below* 10 mm.

Figure 4.44: *Intensity based registration result for case M4 in terms of transformed landmark positions. The circles represent the landmarks that were transformed from the prone position. The blue and the green squares mark the positions of the first and the control observer respectively after transformation transformation from the supine position.*

simulation such that the unloaded configurations from prone and supine align. This results in a biomechanically constrained deformation. The motion on the chest wall is enforced to be parallel to the boundary between the breast and chest wall. A novel unloading mechanism takes advantage of the duality between the forward simulation displacement description and the well established image resampling procedure which is inverse to the simulation.

The viability of the proposed algorithm was first evaluated using a numerical phantom geometry with simulated prone-supine deformations. This provided ground-truth displacements, against which the registration accuracy was evaluated using 500 pseudo-landmarks. An initial misalignment of 19.3 mm was reduced to 11.6 mm by using the unloading methodology with generic material parameters. Optimising such parameters reduced the TRE to 5.4 mm and adding image forces achieved a final registration accuracy of 0.9 mm. While this initial experiment was promising, it also had its limitations. First the displacement magnitude between the original prone and supine image was comparatively small. This can be attributed to the fixed boundary condition on the chest wall, as well as to possibly too stiff material parameters for the ground-truth simulations. Furthermore, the simulated prone and supine images were generated without considering image noise. For a more realistic generation of input images for the registration method, Rician noise should be considered as was done for instance by Schnabel et al. (2003).

To quantify the alignment accuracy for the clinical datasets, the target registration error (TRE) in the central position by the means of manually selected landmarks was measured. Although this is – due to the scale of the deformation at hand – an inherently difficult task, a mean registration error for all clinical cases of 5.6 mm was measured.

Including prior knowledge of the gravity loading into the biomechanically based image registration was shown to be key to successful alignment. The pure biomechanical unloading step accounted for the biggest reduction of the overall meam TRE from 69.7 mm to 14.1 mm and the corresponding deformation recovery. The final corrections were image driven and smaller. They reduced the overall TRE from 14.1 mm to 5.6 mm.

Although the scheme proposed was implemented using the finite difference method, it can also be adapted to integrate the symmetric image derived forces into conventional finite element platforms.

The motion constraint presented here differs significantly from the frictionless sliding used for example by Han et al. (2014) and the fixed displacement constraint widely used elsewhere. Ultimately it allows control of sliding-like motion in a much more subtle way and could provide an experimental platform to investigate motion along the chest wall more precisely.

Having a supine target image is – especially in the context of image guided surgery – typically not standard clinical practice, and imposes a potential limitation on all intensity based registration methods for prone-to-supine breast image alignment. In cases where full three-dimensional images are not available in the supine position, surface scans could be acquired more easily. In this regard, the presented method could be extended for such an application by using an additional target surface on the skin of the model and eliminating the internal image forces.

The use of a mono-modal image force based on the sum of squared differences imposes a limitation on the framework which can be overcome by implementing image derived forces based on multi-modal similarity metrics such as normalised mutual information or other information theory based metrics. Possible implementations can be based on previous work, for instance that presented by Crum et al. (2003).

4.3 POTENTIAL CLINICAL APPLICATIONS

This section reviews a potential clinical field of applications of the developed large deformation, intensity based breast image registration described in the previous sections. The availability of three-dimensionally resolved images depends on individual patient's clinical journey and thus applicability varies on a patient-to-patient basis. Three-dimensionally resolved images as required by intensity driven registration approaches can be seen as the most complete set of source and target information. This stringent requirement may also potentially put limitations on its applicability. Hence it is important to closely look at the patients pathway through the clinic and identify points where such image pairs are already part of the clinical routine. Since the surgical planning and guidance application is discussed in chapter 5 the focus of this section is on radiotherapy.

When a woman is diagnosed with breast cancer, surgery is often part of her individual therapy plan which can also include additional forms of treatment such as chemotherapy and radiotherapy. Where possible lumpectomy (often also referred to as wide local excision) combined with radiotherapy is the preferred treatment of choice. This involves removing only the cancerous tissue with a margin of healthy breast tissue, therefore conserving the unaffected parts of the breast. This has potential benefits over mastectomy, the complete removal of breast tissue, of being more acceptable to patients, offering good cosmetic results and comparably low risk of local recurrence as was shown by Hwang et al. (2013).

The important role of radiotherapy in order to reduce the risk of local recurrence in early breast carcinoma was highlighted for instance in the review article by Offersen et al. (2009) and references therein. As part of radiation therapy, a supine CT planning scan is acquired. Prone MR images on the other hand are usually taken much earlier during the diagnostic or staging phase prior to surgery (NICE, National Institute For Health and Care Excellence, 2009). Hence prone-supine image pairs for the same patient in the current clinical workflow only become available at the time of radiotherapy. This motivates discussion of the possible application of the developed registration technique for radiation therapy: *How could the information contained in the MRI – such as the original extent of the tumour – be exploited to inform the radiation procedure?*

Performing the prone-to-supine registration between pre-surgical MR images and post-surgical CT scans would allow transfer of, for example, the uptake information and derived lesion extent of a prone DCE-MRI scan to the supine CT configuration. When both images are overlaid this could aid the radiotherapy planning process. Two radiation therapy procedures which apply locally varying radiation doses to the breast are the breast boost (Romestaing et al., 1997) and Accelerated Partial Breast Irradiation (APBI) (Baglan et al., 2003).

The current standard procedure for external beam radiotherapy is Whole Breast Irradiation (WBI) and does not necessarily require localised information about the original tumour bed when a homogeneously distributed dose is applied to the whole breast (see e.g. Bartelink et al., 2001; Fisher et al., 2002). During treatment a dose of 50 Gy is delivered in 25 daily fractions over the course of five weeks. However, local tumour bed information becomes a requirement, when additional dose, of typically 16 Gy, is delivered to this region. This is called the breast boost. Bartelink et al. (2001) showed in a randomised trial with 5318 patients that this boost reduced local recurrence just under twofold with larger effects for younger patients. To date this procedure is accepted and recommended in clinical practice.

Accelerated Partial Breast Irradiation on the other hand only irradiates the tumour bed with a margin (Baglan et al., 2003). It was proposed as a departure from the standard WBI procedure which was challenged due to its disadvantages. First the therapy requires five weeks of daily treatment – sometimes longer. This poses a logistical challenge on clinical facilities as well as patients. Second, exposing the whole mammary gland to radiation might not be required, and a focussed application of radiation could be sufficient to reduce the risk of local recurrence. By using accelerated treatment, higher doses per fraction can be applied, resulting in lower numbers of total fractions and thus a faster overall treatment.

Accelerated Partial Breast Irradiation can take several forms to deliver the dose to the tumour bed locally. Interstitial Brachytherapy for example utilises seeds filled with a radioactive substance which are then implanted in the target volume (Baglan et al., 2001). Alternatively a technique called *MammoSite* (Keisch et al., 2003) uses a balloon that is inflated in the surgical cavity with a saline solution. During therapeutic sessions a seed is inserted via a connected catheter into the balloon to deliver the dose to the tumour bed. The advantage here is that no radioactive substances remain in the body between treatments. Both methods however are invasive with the associated risk of infection as reported in the five-year MammoSite experience report by Benitez et al. (2007). Vaidya et al. (2014) proposed a technique for partial breast irradiation that is currently evaluated in the *TARGIT* trial and uses inter-operative radiotherapy. Here, directly after lumpectomy and before the wound is closed, the tumour bed is irradiated by positioning a radiation source contained within an applicator in the surgical cavity delivering 20 Gy in a single fraction. Baglan et al. (2003) on the other hand proposed a non-invasive APBI technique using 3D conformal radiation therapy (3D-CRT).

Intensity based prone-to-supine image registration could aid breast boost therapy as well as APBI in the context of personalised non-homogeneous dose planning. A dose delivery plan is created on the basis of supine CT scans which show the patient in the treatment position, i.e. whilst lying on her back. In these images the clinical target volume to which the radiation is delivered is specified. This includes the surgical cavity, which is currently marked by metallic clips, as well as a safety margin of usually 10 mm (Weed et al., 2004).

The metallic clips are positioned in the cavity wall by the surgeon during lumpectomy. This allows the overall location of the tumour bed in the CT image to be estimated. Ahn et al. (2009) report that the presence of wound seroma is crucial to delineate the surgical cavity in the post-surgical CT scan. They argue, that MRI provides better soft-tissue contrast and could allow more precise delineation of the region which is to be irradiated. Kirby et al. (2009) also report that delineations of the tumour bed when based on MR images result in larger target volumes, when compared to delineations based on CT images. However, the effect on the final irradiated region was reportedly minor. An increasing interest in making use of the advantages of MRI was reported in the overview article by Metcalfe et al. (2013) and highlights the constant development of this field. Interestingly Schmitz et al. (2010) promote to use pre-surgical MRI for more precise planning of the excision and radiotherapy, especially in the context of sub-clinical lesions in the vicinity of the tumour bed which are believed to be sources of local recurrence. In this regard pre-surgical DCE-MRI transformed to the supine position could be utilised to fill in missing information about the original location and extent of the tumour bed which might result in a more accurate planning of the dose delivery.

Some challenges however still remain. The present registration scheme does not consider the surgical intervention between the pre-surgical DCE-MRI and the post-surgical CT scan. Furthermore it is expected that the lumpectomy cavity will decrease in volume over the course of the treatment and thus an additional degree of complexity is introduced. From the clinical perspective it remains to be seen if partial breast irradiation will become widely accepted. A consensus recommendation by ASTRO, the American Society for Radiation Oncology (Smith et al., 2009) states that APBI will never replace WBI for all or even most patients. Suitable patients should show a low risk of local recurrence which to date is difficult to predict reliably. Furthermore suboptimal cosmetic results were reported by Olivotto et al. (2013) which are attributed to the higher and inhomogeneous dose deliveries and associated fibrosis. The radiation boost delivery on the other hand is well accepted in clinical practice and might benefit from added pre-surgical information. Despite these challenges, the capability to register prone and supine images is a significant step towards enhanced utility of information in significantly different patient positions and should open further applications in the future.

4.4 CHAPTER CONCLUSION

The symmetric prone-to-supine intensity driven registration builds on the idea that splitting the large scale deformation into two parts makes the registration problem easier to solve. The basic concept was explored in the first section of this chapter 4.1 and acts as a proof of concept for the approach of aligning the images in the unloaded configuration. It uses the finite element technique as described in detail in chapter 3. The intensity based registration in the zero-gravity state is then performed using a free form deformation registration scheme. It was shown that the biomechanical unloading step from the prone and supine position accounts for the main reduction of the target registration error (see table 4.2 on page 98). Hence this unloading is crucial to transform the images such that the residual deformation lies within the capture range of the intensity based registration.

Although good initial alignment could be achieved between the prone and the supine images, some challenges remain in the sequential scheme. The recovery of the unloaded configuration in this approach, for instance, is based on the iterative prediction-correction scheme. The zero-gravity estimate is updated on the basis of the error between the prone loading simulation and the actual prone loaded MRI configuration. This local difference is pulled back to the current zero-gravity estimate using the deformation gradient. The iterative unloading imposes several challenges for practical applications, especially when this is to be performed in an unsupervised way as, for example, in the Picture project. The number of iterations for the scheme to converge is not fixed and mainly dependent on the volume of the patient's breast. Hence in some cases several gravity increase steps are required. Furthermore, the unloaded mesh can be of bad quality which can become a problem when further simulations are based on the unloaded configuration.

The second limitation of the sequential approach is that there is no feedback from the registration into the biomechanical model. This means that only one unloading simulation is performed and accepted as the final result. Inter-patient variability however suggests that this approach will lead to inaccurate results, since the soft tissue stiffness of adipose and fibroglandular components were reported in the literature to cover a wide range (see table 2.1 on page 51) and hence a material optimisation step as proposed for instance by Han et al. (2014) could further improve the initial alignment. In the same study the motion of the breast tissue on the chest wall was highlighted and thus a traction free sliding boundary condition was applied between the chest wall and pectoralis muscle. The same type of motion was considered in the sequential registration approach by introducing circumferential stretching of the retromammary facets of the model using a prescribed displacement boundary condition. This approach however is inflexible and does not represent patient anatomy.

The nature of the sequential registration is that the biomechanical simulation and the intensity based image registration step are decoupled. Hence in cases where the deformation is not restricted by physical constraints such as volume preservation, physically unrealistic deformations could be introduced. And lastly the mesh generation for finite element simulations is an involved process and can be difficult to achieve.

The novel integrated biomechanical simulation based registration approach presented in section 4.2 aims to address all of the aforementioned disadvantages of the sequential registration. It is based on the finite difference scheme and thus avoids the explicit mesh generation step. Furthermore the unloading is designed such that it exploits the inverse relationship between the forward simulation and the backward image resampling. This makes it possible to recover the unloaded configuration in just one forward simulation step.

The feedback of the image alignment into the simulation is twofold. First the material parameters are optimised globally to improve the alignment before local correction forces are calculated and applied. These image derived forces do not have a real physical basis but can overcome modelling inaccuracies such as contact of the breast with the MR imaging device in the prone position and local stiffness variations that cannot be captured in the global material optimisation step.

The relatively simple constitutive relation, namely the neo-Hookean material description allowed good alignment to be achieved. In future work this could be extended to incorporate more complex, even anisotropic material behaviour if required.

Allowing the breast tissue to move along the chest wall with the motion constraint presented in section 4.2.3.2 presents a more flexible approach compared to either traction free sliding or fixed boundary conditions as was previously presented in the literature. This is due to the motion being determined by the biomechanical material behaviour as well as the image derived forces in this region.

The integrated simulation based registration can produce excellent alignment between prone and supine MR or CT images as well as between prone MR and supine CT images i.e. both intra- and inter-modality registrations can be performed. The biggest contribution to the alignment is due to the unloading and thus it can be concluded that this represents an essential building block for successful large deformation registration. The unloading step resembles the physically correct consideration of the effects of gravity and hence it allows incorporation of prior knowledge about the nature of the deformation. Standard intensity based registration alone is unlikely to be able to recover such degrees of deformation without integration of biomechanical prior knowledge.

In terms of clinical applications the intensity based prone-to-supine registration obviously depends on the availability of three-dimensionally resolved breast images in these different loading configurations. This represents the most complete set of information possible. The most accessible application as was discussed in section 4.3 is in radiation therapy planning. Location of the original tumour registered from pre-surgical MR images to post-surgical CT could assist during planning of Partial Breast Irradiation therapy. Furthermore during standard whole breast radiation additional boost delivery could be planned more precisely with an improved knowledge about the tumour bed location. Surgery between pre- and post operative images however requires further work and validation before it can be translated into clinical practice.

In some cases a supine volume is unavailable or inconvenient to acquire. Hence the following chapter 5 investigates a biomechanically guided surface driven large deformation registration approach.

5

BIOMECHANICAL REGISTRATION: SURFACE DRIVEN

CHAPTER OVERVIEW The building blocks to facilitate patient-specific biomechanical finite element simulations based on structural MR images were established in chapter 3. These include the segmentation of the breast, the discretisation – or meshing – of the segmented geometry, the assembly of the biomechanical model with appropriate constitutive relations and boundary conditions, and the forward loading as well as the unloading simulation from a loaded geometry. As a result, those biomechanical breast models provide a tool to simulate large deformations as they occur when the patient position is changed. The symmetric, intensity driven registration approach presented in chapter 4 used, amongst other aspects, a combination of biomechanical prior-knowledge, material parameter optimisation and intensity information to drive final alignment. In this chapter a surface driven registration scheme is developed that does not require a volumetric target image. Instead, the biomechanically simulated breast shape in a gravity loaded configuration is aligned with a target surface. Similar to the intensity driven registration method, first a material parameter optimisation is carried out to improve the gross alignment, followed by a surface alignment step. The main contribution here is the constrained surface warping that reduces the residual misalignment between the target surface and the biomechanical model. The surface displacements are subsequently applied to the biomechanical model to generate a volumetric displacement vector field.

Carter et al. (2005) point out that the application of biomechanical models to provide information for surgical planning or guidance is, despite being an obvious application, very challenging. To facilitate surgical planning, image information from the pre-surgical prone DCE-MRI needs to be transformed into the surgical supine position. For surgical guidance a further transformation of the transformed image into the coordinate system of the operating room (OR) might be required. This last transformation is known as image-to-physical space registration. To perform the transformation from the prone image data to the surgical position some target information is required, since, as will be shown in this chapter, pure simulation approaches are likely to fail.

In the literature biomechanical models of breast tissues are used to align volumetric prone-supine image pairs to obtain the transformation into the surgical position. This is usually done in a sequential way, where first a biomechanical simulation recovers the gross deformation between the prone and the supine position. In a subsequent step an intensity based registration accounts for residual misalignment (Lee et al., 2010; Carter et al., 2006a; Eiben et al., 2013; Han et al., 2014). An alternative, integrative approach to align prone and supine breast images was presented in chapter 4. In the current clinical workflow, however, 3D prone-supine image pairs are usually not available at the time of surgery.

As an alternative to the prone imaging position, dynamic supine breast MRI was proposed previously by Siegler et al. (2011). This substantial change in MRI acquisition practice would make the information about the extent of the lesion directly accessible in the surgical position. However, to date it has not been adopted into clinical practice, due to limited diagnostic utility and the extended image acquisition time required if performed additionally. Furthermore, breathing motion compensation becomes essential when the supine configuration is adopted during breast MRI acquisition (Siegler et al., 2012), and, since the position of the patients' breast in the scanner is further away from the iso-centre, geometric distortion might occur Ahn et al. (2009). Recently the potential role of supine MRI for image guided interventions was addressed by solving the image-to-physical-space registration task for which the comparably smaller deformation between the image acquisition and the surgical position was exploited (Alderliesten et al., 2010; Conley et al., 2014, 2015). However, the disadvantages of the supine MRI acquisition might be circumvented, if a registration methodology was available, that transformed the prone MR image information to a target, that is more readily available than volumetric images.

Optical surface imaging techniques became widely popular in recent years. This non-invasive and – compared to MRI – relatively low cost and fast imaging modality could easily be used to image the patient in an upright or supine surgical pose. This could provide a valuable adjunct to pre-operative MRI, for surgical planning or guidance. Lago et al. (2012) presented a feasibility study by emulating time-of-flight depth data from volumetric supine scans and used this as target information for their prone-supine registration. Unfortunately a quantitative evaluation is missing from their work. Carter et al. (2008) also present an alignment methodology that incorporates an optically acquired supine target surface, however their method requires an intermediate volumetric supine MR image to compute the complete prone-supine deformation.

In this chapter an image-to-surface registration method which uses a biomechanical model, material parameter optimisation, and surface warping to transform prone MR image data to the supine and upright target surface is developed. The methodology was submitted for presentation at SPIE Medical Imaging 2016 (Eiben et al., 2016b).

5.1 SURFACE ALIGNMENT APPROACH

Similar to the integrative intensity based registration approach presented in section 4.2 the surface driven registration also first establishes global and thereafter local alignment. The components of this approach comprise

- biomechanical simulations including material parameter optimisation and global rigid alignment (see section 5.1.1),
- surface warping using a constrained deformation approach (see section 5.1.2), and
- propagation of the surface matching result to the biomechanical model (see section 5.1.3).

5.1.1 *Material Parameter Optimisation and Global Alignment*

One issue with the clinical applicability of patient specific biomechanical models is that the material parameters are not known and a wide range of elasticity measures has been reported in the literature (cf. section 2.3.1). Han et al. (2014),

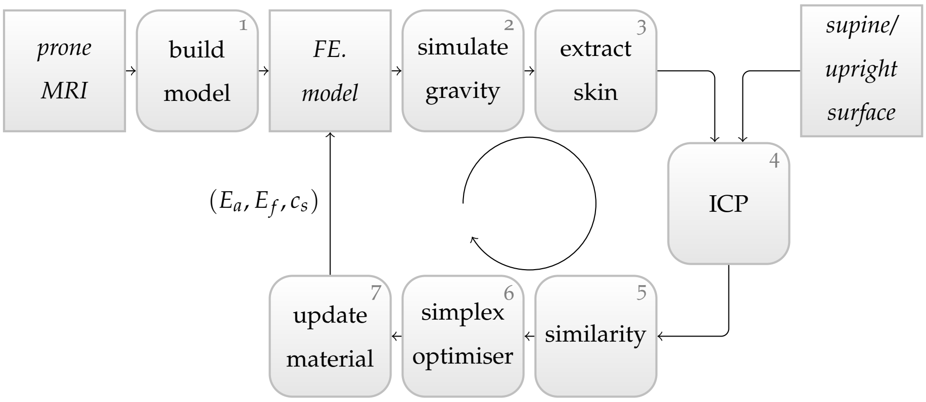

Figure 5.1: *Overview of the material parameter optimisation workflow that aligns the finite element biomechanical model with the upright or supine surface scan. The material parameters of the biomechanical model are optimised so that the rigid alignment of the surface scan and the simulated corresponding position show an improved match in terms of the similarity measure used.*

for instance, addressed this uncertainty in the context of intensity based prone-to-supine registration and proposed an optimisation of the material parameters of a patient specific biomechanical model. This resulted in an improved alignment of the combined transformation of a finite element simulation, an affine and a non-rigid B-spline registration. The Normalised Mutual Information (NMI) value achieved by the final registration was used as the objective measure for the optimisation process.

Since, for an image guided surgery application, volumetric supine target images are usually not available, here a surface match based material optimisation scheme which utilises a gradient free Nelder-Mead algorithm Nelder and Mead (1965) is proposed. Figure 5.1 shows an overview of the material optimisation workflow. Where appropriate, the numbers associated with each processing step (1)-(7) as shown in the figure are referred to in brackets in the text. The following sections describe the different elements in more detail. The final outputs are the optimised material parameters, as well as the homogeneous rigid matrix which is used to produce a transformed target surface mesh S'_{rigid}.

5.1.1.1 *Optimisation Arguments of the Biomechanical Simulation*

The prone MRI is the basis from which a patient specific biomechanical model is built (1). The resulting FE model is used to simulate the prone-to-upright or prone-to-supine position change for a particular patient (2). For a description of the generation process of the biomechanical model, the reader is referred to section 3.2.

The neo-Hookean constitutive relation used in the biomechanical model to simulate the behaviour of adipose and fibroglandular tissue is given by

$$\Psi = \frac{\mu}{2}\left(\hat{I}_{\hat{\mathbf{C}}} - 3\right) + \frac{\kappa}{2}\left(J-1\right)^2, \tag{5.1}$$

where J is the determinant of the deformation gradient, $\hat{I}_{\hat{\mathbf{C}}}$ is the first invariant of the deviatoric right Cauchy-Green tensor $\hat{\mathbf{C}}$ and κ and μ are the bulk and shear modulus respectively which can be expressed in terms of Young's modulus E and Poison's ratio ν:

$$\mu = \frac{E}{2(1+\nu)}, \qquad \kappa = \frac{E}{3(1-2\nu)}. \tag{5.2}$$

The Young's moduli E_a and E_f are optimised for adipose and fibroglandular tissue separately, whereas the Poisson's ratios are kept constant during the optimisation. The skin membrane elements are assigned with the exponential constitutive relation as proposed by Veronda and Westmann (1970)

$$\Psi_{\text{skin}} = \alpha_{\text{s}}\left(\mathrm{e}^{\beta_{\text{s}}(\tilde{I}_{\mathbf{C}}-3)} - 1\right) + c_{\text{s}}(\tilde{II}_{\mathbf{C}} - 3), \tag{5.3}$$

where $\tilde{I}_{\mathbf{C}}$ and $\tilde{II}_{\mathbf{C}}$ denote the first and second invariant of the two-dimensional Cauchy-Green strain tensor (2.19). c_s was chosen as the third free parameter in the optimisation procedure since it is associated with $\tilde{II}_{\mathbf{C}}$, which in turn can be interpreted as a measure for surface area change.

The biomechanical simulation (2) consists of two steps. In the first the effect of gravity is removed by estimating an unloaded configuration Vavourakis et al. (2015). In the second step gravity loading is simulated according to the configuration of the target surface, i.e. upright or supine.

5.1.1.2 *Surface Alignment and Objective Function*

In order to evaluate the similarity between the simulated loaded state and the 3D target surface, the skin surface of the biomechanical model is extracted (3) and aligned to the target. Rigid alignment is established using a standard iterative closest point (ICP) algorithm (4) as was originally proposed by Besl and McKay (1992). Since changes in the material parameters of the biomechanical model also cause changes in the shape of the simulated loaded configuration, the ICP alignment is repeated for each iteration of the optimisation.

The quality of the registration between the reloading simulation and the target surface of the actual gravity loaded patient position is evaluated with an objective function (5). For this purpose the mean Euclidean point-to-surface distance is used. Let $\mathbf{p}_{\text{sim}}(E_{\text{a}}, E_{\text{f}}, c_{\text{s}}) = \{\mathbf{p}_1, \mathbf{p}_2, \ldots, \mathbf{p}_N\}$ be the N points of the moving surface mesh, i.e. the extracted skin points of the biomechanical simulation whose positions depend on the current material parameters. Furthermore let S_{scan} be the target surface, for instance the reconstructed surface of the optical scanner, then the objective function m is given by the mean minimum distance $\mathbf{r}_i(\mathbf{p}_i, S_{\text{scan}})$ of each vertex point $\mathbf{p}_i$ to the surface S_{scan}

$$m = \begin{cases} \frac{1}{N}\sum_{i=1}^{N} |\mathbf{r}_i(\mathbf{p}_{\text{sim}}, S_{\text{scan}})| & \text{if simulation converged} \\ \infty & \text{otherwise.} \end{cases} \tag{5.4}$$

Furthermore information about the convergence of the biomechanical simulation is passed to the optimiser (6) by returning infinity, in cases where the simulation diverged and as a result no loading simulation could be obtained.

5.1.1.3 *Optimisation*

As can be seen from figure 5.1, the evaluation of the objective function (5) involves a series of computations, including two biomechanical simulations, and application of an iterative closest point algorithm. These steps in particular make the process computationally very expensive. Hence the choice of the optimiser (6) that determines the updated material parameters (7) ideally considers

1. a multi-dimensional parameter space,
2. absence of an analytical gradient of the objective function, while
3. requiring a low number of function evaluations.

These points are covered by the Nelder-Mead simplex optimisation algorithm (Nelder and Mead, 1965). The Nelder-Mead optimiser belongs to the group of direct search algorithms (Kolda et al., 2003), which generally do not require a gradient and are thus applicable to noisy data. Discontinuities in the objective function are also handled. The algorithm uses a geometric simplex, whose shape adapts locally to the objective function following heuristics specified in the original publication. This method is widely used because of its simplicity, the low number of function evaluations per iterations and generally a low number of overall iterations. However, this method also has disadvantages such as possible convergence to local minima (Dennis and Torczon, 1991; McKinnon, 1998).

Alternative direct search methods, particle swarm optimisation techniques (Kennedy and Eberhart, 1995), and stochastic methods such as simulated annealing Kirkpatrick et al. (1983) could be an alternative and will be investigated in future work. However such techniques usually require a larger number of function evaluations to converge to the global minimum.

5.1.2 *Surface Warping*

Optimised material parameters alone do not guarantee a sufficiently good alignment between the target surface and the corresponding surface of the gravity loading simulation. This is to some extent due to the MRI scanning and patient support equipment. Figure 5.2 shows an example of how deformations induced by the MR coil have an influence on the biomechanical model and simulation. Even breasts of carefully positioned patients can show severe skin surface indentations especially in the medial region around the sternum Yeh et al. (2014). The physically correct way to approach this deformation in a biomechanical simulation would be an additional surface force, which counteracts this indentation. However, the locally varying magnitude of this force is not known and thus is difficult to introduce into the simulation.

For practical application a simpler alternative is required. Thus correction of the residual misalignment of the loading simulation and the target surface is approached by imposing a displacement constraint on the skin nodes of the bio-

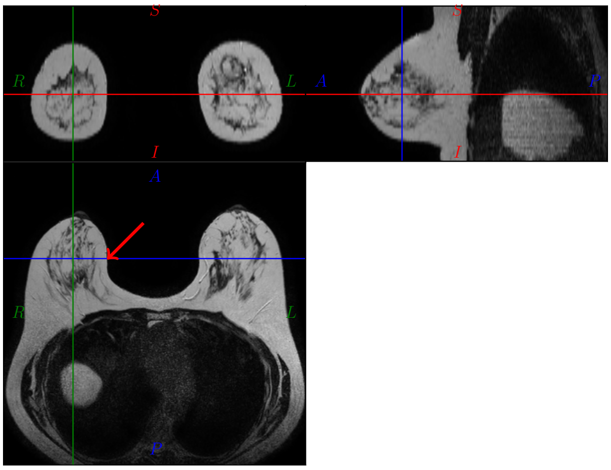

(a) *Orthogonal sections through the MR image.*

(b) *Simulated upright position.*

(c) *Upright surface scan.*

Figure 5.2: *MR image (a), biomechanical upright simulation (b) and scanned 3D surface (c) of the same patient. After the material parameter optimisation procedure the biomechanical model and the 3D target surface are reasonably well aligned. However, artefacts from the MR acquisition in the form of indentations into the simulated skin surface can clearly be observed (red arrows) when compared to the upright surface scan.*

mechanical model. As a result the simulated skin surface is forced to coincide with the skin target surface.

The simplest approach to calculate correction displacements for the biomechanical simulation would be to project the surface nodes from the biomechanical model onto the 3D target skin surface. This procedure however has several disadvantages (i) the projection could result in significant surface area changes and in extreme cases in collapsing elements (ii) the resulting surface elements could be of bad quality and (iii) the displacements are not necessarily smooth.

The components of the proposed surface warping technique are described in the following paragraphs and comprise a displacement calculation D, which drives the skin surface of the biomechanical model towards the target mesh, a Laplacian mesh smoothing step, L, which regularises the mesh, an area constraint, A, which reduces local changes in surface area and finally a self-intersection prevention, I, which avoids mesh intersections.

D: DISPLACEMENT Let $\mathbf{G}$ be the nodal connectivity matrix of the skin surface mesh, then a matrix with smoothing characteristics can be computed by calculating its m_{D}-th power. Furthermore let $\mathbf{r} = \{\mathbf{r}_1(\mathbf{p}_1^{\mathrm{A},n}, S'_{\mathrm{scan}}), \mathbf{r}_2(\mathbf{p}_2^{\mathrm{A},n}, S'_{\mathrm{scan}}), \ldots\}$ be the vector with the closest distances pointing from the current nodal positions $\mathbf{p}_i^{A,n}$ at iteration n to the surface S'_{scan}, then a smooth version of the displacements can be calculated according to $\mathbf{r}' = \mathbf{G}^{m_{\mathrm{D}}}\mathbf{r}$. These smooth displacements are used to update the nodal positions according to the following iterative scheme:

$$\mathbf{p}_i^{\mathrm{D},n} = \mathbf{p}_i^{\mathrm{A},n-1} + s_{\mathrm{D}}\mathbf{r}'_i. \tag{5.5}$$

Due to the smoothing matrix $\mathbf{G}^{m_{\mathrm{D}}}$, displacements smoothly vary between nodes across the mesh surface and thus a smooth deformation is achieved.

L: LAPLACIAN MESH SMOOTHING Mesh regularity often is a desired quality in biomechanical simulations. To control this during the course of the iterations, Laplacian Mesh Smoothing is used (see e.g. (Field, 1988) and references therein). This is particularly useful in cases where the simulated surface normal shows a large angle to the target surface. In such extreme cases the displacement step D could cause the moving elements to collapse. Hence let $w(\mathbf{p}_i^{\mathrm{D},n})$ be the set containing the indices of points connected to a surface mesh point $\mathbf{p}_i^{\mathrm{D},n}$ and $|w|$ the number neighbours, then the displaced node $\mathbf{p}_i^{\mathrm{L}}$ with mesh smoothing characteristics can be computed as

$$\mathbf{p}_i^{\mathrm{L},n} = (1 - s_{\mathrm{L}})\,\mathbf{p}_i^{\mathrm{D},n} + \frac{s_{\mathrm{L}}}{|w|}\sum_{j \in w} \mathbf{p}_j^{\mathrm{D},n} \tag{5.6}$$

This means, that each point aims to move towards the centre of the surrounding points. The scalar weight s_{L} which in all processed cases was selected to be $s_{\mathrm{L}} = 0.1$ controls the amount of smoothing.

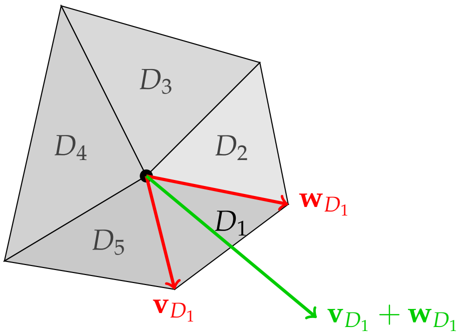

Figure 5.3: *Calculation of the area constraint.*

A: AREA CONSTRAINT Both previous mesh warping steps can introduce local changes to the surface area. In order to reduce the area change, an area correction vector is calculated for each node as follows. Let $D = \{D_1, \ldots, D_j\}$ be the triangular surface elements connected to the current node $\mathbf{p}_i^{\mathrm{L},n}$ as shown in figure 5.3. For each element a deviation from the original surface area A_{0,D_m} (i.e. the area of each triangle before the surface warping is initiated) can be calculated

$$q_{D_m} = \frac{\|\mathbf{v}_{D_m} \times \mathbf{w}_{D_m}\|}{2A_{0,D_m}} - 1. \tag{5.7}$$

Here the vectors $\mathbf{v}_{D_m}$ and $\mathbf{w}_{D_m}$ point from the current central node to the opposite nodes of the triangle D_m. The final correction vector is calculated as

$$\mathbf{p}_i^{\mathrm{A},n} = \mathbf{p}_i^{\mathrm{L},n} + \sum_{d \in D} q_t \frac{\mathbf{v}_t + \mathbf{w}_t}{\|\mathbf{v}_t + \mathbf{w}_t\|}. \tag{5.8}$$

I: INTERSECTION PREVENTION Updating the node positions can result in a self-intersecting mesh. This is most likely the case in the inframammary fold region when the upright position is used as a target configuration. Hence an intersection prevention process in incorporated by sensing possible surface contact in the direction of motion. If a self-intersection is detected, the corresponding node is kept fixed for the rest of the surface warping.

Figure 5.4 shows an example result of the surface warping methodology as described in this section. Note how the deformations that originate from contact of the patients' breast with the MRI coil are effectively reduced. The displacement vector field shows the largest displacement amplitude in the medial breast region. Hence, the corrected mesh represents the actual upright surface more precisely (compare figures 5.2c 5.4c).

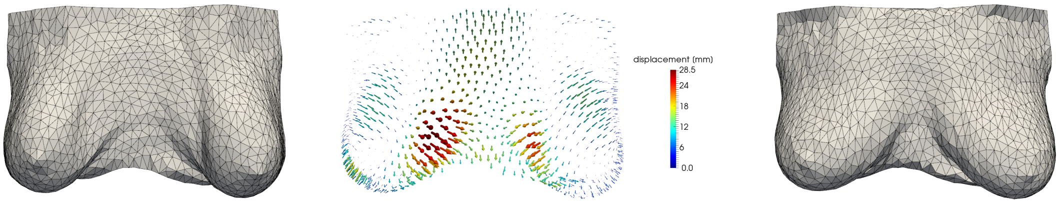

(a) *Model surface after material optimisation*

(b) *Deformation vectors*

(c) *Surface warping result*

Figure 5.4: *Surface warping example. (a) Shows the simulated upright surface after the material optimisation step (see section 5.1.1). The contact of the MRI breast coil propagates to the simulation result. To correct for this effect, a displacement vector field is calculated (b) as described in section 5.1.2. Application of the displacements to the simulated surface results in a corrected surface (c).*

5.1.3 *Volume Mesh Warping*

In a final step the surface displacements calculated in section 5.1.2 are used to update the volume mesh of the biomechanical model with the optimised material parameters obtained in section 5.1.1. While a similar idea was proposed by Ferrant et al. (2001) with an application in brain-shift deformation recovery, here gravity loading and nodal displacement conditions are considered simultaneously. To calculate the volumetric displacements, the last loading simulation from the material parameter optimisation is re-initiated. When the gravity loading is completed, the displacement boundary condition on the skin surface nodes is activated. This imposes the previously calculated surface displacements onto the biomechanical simulation.

The volumetric displacements are now completely defined and can be generated by composing the deformation vector fields of (i) the unloading, (ii) the reloading, and (iii) the prescribed displacement simulations. This allows image warping and landmark transformation from the prone into the loaded configuration to be performed.

5.2 CLINICAL IMAGE AND SURFACE DATA

The data used for the evaluation of the presented surface registration methodology was acquired in the context of the Picture project (c.f. section 3.1) and consisted of three pre-surgical prone MR images and corresponding post-surgical supine CT images. From the prone T_2-weighted MR images, which had a native resolution between $0.52 \times 0.52 \times 3.0\,\mathrm{mm}^3$ and $0.66 \times 0.66 \times 3.0\,\mathrm{mm}^3$, biomechanical models were generated as described in section 3.2. From the CT images, which had a native resolution of $1.07 \times 1.07 \times 3\,\mathrm{mm}^3$, the patient outline was segmented and a corresponding surface mesh was generated to provide the target for the surface registration procedure. For the first patient the method was furthermore evaluated by using a surface scan of the patient standing in the upright position that was captured using an optical surface acquisition system (*3dMD*).

For the evaluation of the alignment accuracy between the MR image and the CT surface corresponding landmarks were selected by a first and a control observer in the contralateral breast as described in section 4.2.9. It is important to note that the volumetric CT images were used only to allow the registration accuracy to be evaluated using internal anatomical structures. The registration algorithm however does neither require nor use volumetric images as target information.

5.3 SURFACE REGISTRATION RESULTS

The first step of the alignment procedure optimises the material parameters with the objective to find a better global match between the biomechanical simulation and the target surface. Figure 5.5 shows the graphs of the material parameters and the objective function during the course of the optimisation procedure. For all patients the Nelder-Mead algorithm reduces the value of the objective function, i.e. the mean distance between skin surface of the biomechanical model and the target CT surface (c.f. figures 5.5c, 5.5f, and 5.5i). The Young's moduli are shown in figures 5.5a, 5.5d, and 5.5g. Here the blue and the green curves represent the material stiffness of the adipose and fibroglandular tissue respectively. The skin parameter c_s is shown in figures 5.5b, 5.5e, and 5.5h. While the optimisation is initialised with a

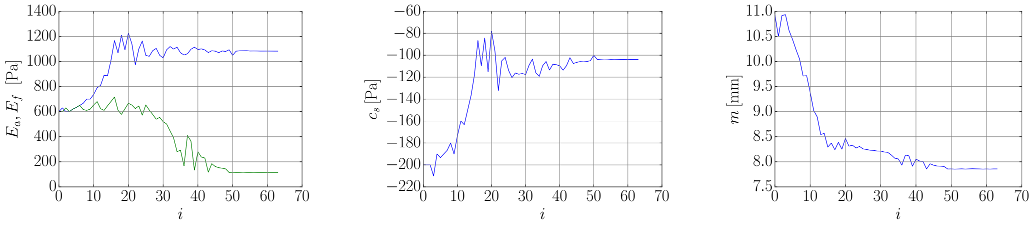

(a) *P1: parameters E_a and E_f* (b) *P1: parameter c_s.* (c) *P1: objective function m*

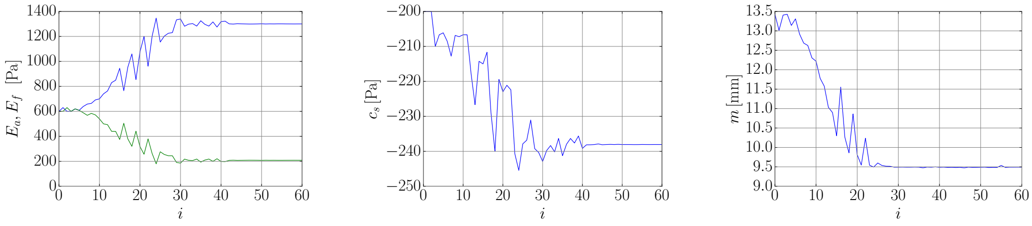

(d) *P2: parameters E_a and E_f* (e) *P2: parameter c_s.* (f) *P2: objective function m*

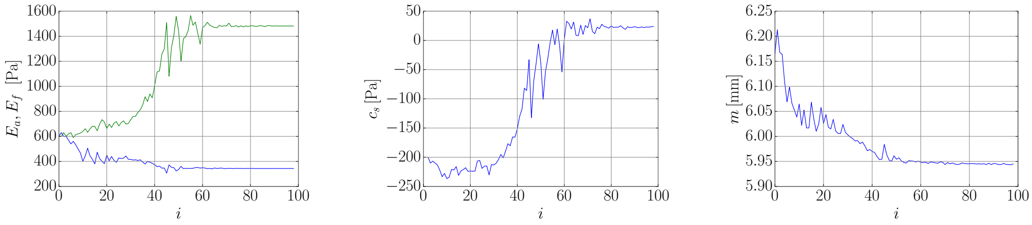

(g) *P3: parameters E_a and E_f* (h) *P3: parameter c_s.* (i) *P3: objective function m*

Figure 5.5: *Results of the material parameter optimisation step for patients $P1$ to $P3$ over the iterations i. In the left column the Young's modulus of the adipose tissue, E_a, is shown in blue, and the one of figbroglandular tissue, E_f, is shown in green. The central column shows the skin parameter c_s and the right column the objective function m according to equation* (5.4).

Table 5.1: *Inter-observer landmark distance (IOD) in terms of landmark distances. All distance values are given in mm, the total number of landmarks are in given in the columns N.*

	IOD all				IOD $d < 15\,\text{mm}$				IOD $d < 10\,\text{mm}$			
Pat.	mean	max	std	N_{all}	mean	max	std	N_{15}	mean	max	std	N_{10}
P1	16.7	41.4	12.8	15	8.2	14.0	5.0	9	3.2	8.1	2.9	4
P2	16.5	37.3	11.2	15	7.9	14.8	4.8	8	5.6	9.1	3.0	6
P3	12.8	52.2	12.8	12	7.5	14.1	3.6	10	5.4	7.7	1.8	7
P1-P3	15.3				7.9				4.7			

simulation using homogeneous material properties, all optimisation results end with a heterogeneous model. For the case $P3$ the optimisation produces a result according to stiffness relations reported in the literature, i.e. the adipose tissue is expected to show softer material behaviour when compared to fibroglandular tissue (c.f figure 5.5g). Cases $P1$ and $P2$ on the other hand show an inverted relation.

The skin parameter is initialised with the value that was originally proposed by Veronda and Westmann (1970), i.e. $c_s = -203.4$Pa. Here, too, the optimisation does not produce a coherent result for all three cases. For $P1$ the value is approximately halved to $c_s = -103.8$Pa, the one for $P2$ is found to produce best results for $c_s = -238.0$Pa. For $P3$ the optimised parameter is $c_s = 24.0$Pa, which nearly eliminates the influence of the second invariant from the strain energy density function.

The evaluation of the combined registration method between prone MRI and supine CT surface was carried out using manually selected internal landmarks. The inter-observer distance (IOD) between a first and a control observer was evaluated by measuring the landmark distance in the supine position for a common prone landmark. Table 5.1 shows the corresponding results. When all landmarks are considered, the overall mean IOD is 15.3mm varying between 13.0mm and 16.7mm. This value reduces to a mean value of 4.7mm varying between 3.2mm and 5.6mm when only those landmarks are included that are not further apart than 10 mm, and hence can be considered more reliable. See section 4.2.9 for a discussion of the 10 mm threshold to eliminate unreliable landmarks.

Table 5.2: *Target registration error before and after surface warping for the evaluated cases in terms of mean, maximum and standard deviation of the TRE (results given in* mm *). The upper part of the table presents the results before and the lower one those after applying the surface warping. The first set of columns reports results for all landmarks from the first and the control observer, whereas the second and third set of columns evaluates only those which were not more than* 15 mm *or* 10 mm *apart respectively.*

	before surface warping								
	TRE all			TRE IOD < 15mm			TRE IOD < 10mm		
Pat.	mean	max.	std.	mean	max.	std.	mean	max.	std.
P1	16.7	29.3	5.8	15.3	24.0	3.8	14.8	24.0	4.3
P2	23.1	54.0	9.1	19.1	24.4	4.4	19.1	24.4	4.3
P3	13.6	34.9	7.2	11.7	21.8	4.6	10.7	19.7	4.4
P1-P3	17.8			15.4			14.9		
	after surface warping								
P1	12.2	37.1	9.2	8.8	19.4	5.5	7.9	19.4	5.7
P2	16.0	48.2	8.6	11.9	17.7	3.3	12.0	15.4	2.7
P3	12.9	29.4	7.3	11.2	22.3	5.5	10.0	22.3	5.3
P1-P3	13.7			10.6			10.0		

Table 5.2 shows the TRE for the sets of landmarks evaluated for inter-observer variability before and after surface warping. Since the landmarks from both observers are equally valid, supine landmarks from both observers were used in order to calculate the TRE against the landmarks transformed from the prone position. This avoids a bias to one observer. Note however, that due to the triangular geometry of the target and source landmarks, according to the triangle inequality the final TRE cannot be below 1/2IOD. The overall mean TRE after the material parameter optimisation – but before the surface alignment – is for the 10 mm thresholded set of landmarks 14.9 mm. This value is reduced to 10.1 mm when the surface alignment is applied to the biomechanical model.

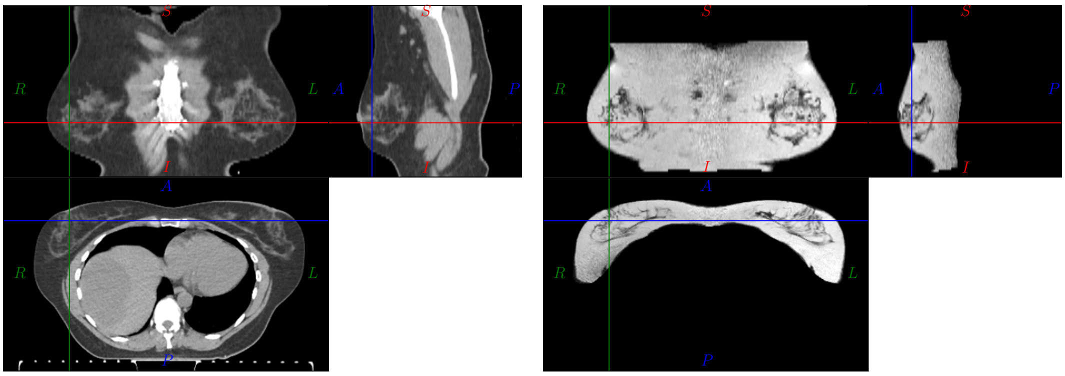

(a) *P1: CT target* (b) *P1: MRI image warped to supine.*

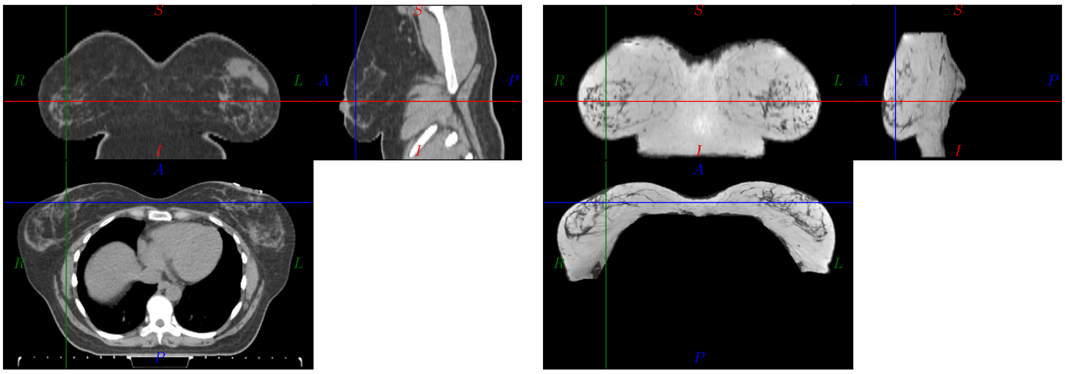

(c) *P2: CT target* (d) *P2: MRI image warped to supine.*

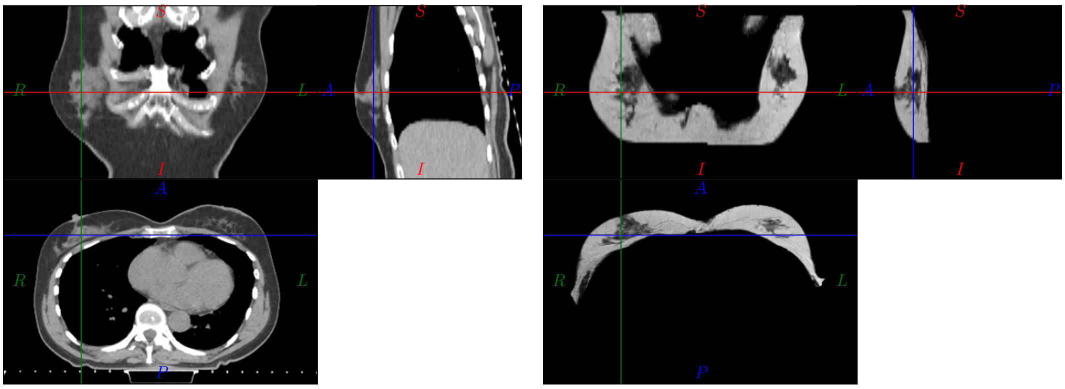

(e) *P3: CT target* (f) *P3: MRI image warped to supine.*

Figure 5.6: *Pure surface driven registration result for all data sets. Breast conserving surgery was carried out on the left breast (right side on the image above) which causes morphological changes to the breast tissue between the MRI and the CT acquisition.*

Figure 5.6 shows the original supine CT image together with the MR image that was warped according to the surface registration result. Note that breast conserving surgery for all three cases was carried out on the left breast (right hand side in the images). While the skin surfaces match is due to the design of the algorithm, it is noteworthy that the retro-mammary boundary also aligns well. Visual comparison suggests also a good alignment of internal structures. However, the anterior-posterior extent of identically appearing structures in both images appear to be smaller for the simulated supine images. This is potentially due to the fixed boundary condition of the biomechanical model used in the retro-mammary region.

The proposed method was also used to register the MR image of P1 with the corresponding surface scan which was acquired with the patient standing in the upright position. Since the common identifiable features in the surface mesh and the MRI are the nipple position only, the evaluation was carried out on this landmark. Figure 5.7 shows the registration result in terms of a volume rendering of the MRI combined with the textured 3D surface mesh (figures 5.7a through to~\ref{subfig:UprightMRIAndSurface}). Figure 5.7e visualises the nipple locations identified in the transformed MRI as green spheres, whereas the nipple locations on the skin surface are identified by cross-hairs projected onto the skin surface. The measured Euclidean distances for the left and right nipple are 10.1 mm and 6.3 mm respectively. Interestingly the nipple position predicted by the biomechanical model is for both breasts too far medial when compared to the target position. This could indicate residual effects of the original medial contact between the breast and the MR coil.

5.4 CLINICAL APPLICATIONS

The main clinical applications for the surface driven registration methodology are surgical planning and guidance, as well as visualisation of cosmetic outcome prediction simulations in a photo-realistic way.

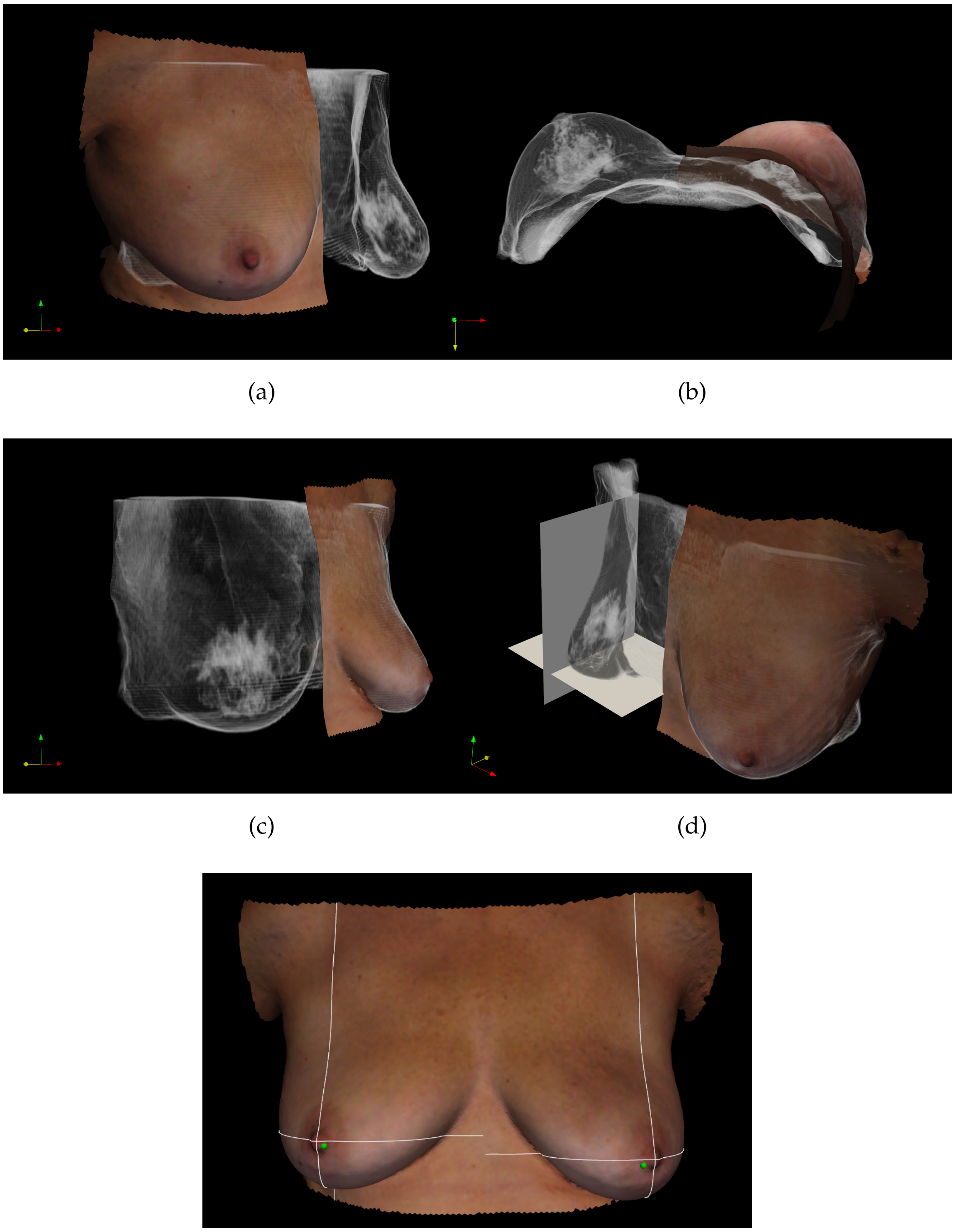

(a) (b)

(c) (d)

(e) *Nipple location comparison*

Figure 5.7: *Result of the surface driven registration approach that aligns a prone MRI to an upright optical 3D surface scan of the same patient. A volume rendering of the transformed MR image and the target surface is shown in figures (a)-(d). Figure (e) shows the nipple location identified in the warped MRI as green spheres and those in the surface scan as cross-hairs.*

5.4.1 *Surgical Planning and Image Guided Surgery*

The alignment of volumetric clinical images with surface data could be used to visualise the extent and location of a cancerous lesion in a patient position different to the original imaging acquisition position. This information might be useful during surgery to achieve cancer free margins, which are a strong predictor for local recurrence (Park et al., 2000). When a lumpectomy specimen shows positive margins in histopathological examination re-excision is required. Waljee et al. (2008) report re-excision rates as high as 60%. An image guided breast surgery system would visualise the lesion so that the surgeon can draw conclusions about the cancer site, and plan the surgical excision trajectory accordingly, especially in cases, where the lesions are not palpable. Figure 5.7a shows the combination of surface images with deformed volumetric MR image data. Although for this visualisation a structural fat-suppressed T2 weighted MR sequence was used, it is easy to exchange this information extracted from contrast enhanced subtraction images. However, for clinical applicability an appropriate visualisation method would need to be investigated in future research.

The registration method presented in this chapter differentiates itself from existing methods that propose image guidance for breast conserving surgery – or significant steps towards this goal – by using only a standard prone MR image and an additional surface scan. Carter et al. (2008) presented a workflow that makes use of an additional supine MR image, that acts as an intermediate modality to which the prone image is registered. In a second step the transformed prone image is then aligned with surface data provided by an optical scanner. Similarly Conley et al. (2014, 2015) also presented an approach that relies on the availability of supine MR images and additional inter-operative US images. They report an overall registration accuracy around 5mm. Since the deformation between the supine imaging position and the supine surgical position is much smaller when compared to the prone-supine deformation this also results in smaller overall alignment errors. Currently it appears that a compromise must be made between additional pre-surgical data acquisition and potential registration accuracy.

5.4.2 *Aesthetic Outcome Prediction of Breast Conserving Surgery*

In the PICTURE project, a mechano-biological simulation framework was established, that allows patient specific surgical simulations to be carried out. In this regard a surgical plan is captured for each patient which records the excised volume, the incision, the mobilisation, and if applicable the direction in which the cavity was closed. This information is post-processed and used as an input into the post-surgical simulation. This simulation predicts the tissue response during the healing process of the wounded breast region by combining mechanical and bio-chemical processes in a multi-scale model. As a result, volumetric displacements occur; an effect observed in patients that might – in extreme cases – lead to disfigurements of the operated breast.

The alignment of the biomechanical model and the surface scan can facilitate a photo-realistic visualisation of the predicted aesthetic outcome of surgery – compensating for any artefacts that are present in the MR-based biomechanical model (c.f. figure 5.2). This visualisation requires two steps to be completed (1) the texturing of the skin surface of the biomechanical model and (2) the projection of the predicted deformation of the mechano-biological simulation onto the aligned surface. Both steps are outlined briefly below.

TEXTURE TRANSFER AND SCAR PREDICTION In order to visualise texture on a meshed geometry, different approaches can be followed. The standard method in computer graphics is the so called *uv*-texture mapping and is presented in most standard text books of this topic, e.g. Foley et al. (1990). With this method each vertex of a mesh is assigned with a two-dimensional *uv*-coordinate. This coordinate defines the corresponding location in a texture image that is then virtually wrapped around the mesh. This method has the advantage, that a high resolution texture can be visualised on a low resolution mesh while providing the illusion of a photo-realistic three-dimensional object. However, in order to transfer the texture of the optical surface scan to the skin surface of the aligned biomechanical model, two prerequisites would need to be fulfilled. First, the texture mapping between both meshes, i.e. surface scan and model, would need to be assigned with unambiguous texture coordinates representing corresponding texture positions. This is the task of so called unwrapping algorithms. In initial experiments simple plane, cylindrical or spherical unwrapping methods were not able to generate unambiguous coordinates on the upright skin surface which resulted in stretching, repetition and discontinuities of the transferred texture. The second prerequisite is the existence of a texture image. This would need to be generated from the optically acquired surface mesh, where each vertex holds an RGB colour value. Such an image could be generated using scattered data interpolated for instance, but in essence this would require several additional processing steps.

As a result, a simpler approach is followed here, where the extracted skin surface of the biomechanical model is first subdivided using the method proposed by Loop (1987). Subsequently the RGB colour value of the closest vertex of the optical surface scan is assigned. Figure 5.8a shows an example result of this method. The high-resolution, coloured skin surface is shown here, as well as the surface of the updated biomechanical model as a black wire-frame.

The surgical plan also contains information about the skin incision in the form of points of a poly-line. This can be used to visualise the scar location. The different steps are visualised in figure 5.9 and again a pragmatic approach is followed, which first assigns a local coordinate system to each line element of the poly line (c.f. figure 5.9a). These local coordinates are used to apply a differential change to the hue, saturation, and brightness values of the transferred skin texture. These changes are pre-calculated from a template scar image as is shown in figure 5.9b. Figure 5.9c and 5.9d shows the skin texture before and after application of the scar visualisation respectively. In cases where the incision line consists of more than one line segment, the process is repeated, until all line segments are processed.

DEFORMATION PROJECTION As a last step the deformation of the mechano-biological simulation (Vavourakis et al., 2016) is projected to the updated and textured biomechanical model. Figure 5.8 shows the combined result of displacement projection, texture transfer and scar visualisation.

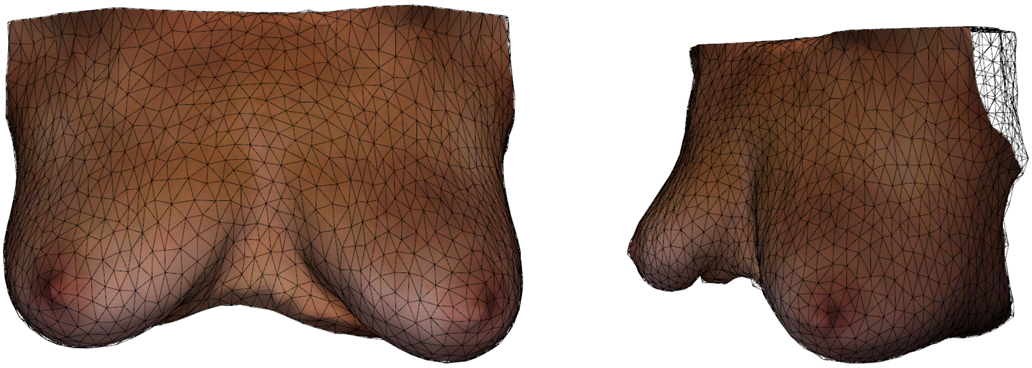

(a) *before surgery*

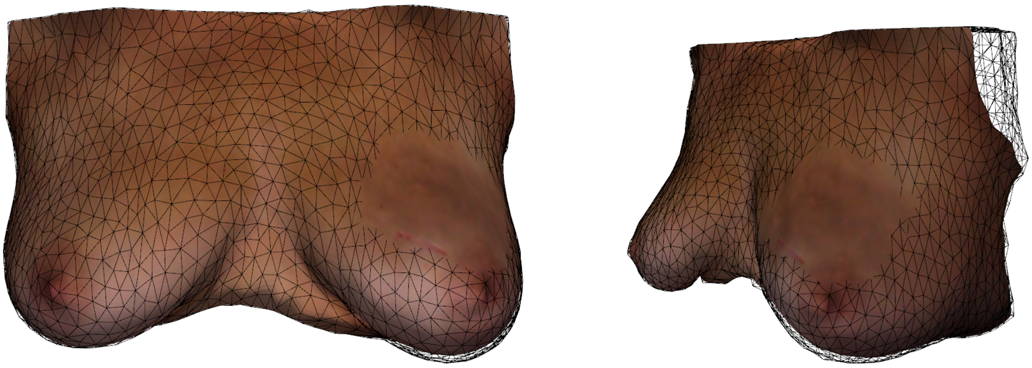

(b) *3 months after surgery*

Figure 5.8: *Frontal and oblique view of the textured surface mesh before (a) and after surgery (b). The breast model deformation is calculated by the biomechanical wound healing simulation (Vavourakis et al., 2016) and thereafter projected onto the transformed biomechanical model of the patient's chest in the upright position. The black wireframe shows the biomechanical model before application of the wound healing displacements (c.f. 5.4c). Where the mesh is in front of or lying on the textured surface it is visible, if behind it is invisible.*

The visual representation of the simulation could be used to aid the communication between surgeon and patient in order to explain the process and potential outcome of a breast conserving surgery treatment. Furthermore, subjective aesthetic assessment by an expert or quantitative aesthetic evaluation could be carried out based on the photo-realistic prediction of breast conserving treatment (Cardoso et al., 2007).

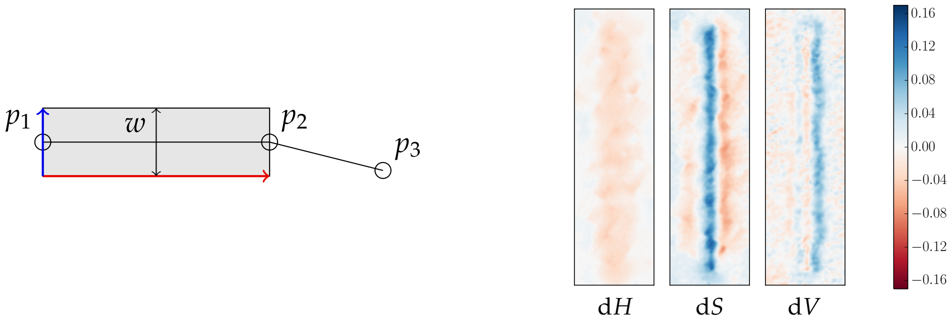

(a) *Local coordinate system defined by the incision points* p_1 *and* p_2 *and the scar width* w.

(b) *Template image with the components hue* $\mathrm{d}H$, *saturation* $\mathrm{d}S$, *and brightness* $\mathrm{d}V$.

(c) *Texture transferred to the biomechanical model.*

(d) *Texture with visualised scar.*

Figure 5.9: *Steps of the scar visualisation procedure. A local coordinate system is used for each element of the reported incision poly-line (a) to apply local colour changes to the surface (b). The skin texture (c) then shows a scar visualisation, that could occur as a result to the incision (d).*

5.5 CHAPTER CONCLUSIONS

Prone-to-supine registration with a future application in image guided surgery faces the challenge, that the target information most likely is not a three-dimensionally resolved image, but an optical surface scan. Hence algorithms are required, which enable the deformation of prone MR images into the supine position using target surface information only.

In this chapter a registration scheme was presented which overcomes two main challenges when biomechanical models are used to simulate the large deformation from prone to supine or from prone to upright. These challenges are (i) the unknown material parameters as well as (ii) additional deformations introduced by the MRI scanning equipment in the prone position. This is achieved by a material optimisation procedure followed by a surface warping step which corrects residual geometric differences between the biomechanical simulation and the target surface.

The material parameter optimisation was able to obtain a closer match between the target surface and the corresponding skin surface of the biomechanical simulation. As expected, the distance could not be removed completely and can be attributed to shortcomings of the biomechanical model, as well as to the contact of the breast with the scanner coil, which distorts the breast shape on which the prone model is based. It is certain that the distortion of the breast shape in the prone position has an effect on the optimisation result, a quantification of that influence however is difficult to establish.

The simplicity of the Nelder-Mead optimisation algorithm was the main motivation for its adoption in this study. However, in future work more sophisticated algorithms could be investigated to incorporate prior knowledge about the ratio of tissue stiffness parameters in terms of additional constraints. Han et al. (2014) for example constrained the ratio between the Young's moduli of fibroglandular and adipose tissues to be greater or equal to one. As a result, an item "ability to handle constraints" could be added to the list of characteristics required from an optimisation procedure that was provided in section 5.1.1.3. However, since the original shape is compromised by the contact of the breast with the MR scanner, potentially simpler approaches that, for example, use a fixed stiffness ratio between adipose and fibroglandular tissue might prove to be sufficient.

The general registration approach, which first optimises the material parameters and then corrects the distortion of the model is a chicken-and-egg problem. Ideally the distortions would be corrected first and only thereafter the material parameters would be optimised. However, it is not possible a-priori to determine which contribution to the misalignment results from incorrect material properties and which is due to the scanner coil contact.

Since the surface alignment strategy presented in this chapter is modular, each component can be improved separately in future work. One aspect currently not covered is for example the initialisation of the global ICP registration step. For any clinical application robustness is a strong prerequisite and clearly, if the rigid alignment fails, this has a knock-on effect on the subsequent processing steps. Initialisation incorporating information about the nipple position could be a viable approach. This would require the detection of the nipple position in the surface data and the volumetric image. Furthermore, if the nipple position was readily available, it could also be used as an additional constraint in the surface warping method.

Despite the challenges still to be addressed with the surface driven registration, the benefits of the approach are twofold. Regarding clinical application, the prone-supine registration could be utilised for surgical planning and initial guidance, since the lesion extent and margin visualisation becomes possible in multiple poses, namely supine, prone and upright. From the biomechanical modelling perspective the information obtained from the material optimisation and surface warping could be utilised in a feedback step to improve the biomechanical model geometry by removing the MRI coil deformation artefacts which then leads to an updated estimation of the unloaded configuration.

6

CONCLUSION

Combining images for detecting and diagnosing breast cancer and using images to better guide interventions, therapies and surgery relies on establishing accurate spatial correspondence between images and between an image and the surgical or interventional scene. The breast undergoes significant deformation when the patient position is changed between imaging procedures and during interventions. Conventional image registration driven by image metrics have been shown to be inadequate and so biomechanical modelling of breast tissue deformation is playing a more and more important role. In the current clinical workflow different positions and corresponding gravitational loadings are selected, either to optimise image acquisition (i.e. prone DCE-MRI), improve patient stability and comfort (i.e. supine radiotherapy treatment), or account for practical circumstances (i.e. supine surgical position). Biomechanical modelling can be employed for simulation of large breast deformation, and thus may allow information to be transformed from one configuration to another. This in turn could have implications for the clinical breast cancer treatment workflow.

Biomechanical models are able to predict the deformation of the breast between different gravity loading configurations by using the principles of continuum mechanics in combination with patient-specific models. However, the accuracy of the predicted deformation is compromised by several assumptions. While it is common practice to account for the breast tissue's heterogeneity in terms of adipose, fibroglandular and skin tissue, further differentiation of the anatomy – for instance identification of Cooper's ligaments or separation into stromal and ductal tissue – does not appear feasible using current clinical imaging modalities. Furthermore, since a large variation of tissue stiffness is reported in the literature, the parameters of a selected constitutive relation are subject to variation. Attachment of the breast to the chest wall poses another uncertainty. While the anatomy suggests that a certain degree of mobility of the breast on the chest is possible, an established and validated approach on how to translate this into appropriate boundary conditions for the retromammary area is lacking. Beyond the uncertainties with respect to the material description and boundary conditions, further image acquisition related complications may arise. This was especially pronounced in the case of prone MR imaging, where clear contact of the breast with the scanner coil can result in significant deformations to the breast. This makes the assumption that the breast is only subject to gravity invalid.

Considering all these limitations related to biomechanical modelling, accurate simulations of large breast tissue deformations that are based on standard clinical images are extremely hard, if not impossible, to achieve. As a result, this thesis explored strategies on how to make best use of both, modelling and image derived information. By this combined approach it becomes possible to take into account target information such as image intensities that is not usually considered by simulation-only approaches and thus improve the alignment quality without contravening the physical laws of tissue deformation. Two distinct approaches were followed:

1. A biomechanically constrained, intensity driven image registration, and
2. a combination of a biomechanical simulation and surface driven correction.

A precursor to the development of the registration methods was an evaluation of biomechanical simulations in chapter 3, which explored the effect of gravity loading and related unloading strategies. The results of the phantom experiment revealed that not considering the pre-stressed nature of the breast in a gravity loaded configuration leads to significant errors (c.f. figures 3.12 and 3.13 on pages 82 and 85 respectively). Furthermore the magnitude of the errors is dependent on the original loading configuration. In this experiment unloading the upright configuration produced the biggest error, when the pre-stresses were ignored and simply the direction of gravity was reversed. Hence, in the following developments the physically correct consideration of gravity loading was considered.

The intensity based, symmetric biomechanically constrained registration methodology that was presented in chapter 4 aimed to provide a coherent prone-to-supine registration framework which considers most of the limitations originating from the pure biomechanical simulation. It considers gravity loading in the images, optimises the material parameters, allows the breast tissue to move along the chest wall, and corrects for residual misalignment by integrating image forces while constraining the overall deformation utilising a neo-Hookean material description.

Removing the effect of gravity has the largest influence on the target registration error which is reduced from a mean TRE of 69.7 mm to 14.1 mm, but only the final intensity driven accumulation of image derived forces can reduce the error further to 5.6 mm. Furthermore, permitting motion of the breast tissue along the chest wall appeared to be an important component. This is clearly illustrated by case P10* that is shown in figures 4.35 (a) and (b) on page 156.

The symmetric registration set-up generates a virtually gravity free configuration of the breast from which any other loading configuration could be simulated. The full transformation from prone to supine can be generated by appropriate composition of the displacement vector fields.

Regarding the clinical applicability, the intensity based registration method is confined to cases where a prone-supine image pair exists. Assuming that no additional supine MRI was acquired, in the current clinical workflow a prone-supine image pair is available where a prone MR image is acquired pre-operatively and a supine CT post operatively to plan radiotherapy. Localised dose delivery calculations are required for radiotherapy, if an additional radiation boost to the tumour bed is given or partial breast irradiation techniques are applied. The registered pre-surgical images could be used to determine, at the very least approximate, the location and extent of the original tumour bed.

As a consequence of the limited availability of prone-supine image pairs, an alternative registration strategy was developed in chapter 5 that only uses surfaces as target information to align a biomechanical model to. This could potentially extend the clinical applicability to surgical planning and image guided surgical procedures, since, as opposed to supine MRI or CT images, optical surfaces can be acquired fast and with relatively low additional cost.

The surface alignment strategy first performs a global material parameter optimisation and rigidly aligns the simulated supine or upright target position to the corresponding target surface. Thereafter, the model is warped, so that it aligns with the target surface. The surface warping is constrained by an area preserving and smoothness term and the resulting surface displacements are then applied to the biomechanical model to correct for residual misalignment.

The results for the first three patients are promising with a final mean TRE of 10 mm, using the same evaluation strategy as for the intensity based registration. This is not as low as the TRE achieved by the intensity based registration presented in chapter 4, but can be attributed to the aspect that volumetric images used for the intensity driven registration contain more information and drive the alignment throughout the breast volume. This does not apply to the surface registration method.

Summarising the above: Two biomechanically guided registration schemes were developed in this thesis to align breast shapes of the same patient but in different positions between which the breast tissue deforms significantly. In addition to biomechanical prior knowledge to predict soft tissue deformations under different gravity loading conditions, target information was integrated to correct final misalignment. The first registration scheme utilised internal structures (chapter 4) and the second used an external surface to drive the alignment (chapter 5). Both methods were shown to achieve a good final alignment for this challenging registration problem and thus could find an application in the clinical workflow.

6.1 LIMITATIONS

Like any other method, the developed registration methods and the underlying biomechanical models also have their limitations.

The main technical limitations of the intensity driven prone-to-supine registration methodology as presented in this thesis are as follows. Using a mono-modal image similarity measure requires the input images either to originate from the same imaging modality, or, as was done in this thesis for the MRI-CT image pairs, a modification of the image intensities from one modality so that these appear equal to those in the other. The computational complexity of the registration method is also high. This could cause difficulties if registrations are to be performed in a time-constrained clinical context.

However, beyond those technical limitations, which are expected to be straight forward to address, the conceptual limitations are more challenging. One major application for the intensity based prone-supine registration identified in section 4.3 was the use of pre-surgical prone DCE-MR images as an adjunct to post-surgical radiotherapy planning scans to facilitate more precise tumour bed delineation and thus more accurate radiation dose delivery. While the prone-supine position change indeed causes the breast to deform significantly, clearly it is not the only change of the breast between pre- and post-surgical imaging. Tissue was removed, the surgical cavity was closed with internal stitches and sutures, wound seroma might have built up and the biological healing process has started. None of these aspects are currently considered in the presented registration.

A technical limitation of the surface registration is the consideration of the breast to be fixed to the chest wall by using a zero-displacement boundary condition during the biomechanical simulations. This is discordant with previous observations. Furthermore, the optimisation strategy that was used to optimise the material parameters does not allow to constrain the ratio of fat and fibroglandular stiffness parameters to a predefined range. This can lead to unrealistic results. Beyond this, a robust initialisation of the Iterative Closest Point registration is essential if this method was to be used in an image guided surgical setting.

A challenging conceptual limitation of the surface registration is inherent to the sequential approach, which first optimises the material parameters and thereafter performs the surface and volume warping. Since the breast is deformed by the MR coil, the optimisation result is influenced by this effect. Depending on the magnitude of contact induced deformations, the optimisation results could vary significantly from the real tissue properties and hence might not be suitable to be used in subsequent simulations. Furthermore, the application of this registration methodology for image guided surgery is limited to pre-incision guidance towards the tumour location. Tissue incision and excision is not considered at the current stage.

Both biomechanically informed registration methods use a simplistic material description that does not account for tissue anisotropies. More sophisticated material models might be required. Beyond the material description, the current registration frameworks are limited to cases where the direction of gravity is the primary cause for deformation. However, in different medical applications large organ deformations also occur, for instance, due to surface pressure caused by insufflation during laporascopic abdominal surgery. Hence, a wider applicability of the methods requires investigation and implementation of appropriate boundary as well as loading conditions.

6.2 FUTURE WORK

When considering viable paths for future work based on the developments in this thesis, incremental improvements could be suggested for each component. For the biomechnanically guide, intensity driven registration this could be

- improvement of the computational efficiency, since parallelisation is due to the nature of the selected numerical method possible, or
- implementation of multi-modal image forces, since these are utilised in standard intensity based registration methods, or
- translation of the method into the finite element world, since this method is known to deal better with complex geometries such as the breast.

The same is true for the biomechanically guided, surface driven alignment strategy, where improvements could comprise

- change of the material optimisation strategy to a more robust optimiser that allows constrained optimisation, or
- revising the surface warping strategy to constrain its deformation based on a physical model, for instance this of an elastic membrane.

These are undoubtedly worthwhile refinements, however, another approach would be to complement the volumetric and surface methods by feeding information from one to the other. For instance in the surface based registration method the zero-displacement boundary condition fixed the breast to the chest wall which appeared to be a limiting factor to the registration accuracy. The intensity based method on the other hand allowed a controlled motion along the chest wall and produced reasonable displacements in this area. Hence, if the volumetric registration was performed for a large number of cases, the displacements along the chest wall could be used to build a motion model, that, when projected on a reasonably low-dimensional space, could be optimised along with the material parameters.

6.2.1 *Exploring Modelling of Tissue Loss*

Technical improvements should furthermore be aligned with and motivated by clinical applications. To achieve this, the conceptual limitations outlined in section 6.1 need to be addressed. The most promising application for the intensity driven prone-supine registration was identified to be in radiotherapy planning.

However, the registration between pre- and post-surgical images of the operated breast does not only pose the challenge of differing patient positions and corresponding shape changes of the breast. During lumpectomy the cancerous tissue and a margin of healthy breast tissue is removed. The surgeon aims to excise a cylindrically shaped lump of tissue which axis is perpendicular to the pectoralis muscle surface and the cylinder axis extents from the pectoralis muscle to the skin. To approach the excision target region, tissue potentially needs to be mobilised by separating breast tissue from the skin and/or from the pectoralis. After excision, depending on the size of the removed the lump, the cavity might be closed by stitching tissue flaps together to prevent cosmetic defects during the healing process. Reconstructive, oncoplastic surgeries involve even more complicated procedures with respect to how tissues are reconfigured in order to remodel the breast shape.

After surgery, healing of the wounded breast region initiates complex, interrelated mechano-biochemical processes. The wounded region inflames, stiffens and contracts.

Addressing all these changes to the breast morphology from a simulation perspective requires consideration of several aspects. First, the surgical intervention separates, removes, and reconfigures internal and skin tissues. Model geometries need to be redefined accordingly to account for removed and separated tissue regions. Second, closing the surgical cavity by stitching could, for instance, be simulated by forcing faces of the rebuilt model geometry together at appropriate locations. This process will require consideration of tissue-tissues contact. Third, biomechanical simulations of internal stitching will induce pre-stressed in the breast which in turn will have an effect on the mechanical behaviour of the breast under different gravity loading conditions. To achieve all this within a reasonable amount of accuracy, a detailed three dimensional surgical plan is a strict requirement.

It would be interesting to explore how such complex biomechanical simulations could be introduced into a registration framework, and to which extent complex simulations could be simplified to approach a system that is robust and easy enough to be handled in a clinical environment.

6.2.2 *Exploring Translation to Clinical Practice*

With respect to the presented surface alignment methodology, surgical guidance would be a prominent clinical application. But in order to introduce such a system into clinical practice several requirements need to be taken care of which are outline as follows.

Improving the registration accuracy itself is one of many aspects that needs to be covered if this method is going to be used in clinical practice. Before considering a guidance system on real patients, first and foremost more cases need to be processed in order to test and improve on the robustness of the proposed method. Biomechanical simulations can sometimes lead to diverging results. For such cases contingency strategies need to be implemented. At the same time the accuracy of the predicted tumour location in the surgical position must be evaluated. While the supine radiotherapy position is similar to the surgical setting, differences still exists especially in terms of the arm position. Tracked ultrasound imaging might be a viable option to quantify the discrepancy between the simulated and the real tumour location and extent in the actual surgical position. Differing arm positions induce shape changes to the pectoralis muscle, which might be necessary to consider explicitly in the biomechanical model. This would be a departure from the fixed boundary condition currently used and identified as a limitation of the method.

Once the accuracy of the supine simulation has been validated, another practical, but important aspect has to be taken into account: visualisation. How is the information about the simulated location and extent of the tumour best presented to the surgeon? Approaches can range from displaying the lesion together with the breast surface on a separate monitor to a full augmented reality environment.

All the technical aspects of course have to be in line with legal requirements such as Ethics Committee and Research and Development (R&D) approvals. It has to be ensured that the patient's safety and clinical outcome is not negatively impacted. The development of a medical device would furthermore have to comply with quality management and assurance system specified by the International Organization for Standardization (ISO), Geneva, Switzerland (2003) (ISO 13485:2003).

Intuitive visualisation, robust performance, and simple usability are just some examples a surgeon might require from an assistance system. However, given the crude methods currently employed to localise lesions prior to excision (i.e. palpation, wire guidance, or manual measurements performed on the skin surface) a patient benefit may be possible to demonstrate.

Ultimately, our research should contribute to a benefit for the patient.

A

LIST OF PUBLICATIONS

Parts of the work described in this thesis were published in and contributed to the following publications:

2013

- Eiben et al. (2013)

  Eiben, B., Han, L., Hipwell, J. H., Mertzanidou, T., Kabus, S., Buelow, T., Lorenz, C., Newstead, G. M., Abe, H., Keshtgar, M., Ourselin, S., and Hawkes, D. J. "Biomechanically guided prone-to-supine image registration of breast MRI using an estimated reference state." In: "EEE 10th International Symposium on Biomedical Imaging (ISBI)," pp. 214–217 (2013). doi:10.1109/ISBI.2013.6556450.

- Tan et al. (2013)

  Tan, T., **Eiben, B.**, Platel, B., Zelst, J., Han, L., Mertzanidou, T., Johnsen, S., Hipwell, J., Mann, R., Hawkes, D., and Karssemeijer, N. "Registration of automated 3d breast ultrasound views." In: Martel, A., Hipwell, J., Schnabel, J., Nielsen, M., Nash, M., Kontos, D., and Karssemeijer, N. (editors), "MICCAI Workshop: Breast Image Analysis," (2013).

2014

- Eiben et al. (2014)

  Eiben, B., Vavourakis, V., Hipwell, J. H., Kabus, S., Lorenz, C., Buelow, T., and Hawkes, D. J. "Breast deformation modelling: comparison of methods to obtain a patient specific unloaded configuration." In: Yaniv, Z. R. and Holmes, D. R. (editors), "Medical Imaging 2014: Image-Guided Procedures, Robotic Interventions, and Modeling," volume 9036 of *SPIE Proceedings*, pp. 903615–903615–8 (2014). doi:10.1117/12.2043607.

- Johnsen et al. (2014)

  Johnsen, S., Taylor, Z., Clarkson, M., Hipwell, J., Modat, M., **Eiben, B.**, Han, L., Hu, Y., Mertzanidou, T., Hawkes, D., and Ourselin, S. "Niftysim: A GPU-based nonlinear finite element package for simulation of soft tissue biomechanics." *International Journal of Computer Assisted Radiology and Surgery*, 10(7):pp. 1077–1095 (2014). doi:10.1007/s11548-014-1118-5.

- Han et al. (2014)

  Han, L., Hipwell, J. H., **Eiben, B.**, Barratt, D., Modat, M., Ourselin, S., and Hawkes, D. J. "A nonlinear biomechanical model based registration method for aligning prone and supine MR breast images." *IEEE Transactions on Medical Imaging*, 33(3):pp. 682–694 (2014). doi:10.1109/TMI.2013.2294539.

- Mertzanidou et al. (2014)

  Mertzanidou, T., Hipwell, J., Johnsen, S., Han, L., **Eiben, B.**, Taylor, Z., Ourselin, S., Huisman, H., Mann, R., Bick, U., Karssemeijer, N., and Hawkes, D. "MRI to X-ray mammography intensity-based registration with simultaneous optimisation of pose and biomechanical transformation parameters." *Medical Image Analysis*, 18(4):pp. 674–683 (2014). doi:10.1016/j.media.2014.03.003.

2015

- Morin et al. (2015)

  Morin, R., **Eiben, B.**, Bidaut, L., Hipwell, J. H., Evans, A., and Hawkes, D. J. "3D ultrasound simulation based on a biomechanical model of prone MRI in breast cancer imaging." In: "IEEE 12th International Symposium on Biomedical Imaging (ISBI)," pp. 264–267 (2015). doi:10.1109/ISBI.2015.7163864.

2016

- Hipwell et al. (2016)

  Hipwell, J. H., Vavourakis, V., Han, L., Mertzanidou, T., **Eiben, B.**, and Hawkes, D. J. "A review of biomechanically informed breast image registration." *Physics in Medicine and Biology*, 61(2):p. R1 (2016). In press.

- Eiben et al. (2016a)

  Eiben, B., Vavourakis, V., Hipwell, J. H., Kabus, S., Buelow, T., Lorenz, C., Mertzanidou, T., Reis, S., Williams, N. R., Keshtgar, M., and Hawkes, D. J. “Symmetric biomechanically guided prone-to-supine breast image registration.” *Annals of Biomedical Engineering*, 44(1):pp.154-173 (2016). doi:10.1007/s10439-015-1496-z.

FORTHCOMING

- Eiben et al. (2016b)

  Eiben, B., Vavourakis, V., Hipwell, J. H., Kabus, S., Lorenz, C., Buelow, T., and Hawkes, D. J. “Surface driven biomechanical breast image registration.” In: “Medical Imaging 2016: Image-Guided Procedures, Robotic Interventions, and Modeling,” SPIE Proceedings (2016). Accepted for oral presentation.

- Vavourakis et al. (2016)

  Vavourakis, V., **Eiben, B.**, Hipwell, J. H., Keshtgar, M., and Hawkes, D. J. “Multiscale mechano-biological finite element modelling of oncoplastic breast surgery interventions: Numerical study towards surgical planning and cosmesis.” *Journal of the Royal Society Interface*. Under review.

B

APPENDIX

B.1 ROTATION AND SMALL STRAIN TENSOR

In section 2.1.1 basic strain measures are introduced such as the Green Strain tensor **E** and its linear approximation ε, the small strain tensor (2.7). Here a simple example of a rigid body rotation is used, to demonstrate that this type of transformation misleadingly results in non-zero strain response of the small strain tensor.

For simplicity this example is given in two dimensions, for which the small strain tensor ε becomes:

$$\begin{aligned}\varepsilon &= \frac{1}{2}\left(\nabla\mathbf{u} + (\nabla\mathbf{u})^{\mathrm{T}}\right) \\ &= \begin{pmatrix} \partial_x u_x & 1/2(\partial_y u_x + \partial_x u_y) \\ 1/2(\partial_y u_x + \partial_x u_y) & \partial_y u_y \end{pmatrix}.\end{aligned} \tag{B.1}$$

Let the deformation be a simple rotation of α about the coordinate centre described by the rotation tensor $\mathbf{R}(\alpha)$, such that the deformed coordinates are given as

$$\mathbf{x} = \mathbf{R}\mathbf{X} = \begin{pmatrix} \cos(\alpha) & -\sin(\alpha) \\ \sin(\alpha) & \cos(\alpha) \end{pmatrix} \begin{pmatrix} X \\ Y \end{pmatrix}. \tag{B.2}$$

Using (B.1) the small strain tensor for this example becomes

$$\varepsilon(\alpha) = \begin{pmatrix} \cos(\alpha) - 1 & 0 \\ 0 & cos(\alpha) - 1 \end{pmatrix}. \tag{B.3}$$

Hence the small strain tensor can only be regarded approximately zero for small rotations $\alpha \approx 0$ for which the well known approximation $\cos(\alpha) \approx 1$ holds.

Clearly, a rigid body rotation does not introduce strains to a body and thus the non-zero response of ε has to be taken into account, if this approximation is made.

The Green Strain tensor on the other hand, does not show this behaviour, and for any rigid body rotation results in a zero-tensor. Since the **E** in equation (2.6) only depends on the stretch tensor **U** and not on the rotation **R** when the deformation radient is decomposed according to (2.3).

B.2 TRUNCATION ERROR AND THE FINITE DIFFERENCE METHOD

The forward and backward difference quotient as used in the finite difference method can be derived from the Taylor series. This approximates a function f around x_0 with:

$$f(x_0 + ih) = f(x_0) + f'(x_0)ih + O(h^2) \tag{B.4}$$

Rewriting the above equation results in

$$f'(x_0) = \frac{f(x_0 + ih) - f(x_0)}{ih} + O(h), \tag{B.5}$$

the well known forward difference quotient.

To investigate the truncation accuracy of the central difference scheme, the Taylor expansion needs to be extended by one additional element:

$$f(x_0 + ih) = f(x_0) + f'(x_0)ih + \frac{f^{(2)}(x_0)}{2!}(ih)^2 + O(h^3) \tag{B.6}$$

Reformulating this for the equidistant but opposite position of x_0, one simply obtains

$$f(x_0 - ih) = f(x_0) - f'(x_0)ih + \frac{f^{(2)}(x_0)}{2!}(ih)^2 + O(h^3) \tag{B.7}$$

By subtracting equation (B.7) from (B.6) the third element of the sum on the right hand side of both equations vanishes resulting – due to the division by $2ih$ – in a truncation error of order $O(h^2)$:

$$f'(x_0) = \frac{f(x_0 + ih) - f(x_0 - ih)}{2ih} + O(h^2) \tag{B.8}$$

BIBLIOGRAPHY

Ahn, K.-H., Hargreaves, B. A., Alley, M. T., Horst, K. C., Luxton, G., Daniel, B. L., and Hristov, D. "MRI guidance for accelerated partial breast irradiation in prone position: Imaging protocol design and evaluation." *International Journal of Radiation Oncology*Biology*Physics*, **75**(1):pp. 285–293 (2009). doi:10.1016/j.ijrobp.2009.03.063.

Alderliesten, T., Loo, C., Paape, A., Muller, S., Rutgers, E., Peeters, M.-J. V., and Gilhuijs, K. "On the feasibility of MRI-guided navigation to demarcate breast cancer for breast-conserving surgery." *Medical Physics*, **37**(6):pp. 2617–2626 (2010). doi:10.1118/1.3429048.

Astola, J., Haavisto, P., and Neuvo, Y. "Vector median filters." *Proceedings of the IEEE*, **78**(4):pp. 678–689 (1990). doi:10.1109/5.54807.

Babarenda Gamage, T. P., Rajagopal, V., Nielsen, P. M. F., and Nash, M. P. "Patient-specific modeling of breast biomechanics with applications to breast cancer detection and treatment." In: Gefen, A. (editor), "Patient-Specific Modeling in Tomorrow's Medicine," volume 09 of *Studies in Mechanobiology, Tissue Engineering and Biomaterials*, pp. 379–412. Springer Berlin Heidelberg (2012). ISBN 978-3-642-24618-0. doi:10.1007/8415_2011_92.

Baglan, K. L., Martinez, A. A., Frazier, R. C., Kini, V. R., Kestin, L. L., Chen, P. Y., Edmundson, G., Mele, E., Jaffray, D., and Vicini, F. A. "The use of high-dose-rate brachytherapy alone after lumpectomy in patients with early-stage breast cancer treated with breast-conserving therapy." *International Journal of Radiation Oncology*Biology*Physics*, **50**(4):pp. 1003 – 1011 (2001). doi:10.1016/S0360-3016(01)01547-4.

Baglan, K. L., Sharpe, M. B., Jaffray, D., Frazier, R. C., Fayad, J., Kestin, L. L., Remouchamps, V., Martinez, A. A., Wong, J., and Vicini, F. A. "Accelerated partial breast irradiation using 3D conformal radiation therapy (3D-CRT)." *International Journal of Radiation Oncology*Biology*Physics*, **55**(2):pp. 302–311 (2003). doi:10.1016/S0360-3016(02)03811-7.

Bajcsy, R. and Kovačič, S. "Multiresolution elastic matching." *Computer Vision, Graphics, and Image Processing*, **46**(1):pp. 1 – 21 (1989). doi:10.1016/S0734-189X(89)80014-3.

Bartelink, H., Horiot, J.-C., Poortmans, P., Struikmans, H., Van den Bogaert, W., Barillot, I., Fourquet, A., Borger, J., Jager, J., Hoogenraad, W., Collette, L., and Pierart, M. "Recurrence rates after treatment of breast cancer with standard radiotherapy with or without additional radiation." *New England Journal of Medicine*, **345**(19):pp. 1378–1387 (2001). doi:10.1056/NEJMoa010874.

Bathe, K. *Finite Element Procedures*. Prentice Hall (2006). ISBN 9780979004902.

Beg, M. F., Miller, M. I., Trouvé, A., and Younes, L. "Computing large deformation metric mappings via geodesic flows of diffeomorphisms." *International Journal of Computer Vision*, **61**(2):pp. 139–157 (2005). doi:10.1023/B:VISI.0000043755.93987.aa.

Belytschko, T., Liu, W. K., and Moran, B. *Nonlinear Finite Elements for Continua and Structures*. Wiley-Blackwell (2000). ISBN 0471987743.

Benitez, P. R., Keisch, M. E., Vicini, F., Stolier, A., Scroggins, T., Walker, A., White, J., Hedberg, P., Hebert, M., Arthur, D., Zannis, V., Quiet, C., Streeter, O., and Silverstein, M. "Five-year results: the initial clinical trial of mammosite balloon brachytherapy for partial breast irradiation in early-stage breast cancer." *The American Journal of Surgery*, **194**(4):pp. 456–462 (2007). doi:10.1016/j.amjsurg.2007.06.010.

Besl, P. and McKay, N. "A method for registration of 3-D shapes." *IEEE Transactions on Pattern Analysis and Machine Intelligence*, **14**(2):pp. 239–256 (1992). doi:10.1109/34.121791.

Bonet, J. and Wood, R. D. *Nonlinear Continuum Mechanics for Finite Element Analysis*. Cambridge University Press, 2nd edition (2008). ISBN 0521838703.

Bowden, A. E., Rabbitt, R. D., and Weiss, J. A. “Anatomical registration and segmentation by warping template finite element models.” In: Jacques, S. L. (editor), “Laser-Tissue Interaction IX,” volume 3254 of *SPIE Proceedings*, pp. 469–476 (1998). doi:10.1117/12.308198.

Bro-Nielsen, M. and Gramkow, C. *Visualization in Biomedical Computing: 4th International Conference, VBC'96 Hamburg, Germamy, September 22–25, 1996 Proceedings*, chapter Fast Fluid Registration of medical images, pp. 265–276. Springer Berlin Heidelberg, Berlin, Heidelberg (1996). ISBN 978-3-540-70739-4. doi:10.1007/BFb0046964.

Broit, C. *Optimal Registration of Deformed Images*. Ph.D. thesis, University of Pennsylvania (1981).

Burger, M., Modersitzki, J., and Ruthotto, L. “A hyperelastic regularization energy for image registration.” *SIAM Journal on Scientific Computing*, **35**(1):pp. B132–B148 (2013). doi:10.1137/110835955.

Cancer Research UK. “Breast cancer statistics.” online (2012). URL accessed 13.09.2013.
URL `www.cancerresearchuk.org/cancer-info/cancerstats/types/breast/`

Cardoso, M. J., Cardoso, J., Amaral, N., Azevedo, I., Barreau, L., Bernardo, M., Christie, D., Costa, S., Fitzal, F., Fougo, J. L., Johansen, J., Macmillan, D., Mano, M. P., Regolo, L., Rosa, J., Teixeira, L., and Vrieling, C. “Turning subjective into objective: The BCCT.core software for evaluation of cosmetic results in breast cancer conservative treatment.” *The Breast*, **16**(5):pp. 456–461 (2007). doi:10.1016/j.breast.2007.05.002.

Cardoso, M. J., Clarkson, M. J., Ridgway, G. R., Modat, M., Fox, N. C., and Ourselin, S. “LoAd: A locally adaptive cortical segmentation algorithm.” *NeuroImage*, **56**(3):pp. 1386–1397 (2011). doi:10.1016/j.neuroimage.2011.02.013.

Carter, T., Tanner, C., Beechey-Newman, N., Barratt, D., and Hawkes, D. “MR navigated breast surgery: Method and initial clinical experience.” In: Metaxas, D., Axel, L., Fichtinger, G., and Székely, G. (editors), “Medical Image Computing and Computer-Assisted Intervention - MICCAI 2008," volume 5242 of *Lecture Notes in Computer Science*, pp. 356–363. Springer Berlin / Heidelberg (2008). doi:10.1007/978-3-540-85990-1_43.

Carter, T., Tanner, C., Crum, W., Beechey-Newman, N., and Hawkes, D. "A framework for image-guided breast surgery." In: Yang, G.-Z., Jiang, T., Shen, D., Gu, L., and Yang, J. (editors), "Medical Imaging and Augmented Reality," volume 4091 of *Lecture Notes in Computer Science*, pp. 203–210. Springer Berlin / Heidelberg (2006a). ISBN 978-3-540-37220-2. doi:10.1007/11812715_26.

Carter, T., Tanner, C., Crum, W., and Hawkes, D. "Biomechanical model initialized non-rigid registration for image-guided breast surgery." In: Miller, K. and Poulikakos, D. (editors), "Computational Biomechanics for Medicine (I)," MICCAI Workshop Proceedings, pp. 104–111 (2006b).

Carter, T. J., Sermesant, M., Cash, D. M., Barratt, D. C., Tanner, C., and Hawkes, D. J. "Application of soft tissue modelling to image-guided surgery." *Medical Engineering & Physics*, **27**(10):pp. 893–909 (2005). doi:10.1016/j.medengphy.2005.10.005.

Carter, T. J., Tanner, C., and Hawkes, D. J. "Determining material properties of the breast for image-guided surgery." In: Miga, M. I. and Wong, K. H. (editors), "Medical Imaging 2009: Visualization, Image-Guided Procedures, and Modeling," volume 7261 of *SPIE Proceedings*, pp. 726124–726124–10 (2009). doi:10.1117/12.810092.

Christensen, G., Rabbitt, R., and Miller, M. "Deformable templates using large deformation kinematics." *Image Processing, IEEE Transactions on*, **5**(10):pp. 1435–1447 (1996). doi:10.1109/83.536892.

Conley, R. H., Meszoely, I. M., Pheiffer, T. S., Weis, J. A., Yankeelov, T. E., and Miga, M. I. "Image to physical space registration of supine breast MRI for image guided breast surgery." In: Yaniv, Z. R. and Holmes, D. R. (editors), "Medical Imaging 2014: Image-Guided Procedures, Robotic Interventions, and Modeling," volume 9036 of *SPIE Proceedings*, pp. 90362N–90362N–8 (2014). doi:10.1117/12.2043817.

Conley, R. H., Meszoely, I. M., Weis, J. A., Pheiffer, T. S., Arlinghaus, L. R., Yankeelov, T. E., and Miga, M. I. "Realization of a biomechanical model-assisted image guidance system for breast cancer surgery using supine MRI." *International Journal of Computer Assisted Radiology and Surgery*, pp. 1–12 (2015). doi:10.1007/s11548-015-1235-9.

Courant, R., Friedrichs, K., and Lewy, H. "Über die partiellen Differenzengleichungen der mathematischen Physik." *Mathematische Annalen*, **100**(1):pp. 32–74 (1928). doi:10.1007/BF01448839.

Crum, W., Camara, O., and Hawkes, D. "Methods for inverting dense displacement fields: Evaluation in brain image registration." In: Ayache, N., Ourselin, S., and Maeder, A. (editors), "Medical Image Computing and Computer-Assisted Intervention – MICCAI 2007," volume 4791 of *Lecture Notes in Computer Science*, pp. 900–907. Springer Berlin / Heidelberg (2007). doi:10.1007/978-3-540-75757-3_109.

Crum, W., Hill, D., and Hawkes, D. "Information theoretic similarity measures in non-rigid registration." In: Taylor, C. and Noble, J. A. (editors), "Information Processing in Medical Imaging," volume 2732 of *Lecture Notes in Computer Science*, pp. 378–387. Springer Berlin Heidelberg (2003). ISBN 978-3-540-40560-3. doi:10.1007/978-3-540-45087-0_32.

Crum, W. R., Tanner, C., and Hawkes, D. J. "Anisotropic multi-scale fluid registration: evaluation in magnetic resonance breast imaging." *Physics in Medicine and Biology*, **50**(21):pp. 5153–5174 (2005). doi:10.1088/0031-9155/50/21/014.

Curtis, C., Shah, S. P., Chin, S., Turashvili, G., Rueda, O. M., Dunning, M. J., Speed, D., Lynch, A. G., Samarajiwa, S., Yuan, Y., Graf, S., Ha, G., Haffari, G., Bashashati, A., Russell, R., McKinney, S., Langerod, A., Green, A., Provenzano, E., Wishart, G., Pinder, S., Watson, P., Markowetz, F., Murphy, L., Ellis, I., Purushotham, A., Borresen-Dale, A., Brenton, J. D., Tavare, S., Caldas, C., and Aparicio, S. "The genomic and transcriptomic architecture of 2,000 breast tumours reveals novel subgroups." *Nature*, **486**(7403):pp. 346–352 (2012). doi:10.1038/nature10983.

Deisboeck, T. S., Wang, Z., Macklin, P., and Cristini, V. "Multiscale cancer modeling." *Annual Review of Biomedical Engineering*, **13**(1):pp. 127–155 (2011). doi:10.1146/annurev-bioeng-071910-124729. PMID: 21529163.

del Palomar, A. P., Calvo, B., Herrero, J., López, J., and Doblaré, M. "A finite element model to accurately predict real deformations of the breast." *Medical Engineering & Physics*, **30**(9):pp. 1089–1097 (2008). doi:10.1016/j.medengphy.2008.01.005.

Dennis, J. E., Jr. and Torczon, V. "Direct Search Methods on Parallel Machines." *SIAM Journal on Optimization*, **1**(4):pp. 448–474 (1991). doi:10.1137/0801027.

Dice, L. R. "Measures of the amount of ecologic association between species." *Ecology*, **26**(3):pp. 297–302 (1945). doi:10.2307/1932409.

Dua, S. M., Gray, R. J., and Keshtgar, M. "Strategies for localisation of impalpable breast lesions." *The Breast*, **20**(3):pp. 246–253 (2011). doi:10.1016/j.breast.2011.01.007.

Dupuis, P., Grenander, U., and Miller, M. "Variational problems on flows of diffeomorphisms for image matching." *QUARTERLY OF APPLIED MATHEMATICS*, **56**(3):pp. 587–600 (1998).

Edelman, L. B., Eddy, J. A., and Price, N. D. "In silico models of cancer." *Wiley Interdisciplinary Reviews: Systems Biology and Medicine*, **2**(4):pp. 438–459 (2010). doi:10.1002/wsbm.75.

Eder, M., Raith, S., Jalali, J., Volf, A., Settles, M., Machens, H.-G., and Kovacs, L. "Comparison of different material models to simulate 3-D breast deformations using finite element analysis." *Annals of Biomedical Engineering*, **42**(4):pp. 843–857 (2014). doi:10.1007/s10439-013-0962-8.

Eiben, B., Han, L., Hipwell, J. H., Mertzanidou, T., Kabus, S., Buelow, T., Lorenz, C., Newstead, G. M., Abe, H., Keshtgar, M., Ourselin, S., and Hawkes, D. J. "Biomechanically guided prone-to-supine image registration of breast MRI using an estimated reference state." In: "IEEE 10th International Symposium on Biomedical Imaging (ISBI)," pp. 214–217 (2013). doi:10.1109/ISBI.2013.6556450.

Eiben, B., Vavourakis, V., Hipwell, J. H., Kabus, S., Buelow, T., Lorenz, C., Mertzanidou, T., Reis, S., Williams, N. R., Keshtgar, M., and Hawkes, D. J. "Symmetric biomechanically guided prone-to-supine breast image registration." *Annals of Biomedical Engineering*, **44**(1):pp. 154–173 (2016a). doi:10.1007/s10439-015-1496-z.

Eiben, B., Vavourakis, V., Hipwell, J. H., Kabus, S., Lorenz, C., Buelow, T., and Hawkes, D. J. “Breast deformation modelling: comparison of methods to obtain a patient specific unloaded configuration.” In: Yaniv, Z. R. and Holmes, D. R. (editors), “Medical Imaging 2014: Image-Guided Procedures, Robotic Interventions, and Modeling,” volume 9036 of *SPIE Proceedings*, pp. 903615–903615–8 (2014). doi:10.1117/12.2043607.

Eiben, B., Vavourakis, V., Hipwell, J. H., Kabus, S., Lorenz, C., Buelow, T., and Hawkes, D. J. “Surface driven biomechanical breast image registration.” In: “Medical Imaging 2016: Image-Guided Procedures, Robotic Interventions, and Modeling,” SPIE Proceedings (2016b). Accepted for oral presentation.

European Cancer Observatory. online (2012). Accessed 10.12.2015.
URL `http://eco.iarc.fr/EUCAN`

Ferlay, J., Steliarova-Foucher, E., Lortet-Tieulent, J., Rosso, S., Coebergh, J. W. W., Comber, H., Forman, D., and Bray, F. “Cancer incidence and mortality patterns in europe: Estimates for 40 countries in 2012.” *European Journal of Cancer*, **49**(6):pp. 1374–1403 (2013). doi:10.1016/j.ejca.2012.12.027.

Ferrant, M., Nabavi, A., Macq, B., Jolesz, F. A., Kikinis, R., and Warfield, S. K. “Registration of 3-d intraoperative MR images of the brain using a finite-element biomechanical model.” *Medical Imaging, IEEE Transactions on*, **20**(12):pp. 1384–1397 (2001). doi:10.1109/42.974933.

Field, D. A. “Laplacian smoothing and delaunay triangulations.” *Communications in Applied Numerical Methods*, **4**(6):pp. 709–712 (1988). doi:10.1002/cnm.1630040603.

Fisher, B., Anderson, S., Bryant, J., Margolese, R. G., Deutsch, M., Fisher, E. R., Jeong, J.-H., and Wolmark, N. “Twenty-year follow-up of a randomized trial comparing total mastectomy, lumpectomy, and lumpectomy plus irradiation for the treatment of invasive breast cancer.” *New England Journal of Medicine*, **347**(16):pp. 1233–1241 (2002). doi:10.1056/NEJMoa022152.

Foley, J. D., van Dam, A., Feiner, S. K., and Hughes, J. F. *Computer Graphics: Principles and Practice*. Addison-Wesley Longman Publishing Co., Inc., Boston, MA, USA, 2nd edition (1990). ISBN 0-201-12110-7.

Fornberg, B. "Generation of finite difference formulas on arbitrarily spaced grids." *Mathematics of Computation*, **51**:pp. 699–706 (1988). doi:10.1090/S0025-5718-1988-0935077-0.

Gefen, A. and Dilmoney, B. "Mechanics of the normal woman's breast." *Technol Health Care*, **15**(4):pp. 259–271 (2007).

Geuzaine, C. and Remacle, J.-F. "Gmsh: A 3-D finite element mesh generator with built-in pre- and post-processing facilities." *International Journal for Numerical Methods in Engineering*, **79**(11):pp. 1309–1331 (2009). doi:10.1002/nme.2579.

Govindjee, S. and Mihalic, P. A. "Computational methods for inverse finite elastostatics." *Computer Methods in Applied Mechanics and Engineering*, **136**(1–2):pp. 47–57 (1996). doi:10.1016/0045-7825(96)01045-6.

Govindjee, S. and Mihalic, P. A. "Computational methods for inverse deformations in quasi-incompressible finite elasticity." *International Journal for Numerical Methods in Engineering*, **43**(5):pp. 821–838 (1998). doi:10.1002/(SICI)1097-0207(19981115)43:5<821::AID-NME453>3.0.CO;2-C.

Han, L., Hipwell, J., Taylor, Z., Tanner, C., Ourselin, S., and Hawkes, D. "Fast deformation simulation of breasts using GPU-based dynamic explicit finite element method." In: Martí, J., Oliver, A., Freixenet, J., and Martí, R. (editors), "Digital Mammography," volume 6136 of *Lecture Notes in Computer Science*, pp. 728–735. Springer Berlin / Heidelberg (2010). doi:10.1007/978-3-642-13666-5_98.

Han, L., Hipwell, J. H., Eiben, B., Barratt, D., Modat, M., Ourselin, S., and Hawkes, D. J. "A nonlinear biomechanical model based registration method for aligning prone and supine MR breast images." *IEEE Transactions on Medical Imaging*, **33**(3):pp. 682–694 (2014). doi:10.1109/TMI.2013.2294539.

Han, L., Hipwell, J. H., Mertzanidou, T., Carter, T., Modat, M., Ourselin, S., and Hawkes, D. J. "A hybrid fem-based method for aligning prone and supine images for image guided breast surgery." In: "IEEE International Symposium on Biomedical Imaging (ISBI): From Nano to Macro," pp. 1239–1242 (2011). doi:10.1109/ISBI.2011.5872626.

Han, L., Hipwell, J. H., Tanner, C., Taylor, Z., Mertzanidou, T., Cardoso, J., Ourselin, S., and Hawkes, D. J. "Development of patient-specific biomechanical models for predicting large breast deformation." *Physics in Medicine and Biology*, **57**(2):pp. 455–472 (2012). doi:10.1088/0031-9155/57/2/455.

Haupt, P. *Continuum Mechanics and Theory of Materials*. Advanced Texts in Physics. Springer Berlin Heidelberg, Berlin, Heidelberg (2002). ISBN 978-3-642-07718-0, 978-3-662-04775-0.

Hill, D. L. G., Batchelor, P. G., Holden, M., and Hawkes, D. J. "Medical image registration." *Physics in Medicine and Biology*, **46**(3):pp. R1–R45 (2001). doi:10.1088/0031-9155/46/3/201.

Hill-Kayser, C. E., Vachani, C., Hampshire, M. K., Lullo, G. A. D., and Metz, J. M. "Cosmetic outcomes and complications reported by patients having undergone breast-conserving treatment." *International Journal of Radiation Oncology*Biology*Physics*, **83**(3):pp. 839–844 (2012). doi:10.1016/j.ijrobp.2011.08.013.

Hipwell, J. H., Vavourakis, V., Han, L., Mertzanidou, T., Eiben, B., and Hawkes, D. J. "A review of biomechanically informed breast image registration." *Physics in Medicine and Biology*, **61**(2):p. R1 (2016). doi:10.1088/0031-9155/61/2/R1.

Hjelmstad, K. D. *Fundamentals of Structural Mechanics*. Springer Science+Business Media, Inc., 2nd edition (2004). ISBN 0-387-23330-X.

Holzapfel, G. A. *Nonlinear Solid Mechanics: A Continuum Approach for Engineering*. John Wiley & Sons (2000). ISBN 0471823198.

Hwang, E. S., Lichtensztajn, D. Y., Gomez, S. L., Fowble, B., and Clarke, C. A. "Survival after lumpectomy and mastectomy for early stage invasive breast cancer." *Cancer*, **119**(7):pp. 1402–1411 (2013). doi:10.1002/cncr.27795.

Ibrahimbegovic, A. *Nonlinear Solid Mechanics*. Solid Mechanics and its Applications. Springer Netherlands (2009). ISBN 978-90-481-2330-8. doi:10.1007/978-90-481-2331-5.

International Organization for Standardization (ISO), Geneva, Switzerland. "13485:2003." (2003). URL accessed 10.2.2016.
URL https://www.iso.org/obp/ui/#!iso:std:36786:en

Johnsen, S., Taylor, Z., Clarkson, M., Hipwell, J., Modat, M., Eiben, B., Han, L., Hu, Y., Mertzanidou, T., Hawkes, D., and Ourselin, S. "Niftysim: A GPU-based nonlinear finite element package for simulation of soft tissue biomechanics." *International Journal of Computer Assisted Radiology and Surgery*, **10**(7):pp. 1077–1095 (2014). doi:10.1007/s11548-014-1118-5.

Kabus, S., Klinder, T., Murphy, K., Ginneken, B., Lorenz, C., and Pluim, J. P. W. *Medical Image Computing and Computer-Assisted Intervention – MICCAI 2009: 12th International Conference, London, UK, September 20-24, 2009, Proceedings, Part I*, chapter Evaluation of 4D-CT Lung Registration, pp. 747–754. Springer Berlin Heidelberg, Berlin, Heidelberg (2009). doi:10.1007/978-3-642-04268-3_92.

Kabus, S. and Lorenz, C. "Fast elastic image registration." In: "Grand Challenges in Medical Image Analysis," MICCAI 2010, pp. 81–89 (2010).

Kaye, A., Stepto, R. F. T., Work, W. J., Alemán, J. V., and Malkin, A. Y. "Definition of terms relating to the non-ultimate mechanical properties of polymers (recommendations 1998)." *Pure and Applied Chemistry*, **70**(3):pp. 701–754 (2009). doi:10.1351/pac199870030701.

Keisch, M., Vicini, F., Kuske, R. R., Hebert, M., White, J., Quiet, C., Arthur, D., Scroggins, T., and Streeter, O. "Initial clinical experience with the mammosite breast brachytherapy applicator in women with early-stage breast cancer treated with breast-conserving therapy." *International Journal of Radiation Oncology*Biology*Physics*, **55**(2):pp. 289–293 (2003). doi:10.1016/S0360-3016(02)04277-3.

Kennedy, J. and Eberhart, R. "Particle swarm optimization." In: "Neural Networks, 1995. Proceedings., IEEE International Conference on," volume 4, pp. 1942–1948 (1995). doi:10.1109/ICNN.1995.488968.

Kirby, A. M., Yarnold, J. R., Evans, P. M., Morgan, V. A., Schmidt, M. A., Scurr, E. D., and deSouza, N. M. "Tumor bed delineation for partial breast and breast boost radiotherapy planned in the prone position: What does MRI add to X-ray CT localization of titanium clips placed in the excision cavity wall?" *International Journal of Radiation Oncology*Biology*Physics*, **74**(4):pp. 1276–1282 (2009). doi:10.1016/j.ijrobp.2009.02.028.

Kirkpatrick, S., Gelatt, C. D., and Vecchi, M. P. "Optimization by simulated annealing." *Science*, **220**(4598):pp. 671–680 (1983). doi:10.1126/science.220.4598.671.

Kolda, T. G., Lewis, R. M., and Torczon, V. "Optimization by direct search: New perspectives on some classical and modern methods." *SIAM Review*, **45**(3):pp. 385–482 (2003). doi:10.1137/S003614450242889.

Kopans, D. B. *Breast Imaging*. Lippincott Williams & Wilkins (2007). ISBN 9780781747684.

Krouskop, T. A., Wheeler, T. M., Kallel, F., Garra, B. S., and Hall, T. "Elastic moduli of breast and prostate tissues under compression." *Ultrasonic Imaging*, **20**(4):pp. 260–274 (1998). doi:10.1177/016173469802000403.

Lago, M. A., Martinez-Martinez, F., Ruperez, M. J., Monserrat, C., and Alcaniz, M. "Breast prone-to-supine deformation and registration using a time-of-flight camera." In: "4th IEEE RAS EMBS International Conference on Biomedical Robotics and Biomechatronics (BioRob)," pp. 1161–1163 (2012). doi:10.1109/BioRob.2012.6290683.

Lapuebla-Ferri, A., del Palomar, A. P., Herrero, J., and Jiménez-Mocholí, A.-J. "A patient-specific fe-based methodology to simulate prosthesis insertion during an augmentation mammoplasty." *Medical Engineering & Physics*, **33**(9):pp. 1094–1102 (2011). doi:10.1016/j.medengphy.2011.04.014.

Lee, A., Schnabel, J., Rajagopal, V., Nielsen, P., and Nash, M. "Breast image registration by combining finite elements and free-form deformations." In: Martí, J., Oliver, A., Freixenet, J., and Martí, R. (editors), "Digital Mammography," volume 6136 of *Lecture Notes in Computer Science*, pp. 736–743. Springer Berlin / Heidelberg (2010). doi:10.1007/978-3-642-13666-5_99.

Loop, C. T. *Smooth Subdivision Surfaces Based on Triangles*. Master's thesis, Department of Mathematics, The University of Utah (1987).
URL `http://research.microsoft.com/apps/pubs/default.aspx?id=68540`

Lorensen, W. E. and Cline, H. E. "Marching cubes: A high resolution 3d surface construction algorithm." *ACM SIGGRAPH Computer Graphics*, **21**(4):pp. 163–169 (1987). doi:10.1145/37402.37422.

Lu, J., Zhou, X., and Raghavan, M. L. "Computational method of inverse elastostatics for anisotropic hyperelastic solids." *International Journal for Numerical Methods in Engineering*, **69**(6):pp. 1239–1261 (2007). doi:10.1002/nme.1807.

Masoudi-Nejad, A., Bidkhori, G., Ashtiani, S. H., Najafi, A., Bozorgmehr, J. H., and Wang, E. "Cancer systems biology and modeling: Microscopic scale and multiscale approaches." *Seminars in Cancer Biology*, **30**:pp. 60 – 69 (2015). doi:10.1016/j.semcancer.2014.03.003.

McClelland, J. R., Hughes, S., Modat, M., Qureshi, A., Ahmad, S., Landau, D. B., Ourselin, S., and Hawkes, D. J. "Inter-fraction variations in respiratory motion models." *Physics in Medicine and Biology*, **56**(1):pp. 251–272 (2011).

McKinnon, K. I. M. "Convergence of the Nelder–Mead Simplex Method to a Nonstationary Point." *SIAM Journal on Optimization*, **9**(1):pp. 148–158 (1998). doi:10.1137/S1052623496303482.

Mertzanidou, T., Hipwell, J., Johnsen, S., Han, L., Eiben, B., Taylor, Z., Ourselin, S., Huisman, H., Mann, R., Bick, U., Karssemeijer, N., and Hawkes, D. "MRI to X-ray mammography intensity-based registration with simultaneous optimisation of pose and biomechanical transformation parameters." *Medical Image Analysis*, **18**(4):pp. 674–683 (2014). doi:10.1016/j.media.2014.03.003.

Metcalfe, P., Liney, G. P., Holloway, L., Walker, A., Barton, M., Delaney, G. P., Vinod, S., and Tomé, W. "The potential for an enhanced role for mri in radiation-therapy treatment planning." *Technology in Cancer Research & Treatment*, **12**(5):pp. 429–446 (2013). doi:10.7785/tcrt.2012.500342.

Miller, M. I., Christensen, G. E., Amit, Y., and Grenander, U. "Mathematical textbook of deformable neuroanatomies." *Proceedings of the National Academy of Sciences*, **90**(24):pp. 11944–11948 (1993).

Modat, M., Ridgway, G. R., Taylor, Z. A., Lehmann, M., Barnes, J., Hawkes, D. J., Fox, N. C., and Ourselin, S. "Fast free-form deformation using graphics processing units." *Computer Methods and Programs in Biomedicine*, **98**(3):pp. 278–284 (2010). doi:10.1016/j.cmpb.2009.09.002.

Modersitzki, J. *Numerical Methods for Image Registration*. Numerical Mathematics and Scientific Computation. Oxford University Press (2004). ISBN 978-0-19-852841-8.

Modersitzki, J. *FAIR: flexible algorithms for image registration*. Society for Industrial and Applied Mathematics, Philadelphia (2009). ISBN 9780898716900 089871690X.

Morin, R., Eiben, B., Bidaut, L., Hipwell, J. H., Evans, A., and Hawkes, D. J. "3D ultrasound simulation based on a biomechanical model of prone MRI in breast cancer imaging." In: "IEEE 12th International Symposium on Biomedical Imaging (ISBI)," pp. 264–267 (2015). doi:10.1109/ISBI.2015.7163864.

Nelder, J. A. and Mead, R. "A simplex method for function minimization." *The Computer Journal*, **7**(4):pp. 308–313 (1965). doi:10.1093/comjnl/7.4.308.

NICE, National Institute For Health and Care Excellence. "Early and locally advanced breast cancer: Diagnosis and treatment (CG80)." online (2009). URL accessed 5.6.2015.
URL `http://www.nice.org.uk/guidance/cg80`

Offersen, B. V., Overgaard, M., Kroman, N., and Overgaard, J. "Accelerated partial breast irradiation as part of breast conserving therapy of early breast carcinoma: A systematic review." *Radiotherapy and Oncology*, **90**(1):pp. 1–13 (2009). doi:10.1016/j.radonc.2008.08.005.

Ogden, R. W. "Large deformation isotropic elasticity - on the correlation of theory and experiment for incompressible rubberlike solids." *Proceedings of the Royal*

Society of London A: Mathematical, Physical and Engineering Sciences, **326**(1567):pp. 565–584 (1972). doi:10.1098/rspa.1972.0026.

O'Hagan, J. J. and Samani, A. "Measurement of the hyperelastic properties of 44 pathological ex vivo breast tissue samples." *Physics in Medicine and Biology*, **54**(8):pp. 2557–2569 (2009). doi:10.1088/0031-9155/54/8/020.

Olivotto, I. A., Whelan, T. J., Parpia, S., Kim, D.-H., Berrang, T., Truong, P. T., Kong, I., Cochrane, B., Nichol, A., Roy, I., Germain, I., Akra, M., Reed, M., Fyles, A., Trotter, T., Perera, F., Beckham, W., Levine, M. N., and Julian, J. A. "Interim cosmetic and toxicity results from RAPID: A randomized trial of accelerated partial breast irradiation using three-dimensional conformal external beam radiation therapy." *Journal of Clinical Oncology*, **31**(32):pp. 4038–4045 (2013). doi:10.1200/JCO.2013.50.5511.

Papież, B. W., Heinrich, M. P., Fehrenbach, J., Risser, L., and Schnabel, J. A. "An implicit sliding-motion preserving regularisation via bilateral filtering for deformable image registration." *Medical Image Analysis*, **18**(8):pp. 1299–1311 (2014). doi:10.1016/j.media.2014.05.005. Special Issue on the 2013 Conference on Medical Image Computing and Computer Assisted Intervention.

Park, C. C., Mitsumori, M., Nixon, A., Recht, A., Connolly, J., Gelman, R., Silver, B., Hetelekidis, S., Abner, A., Harris, J. R., and Schnitt, S. J. "Outcome at 8 years after breast-conserving surgery and radiation therapy for invasive breast cancer: Influence of margin status and systemic therapy on local recurrence." *Journal of Clinical Oncology*, **18**(8):pp. 1668–1675 (2000).

Patete, P., Iacono, M. I., Spadea, M. F., Trecate, G., Vergnaghi, D., Mainardi, L. T., and Baroni, G. "A multi-tissue mass-spring model for computer assisted breast surgery." *Medical Engineering & Physics*, **35**(1):pp. 47–53 (2013). doi:10.1016/j.medengphy.2012.03.008.

Pathmanathan, P., Gavaghan, D. J., Whiteley, J. P., Chapman, S. J., and Brady, J. M. "Predicting tumor location by modeling the deformation of the breast." *IEEE Transactions on Biomedical Engineering*, **55**(10):pp. 2471–2480 (2008). doi:10.1109/TBME.2008.925714.

Rabbitt, R. D., Weiss, J. A., Christensen, G. E., and Miller, M. I. “Mapping of hyperelastic deformable templates using the finite element method.” In: Melter, R. A., Wu, A. Y., Bookstein, F. L., and Green, W. D. K. (editors), “Vision Geometry IV,” volume 2573 of *SPIE Proceedings*, pp. 252–265 (1995). doi:10.1117/12.216419.

Rajagopal, V., Chung, J.-H., Bullivant, D., Nielsen, P. M. F., and Nash, M. P. “Determining the finite elasticity reference state from a loaded configuration.” *International Journal for Numerical Methods in Engineering*, **72**(12):pp. 1434–1451 (2007). doi:10.1002/nme.2045.

Rajagopal, V., Lee, A., Chung, J.-H., Warren, R., Highnam, R. P., Nash, M. P., and Nielsen, P. M. F. “Creating individual-specific biomechanical models of the breast for medical image analysis.” *Academic Radiology*, **15**(11):pp. 1425–1436 (2008a). doi:10.1016/j.acra.2008.07.017.

Rajagopal, V., Nash, M., Highnam, R., and Nielsen, P. “The breast biomechanics reference state for multi-modal image analysis.” In: Krupinski, E. (editor), “Digital Mammography,” volume 5116 of *Lecture Notes in Computer Science*, pp. 385–392. Springer Berlin / Heidelberg (2008b). doi:10.1007/978-3-540-70538-3_54.

Romestaing, P., Lehingue, Y., Carrie, C., Coquard, R., Montbarbon, X., Ardiet, J. M., Mamelle, N., and Gérard, J. P. “Role of a 10-gy boost in the conservative treatment of early breast cancer: results of a randomized clinical trial in lyon, france.” *Journal of Clinical Oncology*, **15**(3):pp. 963–8 (1997).

Roose, L., Loeckx, D., Mollemans, W., Maes, F., and Suetens, P. “Adaptive boundary conditions for physically based follow-up breast MR image registration.” In: Metaxas, D., Axel, L., Fichtinger, G., and Székely, G. (editors), “Medical Image Computing and Computer-Assisted Intervention – MICCAI 2008,” volume 5242 of *Lecture Notes in Computer Science*, pp. 839–846. Springer Berlin / Heidelberg (2008). doi:10.1007/978-3-540-85990-1_101.

Roose, L., Maerteleire, W. D., Mollemans, W., and Suetens, P. “Validation of different soft tissue simulation methods for breast augmentation.” In: Lemke, H. U., Inamura, K., Doi, K., Vannier, M. W., and Farman, A. G. (editors), “CARS 2005: Computer Assisted Radiology and Surgery, Proceedings of the 19th International

Congress and Exhibition," volume 1281 of *International Congress Series*, pp. 485–490 (2005). doi:10.1016/j.ics.2005.03.126.

Roose, L., Mollemans, W., Loeckx, D., Maes, F., and Suetens, P. "Biomechanically based elastic breast registration using mass tensor simulation." In: Larsen, R., Nielsen, M., and Sporring, J. (editors), "Medical Image Computing and Computer-Assisted Intervention – MICCAI 2006," volume 4191 of *Lecture Notes in Computer Science*, pp. 718–725. Springer Berlin / Heidelberg (2006). ISBN 978-3-540-44727-6. doi:10.1007/11866763_88.

Rueckert, D., Hayes, C., Studholme, C., Summers, P., Leach, M., and Hawkes, D. J. "Non-rigid registration of breast MR images using mutual information." In: Wells, W. M., Colchester, A., and Delp, S. (editors), "Medical Image Computing and Computer-Assisted Interventation - MICCAI'98," volume 1496 of *Lecture Notes in Computer Science*, pp. 1144–1152. Springer Berlin / Heidelberg (1998). ISBN 978-3-540-65136-9. doi:10.1007/BFb0056304.

Rueckert, D., Sonoda, L. I., Hayes, C., Hill, D. L. G., Leach, M. O., and Hawkes, D. J. "Nonrigid registration using free-form deformations: application to breast MR images." *IEEE Transactions on Medical Imaging*, **18**(8):pp. 712–721 (1999). doi:10.1109/42.796284.

Ruiter, N. V., Stotzka, R., Muller, T.-O., Gemmeke, H., Reichenbach, J., and Kaiser, W. "Model-based registration of X-ray mammograms and MR images of the female breast." *IEEE Transactions on Nuclear Science*, **53**(1):pp. 204–211 (2006). doi:10.1109/TNS.2005.862983.

Sabczynski, J., Barschdorf, H., Bülow, T., Cardoso, M. J., Cardoso, J. S., Clarke, A., Eiben, B., Gouveia, P., Hawkes, D. J., Hipwell, J. H., Keshtgar, M., Lacher, R., Kutra, D., Liefers, G.-J., Meetz, K., Molenkamp, B., Monteiro, J. P., Mosahebi, A., Oliveira, H. P., Sinkus, R., Stoyanov, D., Vavourakis, V., Velde, C. V. D., Williams, N., Young, S., and Zolfagharnasab, H. "Picture: Predicting the cosmetic outcome of breast cancer surgery." In: "Virtual Physiological Human Conference," (2014).

Samani, A., Bishop, J., Yaffe, M., and Plewes, D. "Biomechanical 3-D finite element modeling of the human breast using MRI data." *IEEE Transactions on Medical Imaging*, **20**(4):pp. 271–279 (2001). doi:10.1109/42.921476.

Samani, A. and Plewes, D. "An inverse problem solution for measuring the elastic modulus of intact ex vivo breast tissue tumours." *Physics in Medicine and Biology*, **52**(5):pp. 1247–1260 (2007). doi:10.1088/0031-9155/52/5/003.

Samani, A., Zubovits, J., and Plewes, D. "Elastic moduli of normal and pathological human breast tissues: an inversion-technique-based investigation of 169 samples." *Physics in Medicine and Biology*, **52**(6):pp. 1565–1576 (2007). doi:10.1088/0031-9155/52/6/002.

Schöberl, J. "NETGEN an advancing front 2D/3D-mesh generator based on abstract rules." *Computing and Visualization in Science*, **1**(1):pp. 41–52 (1997). doi:10.1007/s007910050004.

Schmidt-Richberg, A., Ehrhardt, J., Werner, R., and Handels, H. "Slipping objects in image registration: Improved motion field estimation with direction-dependent regularization." In: Yang, G.-Z., Hawkes, D., Rueckert, D., Noble, A., and Taylor, C. (editors), "Medical Image Computing and Computer-Assisted Intervention – MICCAI 2009: 12th International Conference," pp. 755–762. Springer Berlin Heidelberg, Berlin, Heidelberg (2009). ISBN 978-3-642-04268-3. doi:10.1007/978-3-642-04268-3_93.

Schmitz, A. C., van den Bosch, M. A. A. J., Loo, C. E., Mali, W. P. T. M., Bartelink, H., Gertenbach, M., Holland, R., Peterse, J. L., Rutgers, E. J. T., and Gilhuijs, K. G. "Precise correlation between MRI and histopathology - exploring treatment margins for MRI-guided localized breast cancer therapy." *Radiotherapy and Oncology*, **97**(2):pp. 225–232 (2010). doi:10.1016/j.radonc.2010.07.025.

Schnabel, J., Tanner, C., Castellano-Smith, A., Degenhard, A., Leach, M., Hose, D., Hill, D., and Hawkes, D. "Validation of nonrigid image registration using finite-element methods: application to breast MR images." *Medical Imaging, IEEE Transactions on*, **22**(2):pp. 238–247 (2003). doi:10.1109/TMI.2002.808367.

Schroeder, W., Martin, K., and Lorensen, B. *The Visualization Toolkit An Object-Oriented Approach To 3D Graphics*. Kitware, Inc., 4th edition (2006). ISBN 1-930934-19-X. URL accessed 4.5.2015.
URL `www.vtk.org`

Siegler, P., Ebrahimi, M., Holloway, C. M., Thevathasan, G., Plewes, D. B., and Martel, A. "Supine breast MRI and assessment of future clinical applications." *European Journal of Radiology*, **81, Supplement 1**:pp. S153–S155 (2012). doi:10.1016/S0720-048X(12)70064-5. Extended abstracts and Abstracts of the Sixth International Congress on MR-Mammography.

Siegler, P., Holloway, C. M., Causer, P., Thevathasan, G., and Plewes, D. B. "Supine breast MRI." *Journal of Magnetic Resonance Imaging*, **34**(5):pp. 1212–1217 (2011). doi:10.1002/jmri.22605.

Sinkus, R., Tanter, M., Catheline, S., Lorenzen, J., Kuhl, C., Sondermann, E., and Fink, M. "Imaging anisotropic and viscous properties of breast tissue by magnetic resonance-elastography." *Magnetic Resonance in Medicine*, **53**(2):pp. 372–387 (2005). doi:10.1002/mrm.20355.

Smith, B. D., Arthur, D. W., Buchholz, T. A., Haffty, B. G., Hahn, C. A., Hardenbergh, P. H., Julian, T. B., Marks, L. B., Todor, D. A., Vicini, F. A., Whelan, T. J., White, J., Wo, J. Y., and Harris, J. R. "Accelerated partial breast irradiation consensus statement from the american society for radiation oncology (ASTRO)." *International Journal of Radiation Oncology*Biology*Physics*, **74**(4):pp. 987–1001 (2009). doi:10.1016/j.ijrobp.2009.02.031.

Tan, T., Eiben, B., Platel, B., Zelst, J., Han, L., Mertzanidou, T., Johnsen, S., Hipwell, J., Mann, R., Hawkes, D., and Karssemeijer, N. "Registration of automated 3d breast ultrasound views." In: Martel, A., Hipwell, J., Schnabel, J., Nielsen, M., Nash, M., Kontos, D., and Karssemeijer, N. (editors), "MICCAI Workshop: Breast Image Analysis," (2013).

Tanner, C., Schnabel, J. A., Hill, D. L. G., Hawkes, D. J., Leach, M. O., and Hose, D. R. "Factors influencing the accuracy of biomechanical breast models." *Medical Physics*, **33**(6):pp. 1758–1769 (2006). doi:10.1118/1.2198315.

Tanner, C., White, M., Guarino, S., Hall-Craggs, M. A., Douek, M., and Hawkes, D. J. "Large breast compressions: Observations and evaluation of simulations." *Medical Physics*, **38**(2):pp. 682–690 (2011). doi:10.1118/1.3525837.

Taubin, G., Zhang, T., and Golub, G. "Optimal surface smoothing as filter design." In: Buxton, B. and Cipolla, R. (editors), "Computer Vision — ECCV '96," volume 1064 of *Lecture Notes in Computer Science*, pp. 283–292. Springer Berlin / Heidelberg (1996). ISBN 978-3-540-61122-6. doi:10.1007/BFb0015544.

Taylor, Z. A., Cheng, M., and Ourselin, S. "High-speed nonlinear finite element analysis for surgical simulation using graphics processing units." *IEEE Transactions on Medical Imaging*, **27**(5):pp. 650–663 (2008). doi:10.1109/TMI.2007.913112.

Tomasi, C. and Manduchi, R. "Bilateral filtering for gray and color images." In: "Sixth International Conference on Computer Vision, 1998," pp. 839–846 (1998). doi:10.1109/ICCV.1998.710815.

Trouve, A. "Diffeomorphisms groups and pattern matching in image analysis." *INTERNATIONAL JOURNAL OF COMPUTER VISION*, **28**(3):pp. 213–221 (1998). doi:10.1023/A:1008001603737.

Tustison, N., Avants, B., Cook, P., Zheng, Y., Egan, A., Yushkevich, P., and Gee, J. "N4ITK: Improved N3 bias correction." *IEEE Transactions on Medical Imaging*, **29**(6):pp. 1310–1320 (2010). doi:10.1109/TMI.2010.2046908.

Unnikrishnan, V. U., Unnikrishnan, G. U., and Reddy, J. N. "Biomechanics of breast tumor: effect of collagen and tissue density." *International Journal of Mechanics and Materials in Design*, **8**(3):pp. 257–267 (2012). doi:10.1007/s10999-012-9190-x.

Vaidya, J. S., Wenz, F., Bulsara, M., Tobias, J. S., Joseph, D. J., Keshtgar, M., Flyger, H. L., Massarut, S., Alvarado, M., Saunders, C., Eiermann, W., Metaxas, M., Sperk, E., Sütterlin, M., Brown, D., Esserman, L., Roncadin, M., Thompson, A., Dewar, J. A., Holtveg, H. M. R., Pigorsch, S., Falzon, M., Harris, E., Matthews, A., Brew-Graves, C., Potyka, I., Corica, T., Williams, N. R., and Baum, M. "Risk-adapted targeted intraoperative radiotherapy versus whole-breast radiotherapy for breast cancer: 5-year results for local control and overall survival from the targit-a randomised trial." *The Lancet*, **383**(9917):pp. 603–613 (2014). doi:10.1016/S0140-6736(13)61950-9.

Valette, S. and Chassery, J.-M. "Approximated centroidal voronoi diagrams for uniform polygonal mesh coarsening." *Computer Graphics Forum*, **23**(3):pp. 381–389 (2004). doi:10.1111/j.1467-8659.2004.00769.x.

Van Leemput, K., Maes, F., Vandermeulen, D., and Suetens, P. "Automated model-based tissue classification of MR images of the brain." *IEEE Transactions on Medical Imaging*, **18**(10):pp. 897–908 (1999). doi:10.1109/42.811270.

Vandemeulebroucke, J., Bernard, O., Rit, S., Kybic, J., Clarysse, P., and Sarrut, D. "Automated segmentation of a motion mask to preserve sliding motion in deformable registration of thoracic ct." *Medical Physics*, **39**(2):pp. 1006–1015 (2012). doi:10.1118/1.3679009.

Vavourakis, V., Eiben, B., Hipwell, J. H., Keshtgar, M., and Hawkes, D. "Multiscale mechano-biological finite element modelling of oncoplastic breast surgery interventions: Numerical study towards surgical planning and cosmesis." *Journal of the Royal Society Interface* (2016). Under review.

Vavourakis, V., Hipwell, J. H., and Hawkes, D. J. "An inverse finite element u/p-formulation to predict the unloaded state of in vivo biological soft tissues." *Annals of Biomedical Engineering*, **44**(1):pp. 187–201 (2015). doi:10.1007/s10439-015-1405-5.

Veress, A. I., Phatak, N., and Weiss, J. A. "Deformable image registration with hyperelastic warping." In: Suri, J. S., Wilson, D. L., and Laxminarayan, S. (editors), "Handbook of Biomedical Image Analysis: Registration Models," volume 3 of *Topics in Biomedical Engineering International Book Series*, pp. 487–533. Springer US (2005). ISBN 978-0-306-48607-4. doi:10.1007/0-306-48608-3_12.

Veress, A. I., Weiss, J. A., Klein, G. J., and Gullberg, G. T. "Quantification of 3D left ventricular deformation using hyperelastic warping: comparisons between MRI and PET imaging." In: "Computers in Cardiology, 2002," pp. 709–712 (2002). doi:10.1109/CIC.2002.1166871.

Veronda, D. R. and Westmann, R. A. “Mechanical characterization of skin – finite deformations.” *Journal of Biomechanics*, **3**(1):pp. 111–124 (1970). doi:10.1016/0021-9290(70)90055-2.

Waljee, J. F., Hu, E. S., Newman, L. A., and Alderman, A. K. “Predictors of re-excision among women undergoing breast-conserving surgery for cancer.” *Annals of Surgical Oncology*, **15**(5):pp. 1297–1303 (2008). doi:10.1245/s10434-007-9777-x.

Weed, D. W., Yan, D., Martinez, A. A., Vicini, F. A., Wilkinson, T. J., and Wong, J. “The validity of surgical clips as a radiographic surrogate for the lumpectomy cavity in image-guided accelerated partial breast irradiation.” *International Journal of Radiation Oncology*Biology*Physics*, **60**(2):pp. 484–492 (2004). doi:10.1016/j.ijrobp.2004.03.012.

Weiss, J. A., Rabbitt, R. D., Bowden, A. E., and Maker, B. N. “Incorporation of medical image data in finite element models to track strain in soft tissues.” In: Jacques, S. L. (editor), “Laser-Tissue Interaction IX,” volume 3254 of *SPIE Proceedings*, pp. 477–484 (1998). doi:10.1117/12.308199.

Wellman, P. S., Howe, R. D., Dalton, E., and Kern, K. A. “Breast tissue stiffness in compression is correlated to histological diagnosis.” Technical report, Harvard BioRobotics Laboratory (1999).

Wessel, C., Schnabel, J. A., and Brady, M. “Towards a more realistic biomechanical modelling of breast malignant tumours.” *Physics in Medicine and Biology*, **57**(3):p. 631 (2012). doi:10.1088/0031-9155/57/3/631.

West, J., Fitzpatrick, J. M., Wang, M. Y., Dawant, B. M., Maurer, C. R. J., Kessler, R. M., Maciunas, R. J., Barillot, C., Lemoine, D., Collignon, A., Maes, F., Suetens, P., Vandermeulen, D., van den Elsen, P. A., Napel, S., Sumanaweera, T. S., Harkness, B., Hemler, P. F., Hill, D. L. G., Hawkes, D. J., Studholme, C., Maintz, J. B. A., Viergever, M. A., Malandain, G., Pennec, X., Noz, M. E., Maguire, G. Q. J., Pollack, M., Pelizzari, C. A., Robb, R. A., Hanson, D., and Woods, R. P. “Comparison and evaluation of retrospective intermodality brain image registration techniques.” *Journal of Computer Assisted Tomography*, **21**(4):pp. 554–568 (1997). doi:10.1097/00004728-199707000-00007.

Whiteley, J. P., Gavaghan, D. J., Chapman, S. J., and Brady, J. M. "Non-linear modelling of breast tissue." *Mathematical Medicine and Biology*, **24**(3):pp. 327–345 (2007). doi:10.1093/imammb/dqm006.

Williams, C., Kakadaris, I., Ravi-Chandar, K., Miller, M. J., and Patrick, C. W. "Simulation studies for predicting surgical outcomes in breast reconstructive surgery." In: Ellis, R. E. and Peters, T. M. (editors), "Medical Image Computing and Computer-Assisted Intervention - MICCAI 2003," volume 2878 of *Lecture Notes in Computer Science*, pp. 9–16. Springer Berlin / Heidelberg (2003). ISBN 978-3-540-20462-6. doi:10.1007/978-3-540-39899-8_2.

Yanovsky, I., Le Guyader, C., Leow, A., Thompson, P., and Vese, L. "Nonlinear elastic registration with unbiased regularization in three dimensions." In: Miller, K. and Nielsen, P. M. (editors), "Computational Biomechanics for Medicine III," MICCAI 2008 Workshop Proceedings, pp. 56–67 (2008).

Yeh, E. D., Georgian-Smith, D., Raza, S., Bussolari, L., Pawlisz-Hoff, J., and Birdwell, R. L. "Positioning in breast MR imaging to optimize image quality." *RadioGraphics*, **34**(1):pp. E1–E17 (2014). doi:10.1148/rg.341125193.

Zienkiewicz, O. C., Taylor, R. L., and Zhu, J. Z. *The Finite Element Method: Its Basis and Fundamentals*. Elsevier Science (2013). ISBN 9780080951355.

Zyganitidis, C., Bliznakova, K., and Pallikarakis, N. "A novel simulation algorithm for soft tissue compression." *Medical & Biological Engineering & Computing*, **45**(7):pp. 661–669 (2007). doi:10.1007/s11517-007-0205-y.